ISTANBUL TECHNICAL UNIVERSITY ★ EURASIA INSTITUTE OF EARTH SCIENCES

SUBDUCTION ROLL BACK AND THE GENERATION OF WET AND DECOMPRESSION MELTING

M.Sc. THESIS

Mehmet Barış ŞEN

(602171007)

Department of Solid Earth Sciences

Geodynamics Programme

Thesis Advisor: Assoc. Prof. Dr. Oğuz H. Göğüş

JUNE 2019

ISTANBUL TEKNİK ÜNİVERSİTESİ ★ AVRASYA YER BİLİMLERİ ENSTİTÜSÜ

YİTİM ZONUNUN GERİ ÇEKİLMESİ, SULU VE KURU ERİYİK ÜRETİMİ

YÜKSEK LİSANS TEZİ

Mehmet Barış ŞEN

(602171007)

Katı Yer Bilimleri Departmanı

Jeodinamik Programı

Tez Danışmanı: Doç. Dr. Oğuz H. Göğüş

HAZİRAN 2019

Mehmet Barış ŞEN, a M.Sc. student of ITU Eurasia Institute of Earth Science student ID 602171007, successfully defended the thesis entitled "SUBDUCTION ROLL BACK and THE GENERATION of WET and DECOMPRESSİONMELTING", which he prepared after fulfilling the requirements specified in the associated legislations, before the jury whose signatures are below.

Thesis Advisor:	**Assoc. Prof. Dr. Oğuz Hakan GÖĞÜŞ** Istanbul Technical University	.....
Jury Members:	**Prof. Dr. Hans THYBO** Istanbul Technical University	.....
	Assist. Prof. Dr. Ebru ŞENGÜL ULUOCAK Çanakkale Onsekiz Mart University	.....

Date of Submission : 3 May 2019
Date of Defense : 10 June 2019

To my family,

FOREWORD

I am grateful to my thesis supervisor Assist. Prof. Dr. Oğuz H. Göğüş for his endless support from the beginning of this study. I appreciate Dr. Kosuke Ueda for his kind suggestions on each step of researching. I am indebted to Prof. Dr. Taras Gerya for sharing his I2ElVIS code which allowed me to perform geodynamic modelling. The model computations were processed at Swiss Federal Institute of Technology in Zurich (ETHZ) Euler server.

I would like to thank my teacher Serkan Üner who passed away recently and helped me a lot. I would like to thank my teacher Tuna Eken, who has always been helpful throughout my academic life.

I would like to thank my lovely sister and my dear family for their belief in me, trust and endless support for my entire life and my friends for their helps in various matters. I would like to thank my cousin Mustafa Erdal Türkoğlu for editing.

I would like to thank Yahya Arslan, Ömer Bodur, Ceyhun Erman, Açelya Ballı, Uğurcan Çetiner, Hacı Ahmet Gezgin, and Caner Memiş for their precious friendship during my master life.

TABLE OF CONTENTS

Page

FOREWORD ..... **ix**
TABLE OF CONTENTS ..... **xi**
SYMBOLS ..... **xiii**
LIST OF TABLES ..... **xv**
LIST OF FIGURES ..... **xvi**
SUBDUCTION ROLL BACK AND THE GENERATION OF WET AND DECOMPRESSİONMELTING ..... **xxvi**
SUMMARY ..... **xxvi**
ÖZET ..... **xxviii**
1. INTRODUCTION **1**
1.1. Objective and Scope of the Study **2**
1.2. Subduction Zones of the Earth **2**
1.3. Melt Production and Types **2**
1.3.1. Dry melt **3**
1.3.2. Wet melt 3
1.3.3. Relation between age, temperature and thickness **5**
2. NUMERICAL MODEL DESCRIPTION **7**
2.1. Model design **7**
2.1.1. Initial and boundary conditions **7**
2.1.2. Hydration process **8**
2.1.3. Melting and extraction processes **9**
2.1.4. Rheological model **9**
2.1.4.1. Viscous behavior **10**
2.1.4.2. Elastic behavior **10**
2.1.4.3. Plastic behavior **10**
2.1.5. Conservation equations **10**
3. RESULTS OF NUMERICAL EXPERIMENTS **13**
3.1. Results of Experiment A **14**
3.1.1. Experimental set A1 ..... **14**
3.1.2. Results of A1 ..... **14**
3.1.3. Experimental set A2 ..... **19**
3.1.4. Results of A2 ..... **19**
3.1.5. Experimental set A3 ..... **25**
3.1.6. Results of A3 ..... **25**
3.1.7. Experimental set A4 ..... **30**
3.1.8. Results of A4 ..... **30**
3.1.9. Experimental set A5 ..... **36**
3.1.10. Results of A5 ..... **36**
3.1.11. Experimental set A6 ..... **41**
3.1.12. Results of A6 ..... **41**

3.1.13. Experimental set A7 ..... **47**
3.1.14. Results of A7 ..... **47**
3.1.15. Experimental set A8 ..... **52**
3.1.16. Results of A8 ..... **52**
3.2. Results of Experiment B **58**
3.2.1. Experimental set B1 ..... **58**
3.2.2. Results of B1 ..... **58**
3.2.3. Experimental set B2 ..... **63**
3.2.4. Results of B2 ..... **63**
3.2.5. Experimental set B3 ..... **67**
3.2.6. Results of B3 ..... **67**
3.2.7. Experimental set B4 ..... **71**
3.2.8. Results of B4 ..... **71**
3.2.9. Experimental set B5 ..... **75**
3.2.10. Results of B5 ..... **75**
3.2.11. Experimental set B6 ..... **79**
3.2.12. Results of B6 ..... **79**
3.2.13. Experimental set B7 ..... **83**
3.2.14. Results of B7 ..... **83**
3.2.15. Experimental set B8 ..... **87**
3.2.16. Results of B8 ..... **87**
3.3. Comparison of Experiments **92**
4. OBSERVATIONS AGAINST THE MODEL RESULTS 95
4.1. Comparisons and Correlations for Sunda Arc **96**
4.1.1. Tectonic setting of Sumatra and Java subduction system **96**
4.1.2. Comparison with Sunda Arc **97**
4.2. Comparisons and Correlations for Japan Arc **100**
4.2.1. Tectonic setting of Japan subduction system **100**
4.2.2. Comparison with northeast part of the Japan Arc **105**
5. CONCLUSION 107
REFERENCES 109
APPENDICES 113
Appendix A **115**
Appendix B **120**
Appendix C **125**
Appendix D **130**
Appendix E **135**
Appendix F **140**
Appendix G **145**
Appendix H **150**
Appendix I **155**
CURRICULUM VITAE 157

SYMBOLS

$\boldsymbol{v}$	**:** Velocity Field
$\boldsymbol{\varepsilon}$	**:** Strain
$\boldsymbol{\eta}$	**:** Viscosity
$\boldsymbol{\rho}$	**:** Density
T	**:** Temperature
P	**:** Pressure
$\boldsymbol{C}$	**:** Chemical composition
$\boldsymbol{\sigma}$	**:** Stress
$\boldsymbol{M_0}$	**:** Volumetric degree of melting
$\boldsymbol{A_D}$	**:** Pre-exponential factor
E	**:** Activation energy
$\boldsymbol{\alpha}$	**:** Expansion coefficient
$\boldsymbol{\beta}$	**:** Compressibility coefficient
yr.	**:** Year
Ma	**:** Million year
$\boldsymbol{\rho_{0solid}}$	**:** Standard density of solid rock
$\boldsymbol{\rho_{0molten}}$	**:** Standard density of molten rock
$\boldsymbol{T_{solidus}}$	**:** Solidus temperature
$\boldsymbol{X_{H_2O(po)}}$	**:** Pore water content.
$\boldsymbol{\Delta y}$	**:** Depth.
$\boldsymbol{X_{H_2O(po)}}$	**:** Pore water content.

LIST OF TABLES

Page

Table 3.1: Experiment Parameters. **13**

Table 3.2: Slab Break off table. **93**

Table 3.3: First melt production time table **94**

Table 4.1: Table of geochemistry of Sunda arc modified after Whitford, 1975. ..... **98**

Table I.1: Rheological and thermal properties of modeled rock materials (after T. V. Gerya & Meilick, 2011). **155**

LIST OF FIGURES

Page

Figure 1.1: A general illustration (140km) of a subduction zone taken from Stern (2002). Numerated circles are representing low pressure partial melt field which generates basaltic magma, asthenospheric wedge which generates felsic magma beneath the volcanic front. Dashed lines are representing isotherms, for 500ºC and 1000 ºC. Plate motion is assumed left to right. Major surface formations of subduction zones are shown at the top side of figure as; back arc basin, magmatic arc, fore arc and trench. **1**
Figure 1.2: Decreased pressure effect on solidus curve (Elkins-Tanton, 2007). **3**
Figure 1.3: Illustration of wet melt generation at mantle wedge of subduction zones. Subducted slab which contains water (A), fluids are released from subducted sediments, crust, and serpentine (B), fluids rising into the mantle form wet phases in mantle peridotite (C), maximum depth of stability condition of peridotite breaks down to anwet peridotite (D), The fluid rises vertically, moving away from the subducted slab (E), This descends until the amphibole breaks down again (F) (Stern, 2002)..... **4**
Figure 1.4: Depth variation due to time difference (Turcotte, 2014) . Isotherms are represented with solid lines. Thickness of the lithosphere data of the Pacific Ocean (Turcotte, 2014)..... **5**
Figure 2.1: Model setup for numerical modeling, layers and structures with color representation. **8**
Figure 2.2: The model representation a retreating oceanic-continental subduction with the formation of mantle wedge, magmatic arc and extensional basin with new creating oceanic floor (see text for details).. ..... **12**
Figure 3.1: The results of the Experiment A1, show *melt production graph* (top), *water content with percentage* (middle), and *lithology graph* (bottom) at 12.10 Myr. **15**
Figure 3.2: The results of the Experiment A1, show *melt production graph* (top), *water content with percentage* (middle), and *lithology graph* (bottom) at 12.52 Myr. **15**
Figure 3.3 The results of the Experiment A1, show *melt production graph* (top), *water content with percentage* (middle), and *lithology graph* (bottom) at 13.64 Myr. **16**
Figure 3.4: The results of the Experiment A1, show *melt production graph* (top), *water content with percentage* (middle), and *lithology graph* (bottom) at 13.96 Myr. **16**
Figure 3.5: The results of the Experiment A1, show *melt production graph* (top), *water content with percentage* (middle), and *lithology graph* (bottom) at 14.49 Myr. **17**

Figure 3.6: The results of the Experiment A1, show *melt production graph* (top), *water content with percentage* (middle), and *lithology graph* (bottom) at 14.99 Myr. **17**
Figure 3.7: Result of the Experiment A1 with discrete volumetric melt production rate depending on time. **18**
Figure 3.8: Result of the Experiment A1 with cumulative sum of discrete volumetric melt extraction rate depending on time. **19**
Figure 3.9: The results of the Experiment A2, show *melt production graph* (top), *water content with percentage* (middle), and *lithology graph* (bottom) at 11.95 Myr. **20**
Figure 3.10: The results of the Experiment A2, show *melt production graph* (top), *water content with percentage* (middle), and *lithology graph* (bottom) at 12.26 Myr. **21**
Figure 3.11: The results of the Experiment A2, show *melt production graph* (top), *water content with percentage* (middle), and *lithology graph* (bottom) at 13.05 Myr. **21**
Figure 3.12: The results of the Experiment A2, show *melt production graph* (top), *water content with percentage* (middle), and *lithology graph* (bottom) at 13.76 Myr. **22**
Figure 3.13: The results of the Experiment A2, show *melt production graph* (top), *water content with percentage* (middle), and *lithology graph* (bottom) at 14.22 Myr. **22**
Figure 3.14: The results of the Experiment A2, show *melt production graph* (top), *water content with percentage* (middle), and *lithology graph* (bottom) at 14.48 Myr. **23**
Figure 3.15: Result of experiment A2 with discrete volumetric melt extraction rate depending on time. **24**
Figure 3.16: Result of Experiment A2 with cumulative sum of discrete volumetric melt extraction rate depending on time. **24**
Figure 3.17: The results of the Experiment A3, show *melt production graph* (top), *water content with percentage* (middle), and *lithology graph* (bottom) at 11.86 Myr. **26**
Figure 3.18: The results of the Experiment A3, show *melt production graph* (top), *water content with percentage* (middle), and *lithology graph* (bottom) at 13.64 Myr. **26**
Figure 3.19: The results of the Experiment A3, show *melt production graph* (top), *water content with percentage* (middle), and *lithology graph* (bottom) at 13.69 Myr. **27**
Figure 3.20: The results of the Experiment A3, show *melt production graph* (top), *water content with percentage* (middle), and *lithology graph* (bottom) at 14.00 Myr. **27**
Figure 3.21: The results of the Experiment A3, show *melt production graph* (top), *water content with percentage* (middle), and *lithology graph* (bottom) at 14.28 Myr. **28**
Figure 3.22: The results of the Experiment A3, show *melt production graph* (top), *water content with percentage* (middle), and *lithology graph* (bottom) at 14.30 Myr. **28**
Figure 3.23: Result of the Experiment A3 with discrete volumetric melt extraction rate depending on time. **29**

Figure 3.24: Result of the Experiment A3 with cumulative sum of discrete volumetric melt extraction rate depending on time. **30**
Figure 3.25: The results of the Experiment A4, show *melt production graph* (top), *water content with percentage* (middle), and *lithology graph* (bottom) at 11.86 Myr. **31**
Figure 3.26: The results of the Experiment A4, show *melt production graph* (top), *water content with percentage* (middle), and *lithology graph* (bottom) at 12.20 Myr. **32**
Figure 3.27: The results of the Experiment A4, show *melt production graph* (top), *water content with percentage* (middle), and *lithology graph* (bottom) at 13.45 Myr. **32**
Figure 3.28: The results of the Experiment A4, show *melt production graph* (top), *water content with percentage* (middle), and *lithology graph* (bottom) at 13.76 Myr. **33**
Figure 3.29: The results of the Experiment A4, show *melt production graph* (top), *water content with percentage* (middle), and *lithology graph* (bottom) at 13.92 Myr. **33**
Figure 3.30: The results of the Experiment A4, show *melt production graph* (top), *water content with percentage* (middle), and *lithology graph* (bottom) at 13.95 Myr. **34**
Figure 3.31: Result of the Experiment A4 with discrete volumetric melt extraction rate depending on time. **35**
Figure 3.32: Result of Experiment A4 with cumulative sum of discrete volumetric melt extraction rate depending on time. **35**
Figure 3.33: The results of the Experiment A5, show *melt production graph* (top), *water content with percentage* (middle), and *lithology graph* (bottom) at 11.80 Myr. **37**
Figure 3.34: The results of the Experiment A5, show *melt production graph* (top), *water content with percentage* (middle), and *lithology graph* (bottom) at 12.02 Myr. **37**
Figure 3.35 The results of the Experiment A5, show *melt production graph* (top), *water content with percentage* (middle), and *lithology graph* (bottom) at 12.20 Myr. **38**
Figure 3.36: The results of the Experiment A5, show *melt production graph* (top), *water content with percentage* (middle), and *lithology graph* (bottom) at 12.77 Myr. **38**
Figure 3.37: The results of the Experiment A5, show *melt production graph* (top), *water content with percentage* (middle), and *lithology graph* (bottom) at 14.07 Myr. **39**
Figure 3.38: The results of the Experiment A5, show *melt production graph* (top), *water content with percentage* (middle), and *lithology graph* (bottom) at 14.08 Myr. **39**
Figure 3.39: Result of the Experiment A5 with discrete volumetric melt extraction rate depending on time. **40**
Figure 3.40: Result of the Experiment A5 with cumulative sum of discrete volumetric melt extraction rate depending on time. **41**
Figure 3.41: The results of the Experiment A6, show *melt production graph* (top), *water content with percentage* (middle), and *lithology graph* (bottom) at 11.89 Myr. **42**

Figure 3.42: The results of the Experiment A6, show *melt production graph* (top), *water content with percentage* (middle), and *lithology graph* (bottom) at 13.61 Myr. **43**
Figure 3.43: The results of the Experiment A6, show *melt production graph* (top), *water content with percentage* (middle), and *lithology graph* (bottom) at 13.67 Myr. **43**
Figure 3.44: The results of the Experiment A6, show *melt production graph* (top), *water content with percentage* (middle), and *lithology graph* (bottom) at 13.85 Myr. **44**
Figure 3.45: The results of the Experiment A6, show *melt production graph* (top), *water content with percentage* (middle), and *lithology graph* (bottom) at 13.93 Myr. **44**
Figure 3.46: The results of the Experiment A6, show *melt production graph* (top), *water content with percentage* (middle), and *lithology graph* (bottom) at 13.97 Myr. **45**
Figure 3.47: Result of the Experiment A6 with discrete volumetric melt extraction rate depending on time. **46**
Figure 3.48: Result of the Experiment A6 with cumulative sum of discrete volumetric melt extraction rate depending on time. **46**
Figure 3.49: The results of the Experiment A7, show *melt production graph* (top), *water content with percentage* (middle), and *lithology graph* (bottom) at 11.56 Myr. **48**
Figure 3.50: The results of the Experiment A7, show *melt production graph* (top), *water content with percentage* (middle), and *lithology graph* (bottom) at 11.84 Myr. **48**
Figure 3.51: The results of the Experiment A7, show *melt production graph* (top), *water content with percentage* (middle), and *lithology graph* (bottom) at 13.21 Myr. **49**
Figure 3.52: The results of the Experiment A7, show *melt production graph* (top), *water content with percentage* (middle), and *lithology graph* (bottom) at 13.84 Myr. **49**
Figure 3.53: The results of the Experiment A7, show *melt production graph* (top), *water content with percentage* (middle), and *lithology graph* (bottom) at 13.93 Myr. **50**
Figure 3.54: The results of the Experiment A7, show *melt production graph* (top), *water content with percentage* (middle), and *lithology graph* (bottom) at 14.20 Myr. **50**
Figure 3.55: Result of experiment A7 with discrete volumetric melt extraction rate depending on time. **51**
Figure 3.56: Result of the Experiment A7 with cumulative sum of discrete volumetric melt extraction rate depending on time. **52**
Figure 3.57: The results of the Experiment A8, show *melt production graph* (top), *water content with percentage* (middle), and *lithology graph* (bottom) at 11.72 Myr. **53**
Figure 3.58: The results of the Experiment A8, show *melt production graph* (top), *water content with percentage* (middle), and *lithology graph* (bottom) at 11.81 Myr. **54**
Figure 3.59 The results of the Experiment A8, show *melt production graph* (top), *water content with percentage* (middle), and *lithology graph* (bottom) at 12.40 Myr. **54**

Figure 3.60 The results of the Experiment A8, show *melt production graph* (top), *water content with percentage* (middle), and *lithology graph* (bottom) at 13.86 Myr. **55**
Figure 3.61: The results of the Experiment A4, show *melt production graph* (top), *water content with percentage* (middle), and *lithology graph* (bottom) at 14.08 Myr. **55**
Figure 3.62: The results of the Experiment A8, show *melt production graph* (top), *water content with percentage* (middle), and *lithology graph* (bottom) at 14.10 Myr. **56**
Figure 3.63: Result of experiment A8 with discrete volumetric melt extraction rate depending on time. **57**
Figure 3.64: Result of the Experiment A8 with cumulative sum of discrete volumetric melt extraction rate depending on time. **57**
Figure 3.65: The results of the Experiment B1, show *melt production graph* (top), *water content with percentage* (middle), and *lithology graph* (bottom) at 6.49 Myr. **59**
Figure 3.66: The results of the Experiment A4, show *melt production graph* (top), *water content with percentage* (middle), and *lithology graph* (bottom) at 6.79 Myr. **59**
Figure 3.67: The results of the Experiment B1, show *melt production graph* (top), *water content with percentage* (middle), and *lithology graph* (bottom) at 6.99 Myr. **60**
Figure 3.68: The results of the Experiment B1, show *melt production graph* (top), *water content with percentage* (middle), and *lithology graph* (bottom) at 7.18 Myr. **60**
Figure 3.69: The results of the Experiment B1, show *melt production graph* (top), *water content with percentage* (middle), and *lithology graph* (bottom) at 7.49 Myr. **61**
Figure 3.70: The results of the Experiment B1, show *melt production graph* (top), *water content with percentage* (middle), and *lithology graph* (bottom) at 7.90 Myr. **61**
Figure 3.71: Result of the Experiment B1 with discrete volumetric melt production rate depending on time. **62**
Figure 3.72: Result of the Experiment B1 with cumulative sum of discrete volumetric melt extraction rate depending on time. **63**
Figure 3.73: The results of the Experiment B2, show *melt production graph* (top), *water content with percentage* (middle), and *lithology graph* (bottom) at 7.00 Myr. **64**
Figure 3.74: The results of the Experiment B2, show *melt production graph* (top), *water content with percentage* (middle), and *lithology graph* (bottom) at 7.53 Myr. **64**
Figure 3.75: The results of the Experiment B2, show *melt production graph* (top), *water content with percentage* (middle), and *lithology graph* (bottom) at 7.84 Myr. **65**
Figure 3.76: The results of the Experiment B2, show *melt production graph* (top), *water content with percentage* (middle), and *lithology graph* (bottom) at 8.54 Myr. **65**
Figure 3.77: Result of the Experiment B2 with discrete volumetric melt production rate depending on time. **66**

Figure 3.78: Result of the Experiment B2 with cumulative sum of discrete volumetric melt extraction rate depending on time. **67**
Figure 3.79: The results of the Experiment B3, show *melt production graph* (top), *water content with percentage* (middle), and *lithology graph* (bottom) at 6.24 Myr. **68**
Figure 3.80: The results of the Experiment B3, show *melt production graph* (top), *water content with percentage* (middle), and *lithology graph* (bottom) at 6.55 Myr. **68**
Figure 3.81: The results of the Experiment B3, show *melt production graph* (top), *water content with percentage* (middle), and *lithology graph* (bottom) at 6.78 Myr. **69**
Figure 3.82: The results of the Experiment B3, show *melt production graph* (top), *water content with percentage* (middle), and *lithology graph* (bottom) at 7.44 Myr. 69
Figure 3.83: Result of the Experiment B3 with discrete volumetric melt production rate depending on time. **70**
Figure 3.84: Result of the Experiment B3 with cumulative sum of discrete volumetric melt extraction rate depending on time. **71**
Figure 3.85: The results of the Experiment B4, show *melt production graph* (top), *water content with percentage* (middle), and *lithology graph* (bottom) at 6.47 Myr. **72**
Figure 3.86 The results of the Experiment B4, show *melt production graph* (top), *water content with percentage* (middle), and *lithology graph* (bottom) at 6.69 Myr. **72**
Figure 3.87 The results of the Experiment B4, show *melt production graph* (top), *water content with percentage* (middle), and *lithology graph* (bottom) at 7.00 Myr. **73**
Figure 3.88: The results of the Experiment B4, show *melt production graph* (top), *water content with percentage* (middle), and *lithology graph* (bottom) at 7.35Myr. **73**
Figure 3.89: Result of the Experiment B4 with discrete volumetric melt production rate depending on time. **74**
Figure 3.90: Result of the Experiment B4 with cumulative sum of discrete volumetric melt extraction rate depending on time. **75**
Figure 3.91: The results of the Experiment B5, show *melt production graph* (top), *water content with percentage* (middle), and *lithology graph* (bottom) at 6.46 Myr. **76**
Figure 3.92: The results of the Experiment B5, show *melt production graph* (top), *water content with percentage* (middle), and *lithology graph* (bottom) at 6.64 Myr. **76**
Figure 3.93: The results of the Experiment B5, show *melt production graph* (top), *water content with percentage* (middle), and *lithology graph* (bottom) at 6.78 Myr. **77**
Figure 3.94: The results of the Experiment B5, show *melt production graph* (top), *water content with percentage* (middle), and *lithology graph* (bottom) at 6.99 Myr. **77**
Figure 3.96: Result of the Experiment B5 with discrete volumetric melt production rate depending on time. **78**
Figure 3.97: Result of the Experiment B5 with cumulative sum of discrete volumetric melt extraction rate depending on time. **79**

Figure 3.98: The results of the Experiment B6, show *melt production graph* (top), *water content with percentage* (middle), and *lithology graph* (bottom) at 6.63 Myr. **80**
Figure 3.99: The results of the Experiment B6, show *melt production graph* (top), *water content with percentage* (middle), and *lithology graph* (bottom) at 6.85 Myr. **80**
Figure 3.100: The results of the Experiment B6, show *melt production graph* (top), *water content with percentage* (middle), and *lithology graph* (bottom) at 7.03 Myr. **81**
Figure 3.101: The results of the Experiment B6, show *melt production graph* (top), *water content with percentage* (middle), and *lithology graph* (bottom) at 8.75 Myr. **81**
Figure 3.102: Result of the Experiment B6 with discrete volumetric melt production rate depending on time. **82**
Figure 3.103: Result of the Experiment B6 with cumulative sum of discrete volumetric melt extraction rate depending on time. **83**
Figure 3.104: The results of the Experiment B7, show *melt production graph* (top), *water content with percentage* (middle), and *lithology graph* (bottom) at 6.55 Myr. **84**
Figure 3.105: The results of the Experiment B7, show *melt production graph* (top), *water content with percentage* (middle), and *lithology graph* (bottom) at 6.87 Myr. **84**
Figure 3.106: The results of the Experiment B7, show *melt production graph* (top), *water content with percentage* (middle), and *lithology graph* (bottom) at 7.18 Myr. **85**
Figure 3.107: The results of the Experiment B7, show *melt production graph* (top), *water content with percentage* (middle), and *lithology graph* (bottom) at 8.93 Myr. **85**
Figure 3.108: Result of the Experiment B7 with discrete volumetric melt production rate depending on time. **86**
Figure 3.109: Result of the Experiment B7 with cumulative sum of discrete volumetric melt extraction rate depending on time. **87**
Figure 3.110 The results of the Experiment B8, show *melt production graph* (top), *water content with percentage* (middle), and *lithology graph* (bottom) at 6.53 Myr. **88**
Figure 3.111: The results of the Experiment B8, show *melt production graph* (top), *water content with percentage* (middle), and *lithology graph* (bottom) at 6.81 Myr. **89**
Figure 3.112: The results of the Experiment B8, show *melt production graph* (top), *water content with percentage* (middle), and *lithology graph* (bottom) at 7.34 Myr. **89**
Figure 3.113: The results of the Experiment B8, show *melt production graph* (top), *water content with percentage* (middle), and *lithology graph* (bottom) at 9.09 Myr. **90**
Figure 3.114: Result of the Experiment B8 with discrete volumetric melt production rate depending on time. **91**
Figure 3.115: Result of the Experiment B8 with cumulative sum of discrete volumetric melt extraction rate depending on time. **92**
Figure 4.1: Oceanic lithosphere age distribution. Rectangular region representing rapid changing of oceanic lithosphere age at one subduction system.

Region (A) is Sunda arc. Region (B) is Japan subduction (simply modified after Müller, Sdrolias, Gaina, & Roest, 2008) **95**

Figure 4.2: Map of Sumatra- Java subduction system. Dash line is trench profile. Arrows representing convergent rate of subducting trench (Artemieva, Thybo, & Shulgin, 2016). Yellow, green and blue area is representing oceanic lithosphere age distribution (modified after Müller et al., 2008) .Yellow line is representing right lateral strike slip fault with 3.6-4.9 cm/yr plate motion(Genrich & Stevens, 2000). Volcanic provinces are representing by stars; 1: Salak volcanic province (Calc-alkaline) ad 2: Guntur volcanic province (Tholeiitic). **97**

Figure 4.3: Marine seismic profile from middle part of Sumatra trench (Shulgin et al., 2013) **99**

Figure 4.4: The results of the Experiment 1, show the geodynamic evolution of subduction and its *melt production graph* (top), *water content with percentage* (middle) scaled with colorbar, yellow arrows represents convection current flow and solid white lines illustrates thermal gradients from 700 to 1500 ºC with 200 ºC increment, and *lithology graph* (bottom) in 12.37 Myr. **100**

Figure 4.5: Tectonic evaluation around the Japan islands between Early to Middle Miocene *(~23 – ~5.3 Ma)* (Yamamoto & Hoang, 2009). **101**

Figure 4.6: Trench velocity and oceanic lithosphere age distribution of the western Pacific, showing the subducting slab Map of Japan subduction system. Dash line is trench profile. Arrows representing convergent rate of subducting trench (Artemieva, Thybo, & Shulgin, 2016). Yellow, green and blue area is representing oceanic lithosphere age distribution (Müller et al., 2008) , (modified after Faccenna, Holt, Becker, Lallemand, & Royden, 2018).Red dashed line represents Neogene volcanic front and yellow dached line represents Quaternary volcanic front. **102**

Figure 4.7: Tectonic evolution and magmatism differences at North East Japan. Broken lines are representing indicated 100C isotherm (solidus temperature of wet peridotite) HMA and VF represents normal volcanic front and uncommon near trench volcanic of high magnesian andesites, respectively. The back arc basin occurred during 20-14 Ma with hot asthenospheric injection into mantle wedge during the 30-23 Ma. (Tatsumi et al., 1989) **103**

Figure 4.8: Illustration of the Japan subduction evolution (Yamato, Burov, Agard, Le Pourhiet, & Jolivet, 2008). **104**

Figure 4.9: The results of the Experiment 8, show the geodynamic evolution of subduction and its *melt production graph* (top), *water content with percentage* (middle) scaled with colorbar, yellow arrows represents convection current flow and solid white lines illustrates thermal gradients from 700 to 1500 ºC with 200 ºC increment, and *lithology graph* (bottom) in 13.64 Myr. **105**

Figure A.1: Results of second strain rate invariants with x axis (km), y axis time (km) and second strain rate invariant (color bar.)..... **115**

Figure A.2: Results of full domain material field with x axis (km), y axis time (km). **116**

Figure A.3: Results of density field with x axis (km), y axis time (km) and density values are defined at color bar..... **117**

Figure A.4: Results of temperature field with x axis (km), y axis time (km) and temperature values are defined at color bar..... **118**
Figure A.5: Results of viscosity field with x axis (km), y axis time (km) and viscosity values are defined at color bar..... **119**
Figure B.1: Results of second strain rate invariants with x axis (km), y axis time (km) and second strain rate invariant (color bar.) **120**
Figure B.2: Results of full domain material field with x axis (km), y axis time (km). **121**
Figure B.3: Results of density field with x axis (km), y axis time (km) and density values are defined at color bar. **122**
Figure B.4: Results of temperature field with x axis (km), y axis time (km) and temperature values are defined at color bar. **123**
Figure B.5: Results of viscosity field with x axis (km), y axis time (km) and viscosity values are defined at color bar. **124**
Figure C.1: Results of second strain rate invariants with x axis (km), y axis time (km) and second strain rate invariant (color bar.)..... **125**
Figure C.2: Results of full domain material field with x axis (km), y axis time (km). **126**
Figure C.3: Results of density field with x axis (km), y axis time (km) and density values are defined at color bar..... **127**
Figure C.4: Results of temperature field with x axis (km), y axis time (km) and temperature values are defined at color bar. **128**
Figure C.5: Results of viscosity field with x axis (km), y axis time (km) and viscosity values are defined at color bar..... **129**
Figure D.1: Results of second strain rate invariants with x axis (km), y axis time (km) and second strain rate invariant (color bar.) **130**
Figure D.2: Results of full domain material field with x axis (km), y axis time (km). **131**
Figure D.3: Results of density field with x axis (km), y axis time (km) and density values are defined at color bar. **132**
Figure D.4: Results of temperature field with x axis (km), y axis time (km) and temperature values are defined at color bar. **133**
Figure D.5: Results of viscosity field with x axis (km), y axis time (km) and viscosity values are defined at color bar. **134**
Figure E.1: Results of second strain rate invariants with x axis (km), y axis time (km) and second strain rate invariant (color bar.)..... **135**
Figure E.2: Results of full domain material field with x axis (km), y axis time (km). **136**
Figure E.3: Results of density field with x axis (km), y axis time (km) and density values are defined at color bar..... **137**
Figure E.4: Results of temperature field with x axis (km), y axis time (km) and temperature values are defined at color bar..... **138**
Figure E.5: Results of viscosity field with x axis (km), y axis time (km) and viscosity values are defined at color bar..... **139**
Figure F.1: Results of second strain rate invariants with x axis (km), y axis time (km) and second strain rate invariant (color bar.) **140**
Figure F.2: Results of full domain material field with x axis (km), y axis time (km). **141**

Figure F.3: Results of density field with x axis (km), y axis time (km) and density values are defined at color bar..... **142**
Figure F.4: Results of temperature field with x axis (km), y axis time (km) and temperature values are defined at color bar..... **143**
Figure F.5: Results of viscosity field with x axis (km), y axis time (km) and viscosity values are defined at color bar..... **144**
Figure G.1: Results of second strain rate invariants with x axis (km), y axis time (km) and second strain rate invariant (color bar.)..... **145**
Figure G.2: Results of full domain material field with x axis (km), y axis time (km). **146**
Figure G.3: Results of density field with x axis (km), y axis time (km) and density values are defined at color bar..... **147**
Figure G.4: Results of temperature field with x axis (km), y axis time (km) and temperature values are defined at color bar..... **148**
Figure G.5: Results of viscosity field with x axis (km), y axis time (km) and viscosity values are defined at color bar..... **149**
Figure H.1: Results of second strain rate invariants with x axis (km), y axis time (km) and second strain rate invariant (color bar.)..... **150**
Figure H.2: Results of full domain material field with x axis (km), y axis time (km). **151**
Figure H.3: Results of density field with x axis (km), y axis time (km) and density values are defined at color bar..... **152**
Figure H.4: Results of temperature field with x axis (km), y axis time (km) and temperature values are defined at color bar..... **153**
Figure H.5: Results of viscosity field with x axis (km), y axis time (km) and viscosity values are defined at color bar..... **154**

SUBDUCTION ROLL BACK AND THE GENERATION OF WET AND DECOMPRESSİONMELTING

SUMMARY

Subduction zones are the major element of active tectonics (55.000 km) of planet Eart (Stern, 2002). Subduction zones are regions of the Earth affected by the sinking of relatively cold and dense oceanic lithospheres into the mantle. Geophysical and geological evidences have led to interpretation of oceanic lithosphere subduction beneath the Sunda and Japan subduction region. Active subduction is taking important role to creation of serial volcanic province. These volcanic areas show variable chemical properties such as alkaline and calc-alkaline compositions. Alkaline composition is related with low pressure conditions and common at ridge regions however they are observed at some subduction zones such as Sunda arc. Calc-alkaline magmatism is related with dehydration reactions at subduction slab. Volatiles inside the top of the subducted oceanic lithosphere are releasing at 80 - 200 km depth condition. Volatiles decrease the melting temperature and cause partial melt of mantle wedge (triangular asthenospheric window beneath the volcanic arc). Thickness of the subducting slab is changing with oceanic lithosphere age. Feature of the subduction is dominated by thickness of the slab which is changing with age. Numerous 2D numerical geodynamic experiments (I2ELVIS) in the context of the tectonic evolution of the region are conducted to test the effects of the oceanic lithosphere age on melt generation. Within the scope of the models, the age of the oceanic lithosphere has been tried by increasing the age from 50 million to 120 million years. The plate convergence rate was defined as 4 cm / year and 8 cm/yr. The model boundaries are 1400 km vertical and 4000 km horizontal. as defined. The geology of the layers used in the models is defined as follows; 10 km atmosphere, 2 km. ocean, 20 km. felsic upper continental crust (wet quartzite), 15 km. felsic lower crust (wet kurtzite), 3 km. upper oceanic crust (basalt), 5 km. lower oceanic crust (gabbro) and 2 km. width is used for the zone of weakness hydrated mantle. Model result for subduction are comparable with observations related to the geodynamic evolution of the Sunda. The mantle structure compared by seismic profiles, considering convergent rate of plate motion. Chemical composition distribution of volcanics are correlating with geochemistry studies.

YİTİM BÖLGELERİNDE OKYANUSAL LİTOSFER YAŞINI ERİYİK ÜRETİMİNE ETKİLERİ

ÖZET

Yitim bölgeleri, aktif tektoniğinin temel elemanıdır ve yaklaşık 55.000 km. lik bir kısmını kaplamaktadır (Stern, 2002). Yitim bölgeleri, yeryüzünün nispeten soğuk ve yoğun okyanusal litosferlerinin mantoya batmasından meydana gelen alanlarıdır. Okyanusal litosferin dalması ile oluşam yapının jeokimyasal heterojenliği deniz dibi çökeltileri, mantodan uçucuları ve peridotit içeren okyanus bazaltları ile temsil edilir. Dalan levhanın yapısal özelliklerini belirleyen faktörler şu şekildedir; dalan levhanın termal sıcaklık gradyeni (yaşına bağlı olarak deşikenlik gösterir, dalan levhanın yaşı, yakınsama hızı, manto kamasındaki konveksiyon akımları, dalan levhanın üst yüzeyindeki makaslama kuvvetleri sonucu oluşan ısınma, sıcaklık etkisi altındaki adveksiyon akımları, erozyon ve deformasyonlardır (Artemieva, 2011). Sunda yayının Sumatra-Java bölümünde farklı yaşlarda okyanusal litofosferlerin dalımı, 15 Milyon yıldır devam etmketedir. Aktif dalma batma bölgesinin oluşu seri volkanların oluşumunda önemli rol oynamaktadır. Bu volkanik alanlar, alkalen ve kalk-alkalen bileşimler gibi değişken kimyasal özellikler gösterir. Alkali kompozisyon düşük basınç koşullarıyla ilişkilidir ve okyanus ortası sırt bölgelerinde yaygındır, ancak Sunda arkı gibi bazı yitim bölgelerinde gözlenir. Kalk-alkalen magmatizması, Dalan levhadaki dehidrasyon reaksiyonları ile ilişkilidir. Dalan okyanusal litosferin üst yüzeyindeki uçucular, 80-200 km derinlik koşulunda serbest kalmaktadır. Uçucu maddeler erime sıcaklığını düşürür ve açılan manto penceresinin kısmi erimesine neden olur (volkanik arkın altındaki üçgen astenosferik pencere). Dalan levhanın kalınlığı, okyanusal litosferin yaşı ile birlikte değişmektedir. Bölgenin tektonik evrimi bağlamında çok sayıda 2B sayısal jeodinamik model, okyanus litosfer yaşının eriyik üretimi üzerindeki etkilerini test etmek için üretilmiştir. Modellerde sonlu elemanlar yöntemi kullanılarak hazırlan Eulerian ve hücre işaretleme metodlarının karışımı bir hesaplama yapılmıştır. Her bir sıcaklık, yoğunluk, viskozite gibi materyal parametreleri node adı verilen kesişim çizgileri üzerine aktarılıp yan hücre ile kütle ve ısı korunumu yasalarına dayanarak etkileşime geçmesi sonucu hücre değerleri hesaplanmıştır. 1361x351 node kullanılmıştır. Viskozite, elastisite ve plastik parametreleri ortak çözen metod Taras Gerya tarafından geliştirilmiştir ve adı I2ELVIS'tir. Metodun dayandığı temel prensipler şöyle sıralanabilir; stres kuvvetlerinin yüksek viskozite değerlerinde korunumu, ani sıcaklık iletim sabitlerinde ısının ve kimyasal akışın korunumu, güçlü adveksiyon akımlarındaki yoğunluğun, sıcaklığın ve kimyasal kompozisyonun korunumu (Taras V. Gerya & Yuen, 2003). Modeller kapsamında okyanusal litosferin yaşı 50 milyon yıldan 120 milyon yıla 10'ar artırılarak denemiştir. Plaka yakınsama hızı 4 cm./yıl ve 8 cm./yıl olarak tanımlanıştır. Model sınırları ise düşeyde 1400 km., yatayda 4000 km. olarak tanımlanmıştır. Modellerde kullanılan katmanların jeolojisi şöyle tanımlanmıştır; 10 km atmosfer, 2

km. okyanus, 20 km. felsik üst kıtasal kabuk (ıslak kuartzite), 15 km. felsik alt kabuk (ıslak kurtzite), 3 km. üsk okyanusal kabuk (basalt), 5 km. alt okyanusal kabuk (gabrro) ve 2 km. genişliğinde zayıflık zonu için hidratlaşmış manto kullanılmıştır. Dalma batma ile ilgili model sonucu, Sunda Yayının jeodinamik evrimi ile ilgili gözlemlerle karşılaştırılabilir. Plaka hareketinin yakınsak hızı göz önüne alınarak sismik profillerle karşılaştırıldığında manto yapısı ve volkaniklerin kimyasal bileşim dağılımı jeokimya çalışmaları ile bağıntılıdır.

1. INTRODUCTION

Subduction zones are one of the complex structures of the Earth which are regions dominated by the sinking of relatively cold and dense oceanic lithosphere into the mantle. Subduction also includes geochemical heterogeneity with sea floor sediments, oceanic basalt which contains volatiles and peridotite from depleted mantle.

It is a common assumption that volatiles -especially water and carbon dioxide- play an important role at triggering of partial melting in subduction zones. Besides volatiles control the melting temperature of the rocks in mantle.

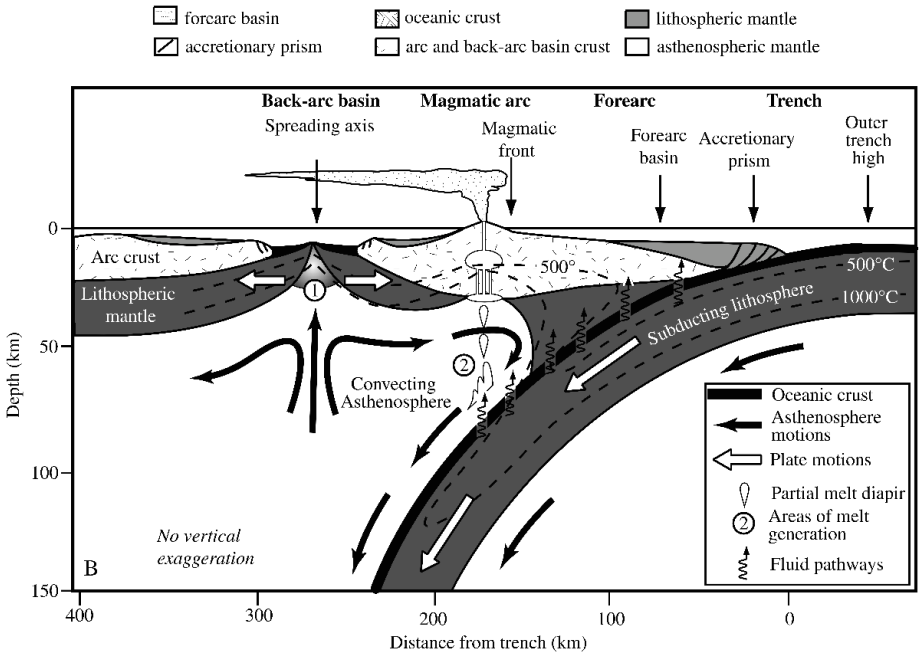

Figure 1.1: A general illustration (140km) of a subduction zone taken from Stern (2002). Numerated circles are representing low pressure partial melt field which generates basaltic magma, asthenospheric wedge which generates felsic magma beneath the volcanic front. Dashed lines are representing isotherms, for 500ºC and 1000ºC. Plate motion is assumed left to right. Major surface formations of subduction zones are shown at the top side of figure as; back arc basin, magmatic arc, fore arc and trench.

Sinking of oceanic lithosphere creates unique structures on the surface such as fore-arc, volcanic-arc and back-arc basins. A ***fore-arc*** basin forms the region between "trench" and the associated volcanic arc. . A ***volcanic arc*** defines a region, where volcanism is extremely activated and back-arc basins are known as the zone where

extensional forces are maximized or dominate. Geophysical methods (seismology, magnetic and gravity etc.) are quite useful and effective to get information about the internal physical properties of subduction zones. In this thesis, we mainly benefit from seismological and geochemical studies in order to test our model results against the observations the seismic method

1.1. Objective and Scope of the Study

There are various geologic/geophysical/geochemical data that examine the existence of a wet (alkaline) melt at subduction zones. Numerous hypotheses have been put forward to explain how mantle wedge is occurred and wet melt generated beneath the subduction arc, back-arc. The objective of this thesis is to try to interpret the geodynamic mechanism of melt production mechanism with 2D numerical modeling method.

Especially, scope of this thesis is based on hypothesis testing which aims to clarify three main tectonic problems of subduction zones:

(1) Examination of the mechanism that controls melt production at subduction zones;
(2) Comparison of types of produced melt pre-, during and post-subduction term; and
(3) investigation of the effect of slab break of on the melt production.

1.2. Subduction Zones of the Earth

Subduction zones occurs where two tectonic plates converge. This process include sediments, mantle lithosphere and oceanic crust. Subduction zones cover the 55.000 km of the Earth tectonic margins (Stern, 2002). Convergent forces trigger sinking of dense oceanic lithosphere into asthenosphere; moreover, subduction zones are dominated by gravitational force.

Convergent margins of the Earth are located at plate boundaries. These margins can be named as “mantle lithosphere recycling zones” of the Earth.

1.3. Melt Production and Types

Great volcanisms generally are located at subduction zones. For this reason various studies are focused on melt generation at these regions. It is a commonly accepted that

hydrated fluids are generated by aqueous melting of mantle peridotite in subduction margins. It is known as flux melting, by decreasing the temperature of the wet solidus (Kushiro, Syono, & Akimoto, 2008; Poli & Schmidt, 2004; Stolper & Newman, 1994). There are two major types of melt generation: **(1)** *wet* and **(2)** *wet melts*, respectively. Each has different formation mechanism that alter the chemical composition.

1.3.1. Dry melt

Composition of wet melt is alkaline. Convection flows at mantle give rise to the pressure reduction at mantle wedges. Due to high temperature and low pressure conditions, dry melt is generated. In (Figure 1.2), low pressure condition is represented with thin lithosphere, in this; geotherm curve is displaced towards the point where dry melt is produced.

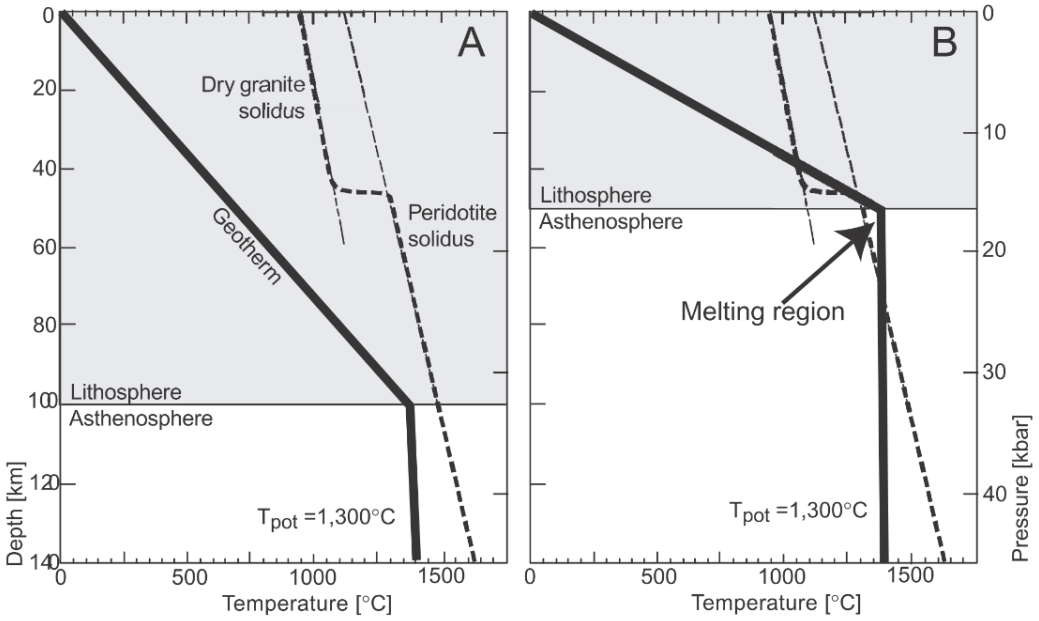

Figure 1.2: Decreased pressure effect on solidus curve (Elkins-Tanton, 2007).

1.3.2. Wet melt

Wet melt is in Calc-alkaline chemical composition. Generation of wet melt is based on volatiles in the mantle lithosphere forming rocks. These volatiles can be comprised of various chemical compositions; carbon dioxide, nitrogen dioxide, are the major components of volatiles. Releasing of volatiles decreases the melting temperature of the rock and which may cause reducing of viscosity and density. (Karato, 2010; Kushiro et al., 2008; Schmidt & Poli, 1998) (see Figure 1.3).

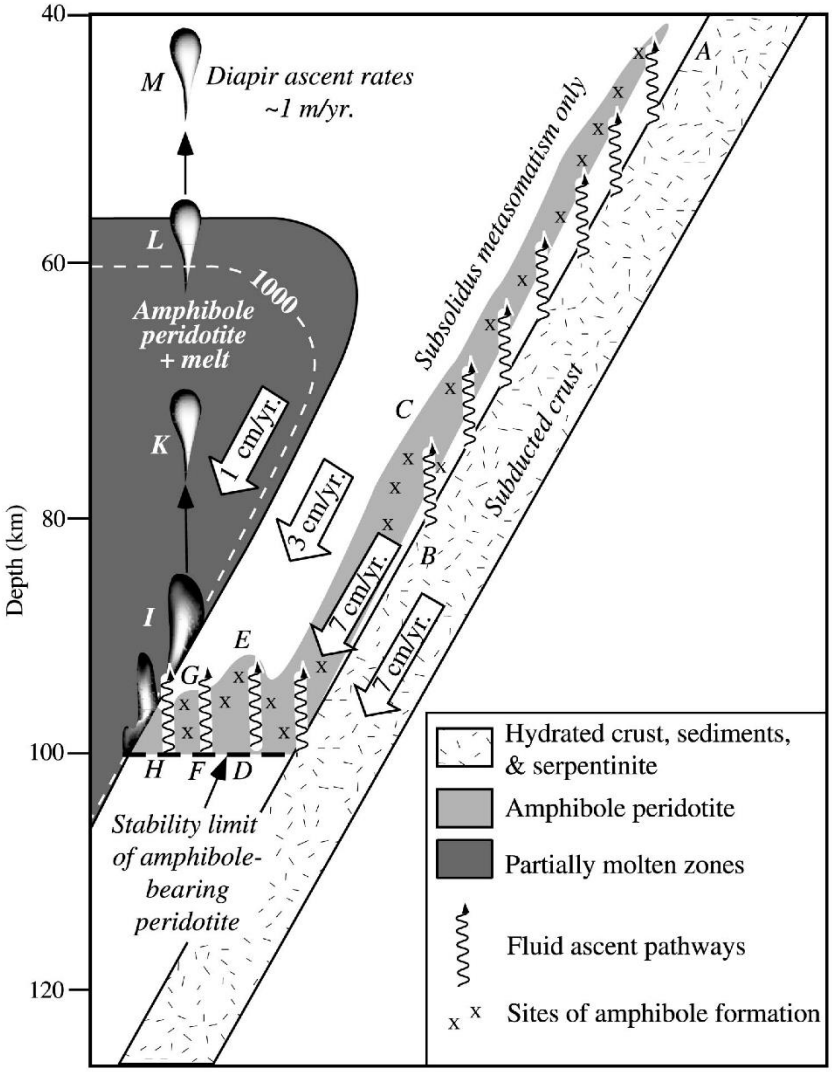

Figure 1.3: Illustration of wet melt generation at mantle wedge of subduction zones. Subducted slab which contains water (A), fluids are released from subducted sediments, crust, and serpentine (B), fluids rising into the mantle form wet phases in mantle peridotite (C), maximum depth of stability condition of peridotite breaks down to wet peridotite (D), The fluid rises vertically, moving away from the subducted slab (E), This descends until the amphibole breaks down again (F) (Stern, 2002).

At volcanic front of island arcs, dehydration conditions for major minerals for Serpentine, Amphibole/chlorite and Phlogopite are respectively ~80km, ~110km depth, ~200km depth (Tatsumi & Eggins, 1995) . Common dehydration reactions are represented below;

$$\text{Serpentine} > \text{olivine} + \text{talc} + H_2O$$

$$\text{Talc} + \text{olivine} > \text{orthopyroxene} + H_2O$$

$$\text{Chlorite} + \text{orthopyroxene} > \text{olivine} + \text{garnet} + H_2O$$

$$\text{Amphibole} > \text{clinopyroxene} + \text{garnet} + H_2O$$

1.3.3. Relation between age, temperature and thickness

Thickening of lithosphere as a result of cooling process of oceanic lithosphere and its thickening within time (Turcotte, 2014) (see Figure 1.4).

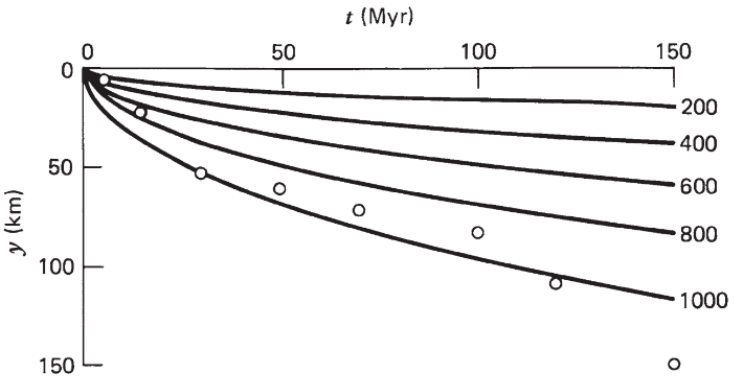

Figure 1.4: Depth variation due to time difference (Turcotte, 2014) . Isotherms are represented with solid lines. Thickness of the lithosphere data of the Pacific Ocean (Turcotte, 2014)

2. NUMERICAL MODEL DESCRIPTION

2.1. Model design

Model setups are designed considering the physical conditions in nature and material parameter. These parameters are based on the assumptions in geodynamic science and geological structures in subduction regions. The parameters and initial boundary conditions used in the following section will be discussed in more detail.

2.1.1. Initial and boundary conditions

2D petrological–thermomechanical numerical model simulates the processes of forced subduction of an oceanic–continental plate beneath a continental plate in a 4000 km×1400 km lithospheric/ upper-mantle section. In initial model, convergence rate it is used as 4 cm/year. Layers have assigned as air, water, continental-oceanic crust, mantle lithosphere, and asthenosphere, respectively at (Figure 2.1).

Plates are determined as two continents abstracted by 700 km of oceanic lithosphere (Figure 2.1). The first layer of the model is atmosphere with 10 km thickness and is located above 2 km of water covering the oceanic domain. Continents defined as 20 km of upper felsic crust (wet quartzite) and 15 km of lower crust (wet quartzite). The initial thickness of the sub-continental lithospheric mantle is 105 km. The oceanic plate is represented by 3 km of upper basaltic crust, and 5 km of lower gabbroic crust (Figure 2.1). The thickness of the lithospheric mantle is a function of chosen initial age (homogeneous for the entire plate width) and calculated using an oceanic geotherm (Ueda, Gerya, & Burg, 2012) .

Values of 10^{18} and 10^{26} Pa.s are the lower and upper limits for the viscosities of all types of rocks which is used in the models.

For the subduction initiation, a weak zone is used which has placed between the crust and the lithosphere-asthenosphere boundary (see Table 1). We also tested a wide range of lithospheric age, which range between 50 Ma to 120Ma (see Table 2.1).

Initial convergence, which is assumed to be dominated by external tectonic plate motion, has defined at internal nodes within both plates with fixed convergence rates (4cm/year).

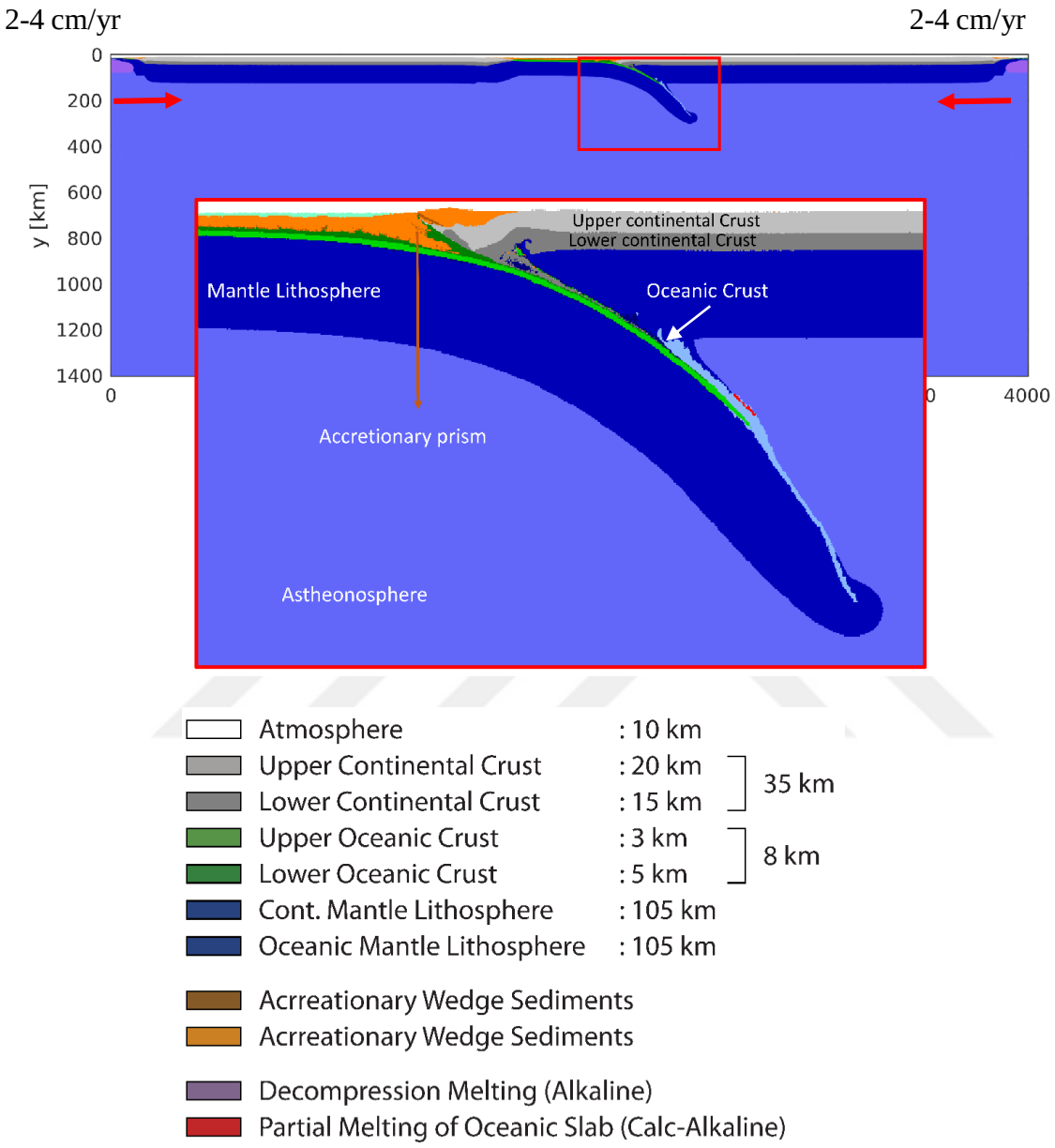

Figure 2.1: Model setup for numerical modeling, layers and structures with color representation.

2.1.2. Hydration process

In the basaltic crust which is changed with hydrothermal source and sediments, water is stored up to 2 %wt at the surface . (Johnson & Pruis, 2003)

$$X_{H_2O\,(wt\%)} = (1 - 0.013\Delta y) X_{H_2O(po)} \tag{2.1}$$

At surface $X_{H_2O(po)}$ is assumed to be equal to %2 and at the 75 km depth it is assumed to be %0 (T. V. Gerya & Meilick, 2011) . ρ_{0solid} and $\rho_{0molten}$ are the standard densities of solid and molten rock, respectively.

2.1.3. Melting and extraction processes

The assumption of calculation is computing that the degree of both wet and wet melting is a linear function of pressure and temperature. The volumetric degree of melting M_0 is calculated using the following equations, where $T_{solidus}$ and $T_{liquidus}$ are respectively solidus temperature and liquidus temperature (Taras V. Gerya & Yuen, 2003) .

$$M_0 = 0 \text{ at } T < T_{solidus.} \tag{2.2}$$

$$M_0 = \frac{T - T_{solidus}}{T_{liquidus} - T_{solidus}} \text{ at } T_{solidus} < T < T_{liquidus,} \tag{2.3}$$

$$M_0 = 1 \text{ at } T > T_{liquidus.} \tag{2.4}$$

The effective density, ρ_{eff} of molten rock is obtained from

$$\rho_{eff} = \rho_{solid}\,(1 - M + M\frac{\rho_{0molten}}{\rho_{0solid}}) \tag{2.5}$$

$$\rho_{solid} = \rho_{0solid}\,.[1 - \alpha(T - 298)].[1 + \beta\,(P - 0.1)\,], \tag{2.6}$$

Where, ρ_{0solid} is calculated from P (MPa) and T (K) units by α.and β are thermal expansion and compressibility of rocks, respectively.

In the later stages of the model, the matrix mechanism produced in the subduction zone is detailed. In the material field of the model, the dark and light gray colors is the continental crust, the dark blue color is mantle lithosphere, the light blue color is asthenosphere, the red color is aqueous melts, and the purple color is dry solution and the lighter blue color represent the hydrated mantle. The figure is detailed with markings. (See Figure 2.2).

2.1.4. Rheological model

The code which is used for modelling processes is considering three type of behavior. These are viscous, elastic and plastic behaviors.

2.1.4.1. Viscous behavior

The rheological model calculation uses the viscosity equation for dislocation creep which is defined at (Ranalli, 1995).

$$\eta_{creep} = \left(\frac{\dot{\varepsilon}}{A}\right)^{1/n} \exp\left(\frac{E}{nRT}\right), \tag{2.7}$$

Where, E (activation energy), η (creep viscosity), n (exponent), A (pre-exponential factor) are determined as flow law parameters.

$$\tau = \eta\dot{\gamma} \tag{2.8}$$

Where the, ε (shear stress), η (viscosity) and $\dot{\gamma}$ (shear rate) are the elements of the equation.

2.1.4.2. Elastic behavior

Elastic behavior of material is calculated with Hook's law which is defined at

$$\sigma = E\,\varepsilon \tag{2.9}$$

Where the, σ (stress), E (elastic modulus), ε (strain) are the component of the equation.

2.1.4.3. Plastic behavior

$$\sigma_{yield} = c + Psin(\varphi) \tag{2.10}$$

Where, σ is the shear stress [Pa], c is the cohesion [Pa], P is the total pressure [Pa] and φ is the internal angle of friction. The plastic behavior is implied with the equation 2.10). The configuration is prepared as a description of the crust, mantle lithosphere and asthenosphere properties. Material parameters are given at Table I.1.

2.1.5. Conservation equations

For the numerical modeling part of this work, a plane strain viscoelastic code I2ELVIS is used which is authored and explained by (Taras V. Gerya & Yuen, 2003). Major principles of modeling scheme are given below;

1. Conserving stresses under extreme viscosity conditions,

2. Conserving heat and chemical fluxes in the face of rapidly changing conductivity, transport coefficient and temperature gradients at the thermal or chemical boundary.

3. Conserving temperature field, chemical compositions, and density in flows with a strongly advection character.

The code is based on a mixture of finite-differences with marker-in-cell technique. In terms, these equations are based on mass conservation theory. Elliptic equations in the velocity field (υ) are Eqs. (2-1) and (2-2).

$$\frac{\partial_{\sigma_{xx}}}{\partial_x} + \frac{\partial_{\sigma_{xz}}}{\partial_z} = \frac{\partial P}{\partial_x} - \rho(T, C)g_x \tag{2.11}$$

$$\sigma_{xx} = 2\eta\varepsilon_{xx} \tag{2.12}$$

$$\sigma_{xz} = 2\eta\varepsilon_{xz} \tag{2.13}$$

$$\sigma_{zz} = 2\eta\varepsilon_{zz} \tag{2.14}$$

$$\varepsilon_{zz} = \frac{\partial_{\upsilon_x}}{x} \tag{2.15}$$

$$\varepsilon_{xz} = \frac{1}{2}\left(\frac{\partial_{\upsilon_x}}{z} + \frac{\partial_{\upsilon_z}}{\partial_x}\right) \tag{2.16}$$

$$\varepsilon_{zz} = \frac{\partial_{\upsilon_z}}{\partial_z} \tag{2.17}$$

$$\sigma_{xx} = 2\eta\varepsilon_{xx} \tag{2.18}$$

These equations are followed by the basic relationship between the stress (σ) and strain-rate (ε), where η represents the viscosity, which depends on the temperature (T), pressure (P), chemical components (C) and strain-rate.

The mass conservation equations is given by the continuity equation which conducts density in equity of buoyancy forces. Equations regulate temperature and volatile content in terms:

$$\frac{\partial_{\upsilon_x}}{\partial_x} + \frac{\partial_{\upsilon_z}}{\partial_z} = 0 \tag{2.19}$$

Combination of moving marker technique (marker in cell) is used for solving (2.19) which is based on finite control volume method.

In marker-in-cell method, markers carry information on composition (which is used to define density, viscosity and shear modulus) and stresses (in viscoelastic case).

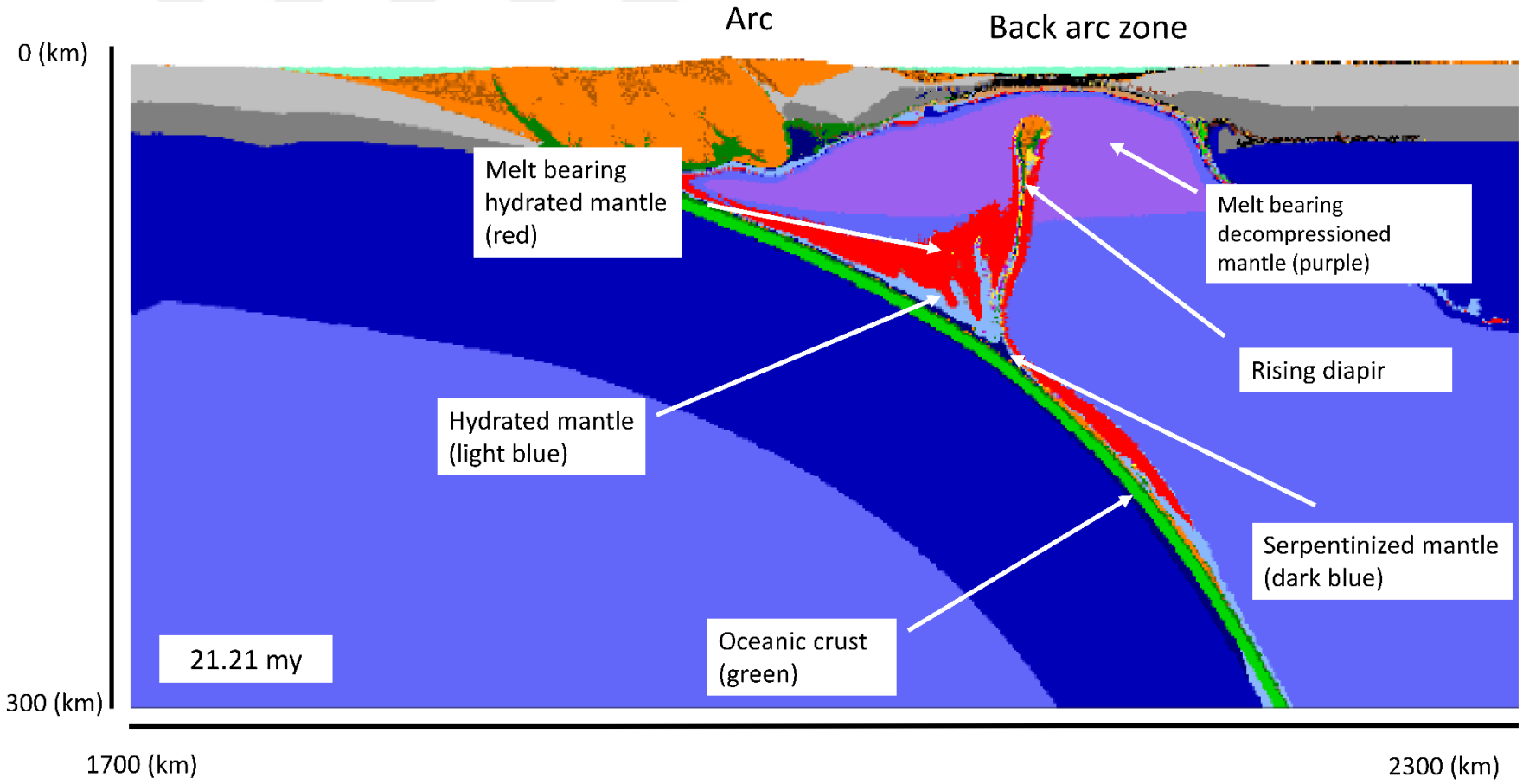

Figure 2.2: The model representation a retreating oceanic-continental subduction with the formation of mantle wedge, magmatic arc and extensional basin with new creating oceanic floor (see text for details).

3. RESULTS OF NUMERICAL EXPERIMENTS

To start our investigation we began witha convergence rate of totally 4 cm/yr from both sides (right and left) of model convergece rate changed to 8 cm/yr. In the models, the lithosphere has composed of a 35 km thick continental crust, a 8 km thick oceanic crust and a 113 km thick mantle lithosphere.. The rheologies are determined as wet quartzite in continental crust, gabbro/basalt in oceanic crust, wetolivine in mantle lithosphere and wetolivine in asthenosphere (Ranalli, 1995). Reference densities of continental crust, oceanic crust and mantle lithosphere and asthenosphere are 2700 kg/m^3, 3000 kg/m^3, 3300 kg/m^3 and 3300 kg/m^3, respectively (Table I.1). Based on this reference model, we performed numerical experiments by independently varying oceanic lithosphere ages (Table 3.1).

Table 3.1: Experiment Parameters.

Experiment Number	Oceanic Mantle Lithosphere Age (Ma)	Convergent Rate (cm/yr)
A1	50	4
A2	60	4
A3	70	4
A4	80	4
A5	90	4
A6	100	4
A7	110	4
A8	120	4
B1	50	8
B2	60	8
B3	70	8
B4	80	8
B5	90	8
B6	100	8
B7	110	8
B8	120	8

3.1. Results of Experiment A

In Experiment A, convergence rate is determined as 4 cm/yr (slow convergence rate). Oceanic lithosphere age is changing periodic increment (see Table 2.1).

3.1.1. Experimental set A1

In experimental set A1 , it is imposed that a convergence rate of 4 cm/yr from both side(right and left) of model Oceanic lithosphere age is determined as 50 Ma.Oceanic lithosphere thickness incresed due to modelling process. In models 35 km in thick continental crust , 8 km ocenaic cruscrust and 80 km in thick mantle lithosphere as determined. The rheologies determined as wet quartzite in contienetal crust (Ranalli, 1995), gabbro/basalt in oceanic crust (Ranalli, 1995) ,wetolivine in mantle lithosphere (Ranalli, 1995) and wetolivine in asthenosphere. Reference densities of continental crust, oceanic crust and mantle lithosphere and asthenosphere is 2700 kg/m3, 3000 kg/m3, 3300 kg/m3 and 3300 kg/m3, respectively.

3.1.2. Results of A1

After 12.10 m.y., at this stage, wet melt production was higher than wet melt production and both concentrated back arc. Convection currents in the mantle are upward and high in intensity (Figure 3.1). After 12.52 m.y wet melt production is more dominant than wet melt production (Figure 3.2). After then13.64 m.y wet melt production is regional and high, but wet melt production is spread over a larger area. The intensity of the convection currents in the mantle is low (Figure 3.3). After 13.96 m.y wet melt production migrated to tranch. Wet and wet melt types are co-produced in a small area under the accrationary prism (Figure 3.4). After 14.49 m.y wet melt production is more and spread than wet melt production. Convection currents in mantle have counterclockwise movement against subduction mechanism and its intensity is high (Figure 3.5). Then after 14.99 m.y at this stage, the production of wet melt is high against the observation of wet melt production. The intensity of the convection currents in the mantle is high. (Figure 3.6).

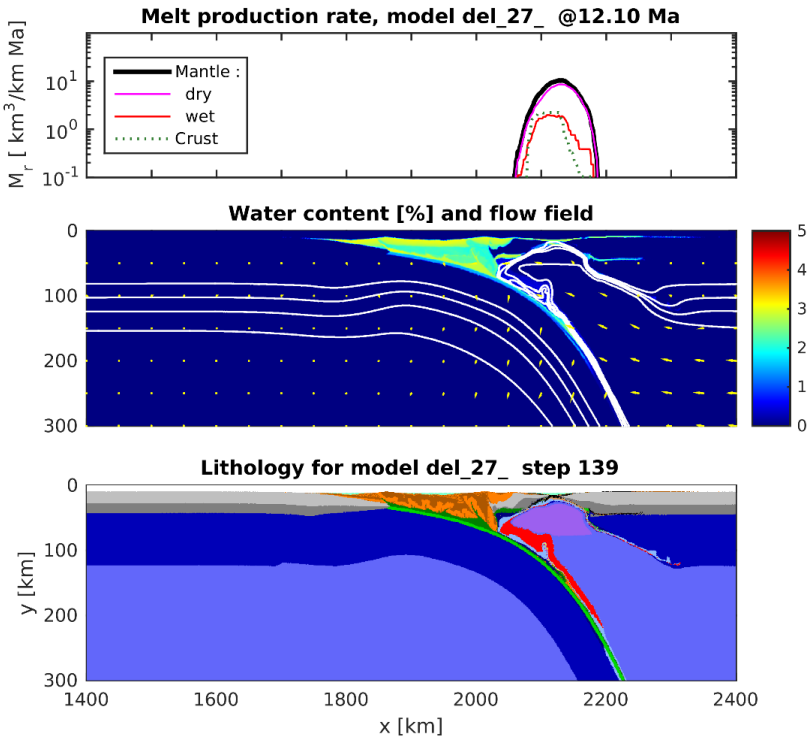

Figure 3.1: The results of the Experiment A1, show *melt production graph* (top), *water content with percentage* (middle), and *lithology graph* (bottom) at 12.10 Myr.

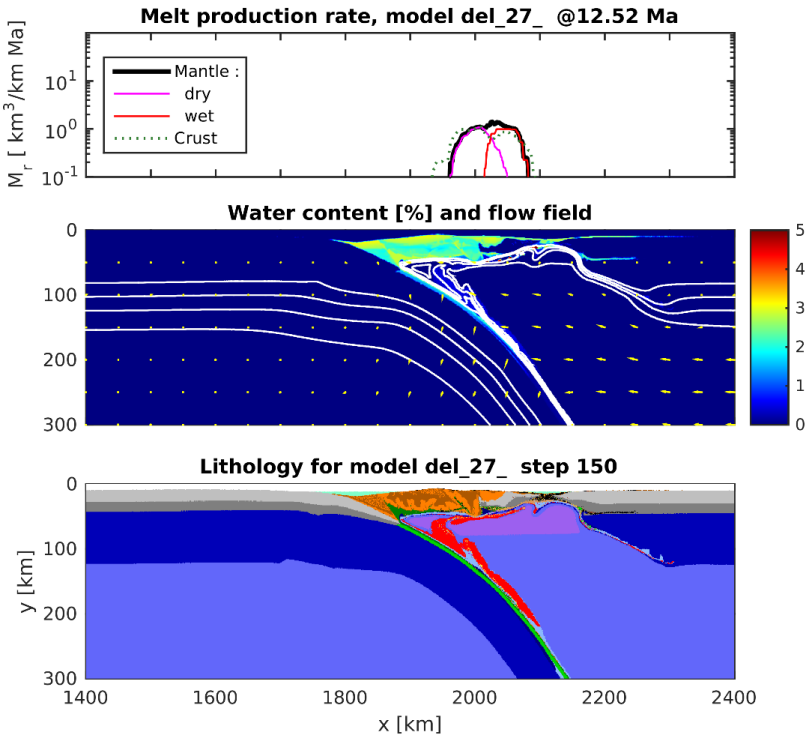

Figure 3.2: The results of the Experiment A1, show *melt production graph* (top), *water content with percentage* (middle), and *lithology graph* (bottom) at 12.52 Myr.

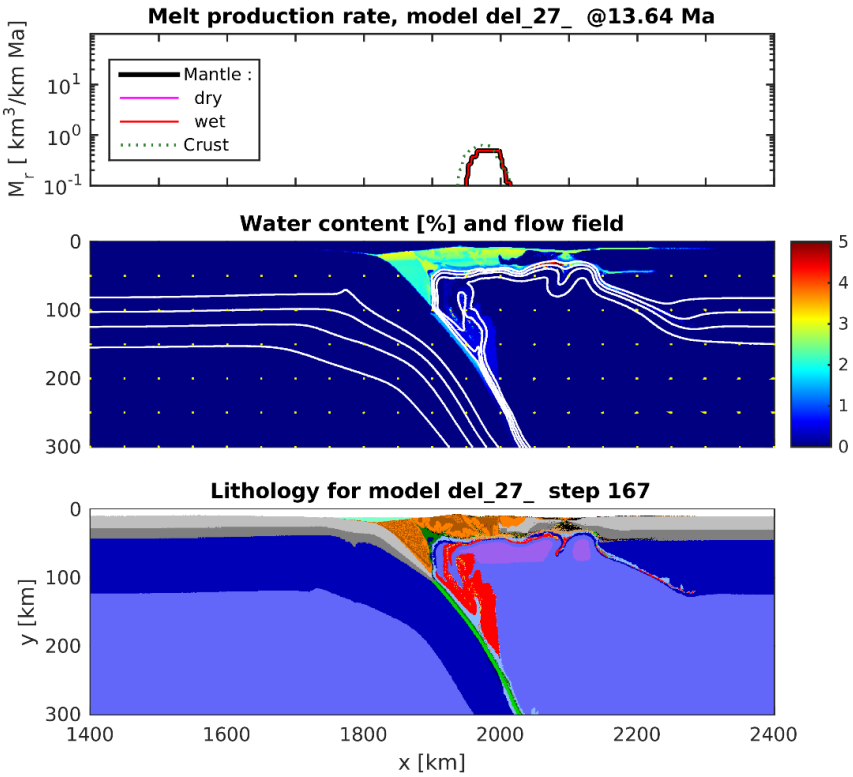

Figure 3.3 The results of the Experiment A1, show *melt production graph* (top), *water content with percentage* (middle), and *lithology graph* (bottom) at 13.64 Myr.

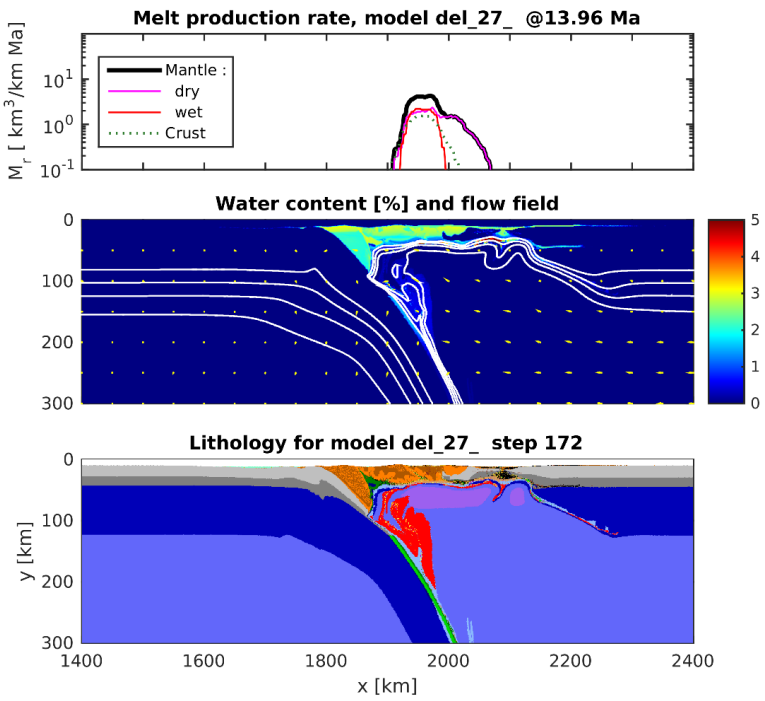

Figure 3.4: The results of the Experiment A1, show *melt production graph* (top), *water content with percentage* (middle), and *lithology graph* (bottom) at 13.96 Myr.

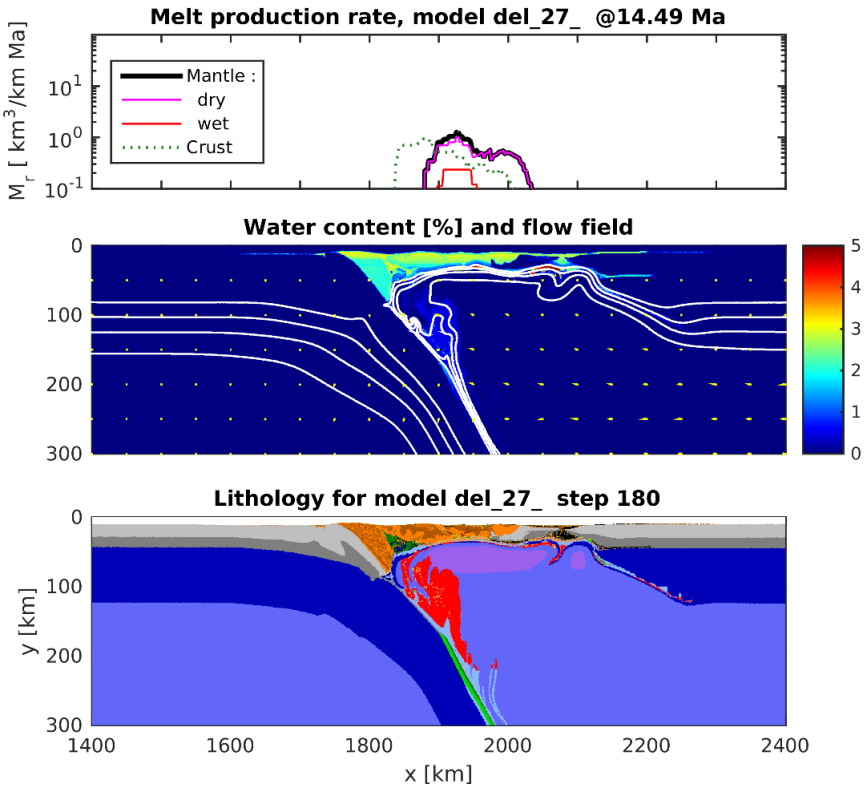

Figure 3.5: The results of the Experiment A1, show *melt production graph* (top), *water content with percentage* (middle), and *lithology graph* (bottom) at 14.49 Myr.

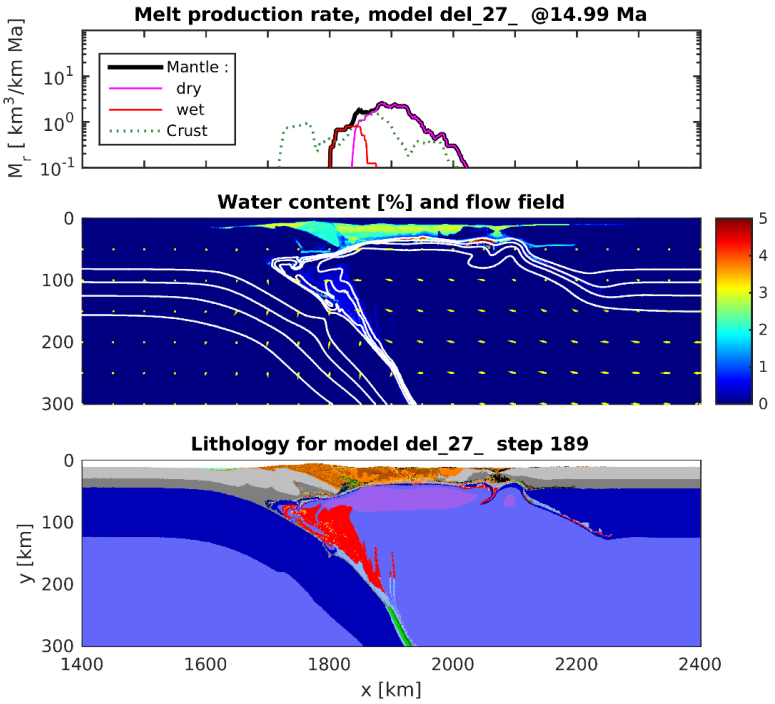

Figure 3.6: The results of the Experiment A1, show *melt production graph* (top), *water content with percentage* (middle), and *lithology graph* (bottom) at 14.99 Myr.

In the melt extraction graphs, the models show a two-peak attitude. This behavior has a direct relationship to the movement of subduction slab. The withdrawal of the slab 12 million years after the start of the model rapidly changes the dynamics in the mantle and causes a serious increase in melt production. This increase is supported by changes in mantle convection movements. Wet melt extraction is represented with red color and it takes ~200 km^3 maximum melt extraction value. Dry melt extraction is represented with purple color and it takes ~500 km^3 maximum melt extraction value. Crustal deformation extraction is represented with green color and it takes ~500 km^3 maximum melt extraction value (Figure 3.7)

Total melt extraction is represented with black color and it takes ~800 km^3 maximum melt extraction value. The graph, in which each is represented on top of each other, shows the direct relationship between each other. In the total melt production graphs of this model, the first jump value is higher than the secondary jump value and value is about ~400 km^3

The sudden jumps in the graph showing the cumulative sum based on time represent the sudden dynamic changes made by the subduction slab. These changes correspond to ~ 12, ~ 14 and ~ 15 million years for the model. In the 12 and 15 million years, only the wet melt graph showed a sudden change, while in the 14 million years both the wet and wet melt graph showed a sudden increase (Figure 3.8).

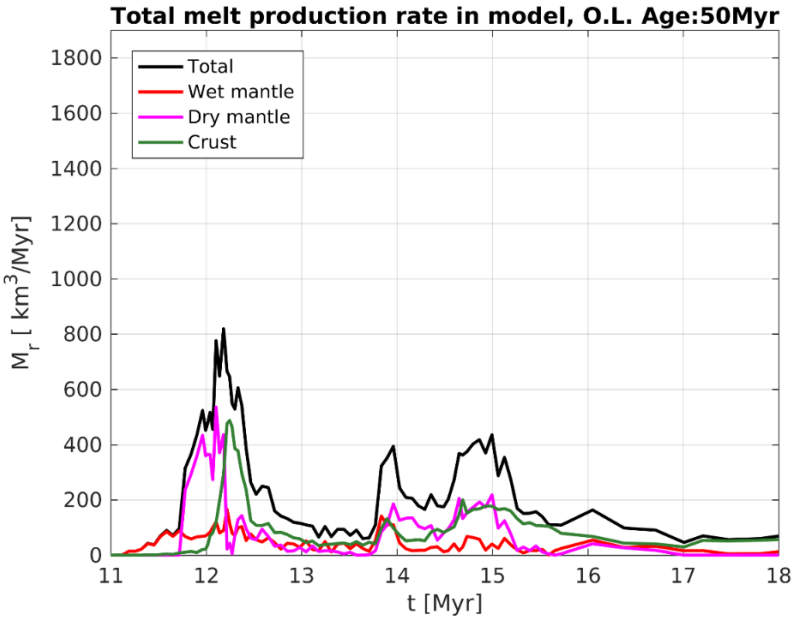

Figure 3.7: Result of the Experiment A1 with discrete volumetric melt production rate depending on time.

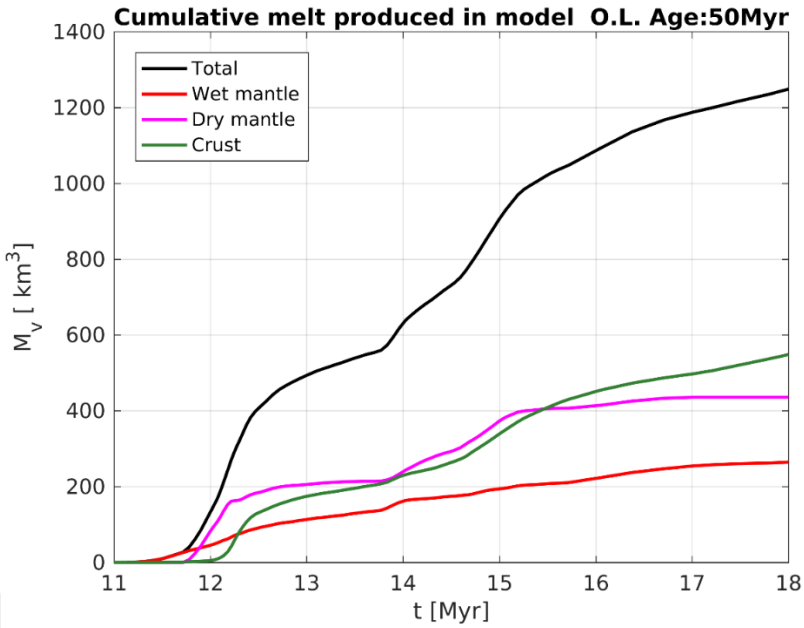

Figure 3.8: Result of the Experiment A1 with cumulative sum of discrete volumetric melt extraction rate depending on time.

3.1.3. Experimental set A2

In experimental set A2 , it is imposed that a convergence rate of 4 cm/yr from both side(right and left) of model Oceanic lithosphere age is determined as 60 Ma.Oceanic lithosphere thickness incresed due to modelling process. In models 35 km in thick continental crust , 8 km ocenaic cruscrust and 80 km in thick mantle lithosphere as determined. The rheologies determined as wet quartzite in contienetal crust (Ranalli, 1995), gabbro/basalt in oceanic crust (Ranalli, 1995) ,wetolivine in mantle lithosphere (Ranalli, 1995) and wetolivine in asthenosphere. Reference densities of continental crust, oceanic crust and mantle lithosphere and asthenosphere is 2700 kg/m3, 3000 kg/m3, 3300 kg/m3 and 3300 kg/m3, respectively.

3.1.4. Results of A2

After 11.95 m.y. the mantle wedge was opened and the asthenosphere entered under the crust up to the back arc. Wet melt production is dominant compared to wet melt production (Figure 3.9). After 12.26 m.y mantle wedge is developed and significantly matle lithosphere is removed. The production of the wet melt became binary and is higher than the wet melt production (Figure 3.10). After 13.05 m.y At this stage, melt production has decreased. Wet melt production is significantly more than wet melt production (Figure 3.11). After 13.76 m.y wet melt production is regionally high and

close to the trench, but wet melt production is spread over the accreationary prism (Figure 3.12). After 14.22 m.y.,at this stage, melt production decreased, and wet melt production migrated to the trench side (Figure 3.13).In the final stage of the model is at 14.48 m.y . At this stage, the wet melt production is small and migrated towards the trance, but wet melt production is located entirely on the accreationary prism. Mantle lithosphere and continental crust were separated and the asthenosphere entered this range.In this model, subduction slab sink into the asthenosphere and bended.Slab break off is not observed (Figure 3.14).

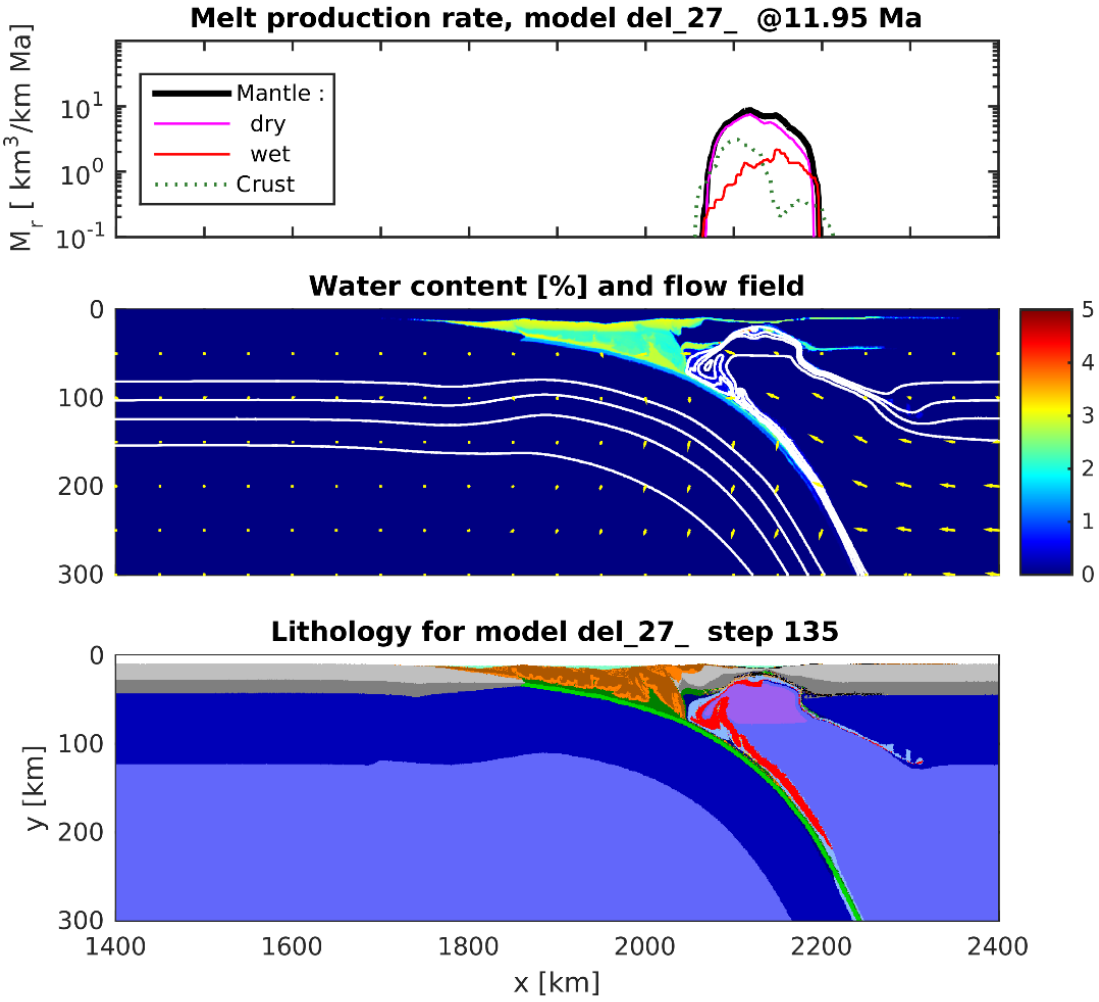

Figure 3.9: The results of the Experiment A2, show *melt production graph* (top), *water content with percentage* (middle), and *lithology graph* (bottom) at 11.95 Myr.

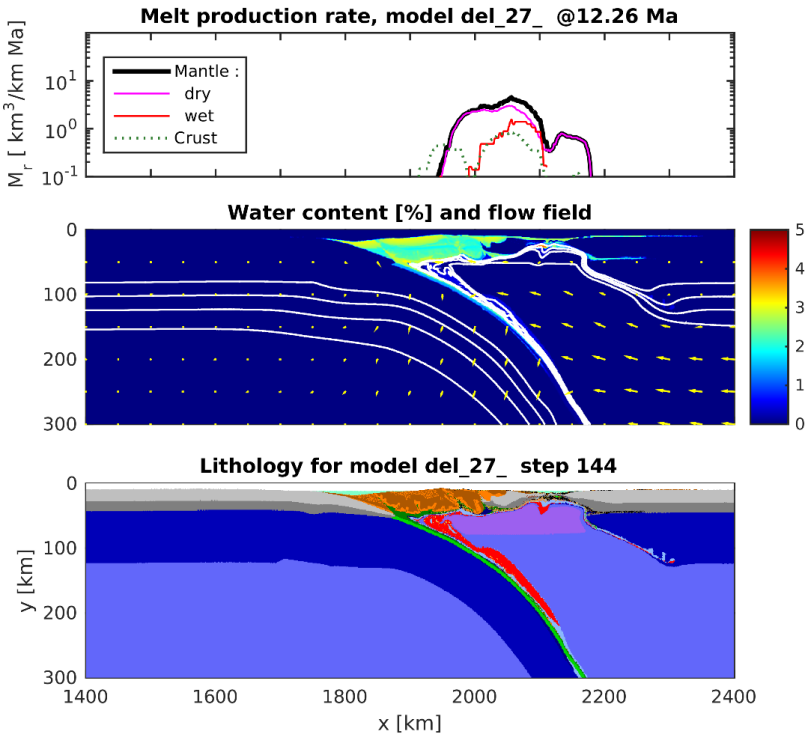

Figure 3.10: The results of the Experiment A2, show *melt production graph* (top), *water content with percentage* (middle), and *lithology graph* (bottom) at 12.26 Myr.

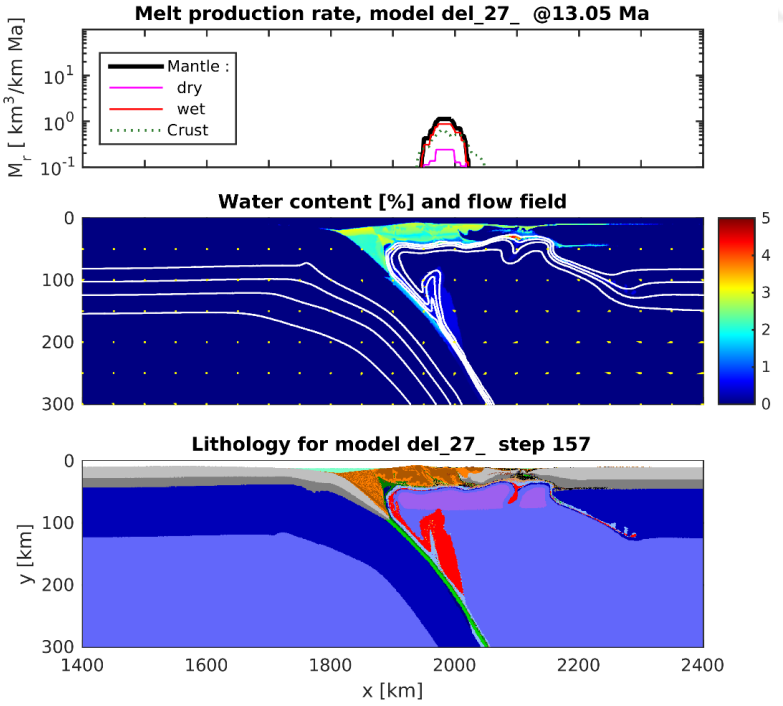

Figure 3.11: The results of the Experiment A2, show *melt production graph* (top), *water content with percentage* (middle), and *lithology graph* (bottom) at 13.05 Myr.

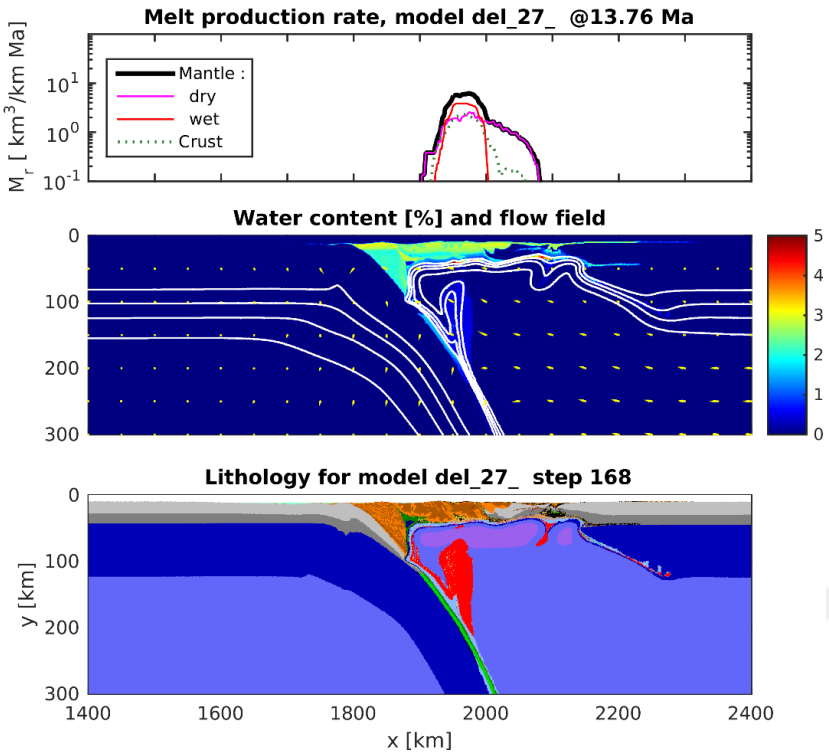

Figure 3.12: The results of the Experiment A2, show *melt production graph* (top), *water content with percentage* (middle), and *lithology graph* (bottom) at 13.76 Myr.

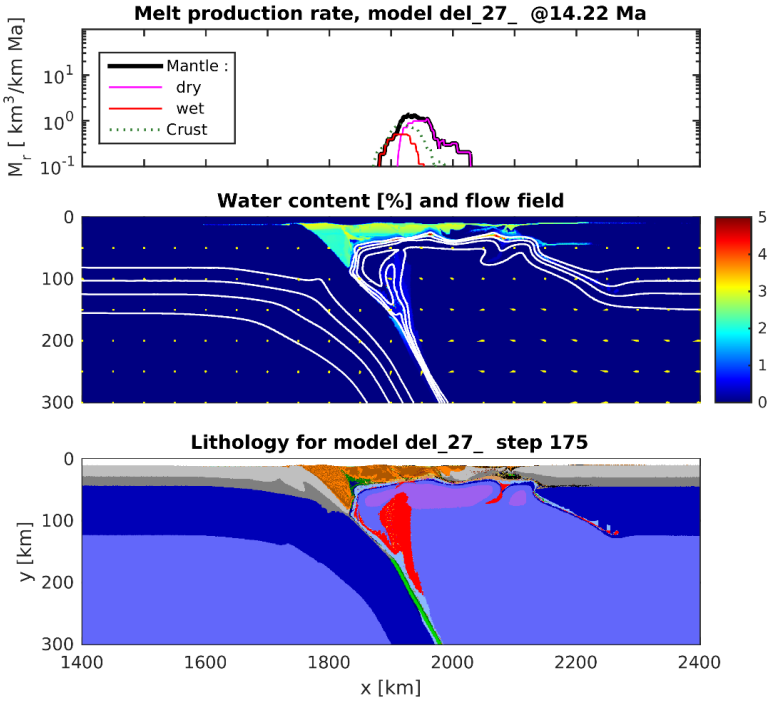

Figure 3.13: The results of the Experiment A2, show *melt production graph* (top), *water content with percentage* (middle), and *lithology graph* (bottom) at 14.22 Myr.

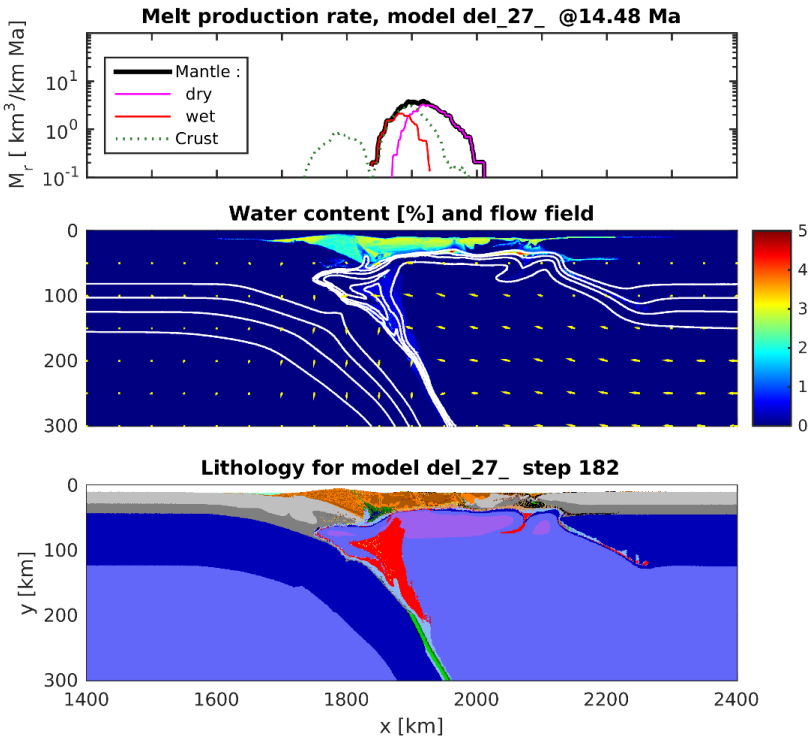

Figure 3.14: The results of the Experiment A2, show *melt production graph* (top), *water content with percentage* (middle), and *lithology graph* (bottom) at 14.48 Myr.

In the melt extraction graphs, the models show a two-peak attitude. This behavior has a direct relationship to the movement of subduction slab. The withdrawal of the slab 12 million years after the start of the model rapidly changes the dynamics in the mantle and causes a serious increase in melt production. This increase is supported by changes in mantle convection movements. Wet melt extraction is represented with red color and it takes ~200 km^3 maximum melt extraction value. Dry melt extraction is represented with purple color and it takes ~500 km^3 maximum melt extraction value. Crustal deformation extraction is represented with green color and it takes ~500 km^3 maximum melt extraction value.

Total melt extraction is represented with black color and it takes ~800 km^3 maximum melt extraction value. The graph, in which each is represented on top of each other, shows the direct relationship between each other in the total melt production graphs of this model, the first jump value is higher than the secondary jump value (Figure 3.15).

The sudden jumps in the graph showing the cumulative sum based on time represent the sudden dynamic changes made by the subduction slab. These changes correspond to ~ 12, ~ 14 and ~ 15 million years for the model. In the 12 and 15 million years, only

the wet melt graph showed a sudden change, while in the 14 million years both the wet and wet melt graph showed a sudden increase (Figure 3.16).

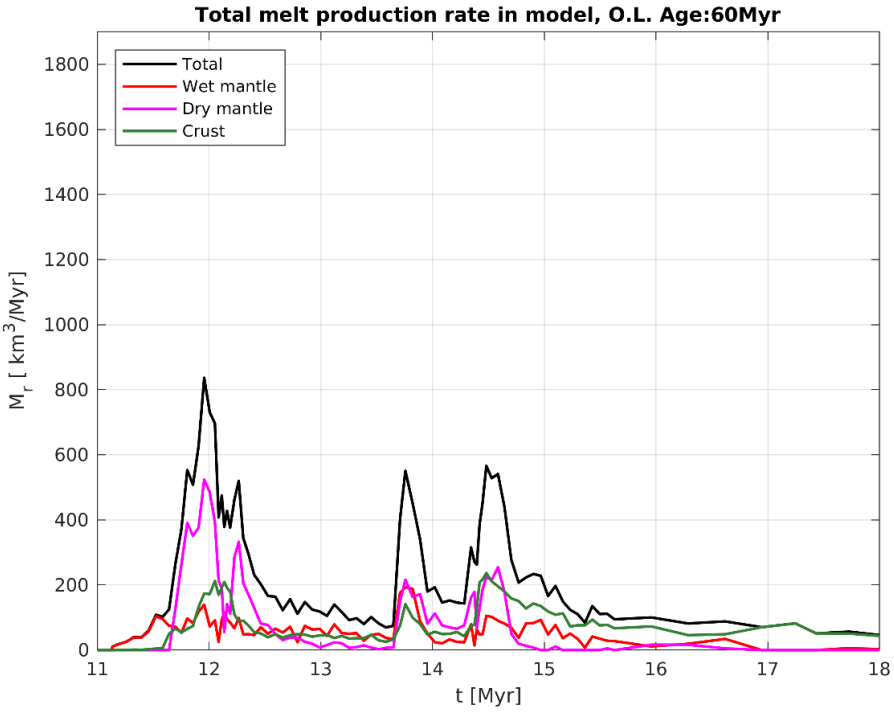

Figure 3.15: Result of experiment A2 with discrete volumetric melt extraction rate depending on time.

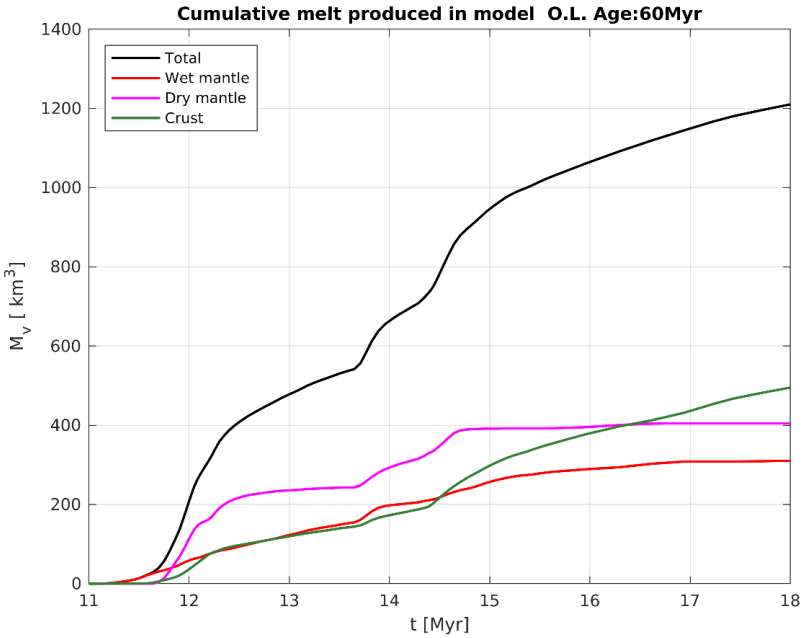

Figure 3.16: Result of Experiment A2 with cumulative sum of discrete volumetric melt extraction rate depending on time.

3.1.5. Experimental set A3

In experimental set A3 , it is imposed that a convergence rate of 4 cm/yr from both side(right and left) of model Oceanic lithosphere age is determined as 70 Ma.Oceanic lithosphere thickness incresed due to modelling process. In models 35 km in thick continental crust , 8 km ocenaic cruscrust and 80 km in thick mantle lithosphere as determined. The rheologies determined as wet quartzite in contienetal crust (Ranalli, 1995), gabbro/basalt in oceanic crust (Ranalli, 1995) ,wetolivine in mantle lithosphere (Ranalli, 1995) and wetolivine in asthenosphere. Reference densities of continental crust, oceanic crust and mantle lithosphere and asthenosphere is 2700 kg/m3, 3000 kg/m3, 3300 kg/m3 and 3300 kg/m3, respectively.

3.1.6. Results of A3

After 11.86 m.y., at this stage, wet melt production was higher than wet melt production and both concentrated back arc. Convection currents in the mantle are upward and high in intensity (Figure 3.17). After 12.47 m.y wet melt production is more dominant than wet melt production (Figure 3.18). After then13.69 m.y wet melt production is regional and high, but wet melt production is spread over a larger area. The intensity of the convection currents in the mantle is low (Figure 3.19). After 14.00 m.y wet melt production migrated to tranch. Wet and wet melt types are co-produced in a small area under the accrationary prism (Figure 3.20). After 14.28 m.y wet melt production is more and spread than wet melt production. Convection currents in mantle have counterclockwise movement against subduction mechanism and its intensity is high (Figure 3.21). In the final stage, after 14.31 m.y the slab was broken and the convection currents in the mantle reached their highest level (Figure 3.22).

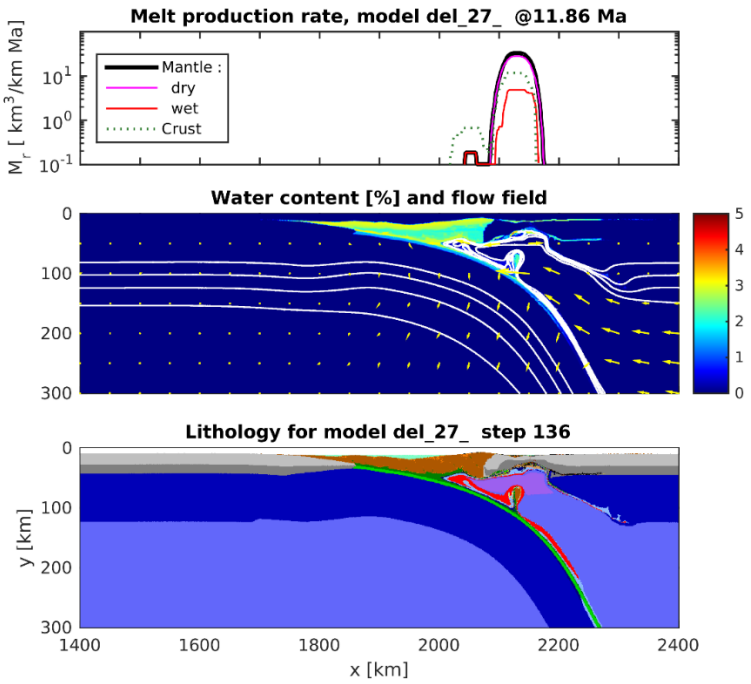

Figure 3.17: The results of the Experiment A3, show *melt production graph* (top), *water content with percentage* (middle), and *lithology graph* (bottom) at 11.86 Myr.

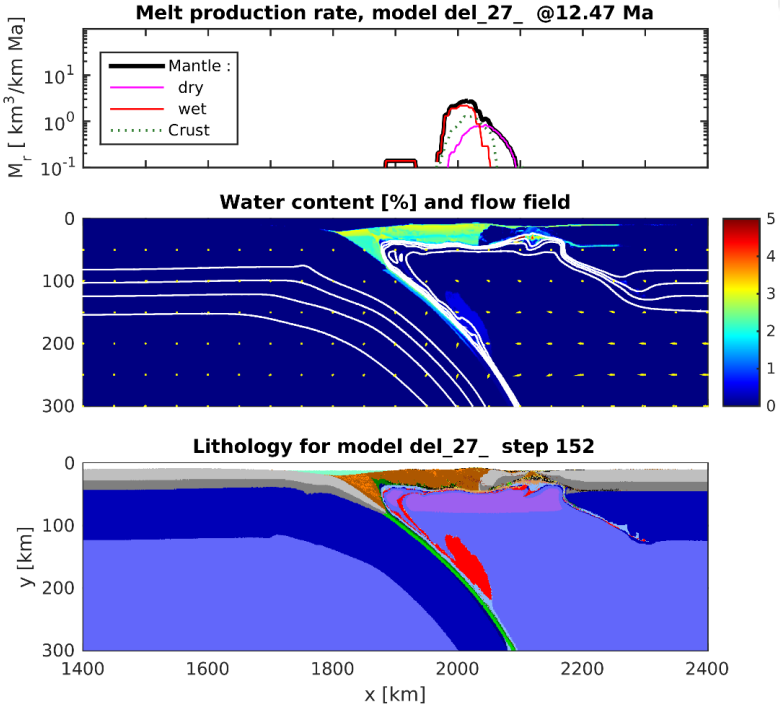

Figure 3.18: The results of the Experiment A3, show *melt production graph* (top), *water content with percentage* (middle), and *lithology graph* (bottom) at 13.64 Myr.

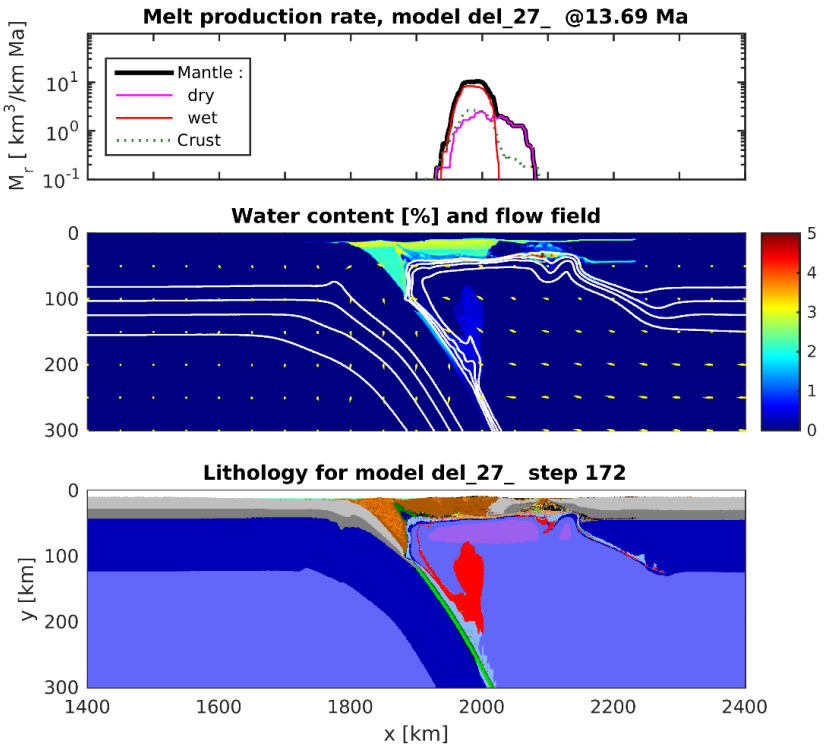

Figure 3.19: The results of the Experiment A3, show *melt production graph* (top), *water content with percentage* (middle), and *lithology graph* (bottom) at 13.69 Myr.

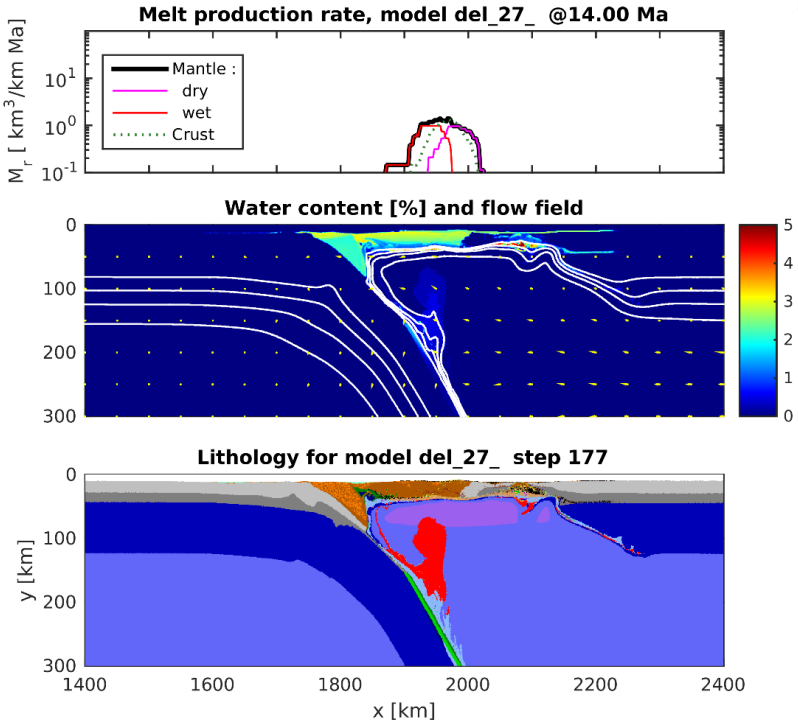

Figure 3.20: The results of the Experiment A3, show *melt production graph* (top), *water content with percentage* (middle), and *lithology graph* (bottom) at 14.00 Myr.

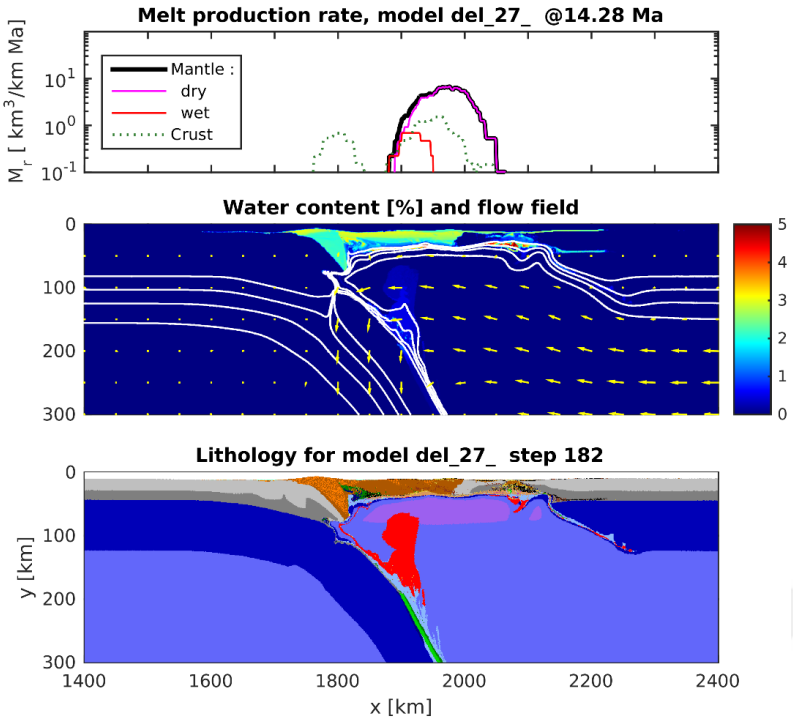

Figure 3.21: The results of the Experiment A3, show *melt production graph* (top), *water content with percentage* (middle), and *lithology graph* (bottom) at 14.28 Myr.

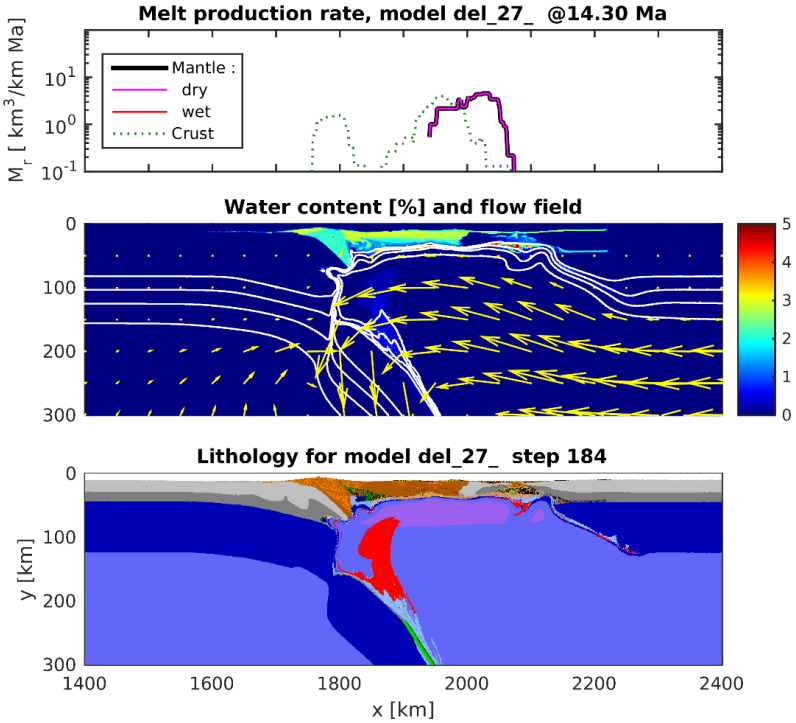

Figure 3.22: The results of the Experiment A3, show *melt production graph* (top), *water content with percentage* (middle), and *lithology graph* (bottom) at 14.30 Myr.

In the melt extraction graphs, the models show a two-peak attitude. This behavior has a direct relationship to the movement of subduction slab. The withdrawal of the slab 11.5 million years after the start of the model rapidly changes the dynamics in the mantle and causes a serious increase in melt production. This increase is supported by changes in mantle convection movements. Wet melt extraction is represented with red color and it takes ~200 km^3 maximum melt extraction value. Dry melt extraction is represented with purple color and it takes ~1500 km^3 maximum melt extraction value. Crustal deformation extraction is represented with green color and it takes ~1000 km^3 maximum melt extraction value. Total melt extraction is represented with black color and it takes ~1500 km^3 maximum melt extraction value. The graph, in which each is represented on top of each other, shows the direct relationship between each other

In the total melt production graphs of this model, the first jump value is higher than the secondary jump value (Figure 3.25).

The sudden jumps in the graph showing the cumulative sum based on time represent the sudden dynamic changes made by the subduction slab. These changes correspond to ~ 12, ~ 13.5 and ~ 14.5 million years for the model. In the 12 and 14.5 million years, only the wet melt graph showed a sudden change, while in the 13.5 million years both the wet and wet melt graph showed a sudden increase (Figure 3.24).

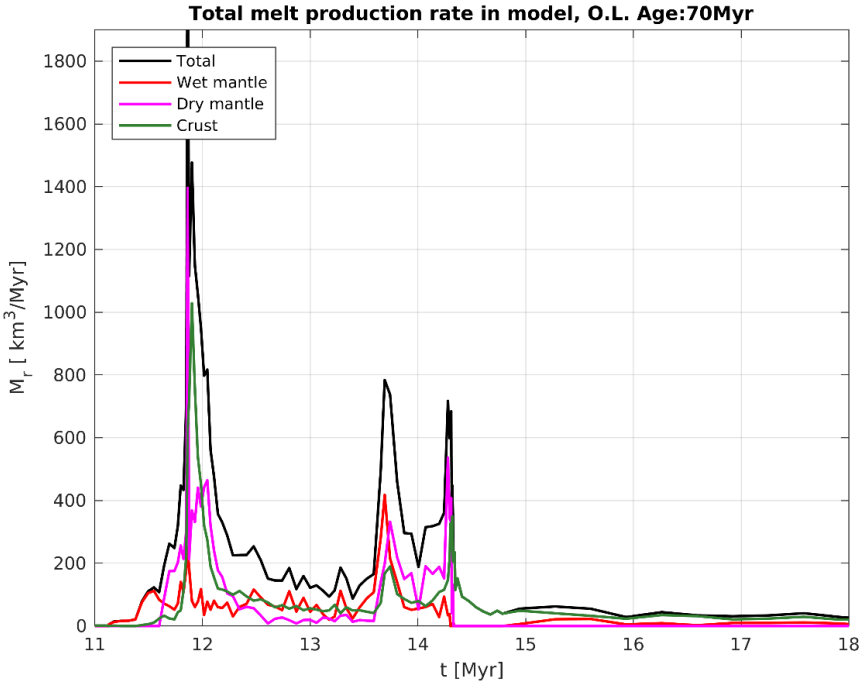

Figure 3.23: Result of the Experiment A3 with discrete volumetric melt extraction rate depending on time.

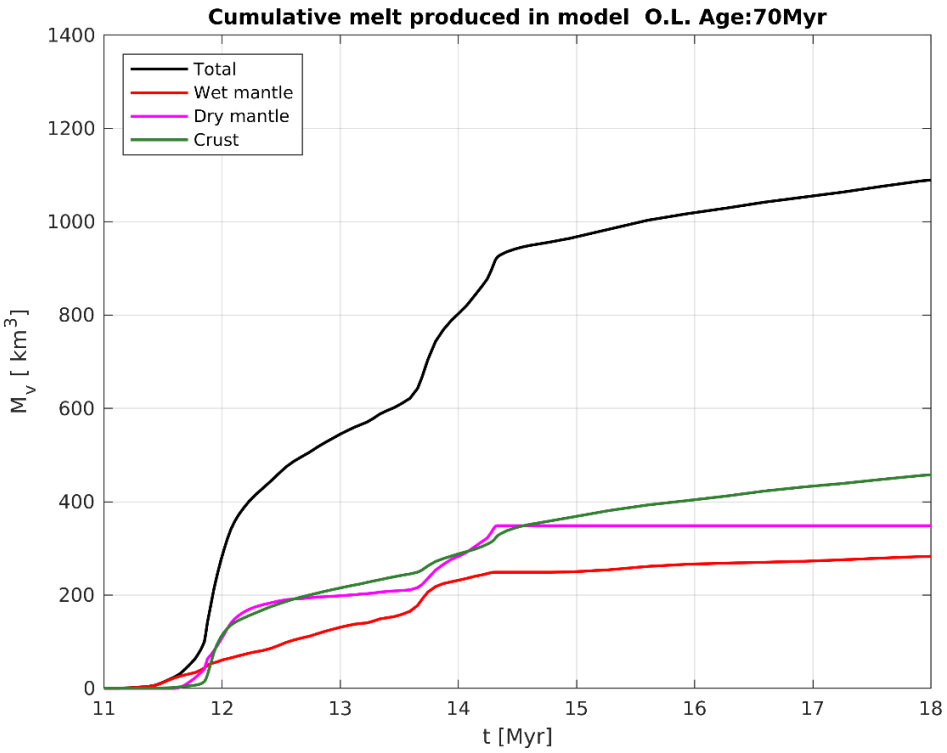

Figure 3.24: Result of the Experiment A3 with cumulative sum of discrete volumetric melt extraction rate depending on time.

3.1.7. Experimental set A4

In experimental set A4 , it is imposed that a convergence rate of 4 cm/yr from both side(right and left) of model Oceanic lithosphere age is determined as 80 Ma.Oceanic lithosphere thickness incresed due to modelling process. In models 35 km in thick continental crust , 8 km ocenaic cruscrust and 80 km in thick mantle lithosphere as determined. The rheologies determined as wet quartzite in contienetal crust (Ranalli, 1995), gabbro/basalt in oceanic crust (Ranalli, 1995) ,wetolivine in mantle lithosphere (Ranalli, 1995) and wetolivine in asthenosphere. Reference densities of continental crust, oceanic crust and mantle lithosphere and asthenosphere is 2700 kg/m3, 3000 kg/m3, 3300 kg/m3 and 3300 kg/m3, respectively.

3.1.8. Results of A4

After 11.86 m.y. At this stage, the wet melt production type is more than the wet melt production and it is spread. The wet melt type is concentrated in two regions. The convection currents in the mantle are upward (Figure 3.25).After 12.20 m.y. at this stage, melt production decreased.Wet melt production is concentrated in three regions

and is higher than wet melt production (Figure 3.26). After 13.45 m.y Melt production increased and wet melt production concentrated regionally. Convection currents in the mantle are stagnant (Figure 3.27). After 13.76 m.y at this stage, melt production has fallen. Wet melt production has spread and wet plum production is small and regional (Figure 3.28). After 13.92 m.y wet melt production is more and spread than wet melt production. Convection currents in mantle have counterclockwise movement against subduction mechanism and its intensity is high (Figure 3.29). In the latest stage of the model, after 13.95 m.y no melt production was observed at this stage. Only crustal deformation was observed (Figure 3.30).

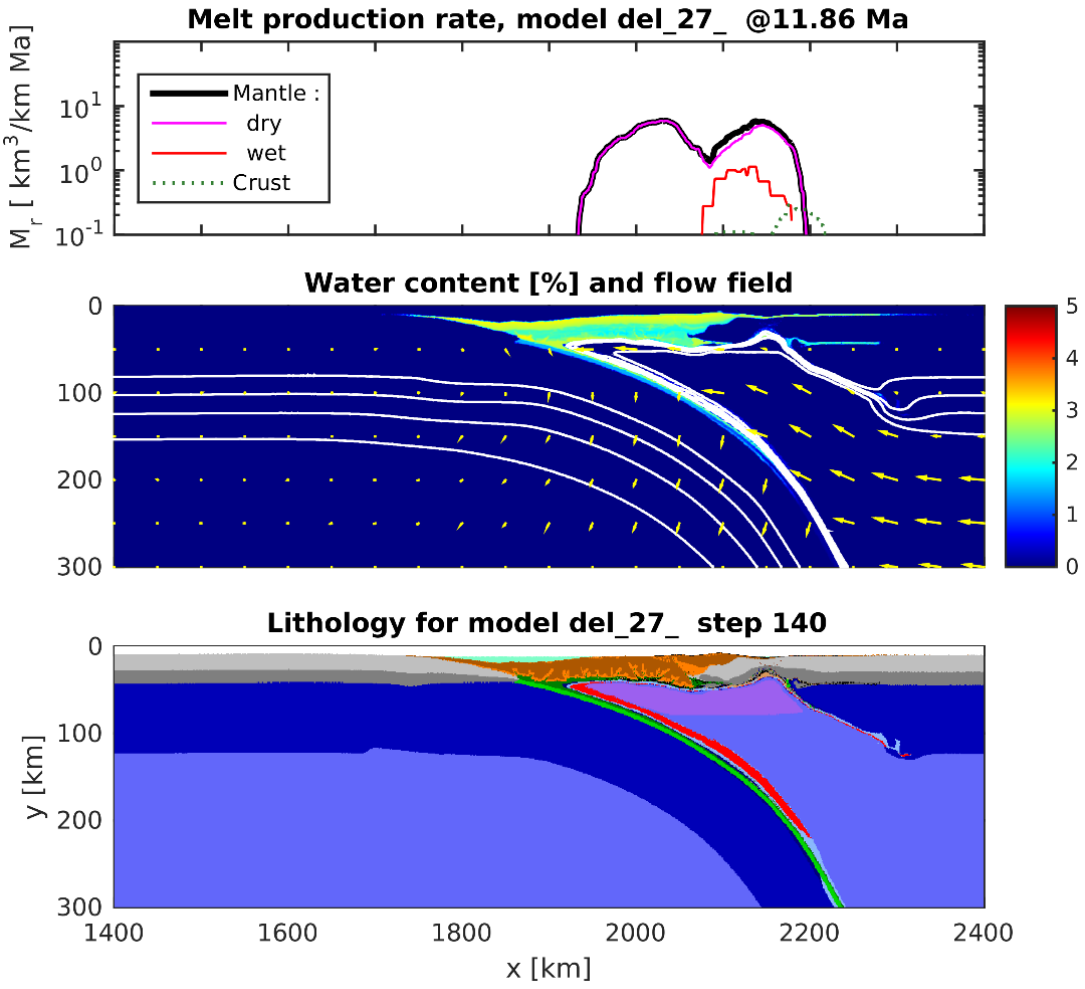

Figure 3.25: The results of the Experiment A4, show *melt production graph* (top), *water content with percentage* (middle), and *lithology graph* (bottom) at 11.86 Myr.

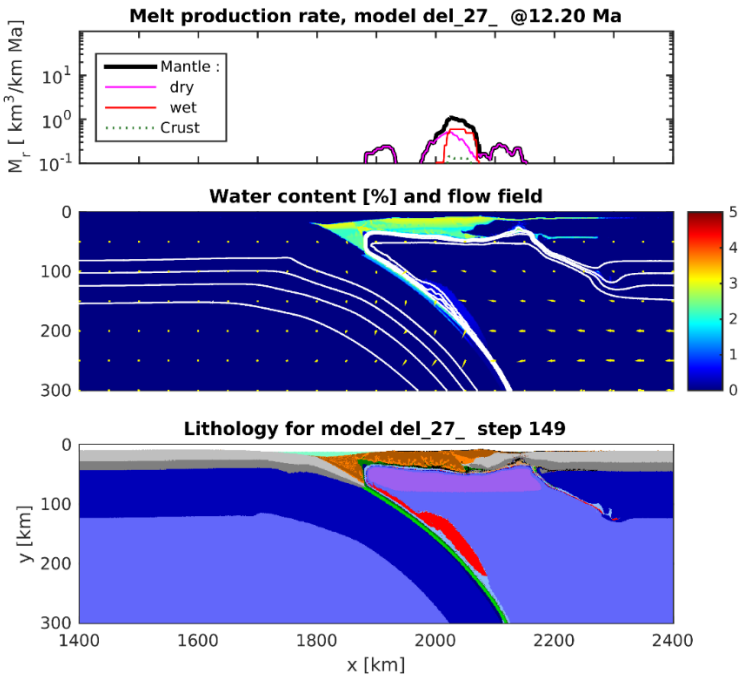

Figure 3.26: The results of the Experiment A4, show *melt production graph* (top), *water content with percentage* (middle), and *lithology graph* (bottom) at 12.20 Myr.

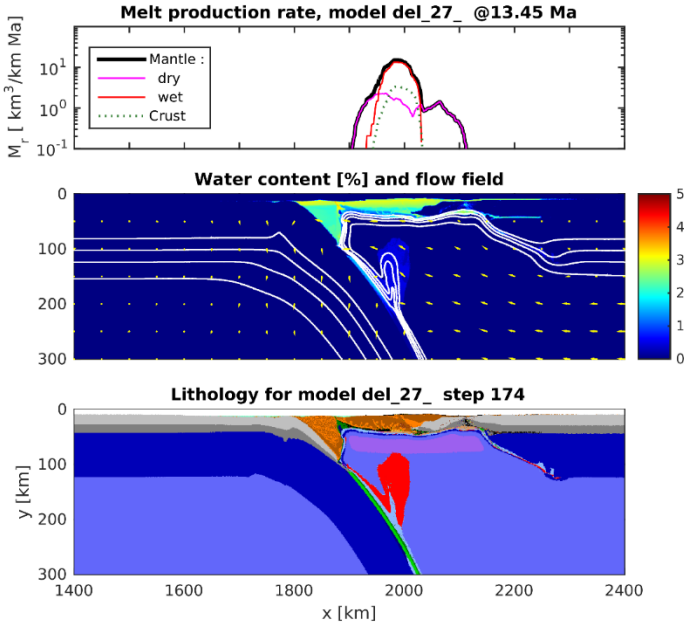

Figure 3.27: The results of the Experiment A4, show *melt production graph* (top), *water content with percentage* (middle), and *lithology graph* (bottom) at 13.45 Myr.

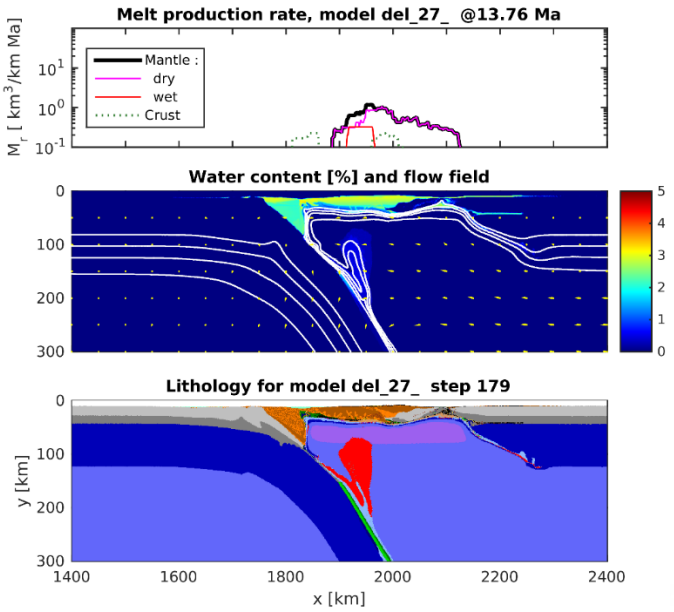

Figure 3.28: The results of the Experiment A4, show *melt production graph* (top), *water content with percentage* (middle), and *lithology graph* (bottom) at 13.76 Myr.

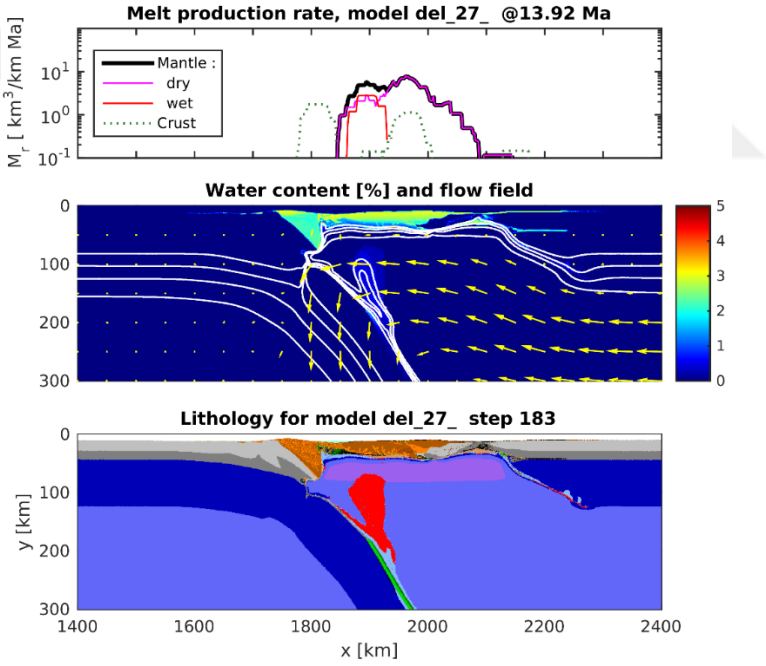

Figure 3.29: The results of the Experiment A4, show *melt production graph* (top), *water content with percentage* (middle), and *lithology graph* (bottom) at 13.92 Myr.

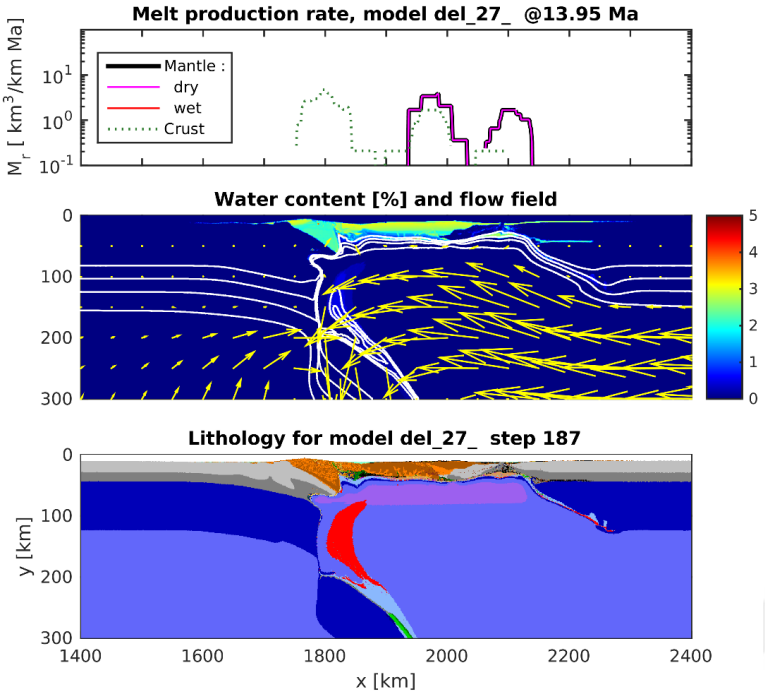

Figure 3.30: The results of the Experiment A4, show *melt production graph* (top), *water content with percentage* (middle), and *lithology graph* (bottom) at 13.95 Myr.

In the melt extraction graphs, the models show a two-peak attitude. This behavior has a direct relationship to the movement of subduction slab. The withdrawal of the slab 11.5 million years after the start of the model rapidly changes the dynamics in the mantle and causes a serious increase in melt production. This increase is supported by changes in mantle convection movements. Wet melt extraction is represented with red color and it takes ~200 km^3 maximum melt extraction value. Dry melt extraction is represented with purple color and it takes ~900 km^3 maximum melt extraction value. Crustal deformation extraction is represented with green color and it takes ~500 km^3 maximum melt extraction value. Total melt extraction is represented with black color and it takes ~1100 km^3 maximum melt extraction value. The graph, in which each is represented on top of each other, shows the direct relationship between each other

In the total melt production graphs of this model, the second jump value is higher than the first jump value (Figure 3.31).

The sudden jumps in the graph showing the cumulative sum based on time represent the sudden dynamic changes made by the subduction slab. These changes correspond to ~ 11.5, ~ 13.5 and ~ 14 million years for the model. In the 11.5 and 14 million years,

only the wet melt graph showed a sudden change, while in the 13.5 million years both the wet and wet melt graph showed a sudden increase (Figure 3.32).

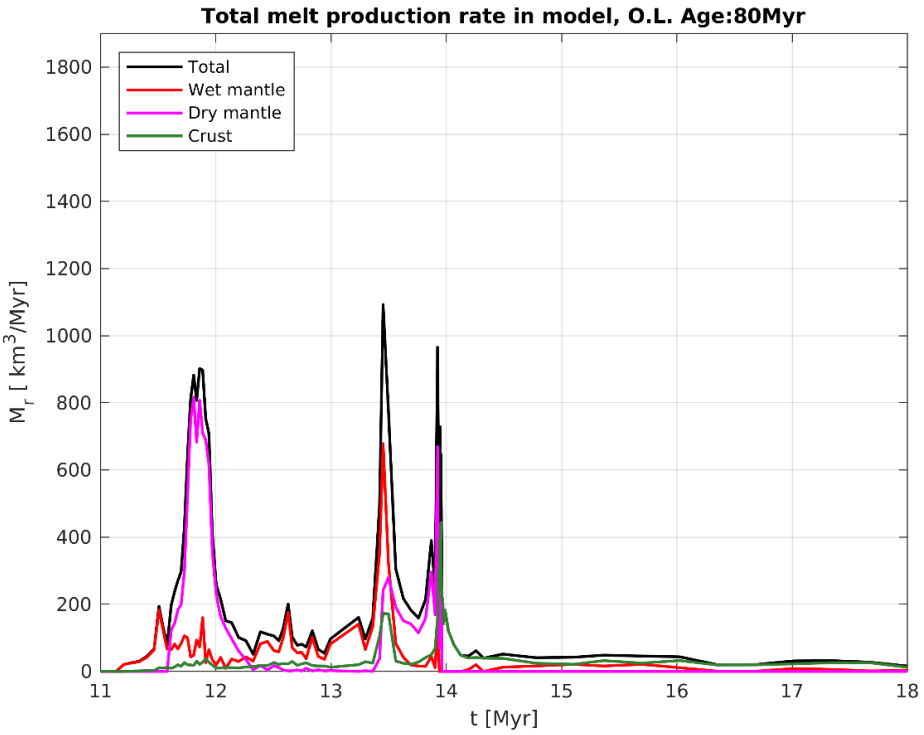

Figure 3.31: Result of the Experiment A4 with discrete volumetric melt extraction rate depending on time.

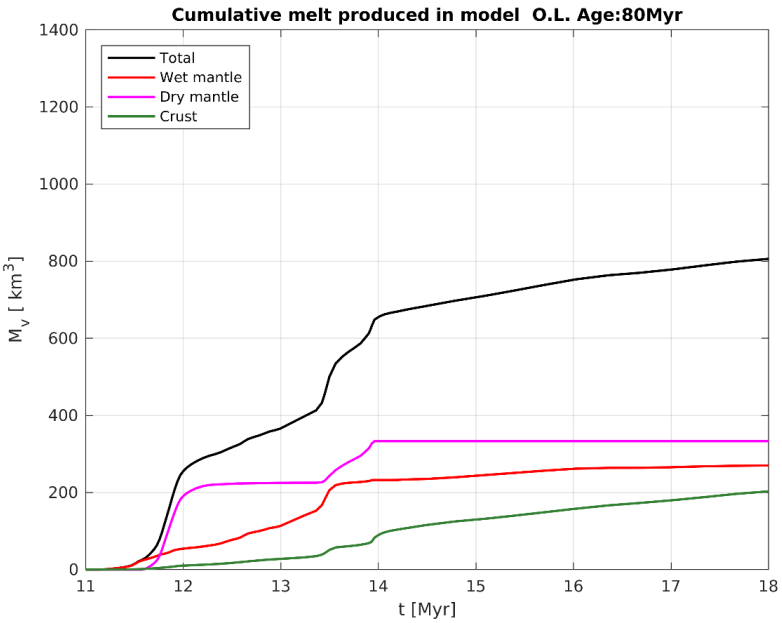

Figure 3.32: Result of Experiment A4 with cumulative sum of discrete volumetric melt extraction rate depending on time.

3.1.9. Experimental set A5

In experimental set A5 , it is imposed that a convergence rate of 4 cm/yr from both side(right and left) of model Oceanic lithosphere age is determined as 90 Ma.Oceanic lithosphere thickness incresed due to modelling process. In models 35 km in thick continental crust , 8 km ocenaic cruscrust and 80 km in thick mantle lithosphere as determined. The rheologies determined as wet quartzite in contienetal crust (Ranalli, 1995), gabbro/basalt in oceanic crust (Ranalli, 1995) ,wetolivine in mantle lithosphere (Ranalli, 1995) and wetolivine in asthenosphere. Reference densities of continental crust, oceanic crust and mantle lithosphere and asthenosphere is 2700 kg/m3, 3000 kg/m3, 3300 kg/m3 and 3300 kg/m3, respectively.

3.1.10. Results of A5

After 11.80 m.y., at this stage, wet melt production was higher than wet melt production and both concentrated back arc. Convection currents in the mantle are upward and high in intensity (Figure 3.33). After then 12.20 m.y wet melt production is regional and high, but wet melt production is spread over a larger area. The intensity of the convection currents in the mantle is low (Figure 3.34). After 12.77 m.y wet melt production migrated to tranch. Wet and wet melt types are co-produced in a small area under the accrationary prism(Figure 3.35). After 14.07 m.y wet melt production is more and spread than wet melt production. Convection currents in mantle have counterclockwise movement against subduction mechanism and its intensity is high (Figure 3.36). Then after 14.08 m.y at this stage, the production of wet melt is high against the observation of wet melt production. The intensity of the convection currents in the mantle is high. The slab itself was thinner at a depth of 150 km (Figure 3.37). In the final stage, after 14.09 m.y the slab was broken and the convection currents in the mantle reached their highest level (Figure 3.38).

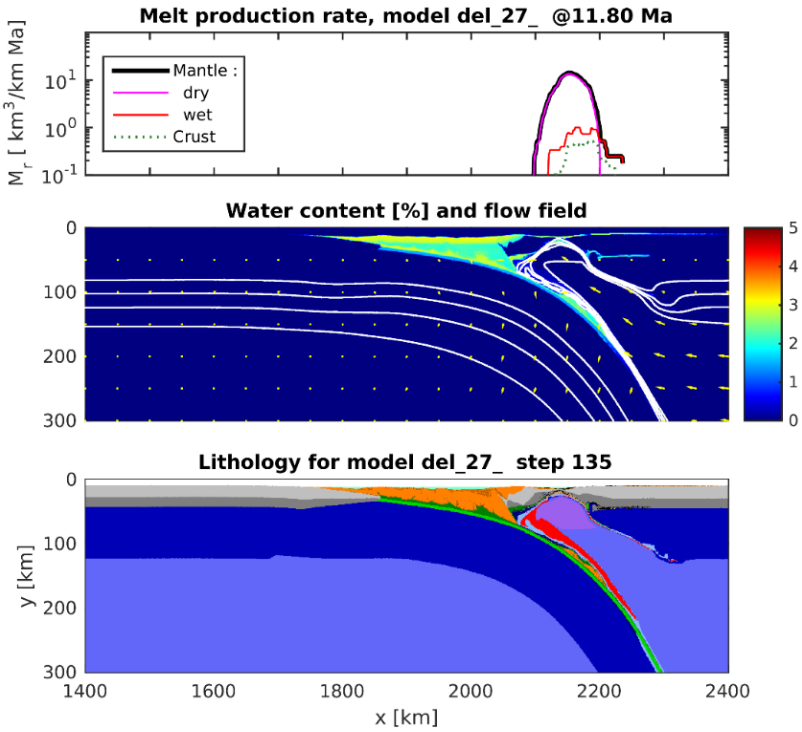

Figure 3.33: The results of the Experiment A5, show *melt production graph* (top), *water content with percentage* (middle), and *lithology graph* (bottom) at 11.80 Myr.

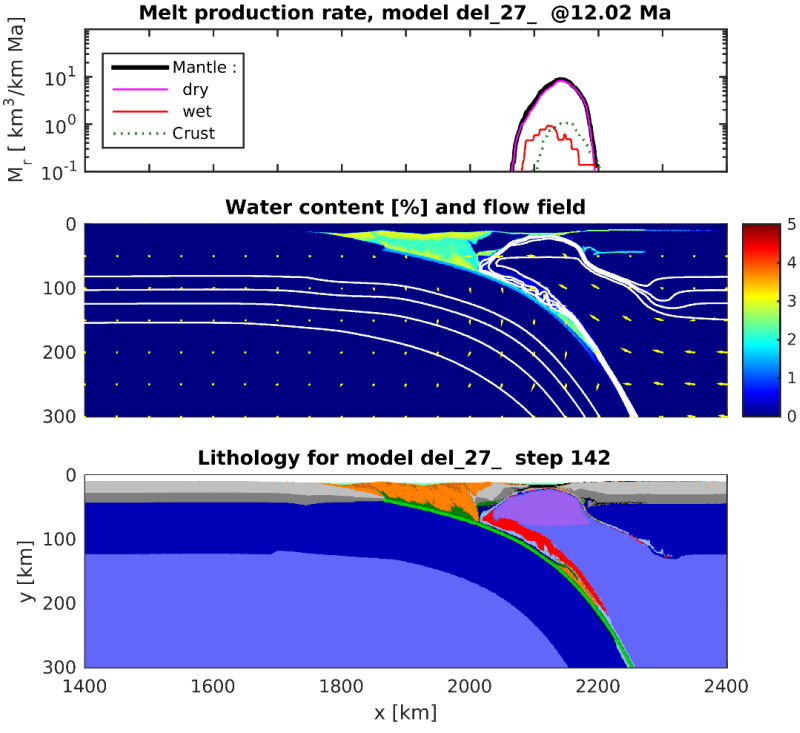

Figure 3.34: The results of the Experiment A5, show *melt production graph* (top), *water content with percentage* (middle), and *lithology graph* (bottom) at 12.02 Myr.

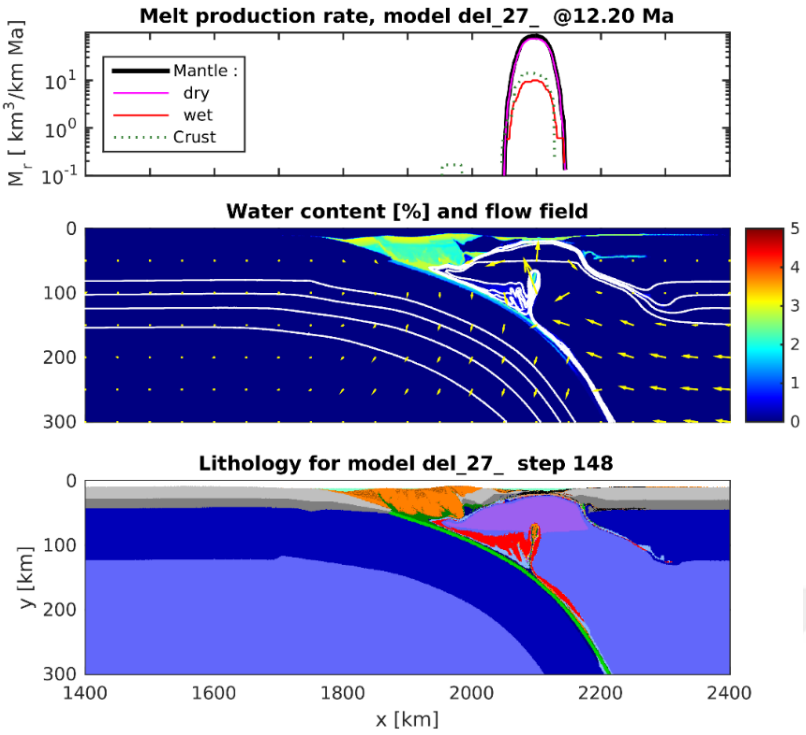

Figure 3.35 The results of the Experiment A5, show *melt production graph* (top), *water content with percentage* (middle), and *lithology graph* (bottom) at 12.20 Myr.

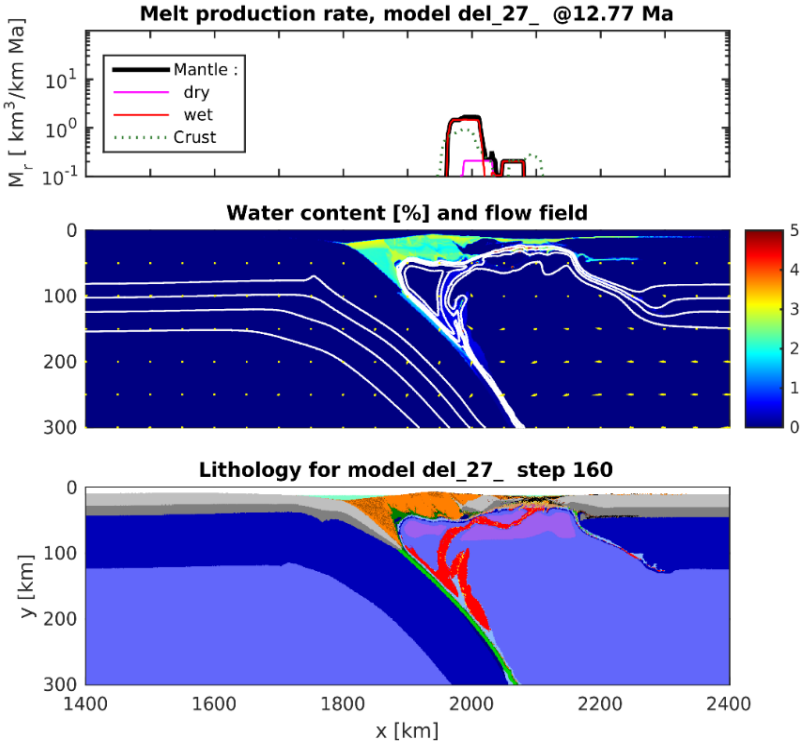

Figure 3.36: The results of the Experiment A5, show *melt production graph* (top), *water content with percentage* (middle), and *lithology graph* (bottom) at 12.77 Myr.

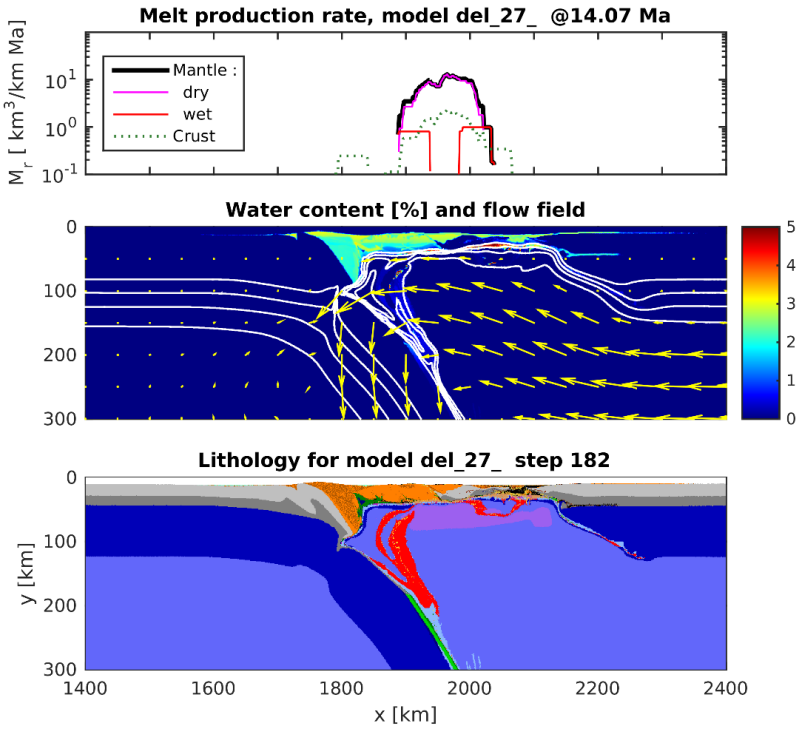

Figure 3.37: The results of the Experiment A5, show *melt production graph* (top), *water content with percentage* (middle), and *lithology graph* (bottom) at 14.07 Myr.

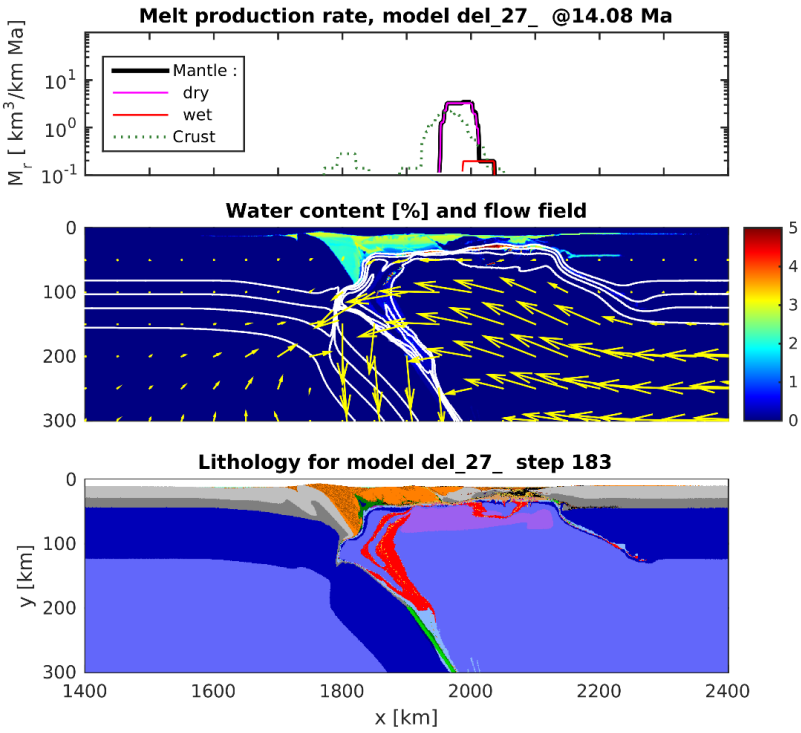

Figure 3.38: The results of the Experiment A5, show *melt production graph* (top), *water content with percentage* (middle), and *lithology graph* (bottom) at 14.08 Myr.

In the melt extraction graphs, the models show a two-peak attitude. This behavior has a direct relationship to the movement of subduction slab. The withdrawal of the slab 11.5 million years after the start of the model rapidly changes the dynamics in the mantle and causes a serious increase in melt production. This increase is supported by changes in mantle convection movements. Wet melt extraction is represented with red color and it takes ~200 km^3 maximum melt extraction value. Dry melt extraction is represented with purple color and it takes ~900 km^3 maximum melt extraction value. Crustal deformation extraction is represented with green color and it takes ~500 km^3 maximum melt extraction value. Total melt extraction is represented with black color and it takes ~1100 km^3 maximum melt extraction value. The graph, in which each is represented on top of each other, shows the direct relationship between each other

In the total melt production graphs of this model, the second jump value is higher than the first jump value (Figure 3.39).

The sudden jumps in the graph showing the cumulative sum based on time represent the sudden dynamic changes made by the subduction slab. These changes correspond to ~ 11.5, ~ 13.5 and ~ 14 million years for the model. In the 11.5 and 14 million years, only the wet melt graph showed a sudden change, while in the 13.5 million years both the wet and wet melt graph showed a sudden increase (Figure 3.40).

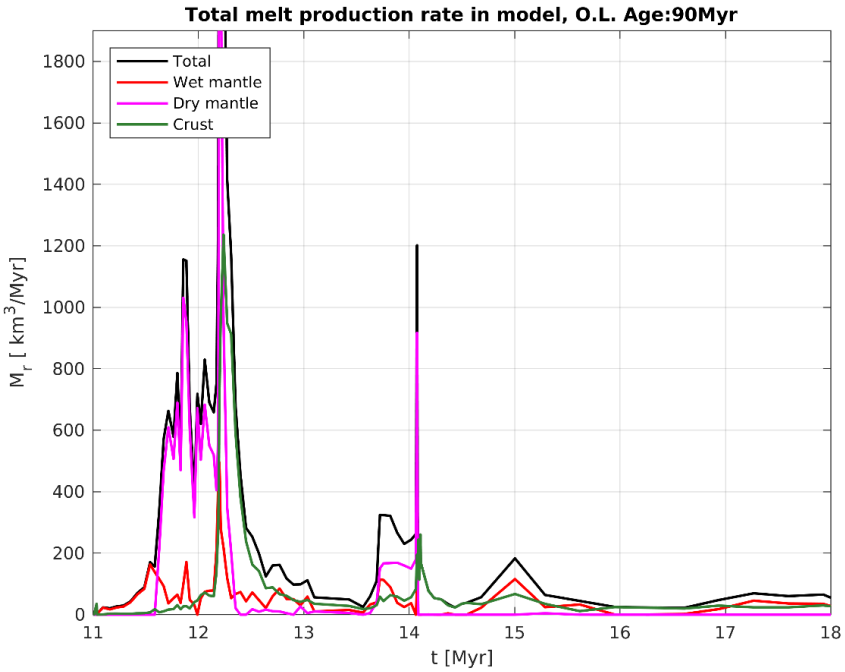

Figure 3.39: Result of the Experiment A5 with discrete volumetric melt extraction rate depending on time.

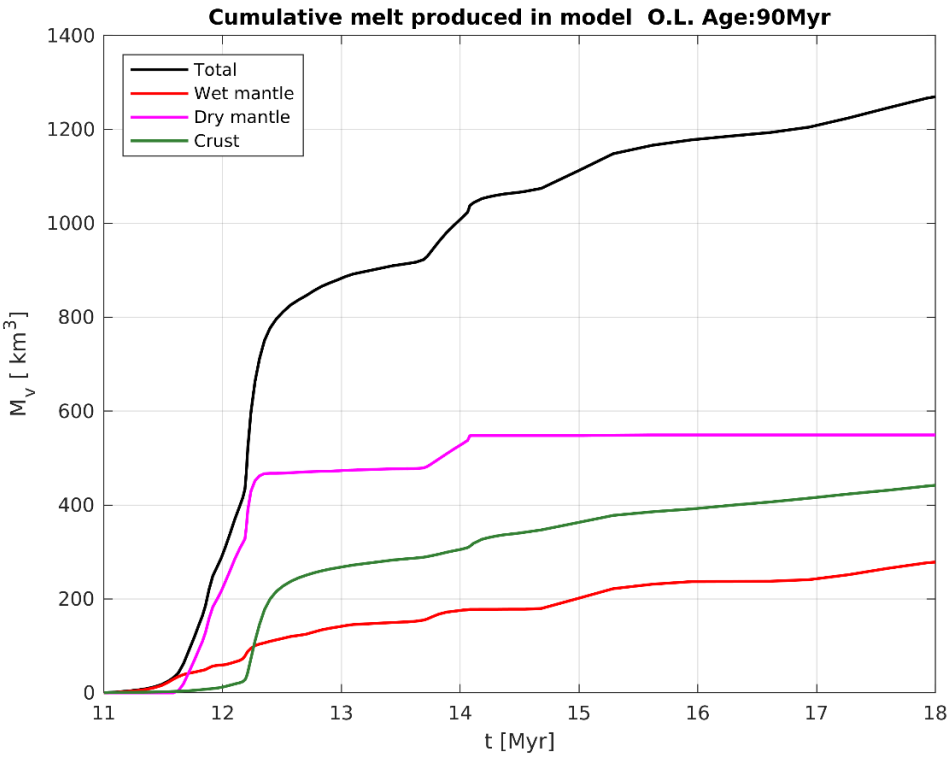

Figure 3.40: Result of the Experiment A5 with cumulative sum of discrete volumetric melt extraction rate depending on time.

3.1.11. Experimental set A6

In experimental set A5 , it is imposed that a convergence rate of 4 cm/yr from both side(right and left) of model Oceanic lithosphere age is determined as 100 Ma.Oceanic lithosphere thickness incresed due to modelling process. In models 35 km in thick continental crust , 8 km ocenaic cruscrust and 80 km in thick mantle lithosphere as determined. The rheologies determined as wet quartzite in contienetal crust (Ranalli, 1995), gabbro/basalt in oceanic crust (Ranalli, 1995) ,wetolivine in mantle lithosphere (Ranalli, 1995) and wetolivine in asthenosphere. Reference densities of continental crust, oceanic crust and mantle lithosphere and asthenosphere is 2700 kg/m3, 3000 kg/m3, 3300 kg/m3 and 3300 kg/m3, respectively.

3.1.12. Results of A6

After 11.89 m.y. At this stage, the wet melt production type is more than the wet melt production and it is spread. The wet melt type is concentrated in two regions. The convection currents in the mantle are upward (Figure 3.41). After 13.61 m.y. at this stage, melt production decreased.Wet melt production is concentrated in three regions

and is higher than wet melt production (Figure 3.42). After 13.67 m.y Melt production increased and wet melt production concentrated regionally. Convection currents in the mantle are stagnant (Figure 3.43). After 13.85 m.y at this stage, melt production has fallen. Wet melt production has spread and wet plum production is small and regional (Figure 3.44). After 13.93 m.y wet melt production is more and spread than wet melt production. Convection currents in mantle have counterclockwise movement against subduction mechanism and its intensity is high (Figure 3.45). After 13.97 m.y the intensity of the convection currents increased and the slab was broken.Wet melt production was concentrated in two regions and no wet melt production was observed (Figure 3.46).

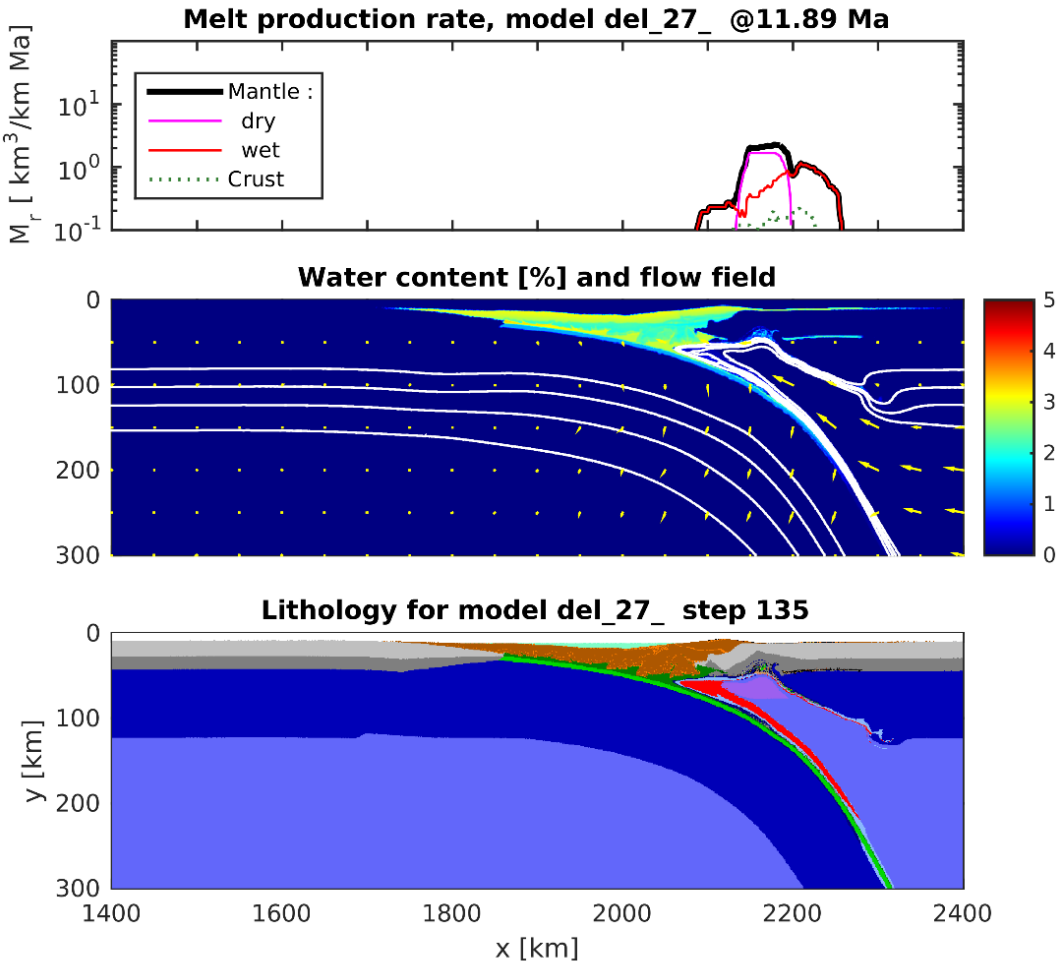

Figure 3.41: The results of the Experiment A6, show *melt production graph* (top), *water content with percentage* (middle), and *lithology graph* (bottom) at 11.89 Myr.

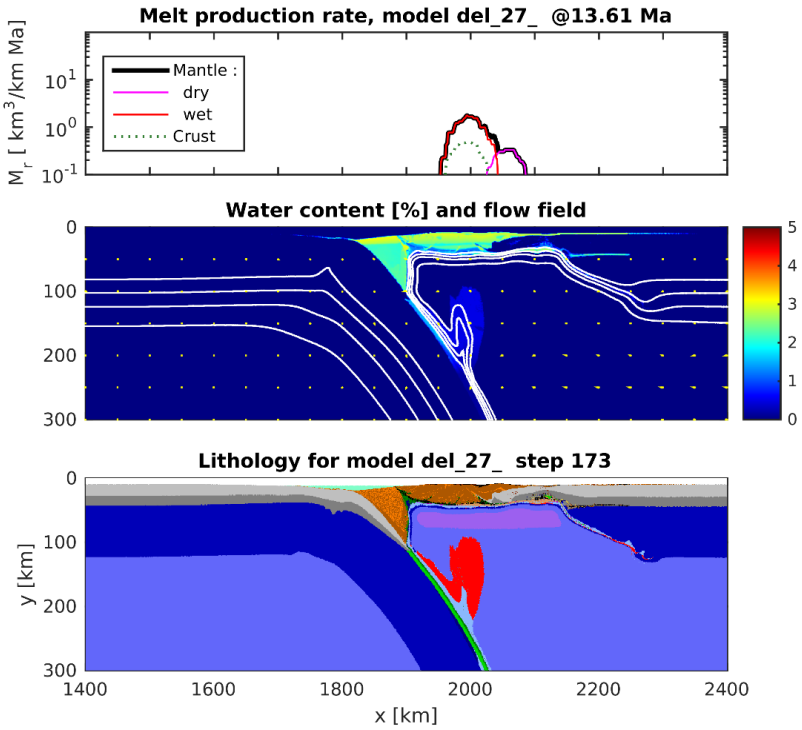

Figure 3.42: The results of the Experiment A6, show *melt production graph* (top), *water content with percentage* (middle), and *lithology graph* (bottom) at 13.61 Myr.

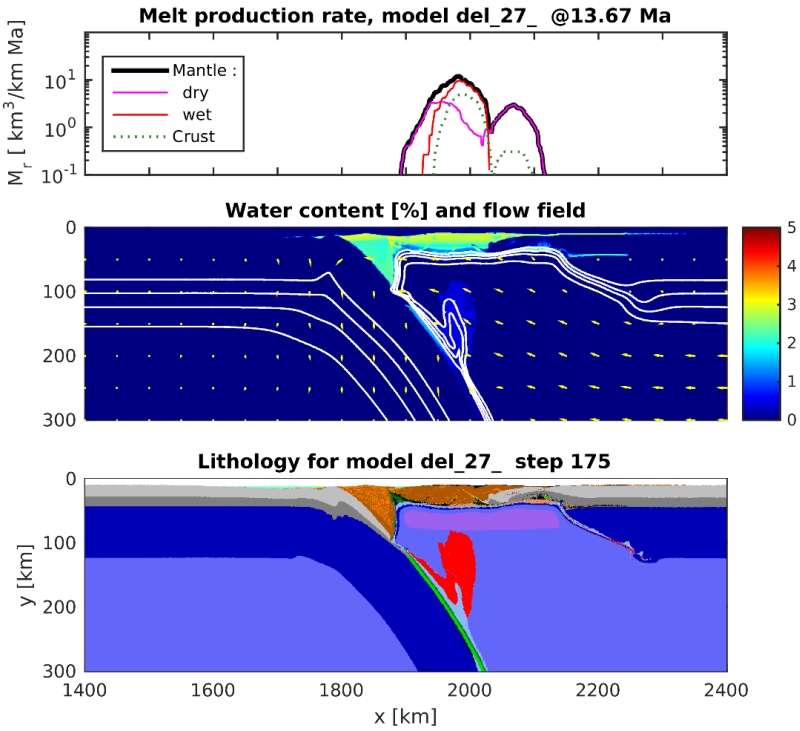

Figure 3.43: The results of the Experiment A6, show *melt production graph* (top), *water content with percentage* (middle), and *lithology graph* (bottom) at 13.67 Myr.

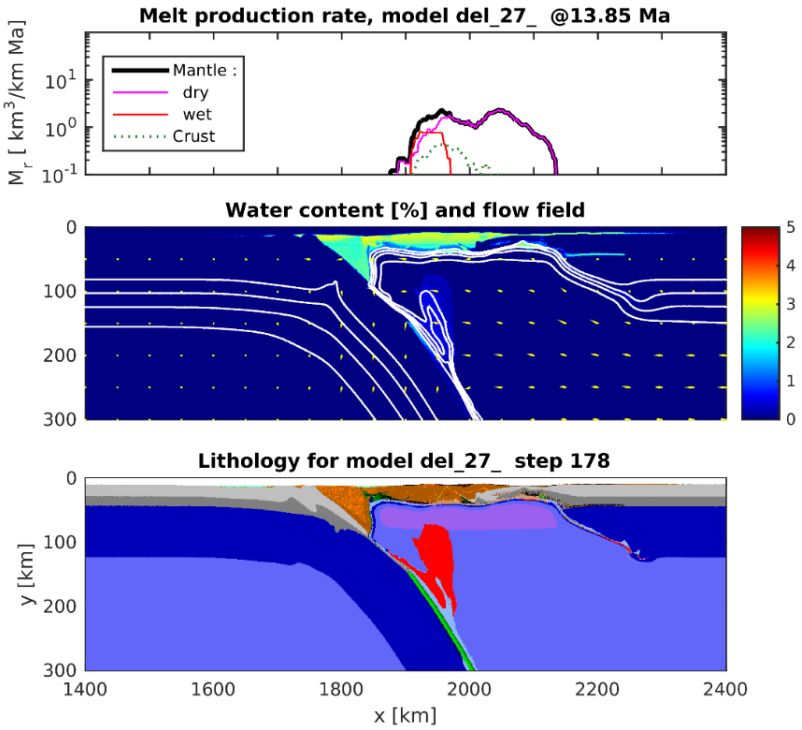

Figure 3.44: The results of the Experiment A6, show *melt production graph* (top), *water content with percentage* (middle), and *lithology graph* (bottom) at 13.85 Myr.

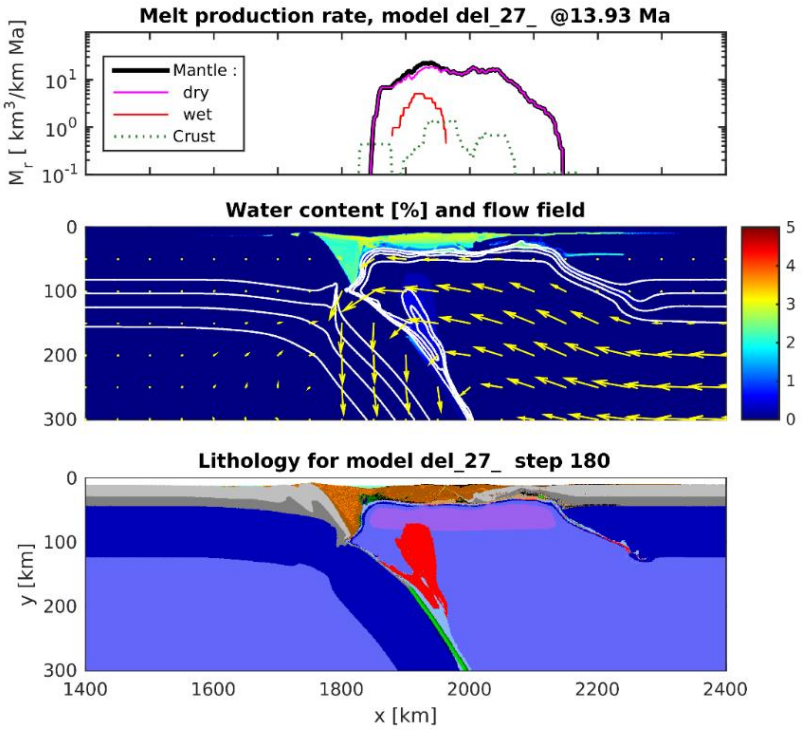

Figure 3.45: The results of the Experiment A6, show *melt production graph* (top), *water content with percentage* (middle), and *lithology graph* (bottom) at 13.93 Myr.

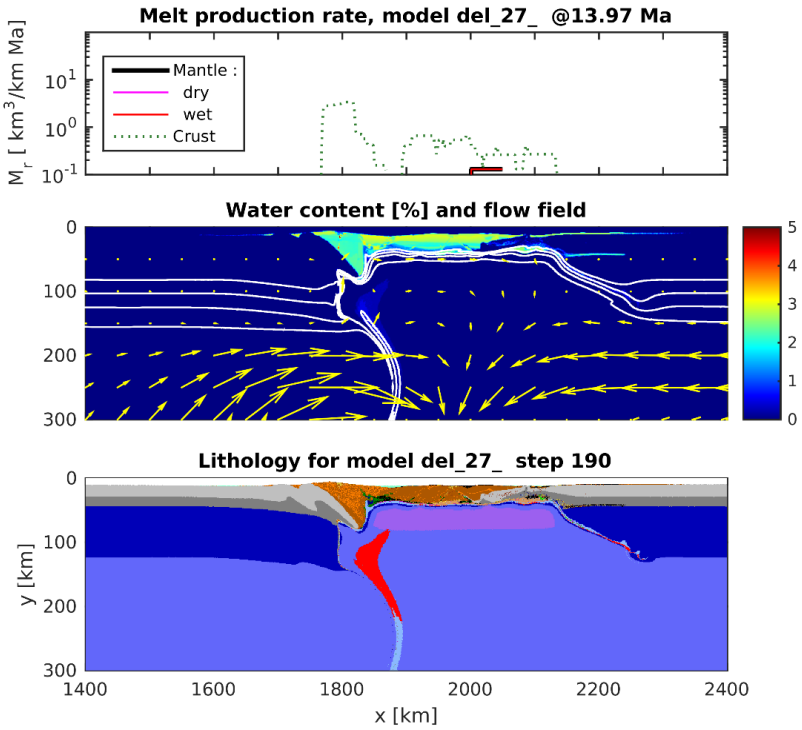

Figure 3.46: The results of the Experiment A6, show *melt production graph* (top), *water content with percentage* (middle), and *lithology graph* (bottom) at 13.97 Myr.

In the melt extraction graphs, the models show a two-peak attitude. This behavior has a direct relationship to the movement of subduction slab. The withdrawal of the slab 11.5 million years after the start of the model rapidly changes the dynamics in the mantle and causes a serious increase in melt production. This increase is supported by changes in mantle convection movements. Wet melt extraction is represented with red color and it takes ~200 km^3 maximum melt extraction value. Dry melt extraction is represented with purple color and it takes ~900 km^3 maximum melt extraction value. Crustal deformation extraction is represented with green color and it takes ~500 km^3 maximum melt extraction value. Total melt extraction is represented with black color and it takes ~1100 km^3 maximum melt extraction value. The graph, in which each is represented on top of each other, shows the direct relationship between each other

In the total melt production graphs of this model, the second jump value is higher than the first jump value (Figure 3.47).

The sudden jumps in the graph showing the cumulative sum based on time represent the sudden dynamic changes made by the subduction slab. These changes correspond to ~ 11.5, ~ 13.5 and ~ 14 million years for the model. In the 11.5 and 14 million years,

only the wet melt graph showed a sudden change, while in the 13.5 million years both the wet and wet melt graph showed a sudden increase (Figure 3.48).

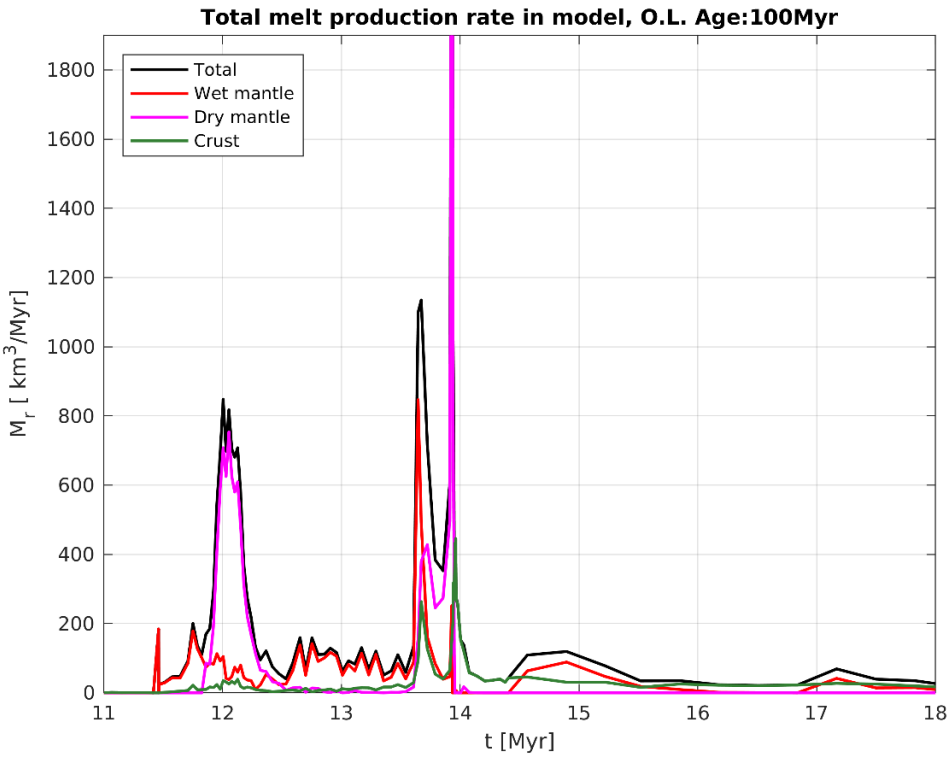

Figure 3.47: Result of the Experiment A6 with discrete volumetric melt extraction rate depending on time.

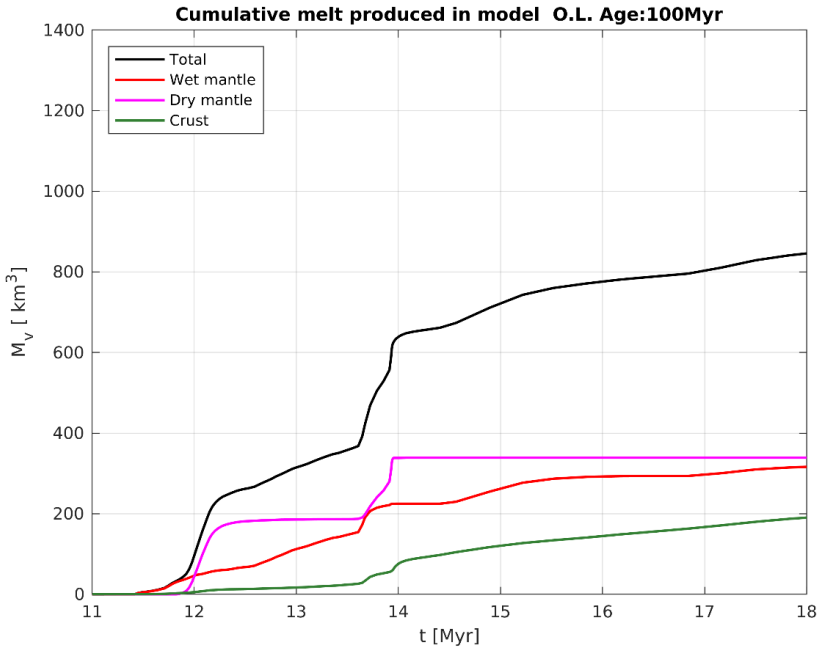

Figure 3.48: Result of the Experiment A6 with cumulative sum of discrete volumetric melt extraction rate depending on time.

3.1.13. Experimental set A7

In experimental set A5 , it is imposed that a convergence rate of 4 cm/yr from both side(right and left) of model Oceanic lithosphere age is determined as 110 Ma.Oceanic lithosphere thickness incresed due to modelling process. In models 35 km in thick continental crust , 8 km ocenaic cruscrust and 80 km in thick mantle lithosphere as determined. The rheologies determined as wet quartzite in contienetal crust (Ranalli, 1995), gabbro/basalt in oceanic crust (Ranalli, 1995) ,wetolivine in mantle lithosphere (Ranalli, 1995) and wetolivine in asthenosphere. Reference densities of continental crust, oceanic crust and mantle lithosphere and asthenosphere is 2700 kg/m3, 3000 kg/m3, 3300 kg/m3 and 3300 kg/m3, respectively.

3.1.14. Results of A7

After 11.56 m.y., at this stage, wet melt production was higher than wet melt production and both concentrated back arc. Convection currents in the mantle are upward and high in intensity (Figure 3.49). After 11.84 m.y wet melt production is more dominant than wet melt production (Figure 3.50). After then 13.21 m.y wet melt production is regional and high, but wet melt production is spread over a larger area. The intensity of the convection currents in the mantle is low (Figure 3.51). After 13.84 m.y wet melt production migrated to tranch. Wet and wet melt types are co-produced in a small area under the accrationary prism (Figure 3.52). After 13.93 m.y wet melt production is more and spread than wet melt production. Convection currents in mantle have counterclockwise movement against subduction mechanism and its intensity is high (Figure 3.53). In the final stage, after 14.20 m.y the slab was broken and the convection currents in the mantle reached their highest level (Figure 3.54).

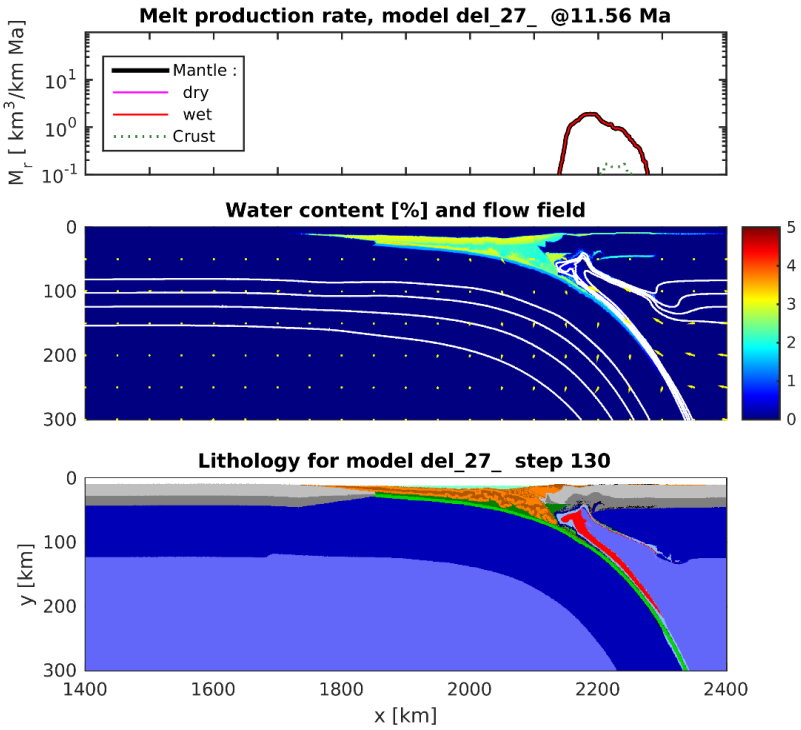

Figure 3.49: The results of the Experiment A7, show *melt production graph* (top), *water content with percentage* (middle), and *lithology graph* (bottom) at 11.56 Myr.

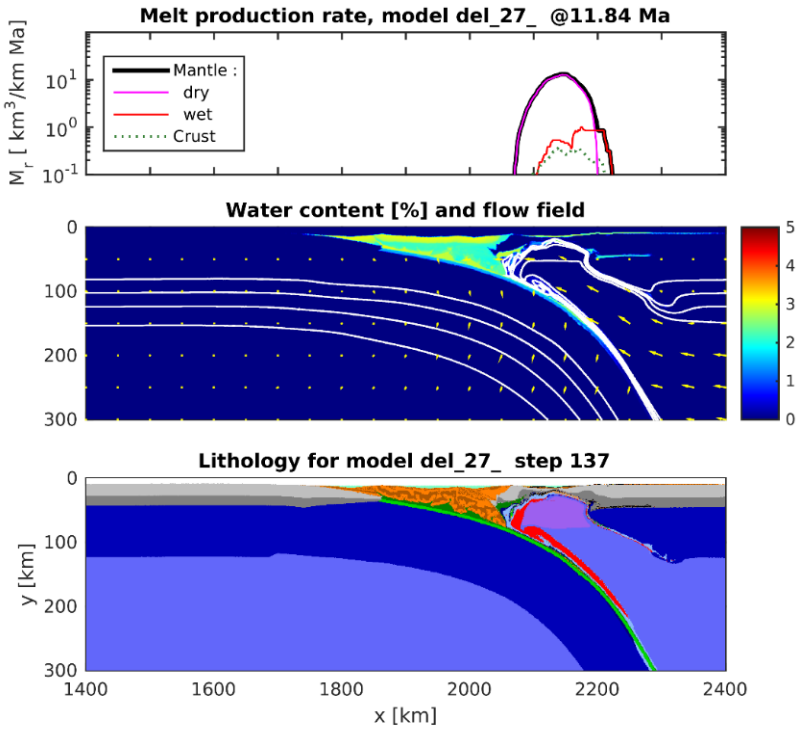

Figure 3.50: The results of the Experiment A7, show *melt production graph* (top), *water content with percentage* (middle), and *lithology graph* (bottom) at 11.84 Myr.

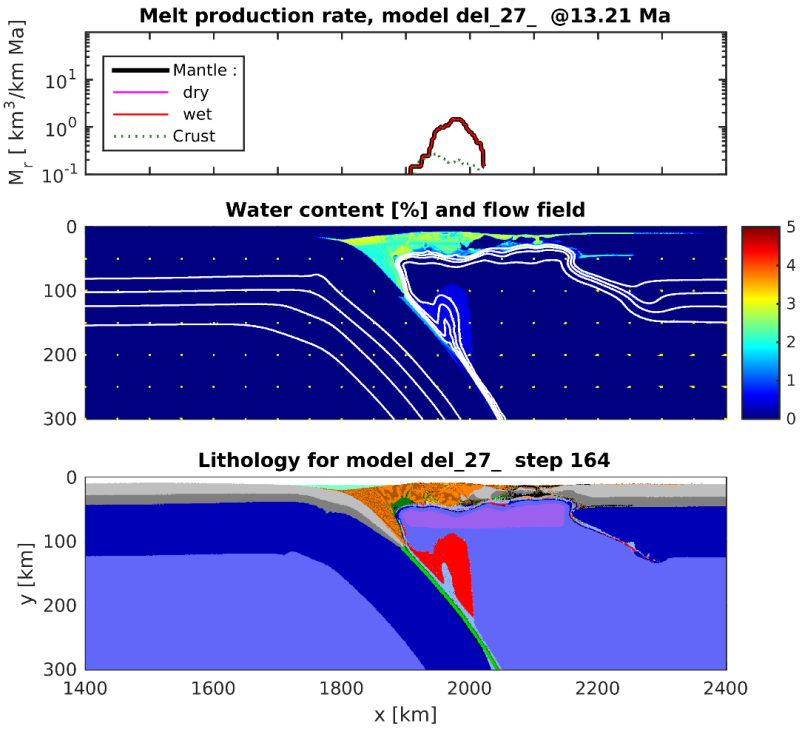

Figure 3.51: The results of the Experiment A7, show *melt production graph* (top), *water content with percentage* (middle), and *lithology graph* (bottom) at 13.21 Myr.

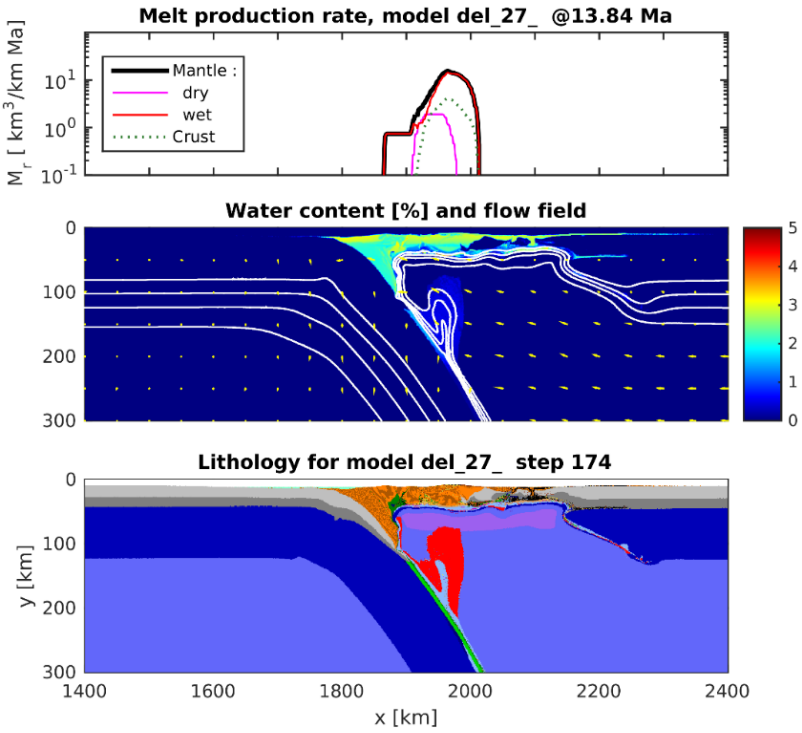

Figure 3.52: The results of the Experiment A7, show *melt production graph* (top), *water content with percentage* (middle), and *lithology graph* (bottom) at 13.84 Myr.

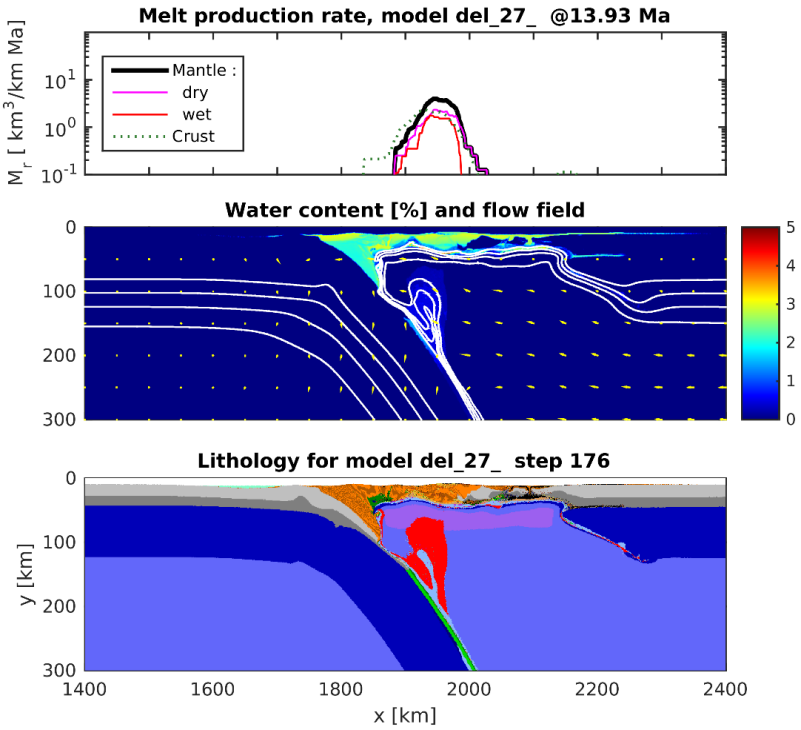

Figure 3.53: The results of the Experiment A7, show *melt production graph* (top), *water content with percentage* (middle), and *lithology graph* (bottom) at 13.93 Myr.

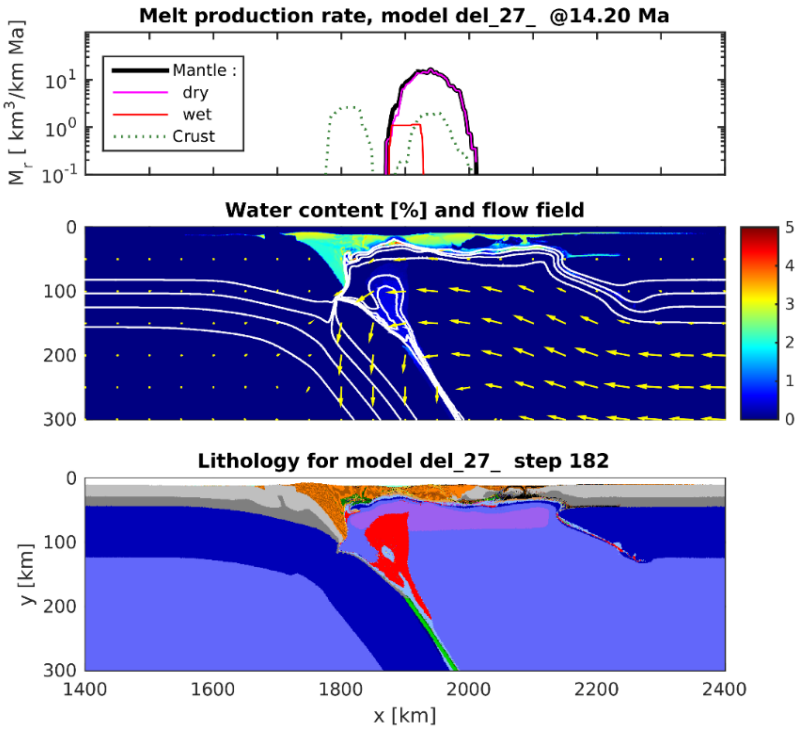

Figure 3.54: The results of the Experiment A7, show *melt production graph* (top), *water content with percentage* (middle), and *lithology graph* (bottom) at 14.20 Myr.

In the melt extraction graphs, the models show a two-peak attitude. This behavior has a direct relationship to the movement of subduction slab. The withdrawal of the slab 11.5 million years after the start of the model rapidly changes the dynamics in the mantle and causes a serious increase in melt production. This increase is supported by changes in mantle convection movements. Wet melt extraction is represented with red color and it takes ~200 km^3 maximum melt extraction value. Dry melt extraction is represented with purple color and it takes ~900 km^3 maximum melt extraction value. Crustal deformation extraction is represented with green color and it takes ~500 km^3 maximum melt extraction value. Total melt extraction is represented with black color and it takes ~1100 km^3 maximum melt extraction value. The graph, in which each is represented on top of each other, shows the direct relationship between each other

In the total melt production graphs of this model, the second jump value is higher than the first jump value (Figure 3.55).

The sudden jumps in the graph showing the cumulative sum based on time represent the sudden dynamic changes made by the subduction slab. These changes correspond to ~ 11.5, ~ 13.5 and ~ 14 million years for the model. In the 11.5 and 14 million years, only the wet melt graph showed a sudden change, while in the 13.5 million years both the wet and wet melt graph showed a sudden increase (Figure 3.56).

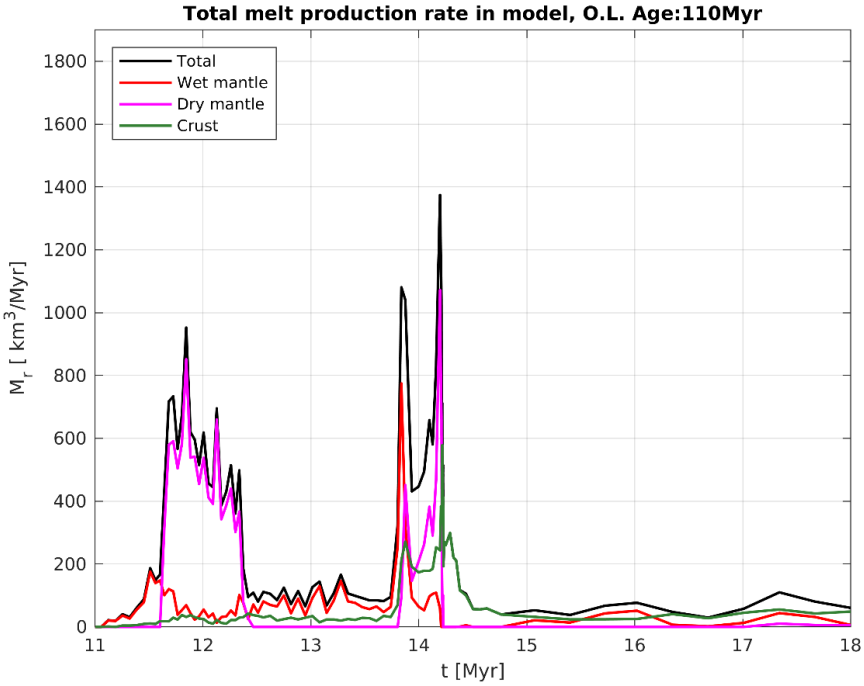

Figure 3.55: Result of experiment A7 with discrete volumetric melt extraction rate depending on time.

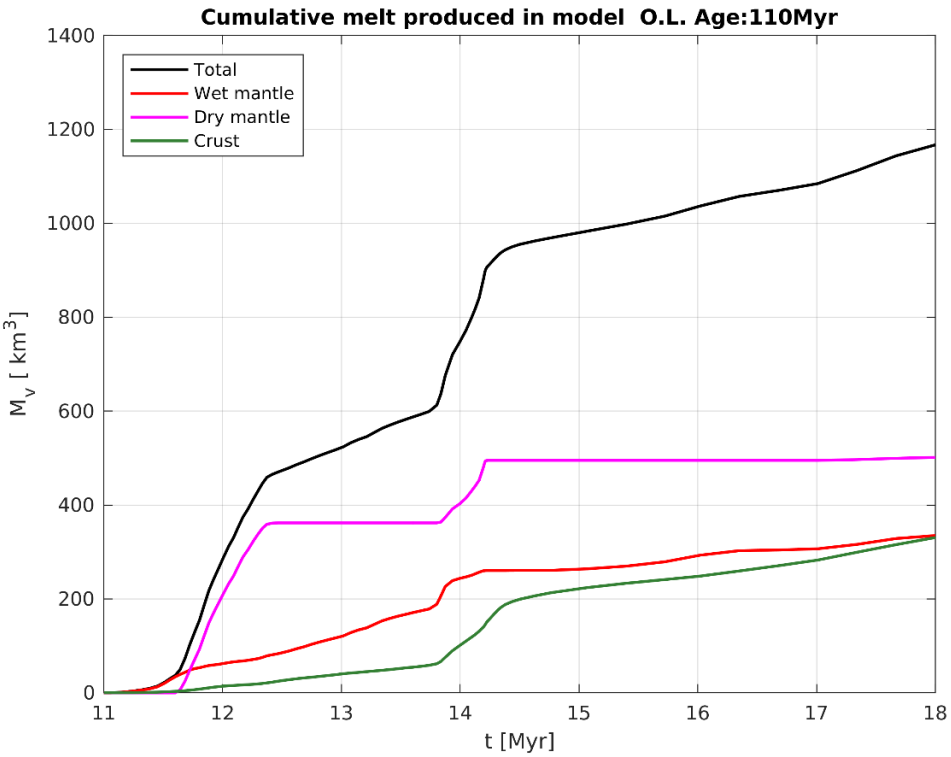

Figure 3.56: Result of the Experiment A7 with cumulative sum of discrete volumetric melt extraction rate depending on time.

3.1.15. Experimental set A8

In experimental set A5 , it is imposed that a convergence rate of 4 cm/yr from both side(right and left) of model Oceanic lithosphere age is determined as 120 Ma.Oceanic lithosphere thickness incresed due to modelling process. In models 35 km in thick continental crust , 8 km ocenaic cruscrust and 80 km in thick mantle lithosphere as determined. The rheologies determined as wet quartzite in contienetal crust (Ranalli, 1995), gabbro/basalt in oceanic crust (Ranalli, 1995) ,wetolivine in mantle lithosphere (Ranalli, 1995) and wetolivine in asthenosphere. Reference densities of continental crust, oceanic crust and mantle lithosphere and asthenosphere is 2700 kg/m3, 3000 kg/m3, 3300 kg/m3 and 3300 kg/m3, respectively.

3.1.16. Results of A8

After 11.72 m.y. At this stage, the wet melt production type is more than the wet melt production and it is spread. The wet melt type is concentrated in two regions. The convection currents in the mantle are upward (Figure 3.57). After 11.81 m.y. at this stage, melt production decreased.Wet melt production is concentrated in three regions

and is higher than wet melt production (Figure 3.58). After 12.40 m.y Melt production increased and wet melt production concentrated regionally. Convection currents in the mantle are stagnant (Figure 3.59). After 13.86 m.y at this stage, melt production has fallen. Wet melt production has spread and wet plum production is small and regional (Figure 3.60). After 14.08 m.y wet melt production is more and spread than wet melt production. Convection currents in mantle have counterclockwise movement against subduction mechanism and its intensity is high (Figure 3.61). In the latest stage of the model , after 14.10 m.y no melt production was observed at this stage. Only crustal deformation was observed (Figure 3.62).

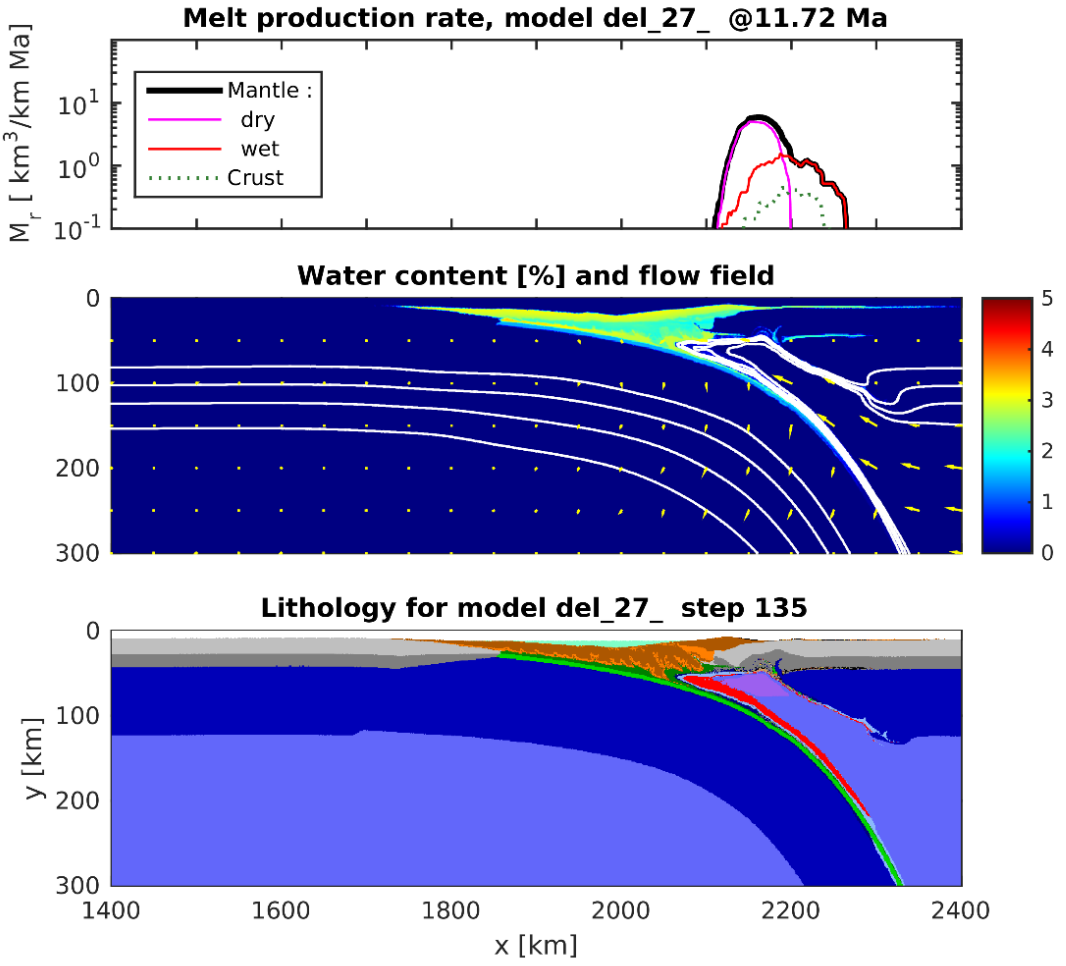

Figure 3.57: The results of the Experiment A8, show *melt production graph* (top), *water content with percentage* (middle), and *lithology graph* (bottom) at 11.72 Myr.

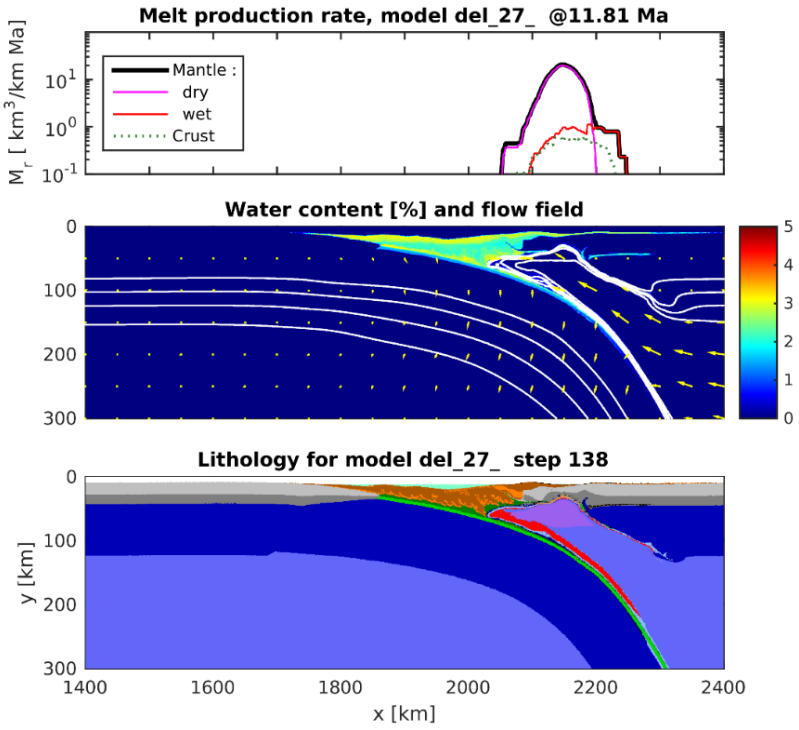

Figure 3.58: The results of the Experiment A8, show *melt production graph* (top), *water content with percentage* (middle), and *lithology graph* (bottom) at 11.81 Myr.

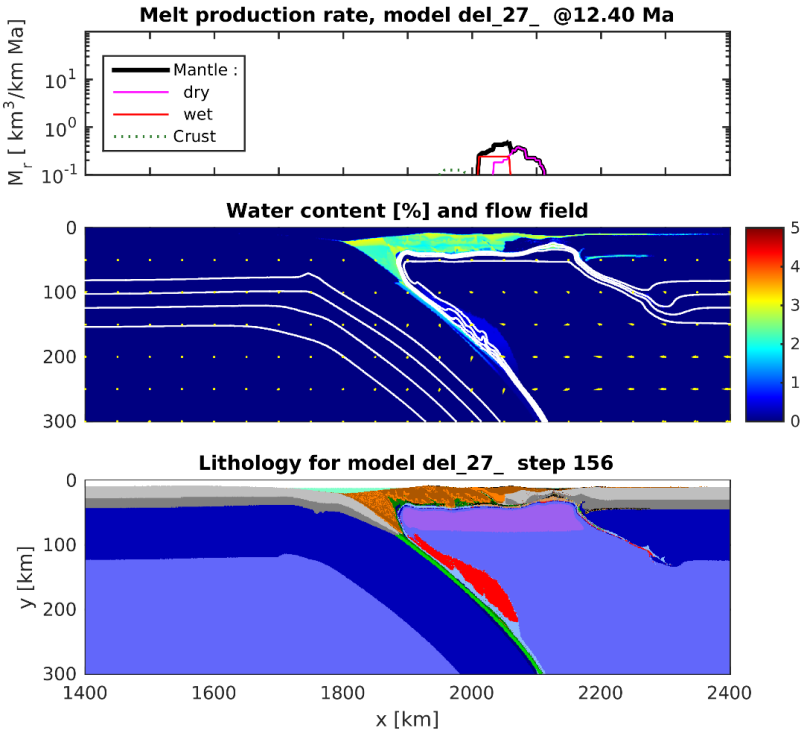

Figure 3.59 The results of the Experiment A8, show *melt production graph* (top), *water content with percentage* (middle), and *lithology graph* (bottom) at 12.40 Myr.

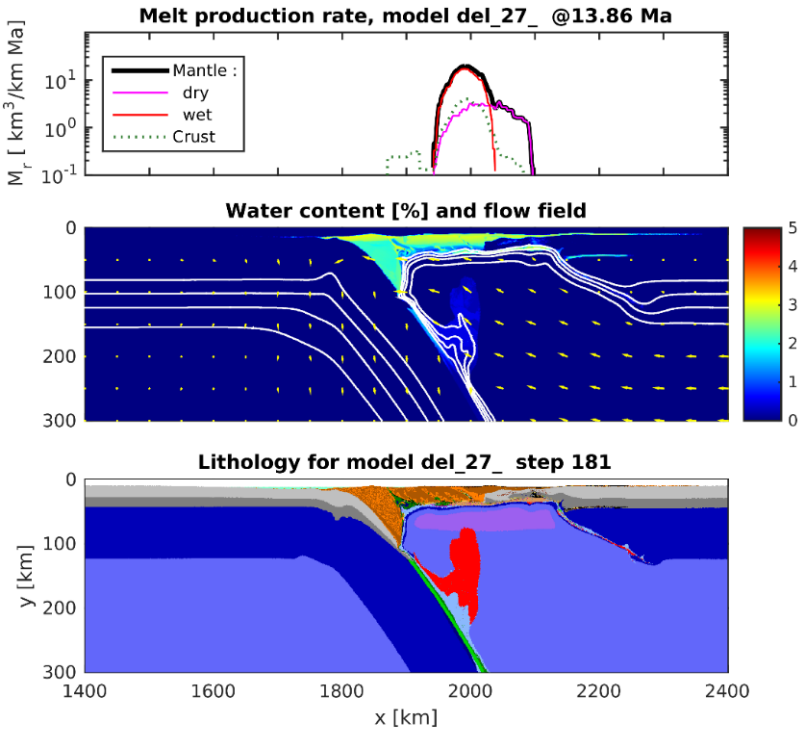

Figure 3.60 The results of the Experiment A8, show *melt production graph* (top), *water content with percentage* (middle), and *lithology graph* (bottom) at 13.86 Myr.

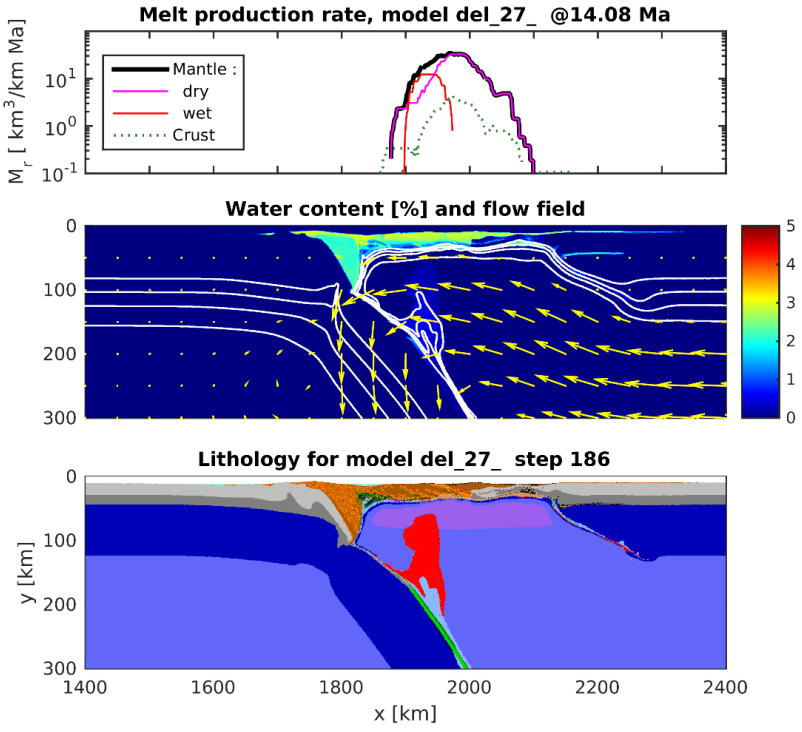

Figure 3.61: The results of the Experiment A4, show *melt production graph* (top), *water content with percentage* (middle), and *lithology graph* (bottom) at 14.08 Myr.

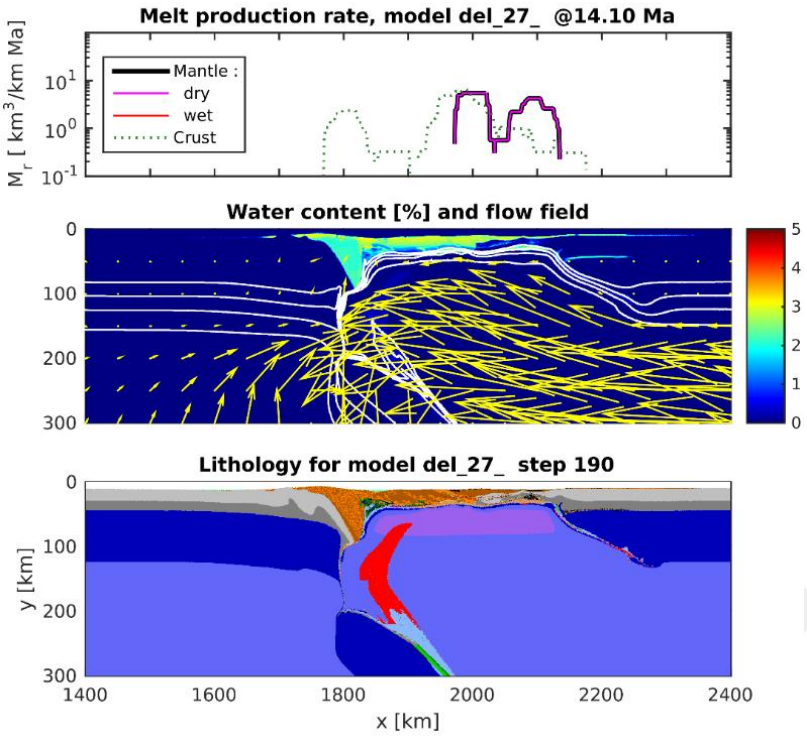

Figure 3.62: The results of the Experiment A8, show *melt production graph* (top), *water content with percentage* (middle), and *lithology graph* (bottom) at 14.10 Myr.

In the melt extraction graphs, the models show a two-peak attitude. This behavior has a direct relationship to the movement of subduction slab. The withdrawal of the slab 11.5 million years after the start of the model rapidly changes the dynamics in the mantle and causes a serious increase in melt production. This increase is supported by changes in mantle convection movements. Wet melt extraction is represented with red color and it takes ~200 km^3 maximum melt extraction value. Dry melt extraction is represented with purple color and it takes ~900 km^3 maximum melt extraction value. Crustal deformation extraction is represented with green color and it takes ~500 km^3 maximum melt extraction value. Total melt extraction is represented with black color and it takes ~1100 km^3 maximum melt extraction value. The graph, in which each is represented on top of each other, shows the direct relationship between each other

In the total melt production graphs of this model, the second jump value is higher than the first jump value (Figure 3.63).

The sudden jumps in the graph showing the cumulative sum based on time represent the sudden dynamic changes made by the subduction slab. These changes correspond to ~ 11.5, ~ 13.5 and ~ 14 million years for the model. In the 11.5 and 14 million years,

only the wet melt graph showed a sudden change, while in the 13.5 million years both the wet and wet melt graph showed a sudden increase (Figure 3.64).

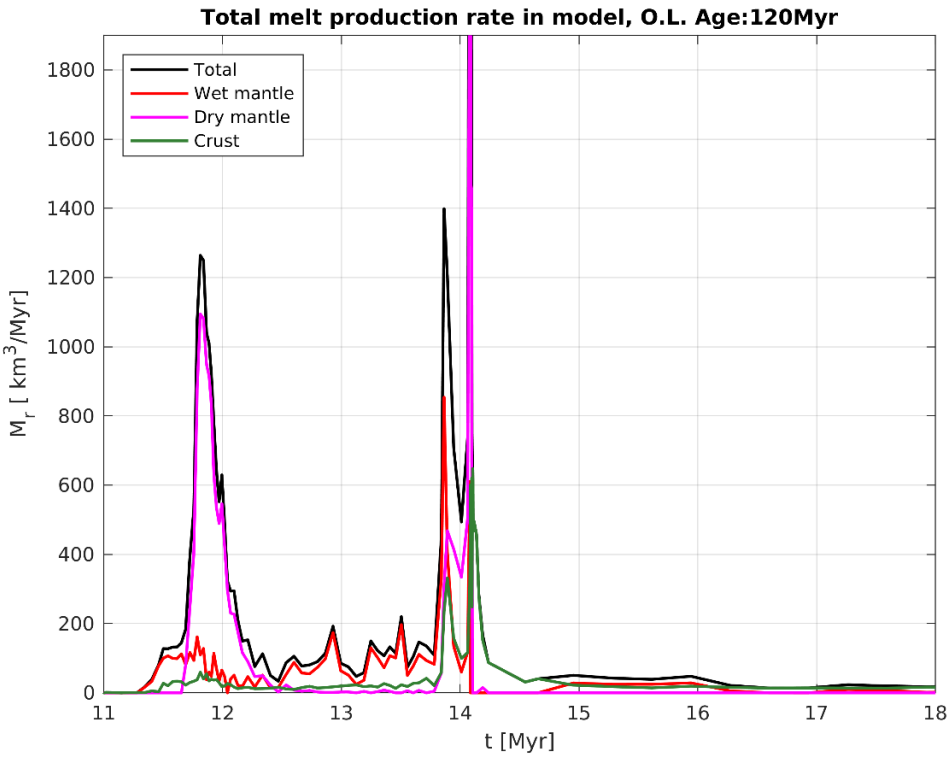

Figure 3.63: Result of experiment A8 with discrete volumetric melt extraction rate depending on time.

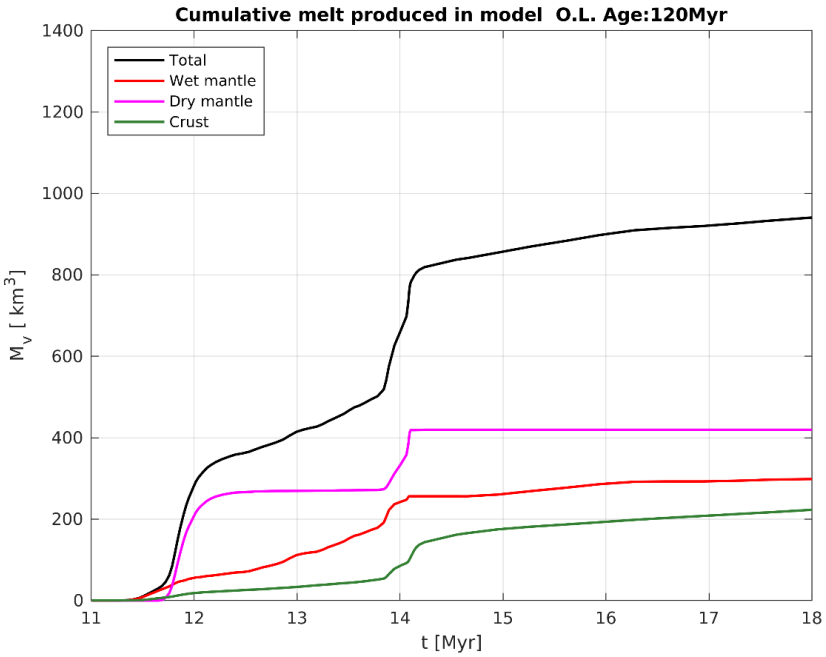

Figure 3.64: Result of the Experiment A8 with cumulative sum of discrete volumetric melt extraction rate depending on time.

3.2. Results of Experiment B

In Experiment B, convergence rate is determined as 8 cm/yr (slow convergence rate).Oceanic lithosphere age is changing periodic increment (see Table 2.1).

3.2.1. Experimental set B1

In experimental set B1 , it is imposed that a convergence rate of 8 cm/yr from both side(right and left) of model Oceanic lithosphere age is determined as 50 Ma.Oceanic lithosphere thickness incresed due to modelling process. In models 35 km in thick continental crust , 8 km ocenaic cruscrust and 80 km in thick mantle lithosphere as determined. The rheologies determined as wet quartzite in contienetal crust (Ranalli, 1995), gabbro/basalt in oceanic crust (Ranalli, 1995) ,wetolivine in mantle lithosphere (Ranalli, 1995) and wetolivine in asthenosphere. Reference densities of continental crust, oceanic crust and mantle lithosphere and asthenosphere is 2700 kg/m3, 3000 kg/m3, 3300 kg/m3 and 3300 kg/m3, respectively.

3.2.2. Results of B1

After 6.49 m.y wet melt production was not observed at this stage, but a small amount of wet melt production was observed (Figure 3.65). After 6.79 m.y wet melt production increased. Convection currents in mantle increased (Figure 3.66). After 6.99 m.y at this stage, the asthenosphere entered under the crust and wet melt production increased and spread along the accreationary prism (Figure 3.67). After 7.18 m. dry and wet melt production is observed. Dry melt is close to the trance and wet plum production is concentrated at back arc basin (Figure 3.68). After 7.49 m.y a small amount of wet melt production was observed, while the dry melt was not observed (Figure 3.69).

In the final stage of the model is after 7.90 m.y . a small amount of wet melt was observed on the accreationary prism (Figure 3.70) .

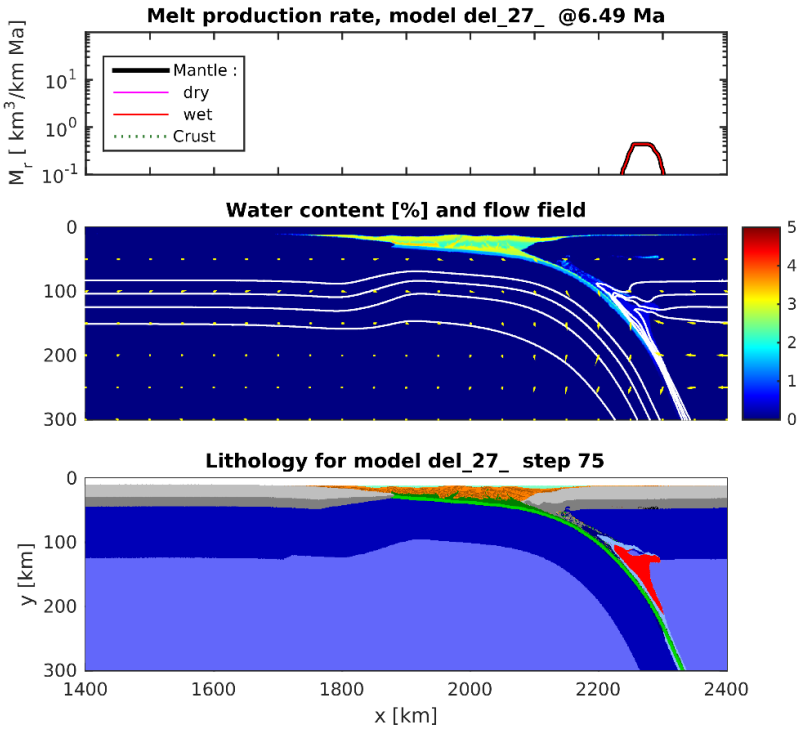

Figure 3.65: The results of the Experiment B1, show *melt production graph* (top), *water content with percentage* (middle), and *lithology graph* (bottom) at 6.49 Myr.

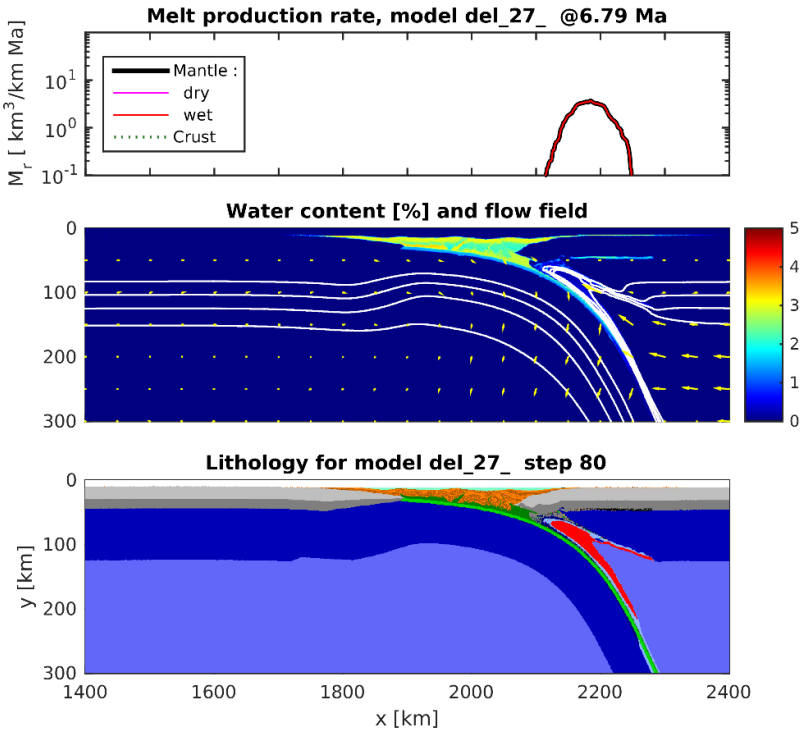

Figure 3.66: The results of the Experiment A4, show *melt production graph* (top), *water content with percentage* (middle), and *lithology graph* (bottom) at 6.79 Myr.

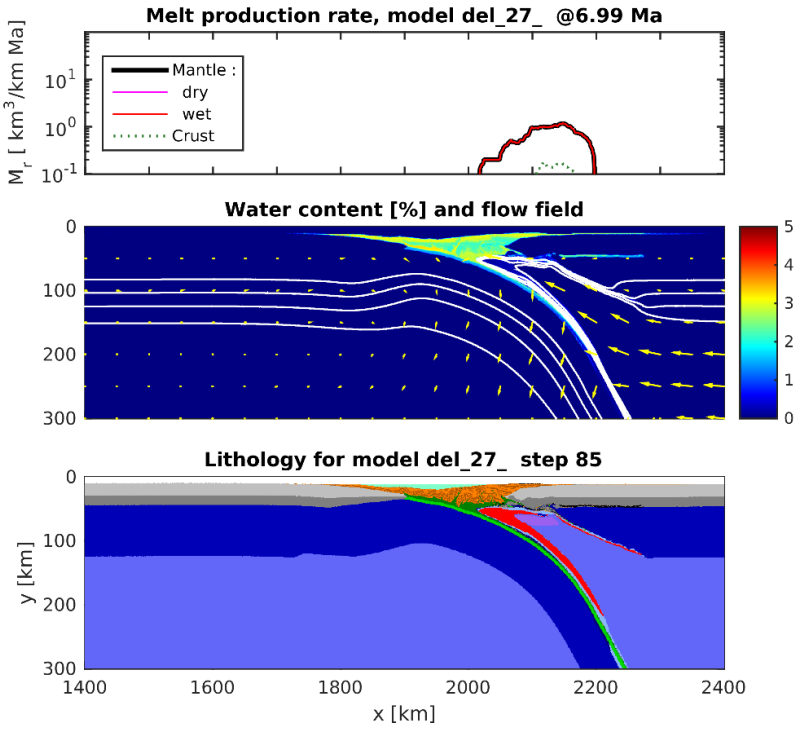

Figure 3.67: The results of the Experiment B1, show *melt production graph* (top), *water content with percentage* (middle), and *lithology graph* (bottom) at 6.99 Myr.

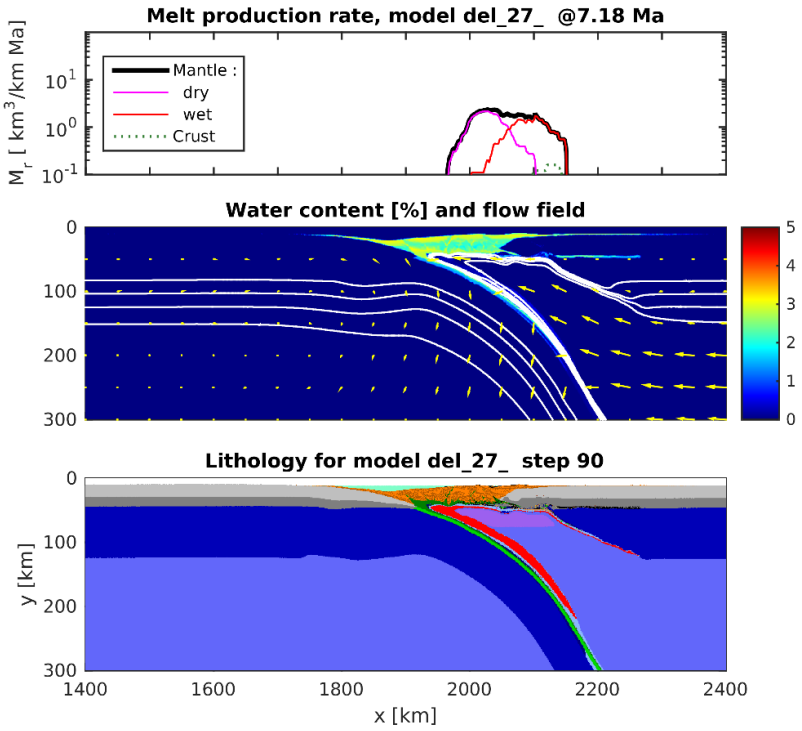

Figure 3.68: The results of the Experiment B1, show *melt production graph* (top), *water content with percentage* (middle), and *lithology graph* (bottom) at 7.18 Myr.

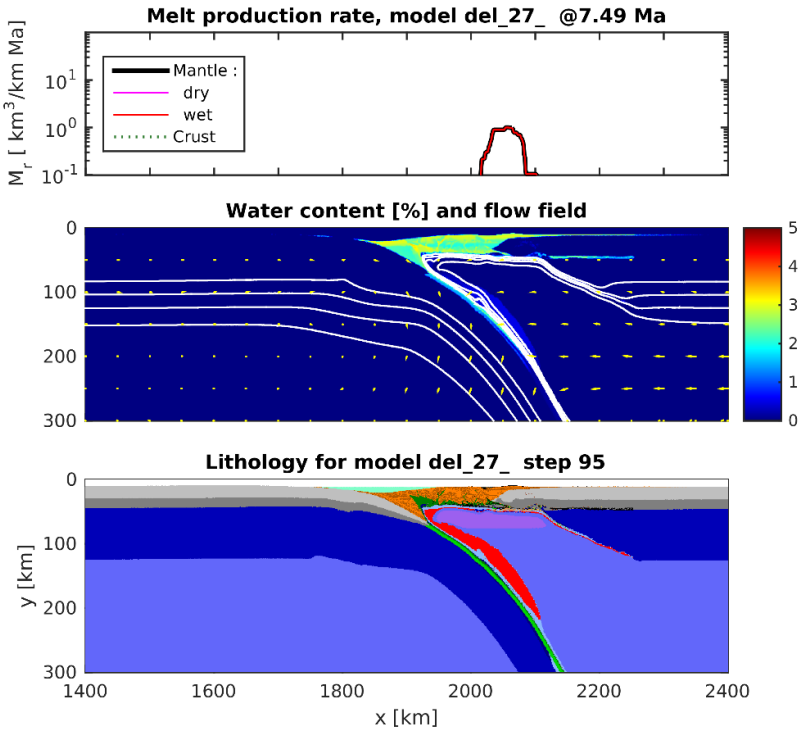

Figure 3.69: The results of the Experiment B1, show *melt production graph* (top), *water content with percentage* (middle), and *lithology graph* (bottom) at 7.49 Myr.

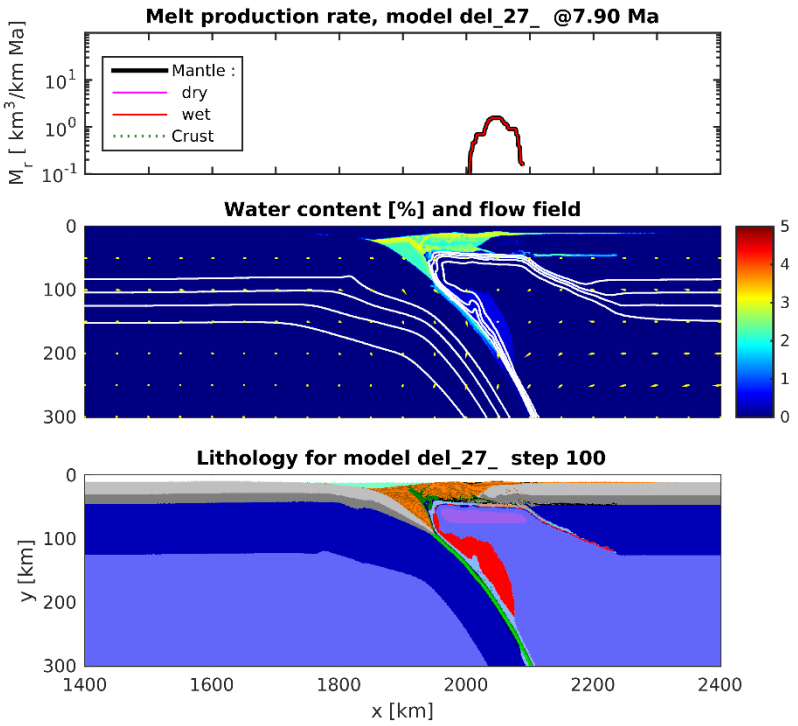

Figure 3.70: The results of the Experiment B1, show *melt production graph* (top), *water content with percentage* (middle), and *lithology graph* (bottom) at 7.90 Myr.

In the melt extraction graphs, the models show a two-peak attitude. This behavior has a direct relationship to the movement of subduction slab. The withdrawal of the slab 6.5 million years after the start of the model rapidly changes the dynamics in the mantle and causes a serious increase in melt production. This increase is supported by changes in mantle convection movements. Wet melt extraction is represented with red color and it takes ~200 km^3 maximum melt extraction value. Dry melt extraction is represented with purple color and it takes ~150 km^3 maximum melt extraction value. Dry melt have one peak value at 7.25 million year. Crustal deformation extraction is represented with green color and it takes ~50 km^3 maximum melt extraction value. Total melt extraction is represented with black color and it takes ~300 km^3 maximum melt extraction value. The graph, in which each is represented on top of each other, shows the direct relationship between each other

In the total melt production graphs of this model, the first jump value is higher than the secondary jump value (Figure 3.71).

The sudden jumps in the graph showing the cumulative sum based on time represent the sudden dynamic changes made by the subduction slab. These changes correspond to ~ 7.5 and ~ 9.75 million years for the model (Figure 3.72).

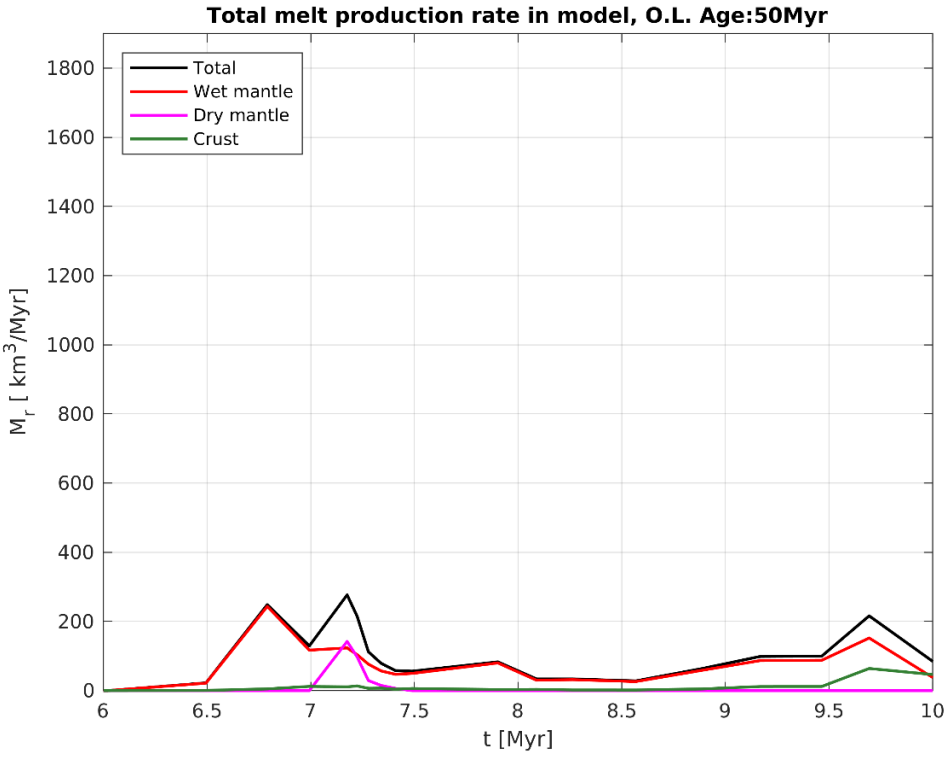

Figure 3.71: Result of the Experiment B1 with discrete volumetric melt production rate depending on time.

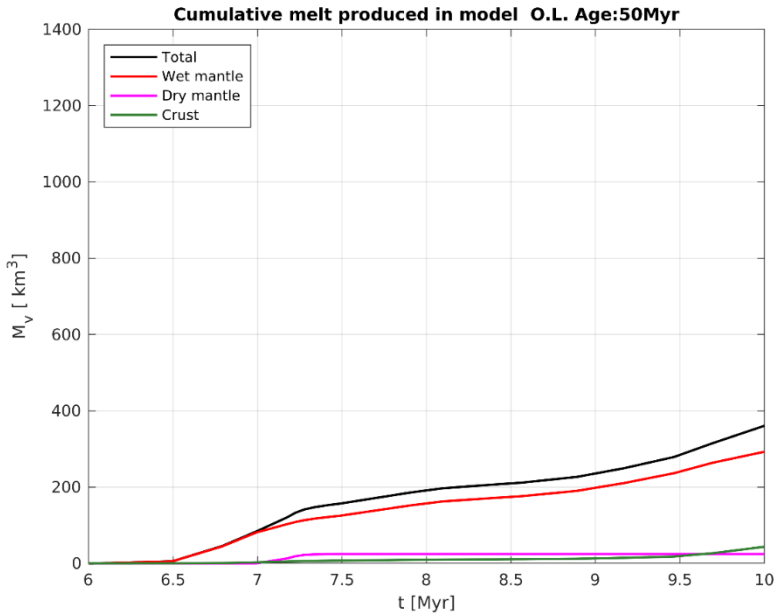

Figure 3.72: Result of the Experiment B1 with cumulative sum of discrete volumetric melt extraction rate depending on time.

3.2.3. Experimental set B2

In experimental set B2 , it is imposed that a convergence rate of 8 cm/yr from both side(right and left) of model Oceanic lithosphere age is determined as 60 Ma.Oceanic lithosphere thickness incresed due to modelling process. In models 35 km in thick continental crust , 8 km ocenaic cruscrust and 80 km in thick mantle lithosphere as determined. The rheologies determined as wet quartzite in contienetal crust (Ranalli, 1995), gabbro/basalt in oceanic crust (Ranalli, 1995) ,wetolivine in mantle lithosphere (Ranalli, 1995) and wetolivine in asthenosphere. Reference densities of continental crust, oceanic crust and mantle lithosphere and asthenosphere is 2700 kg/m3, 3000 kg/m3, 3300 kg/m3 and 3300 kg/m3, respectively.

3.2.4. Results of B2

After 7.00 m.y large amounts of wet and dry melt were observed. The asthenosphere came under the crust and the mantle wedge was opened (Figure 3.73).After 7.53 m.y Wet and dry production decreased and concentrated in a small area (Figure 3.74). After 7.84 m.y at this stage, the asthenosphere entered under the crust and wet melt production increased and spread along the accreationary prism (Figure 3.75).

In the final stage of the model is after 8.54 m.y small amount of wet melt production was observed. At this stage, dry melt production was not observed (Figure 3.76).

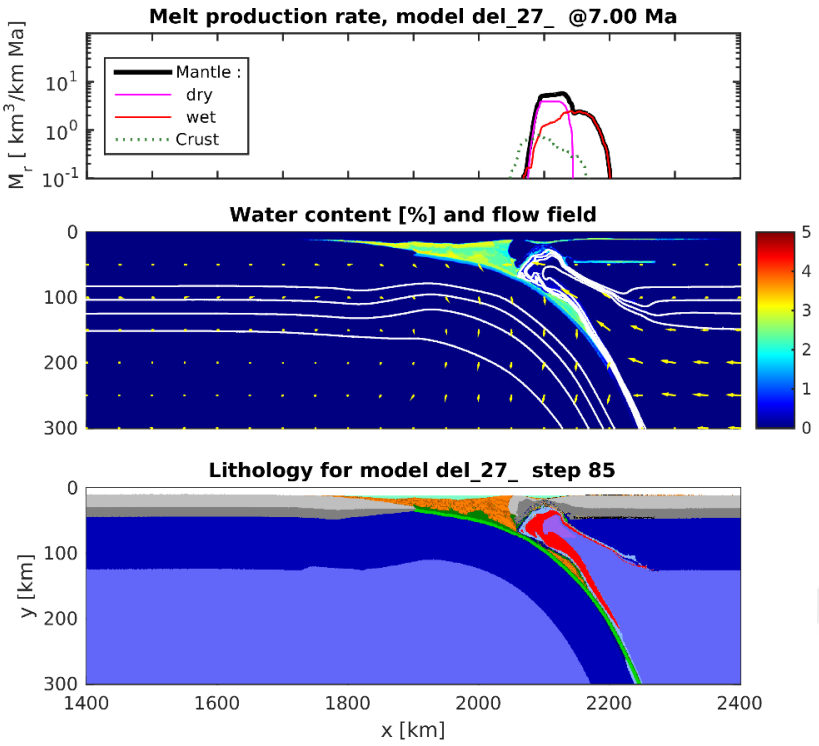

Figure 3.73: The results of the Experiment B2, show *melt production graph* (top), *water content with percentage* (middle), and *lithology graph* (bottom) at 7.00 Myr.

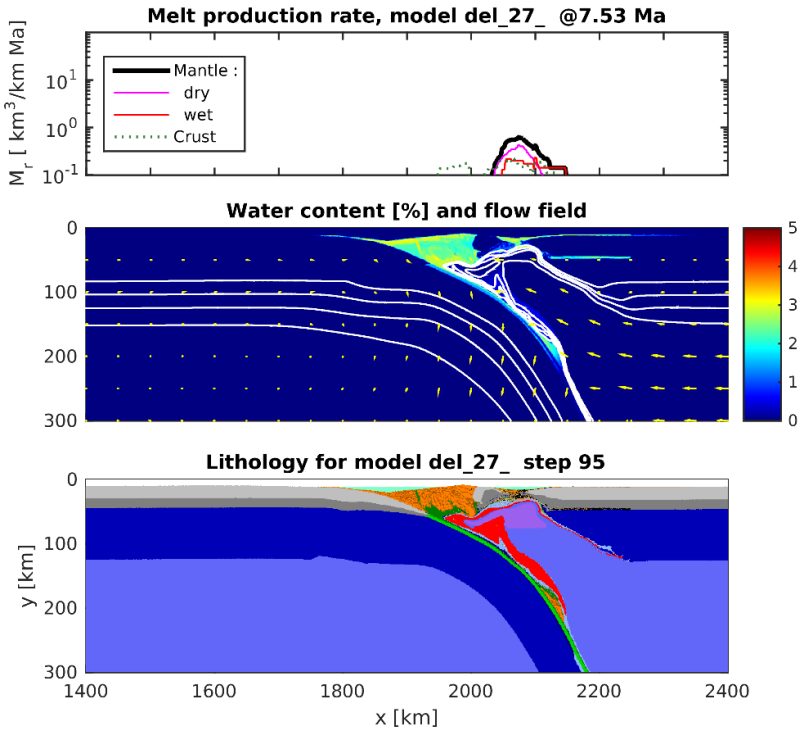

Figure 3.74: The results of the Experiment B2, show *melt production graph* (top), *water content with percentage* (middle), and *lithology graph* (bottom) at 7.53 Myr.

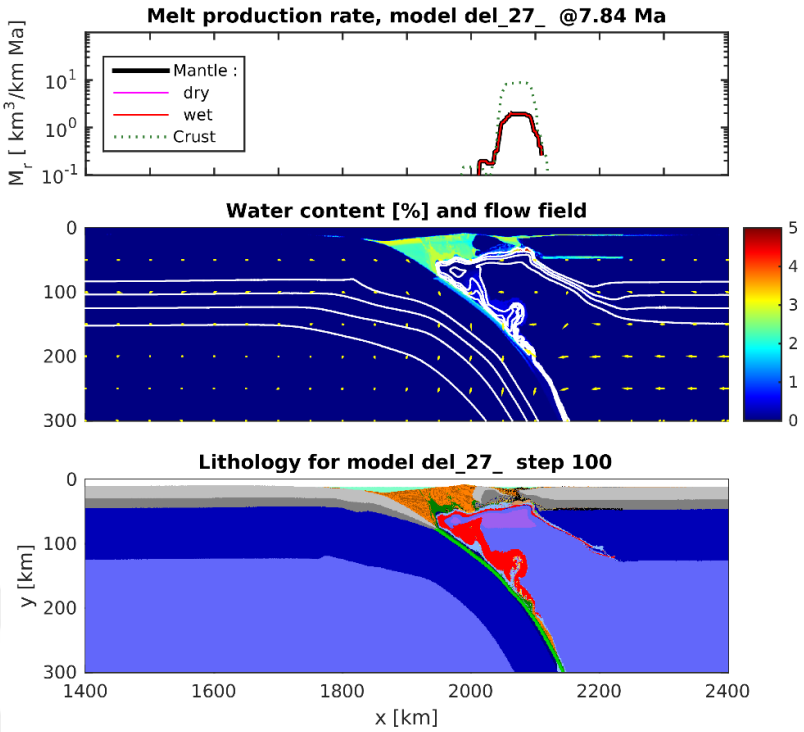

Figure 3.75: The results of the Experiment B2, show *melt production graph* (top), *water content with percentage* (middle), and *lithology graph* (bottom) at 7.84 Myr.

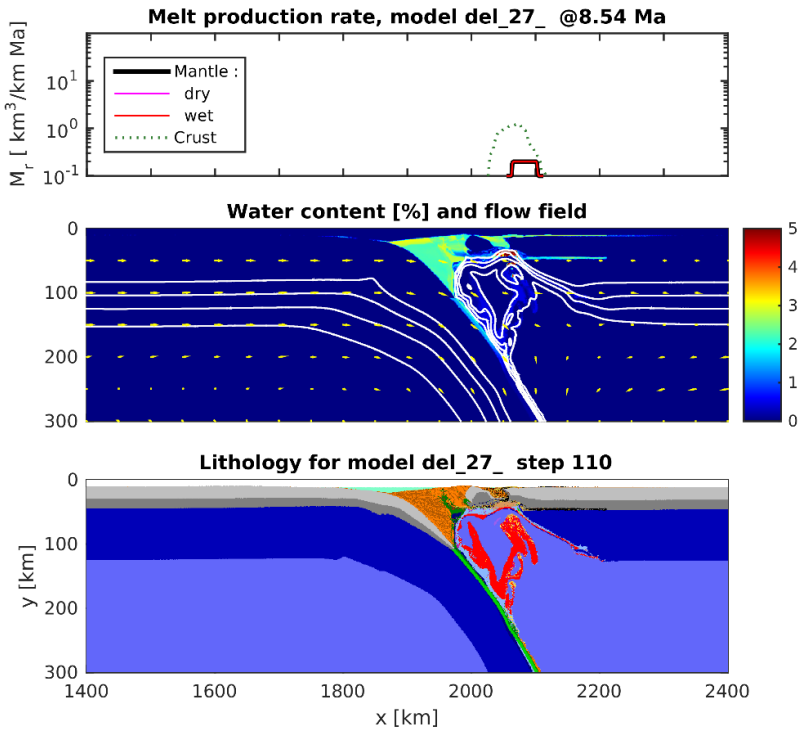

Figure 3.76: The results of the Experiment B2, show *melt production graph* (top), *water content with percentage* (middle), and *lithology graph* (bottom) at 8.54 Myr.

In the melt extraction graphs, the models show a two-peak attitude. This behavior has a direct relationship to the movement of subduction slab. The withdrawal of the slab 6.75 million years after the start of the model rapidly changes the dynamics in the mantle and causes a serious increase in melt production. This increase is supported by changes in mantle convection movements. Wet melt extraction is represented with red color and it takes ~250 km^3 maximum melt extraction value. Dry melt extraction is represented with purple color and it takes ~250 km^3 maximum melt extraction value. Crustal deformation extraction is represented with green color and it takes ~450 km^3 maximum melt extraction value. Total melt extraction is represented with black color and it takes ~550 km^3 maximum melt extraction value. The graph, in which each is represented on top of each other, shows the direct relationship between each other

In the total melt production graphs of this model, the second jump value is higher than the first jump value (Figure 3.77).

The sudden jumps in the graph showing the cumulative sum based on time represent the sudden dynamic changes made by the subduction slab. These changes correspond to ~ 7 and ~ 8 million years for the model (Figure 3.78).

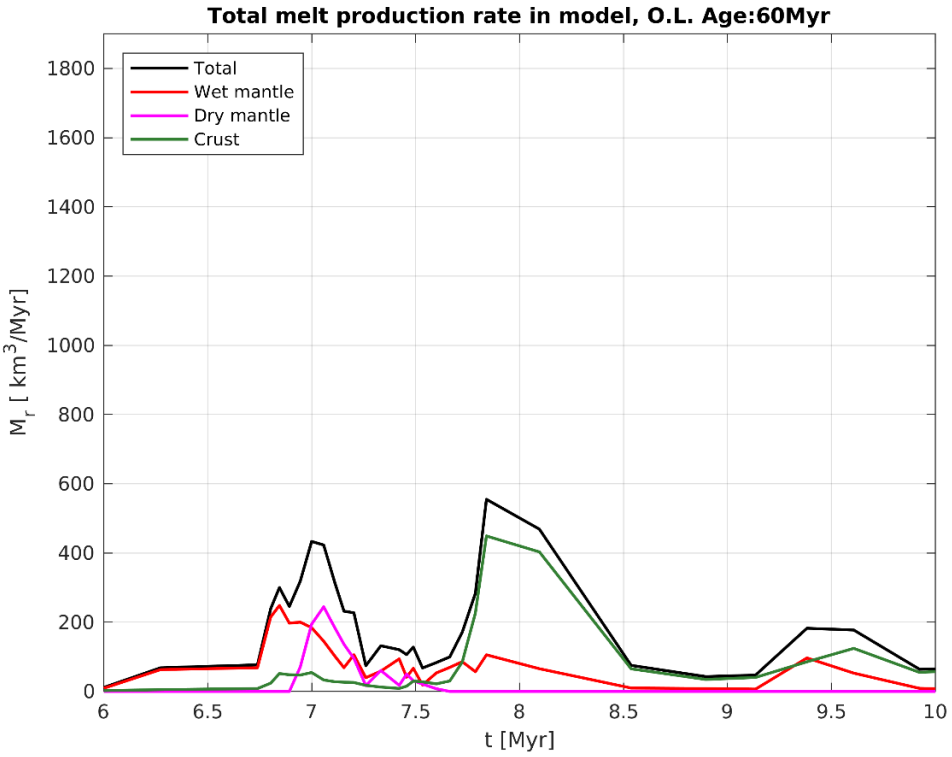

Figure 3.77: Result of the Experiment B2 with discrete volumetric melt production rate depending on time.

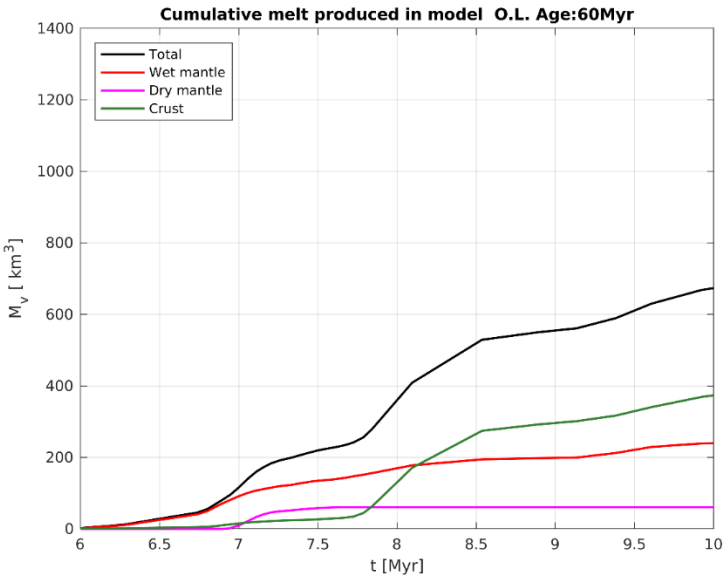

Figure 3.78: Result of the Experiment B2 with cumulative sum of discrete volumetric melt extraction rate depending on time.

3.2.5. Experimental set B3

In experimental set B3 , it is imposed that a convergence rate of 8 cm/yr from both side(right and left) of model Oceanic lithosphere age is determined as 70 Ma.Oceanic lithosphere thickness incresed due to modelling process. In models 35 km in thick continental crust , 8 km ocenaic cruscrust and 80 km in thick mantle lithosphere as determined. The rheologies determined as wet quartzite in contienetal crust (Ranalli, 1995), gabbro/basalt in oceanic crust (Ranalli, 1995) ,wetolivine in mantle lithosphere (Ranalli, 1995) and wetolivine in asthenosphere. Reference densities of continental crust, oceanic crust and mantle lithosphere and asthenosphere is 2700 kg/m3, 3000 kg/m3, 3300 kg/m3 and 3300 kg/m3, respectively.

3.2.6. Results of B3

After 6.24 m.y. astenosphere began to enter the mantle wedge. Only wet melt production was observed (Figure 3.79). After 6.55 m.y , only wet melt production is observed. The asthenosphere partially came under the crust (Figure 3.80). After 6.78 m.y. dry melt production increased regionally and wet melt production expanded. The convection currents in the mantle are upward (Figure 3.81).

In the final stage of the model is after 7.44 m.y small amount of wet melt production observed. The convection currents in the mantle are stable (Figure 3.82).

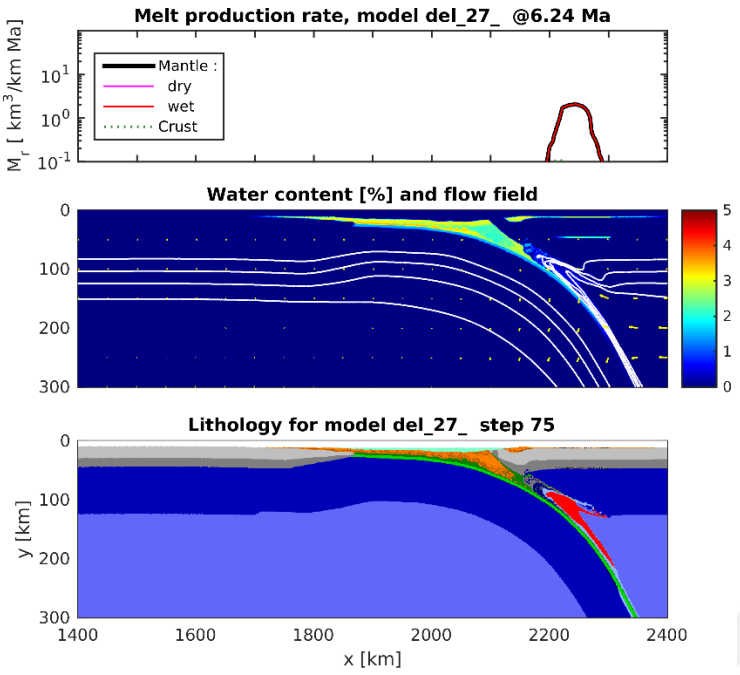

Figure 3.79: The results of the Experiment B3, show *melt production graph* (top), *water content with percentage* (middle), and *lithology graph* (bottom) at 6.24 Myr.

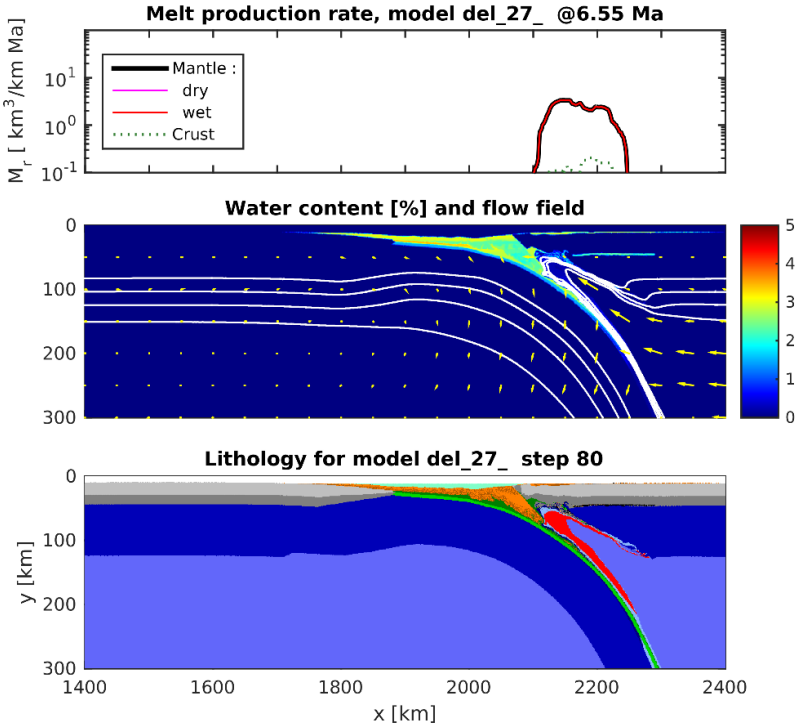

Figure 3.80: The results of the Experiment B3, show *melt production graph* (top), *water content with percentage* (middle), and *lithology graph* (bottom) at 6.55 Myr.

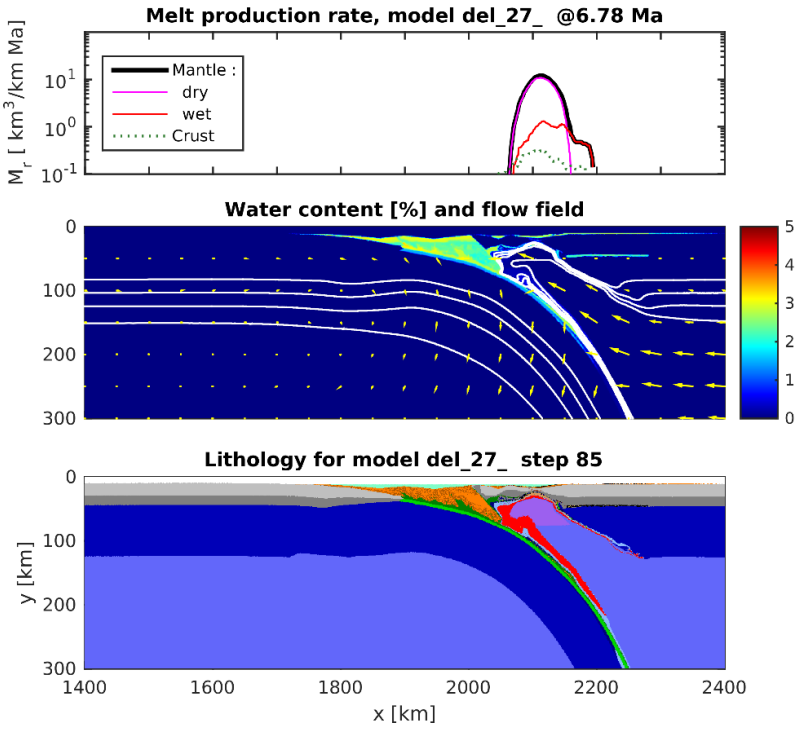

Figure 3.81: The results of the Experiment B3, show *melt production graph* (top), *water content with percentage* (middle), and *lithology graph* (bottom) at 6.78 Myr.

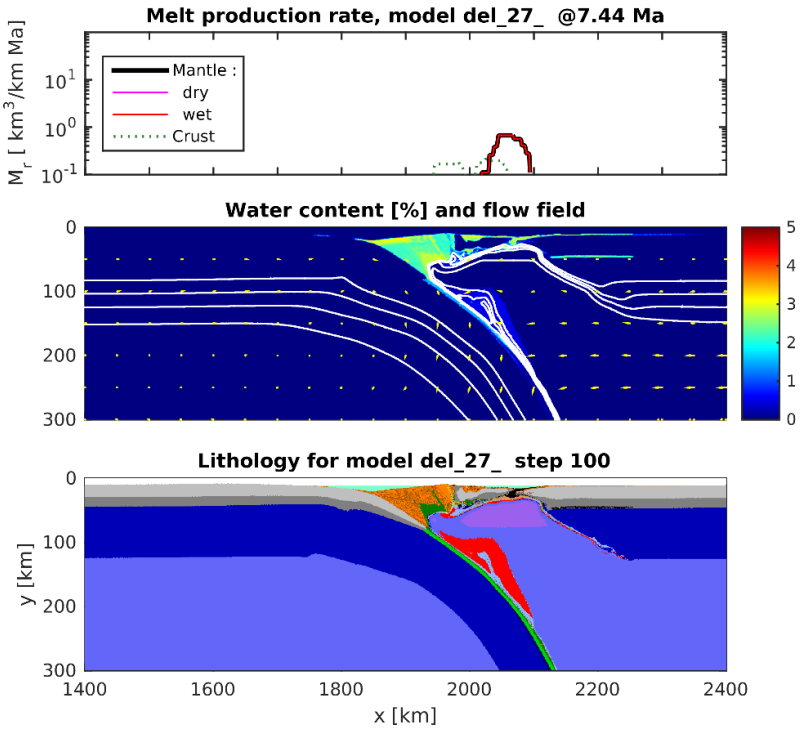

Figure 3.82: The results of the Experiment B3, show *melt production graph* (top), *water content with percentage* (middle), and *lithology graph* (bottom) at 7.44 Myr.

In the melt extraction graphs, the models show a two-peak attitude. This behavior has a direct relationship to the movement of subduction slab. The withdrawal of the slab 6.75 million years after the start of the model rapidly changes the dynamics in the mantle and causes a serious increase in melt production. This increase is supported by changes in mantle convection movements. Wet melt extraction is represented with red color and it takes ~300 km^3 maximum melt extraction value. Dry melt extraction is represented with purple color and it takes ~550 km^3 maximum melt extraction value. Crustal deformation extraction is represented with green color and it takes ~200 km^3 maximum melt extraction value. Total melt extraction is represented with black color and it takes ~700 km^3 maximum melt extraction value. The graph, in which each is represented on top of each other, shows the direct relationship between each other

In the total melt production graphs of this model, the first jump value is higher than the second jump value (Figure 3.83).

The sudden jumps in the graph showing the cumulative sum based on time represent the sudden dynamic changes made by the subduction slab. These changes correspond to ~ 6.75 and ~ 9.25 million years for the model (Figure 3.84).

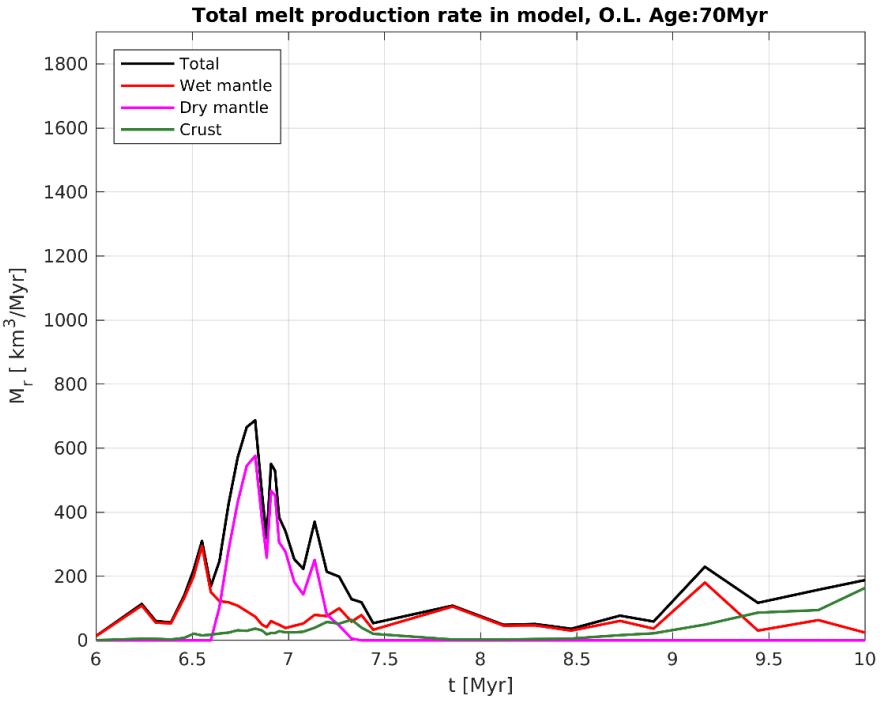

Figure 3.83: Result of the Experiment B3 with discrete volumetric melt production rate depending on time.

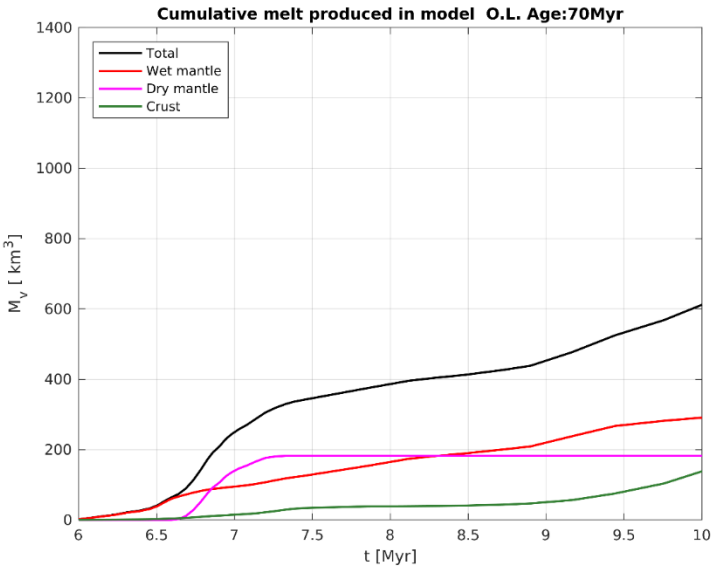

Figure 3.84: Result of the Experiment B3 with cumulative sum of discrete volumetric melt extraction rate depending on time.

3.2.7. Experimental set B4

In experimental set B4 , it is imposed that a convergence rate of 8 cm/yr from both side(right and left) of model Oceanic lithosphere age is determined as 80 Ma.Oceanic lithosphere thickness incresed due to modelling process. In models 35 km in thick continental crust , 8 km ocenaic cruscrust and 80 km in thick mantle lithosphere as determined. The rheologies determined as wet quartzite in contienetal crust (Ranalli, 1995), gabbro/basalt in oceanic crust (Ranalli, 1995) ,wetolivine in mantle lithosphere (Ranalli, 1995) and wetolivine in asthenosphere. Reference densities of continental crust, oceanic crust and mantle lithosphere and asthenosphere is 2700 kg/m3, 3000 kg/m3, 3300 kg/m3 and 3300 kg/m3, respectively.

3.2.8. Results of B4

After 6.47 m.y. only wet melt production is observed. The asthenosphere partially came under the crust (Figure 3.85). After 6.69 dry melt production increased regionally and wet melt production expanded (Figure 3.86). After 7.00 m.y dry melt production has migrated to the trench side. Wet and dry melt production is regional and high (Figure 3.87).

In the final stage of the model is after 7.35 m.y a small amount of wet melt production was observed. Convection currents in the mantle are stable (Figure 3.88).

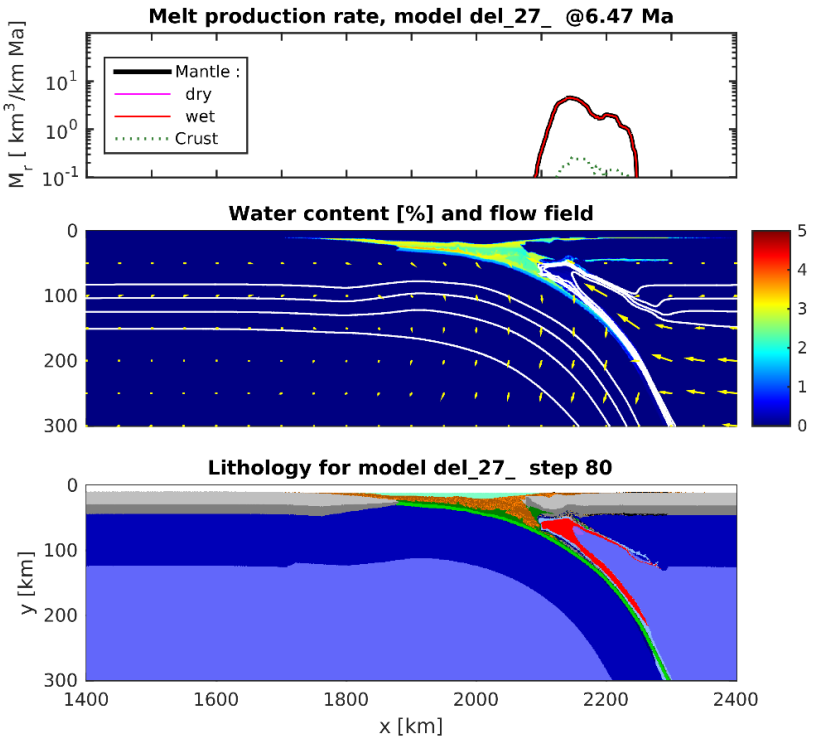

Figure 3.85: The results of the Experiment B4, show *melt production graph* (top), *water content with percentage* (middle), and *lithology graph* (bottom) at 6.47 Myr.

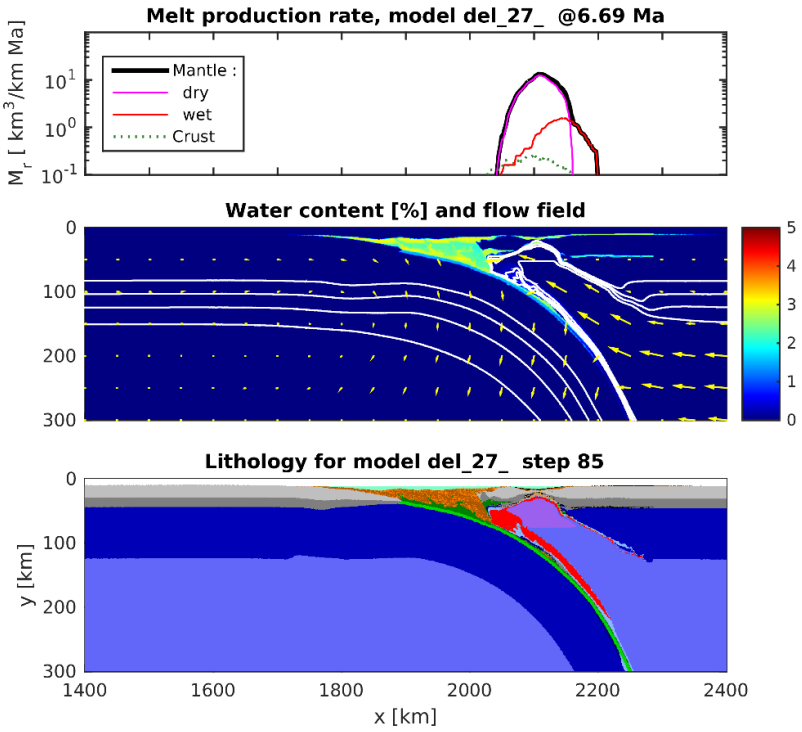

Figure 3.86 The results of the Experiment B4, show *melt production graph* (top), *water content with percentage* (middle), and *lithology graph* (bottom) at 6.69 Myr.

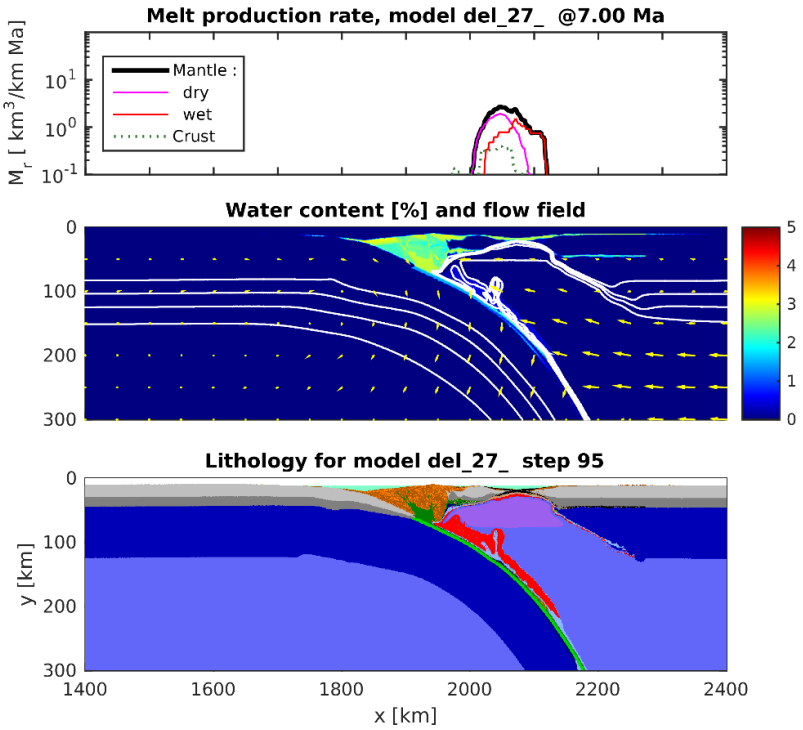

Figure 3.87 The results of the Experiment B4, show *melt production graph* (top), *water content with percentage* (middle), and *lithology graph* (bottom) at 7.00 Myr.

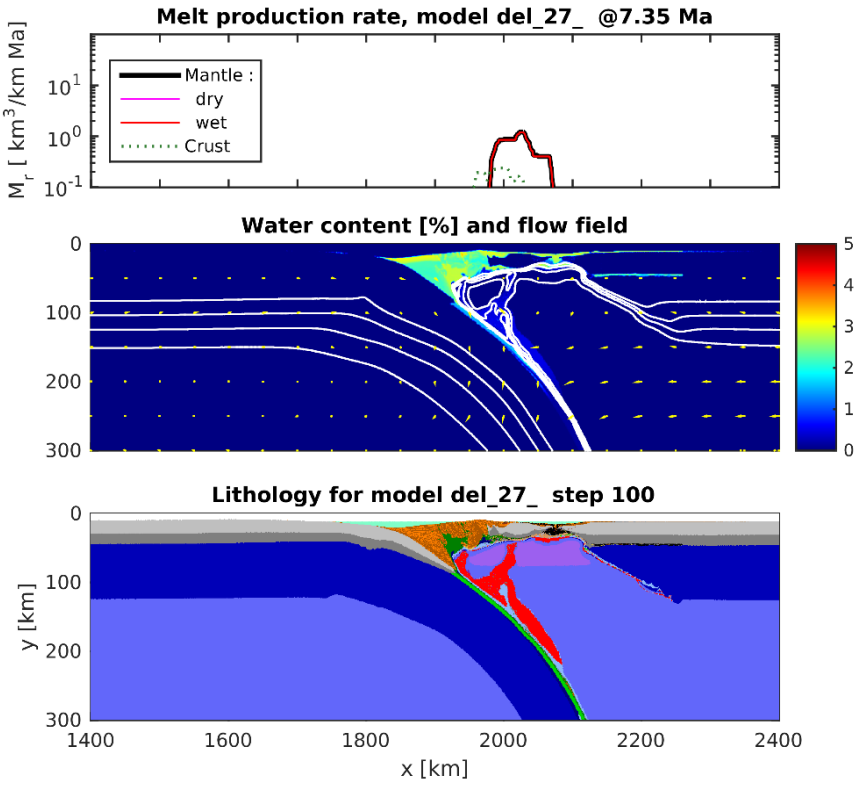

Figure 3.88: The results of the Experiment B4, show *melt production graph* (top), *water content with percentage* (middle), and *lithology graph* (bottom) at 7.35Myr.

In the melt extraction graphs, the models show a two-peak attitude. This behavior has a direct relationship to the movement of subduction slab. The withdrawal of the slab 6.75 million years after the start of the model rapidly changes the dynamics in the mantle and causes a serious increase in melt production. This increase is supported by changes in mantle convection movements. Wet melt extraction is represented with red color and it takes ~350 km^3 maximum melt extraction value. Dry melt extraction is represented with purple color and it takes ~700 km^3 maximum melt extraction value. Crustal deformation extraction is represented with green color and it takes ~150 km^3 maximum melt extraction value. Total melt extraction is represented with black color and it takes ~900 km^3 maximum melt extraction value. The graph, in which each is represented on top of each other, shows the direct relationship between each other

In the total melt production graphs of this model, the first jump value is higher than the second jump value (Figure 3.89).

The sudden jumps in the graph showing the cumulative sum based on time represent the sudden dynamic changes made by the subduction slab. These changes correspond to ~ 6.75 and ~ 9.25 million years for the model (Figure 3.90).

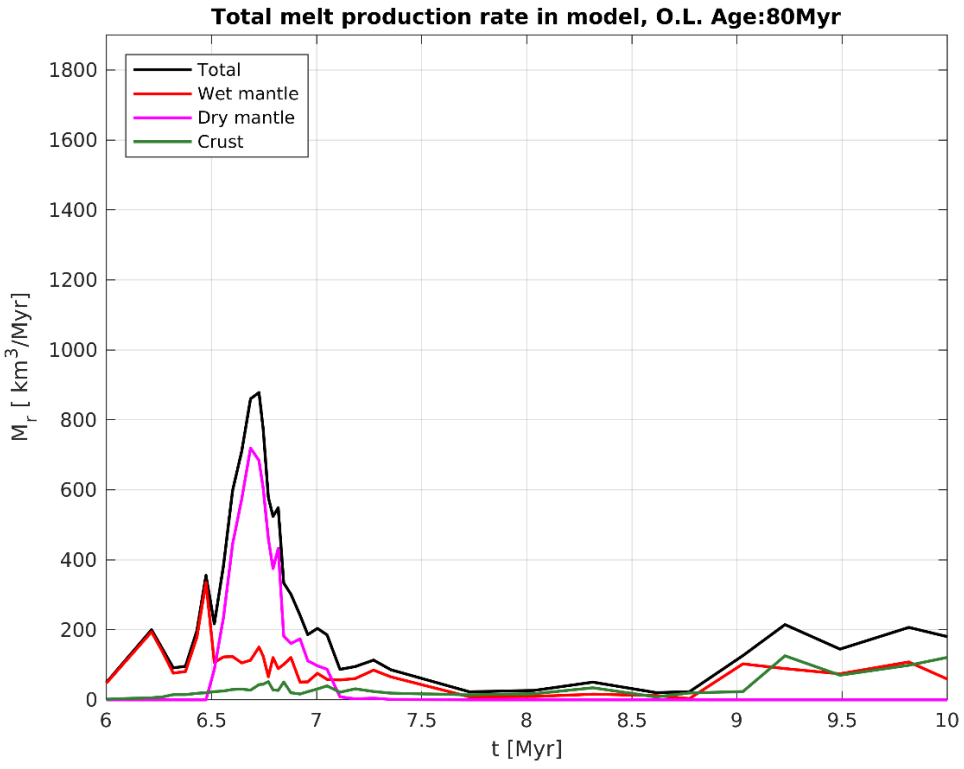

Figure 3.89: Result of the Experiment B4 with discrete volumetric melt production rate depending on time.

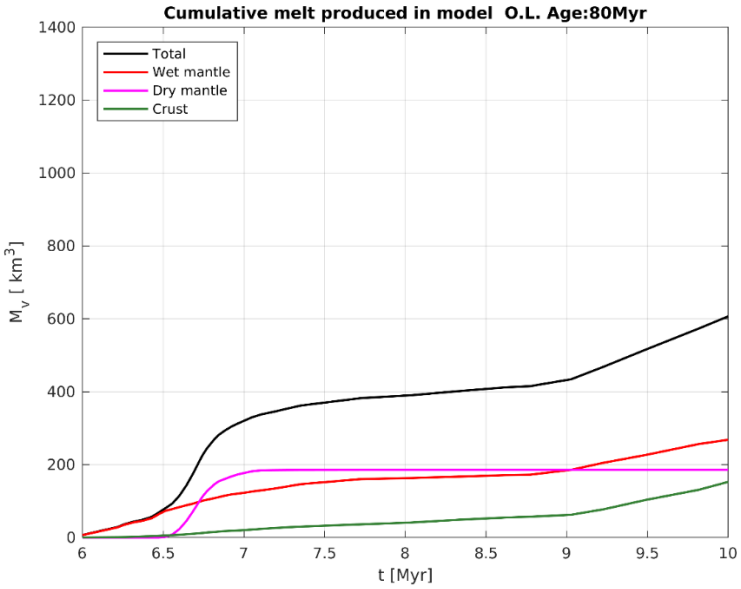

Figure 3.90: Result of the Experiment B4 with cumulative sum of discrete volumetric melt extraction rate depending on time.

3.2.9. Experimental set B5

In experimental set B5 , it is imposed that a convergence rate of 8 cm/yr from both side(right and left) of model Oceanic lithosphere age is determined as 90 Ma.Oceanic lithosphere thickness incresed due to modelling process. In models 35 km in thick continental crust , 8 km ocenaic cruscrust and 80 km in thick mantle lithosphere as determined. The rheologies determined as wet quartzite in contienetal crust (Ranalli, 1995), gabbro/basalt in oceanic crust (Ranalli, 1995) ,wetolivine in mantle lithosphere (Ranalli, 1995) and wetolivine in asthenosphere. Reference densities of continental crust, oceanic crust and mantle lithosphere and asthenosphere is 2700 kg/m3, 3000 kg/m3, 3300 kg/m3 and 3300 kg/m3, respectively.

3.2.10. Results of B5

After 6.46 m.y. a significant amount of wet melt production has been observed and the intensity of the convection currents in the mantle is high (Figure 3.91). After 6.64 m.y Wet and dry melt production was observed in significant quantities. Both types of melt production were concentrated in two regions. The intensity of the convection currents in the mantle is high and upward (Figure 3.92). After 6.78 m.y the production of dry melt is high and spread along the accretionary prism. Wet melt production is low and divided into two regions (Figure 3.93). After 6.99 m.y wet and dry melt types are produced in small amounts and are regional.

In the final stage of the model is after 9.43 m.y significant wet melt production was observed at this stage and concentrated in one region (Figure 3.94).

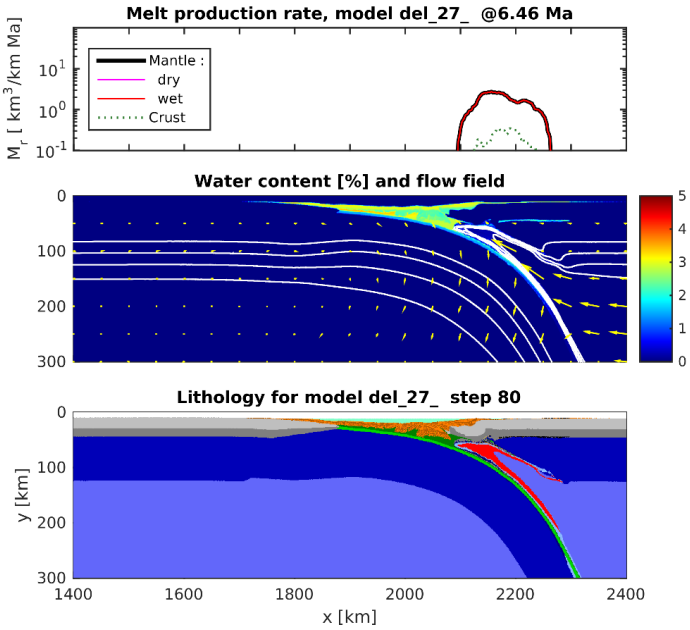

Figure 3.91: The results of the Experiment B5, show *melt production graph* (top), *water content with percentage* (middle), and *lithology graph* (bottom) at 6.46 Myr.

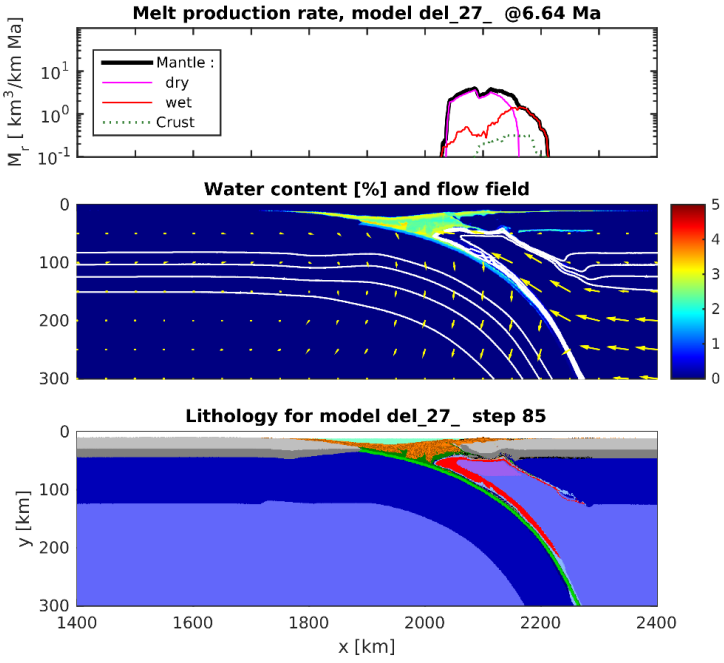

Figure 3.92: The results of the Experiment B5, show *melt production graph* (top), *water content with percentage* (middle), and *lithology graph* (bottom) at 6.64 Myr.

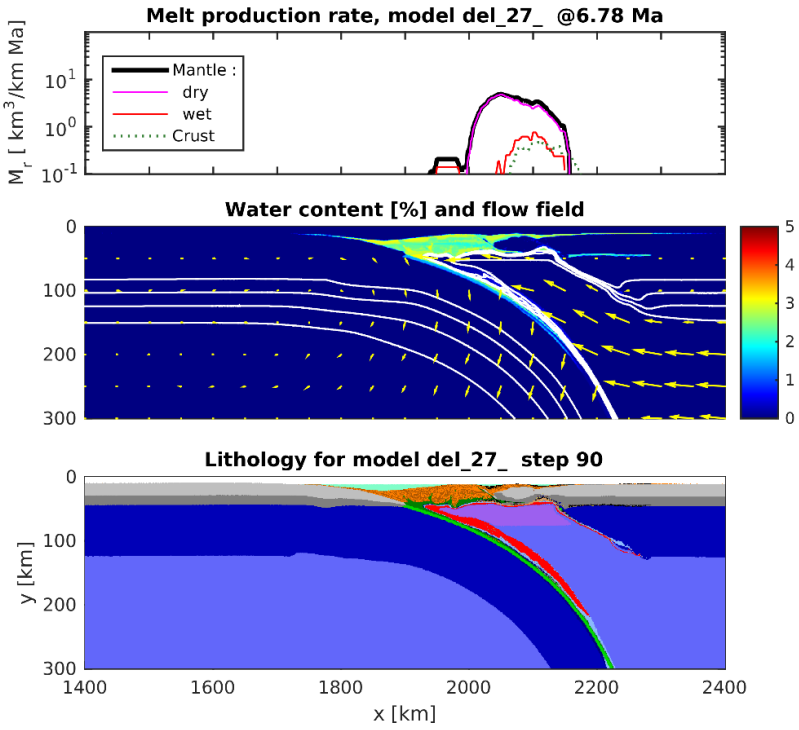

Figure 3.93: The results of the Experiment B5, show *melt production graph* (top), *water content with percentage* (middle), and *lithology graph* (bottom) at 6.78 Myr.

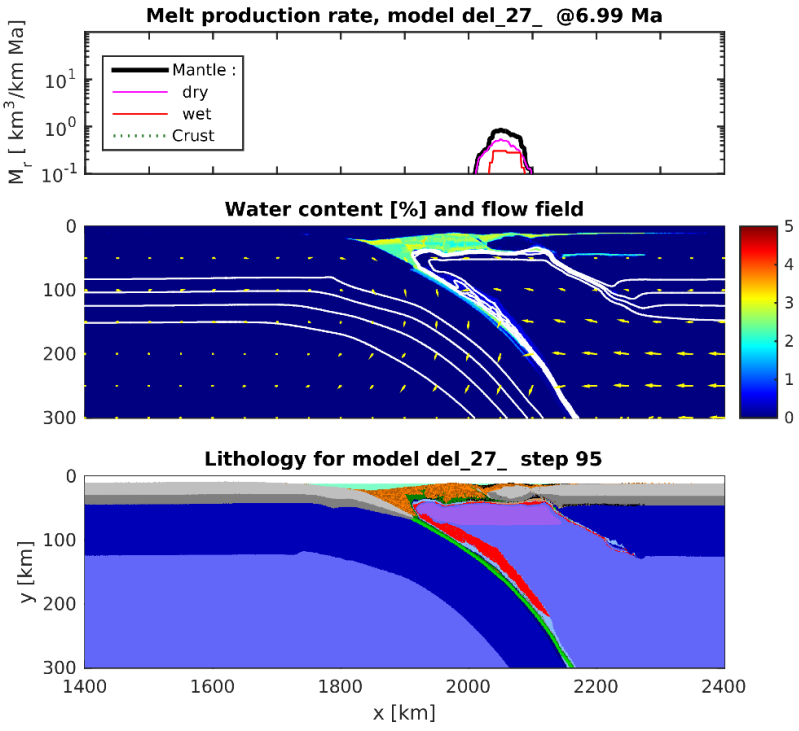

Figure 3.94: The results of the Experiment B5, show *melt production graph* (top), *water content with percentage* (middle), and *lithology graph* (bottom) at 6.99 Myr.

In the melt extraction graphs, the models show a two-peak attitude. This behavior has a direct relationship to the movement of subduction slab. The withdrawal of the slab 6.75 million years after the start of the model rapidly changes the dynamics in the mantle and causes a serious increase in melt production. This increase is supported by changes in mantle convection movements. Wet melt extraction is represented with red color and it takes ~300 km^3 maximum melt extraction value. Dry melt extraction is represented with purple color and it takes ~550 km^3 maximum melt extraction value. Crustal deformation extraction is represented with green color and it takes ~150 km^3 maximum melt extraction value. Total melt extraction is represented with black color and it takes ~750 km^3 maximum melt extraction value. The graph, in which each is represented on top of each other, shows the direct relationship between each other

In the total melt production graphs of this model, the first jump value is higher than the second jump value (Figure 3.95).

The sudden jumps in the graph showing the cumulative sum based on time represent the sudden dynamic changes made by the subduction slab. These changes correspond to ~ 6.75 and ~ 8.75 million years for the model (Figure 3.96).

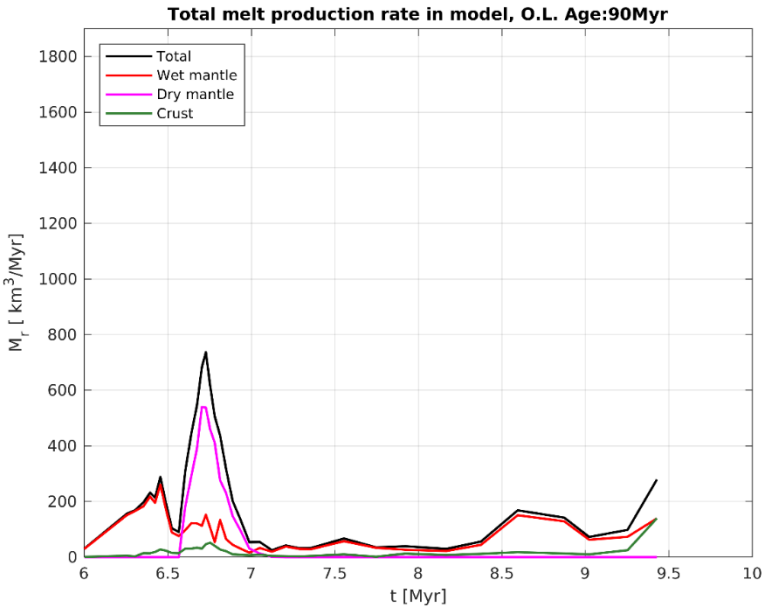

Figure 3.95: Result of the Experiment B5 with discrete volumetric melt production rate depending on time.

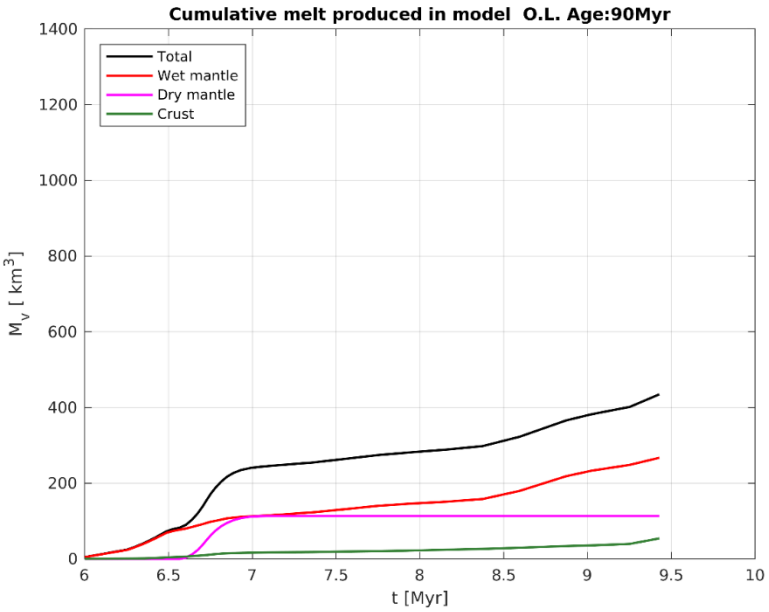

Figure 3.96: Result of the Experiment B5 with cumulative sum of discrete volumetric melt extraction rate depending on time.

3.2.11. Experimental set B6

In experimental set B6 , it is imposed that a convergence rate of 8 cm/yr from both side(right and left) of model Oceanic lithosphere age is determined as 100 Ma.Oceanic lithosphere thickness incresed due to modelling process. In models 35 km in thick continental crust , 8 km ocenaic cruscrust and 80 km in thick mantle lithosphere as determined. The rheologies determined as wet quartzite in contienetal crust (Ranalli, 1995), gabbro/basalt in oceanic crust (Ranalli, 1995) ,wetolivine in mantle lithosphere (Ranalli, 1995) and wetolivine in asthenosphere. Reference densities of continental crust, oceanic crust and mantle lithosphere and asthenosphere is 2700 kg/m3, 3000 kg/m3, 3300 kg/m3 and 3300 kg/m3, respectively.

3.2.12. Results of B6

After 6.46 m.y dry melt production is high and concentrated in a region. Wet melt production is widespread (Figure 3.97). After 6.85 m.y Wet and dry production is high and spread. The intensity of the convection currents in the mantle is high and upward (Figure 3.98). After 7.03 m.y dry melt production is made and shows dual properties. Wet melt production is concentrated in two regions (Figure 3.99).

In the final stage of the model is after 7.75 m.y melt production was not observed. Wet melt production was concentrated in a region (Figure 3.100).

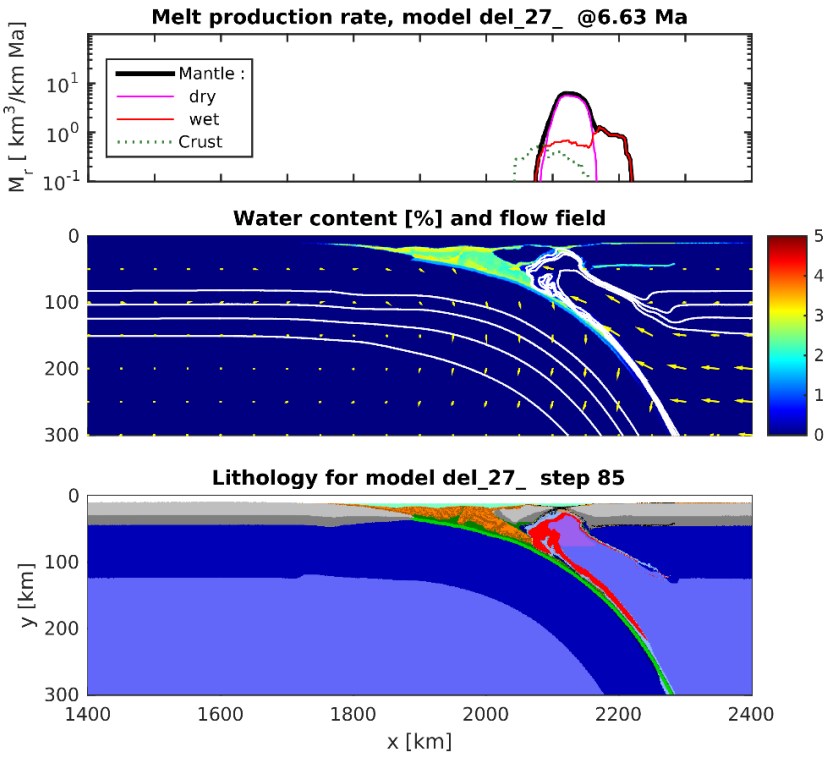

Figure 3.97: The results of the Experiment B6, show *melt production graph* (top), *water content with percentage* (middle), and *lithology graph* (bottom) at 6.63 Myr.

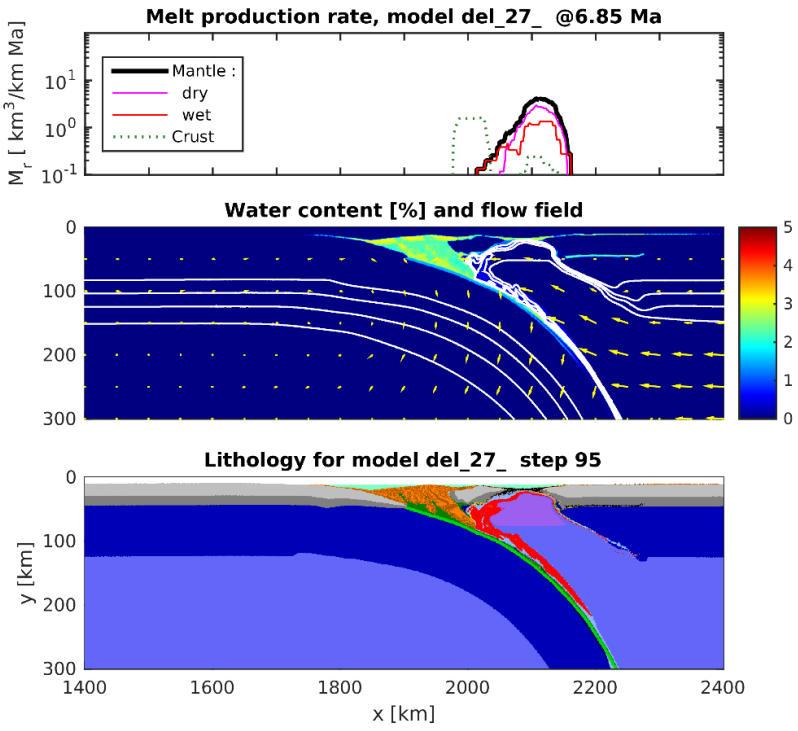

Figure 3.98: The results of the Experiment B6, show *melt production graph* (top), *water content with percentage* (middle), and *lithology graph* (bottom) at 6.85 Myr.

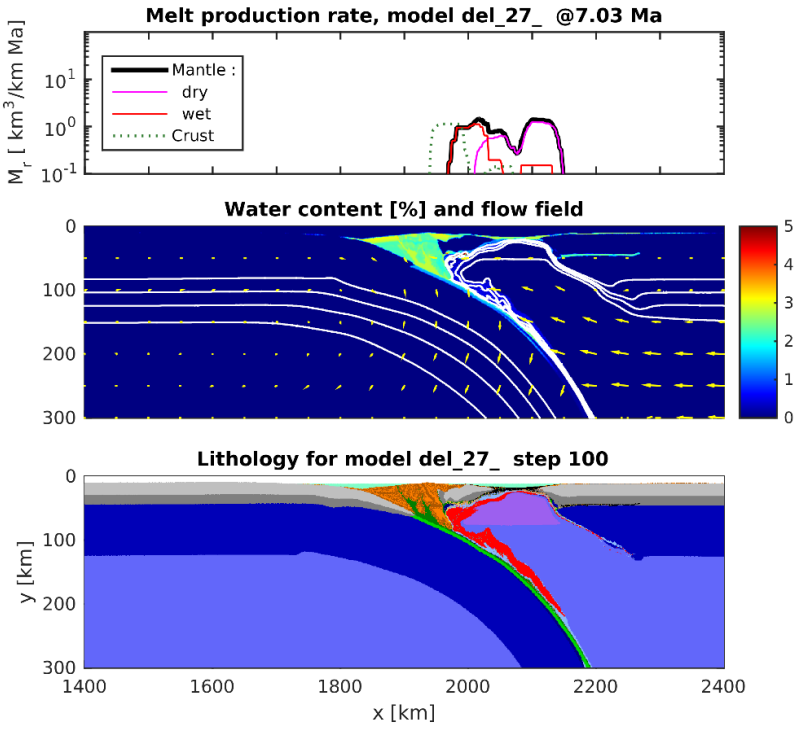

Figure 3.99: The results of the Experiment B6, show *melt production graph* (top), *water content with percentage* (middle), and *lithology graph* (bottom) at 7.03 Myr.

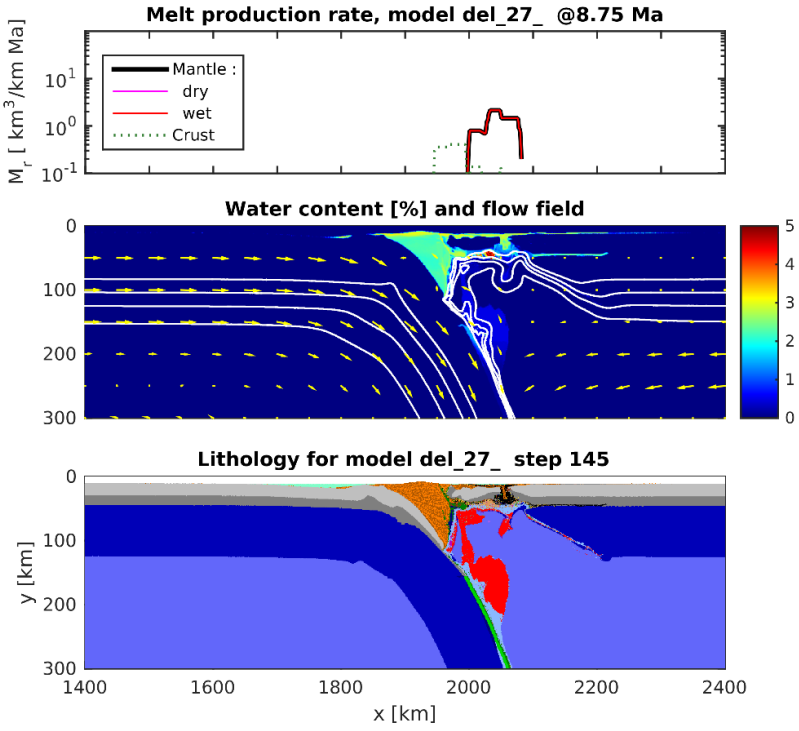

Figure 3.100: The results of the Experiment B6, show *melt production graph* (top), *water content with percentage* (middle), and *lithology graph* (bottom) at 8.75 Myr.

In the melt extraction graphs, the models show a two-peak attitude. This behavior has a direct relationship to the movement of subduction slab. The withdrawal of the slab 6.75 million years after the start of the model rapidly changes the dynamics in the mantle and causes a serious increase in melt production. This increase is supported by changes in mantle convection movements. Wet melt extraction is represented with red color and it takes ~150 km^3 maximum melt extraction value. Dry melt extraction is represented with purple color and it takes ~500 km^3 maximum melt extraction value. Crustal deformation extraction is represented with green color and it takes ~150 km^3 maximum melt extraction value. Total melt extraction is represented with black color and it takes ~700 km^3 maximum melt extraction value. The graph, in which each is represented on top of each other, shows the direct relationship between each other

In the total melt production graphs of this model, the first jump value is higher than the second jump value (Figure 3.101).

The sudden jumps in the graph showing the cumulative sum based on time represent the sudden dynamic changes made by the subduction slab. These changes correspond to ~ 6.75 and ~ 8.75 million years for the model (Figure 3.102).

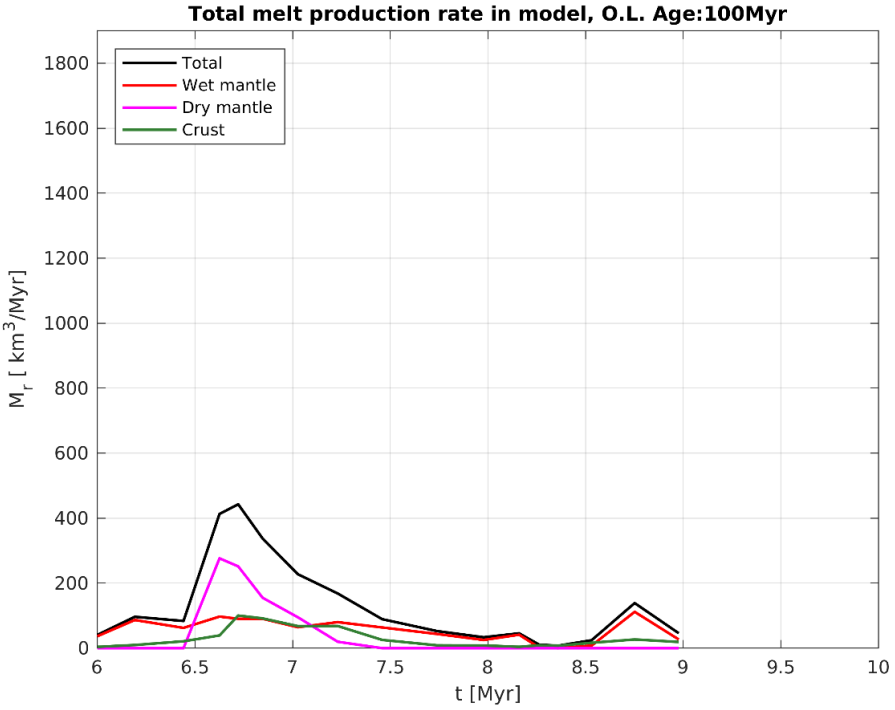

Figure 3.101: Result of the Experiment B6 with discrete volumetric melt production rate depending on time.

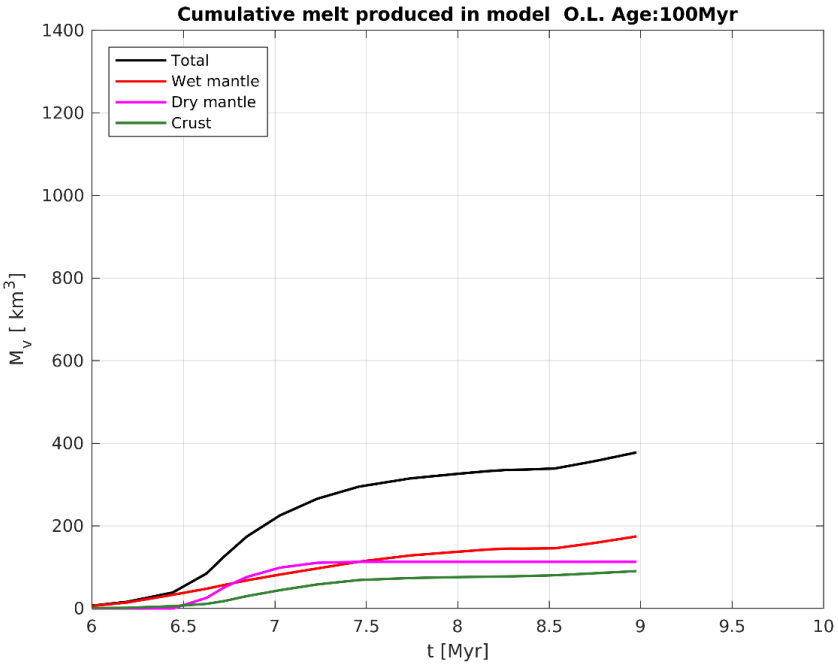

Figure 3.102: Result of the Experiment B6 with cumulative sum of discrete volumetric melt extraction rate depending on time.

3.2.13. Experimental set B7

In experimental set B7 , it is imposed that a convergence rate of 8 cm/yr from both side(right and left) of model Oceanic lithosphere age is determined as 110 Ma.Oceanic lithosphere thickness incresed due to modelling process. In models 35 km in thick continental crust , 8 km ocenaic cruscrust and 80 km in thick mantle lithosphere as determined. The rheologies determined as wet quartzite in contienetal crust (Ranalli, 1995), gabbro/basalt in oceanic crust (Ranalli, 1995) ,wetolivine in mantle lithosphere (Ranalli, 1995) and wetolivine in asthenosphere. Reference densities of continental crust, oceanic crust and mantle lithosphere and asthenosphere is 2700 kg/m3, 3000 kg/m3, 3300 kg/m3 and 3300 kg/m3, respectively.

3.2.14. Results of B7

After 6.55 m.y. dry melt production is high and concentrated in a region. Wet melt production is small and spread. The intensity of the convection currents in the mantle is high (Figure 3.103). After 6.87 m.y. dry melt production has a triple structure. Wet melt production is significantly less and has been observed in four different regions (Figure 3.104). After 7.18 m.y. Wet melt production is more and spread than dry melt production. Dry melt production has migrated to trench side (Figure 3.105).

In the final stage of the model is after 8.93 wet melt production is concentrated in two different regions. Dry melt production is not observed (Figure 3.106).

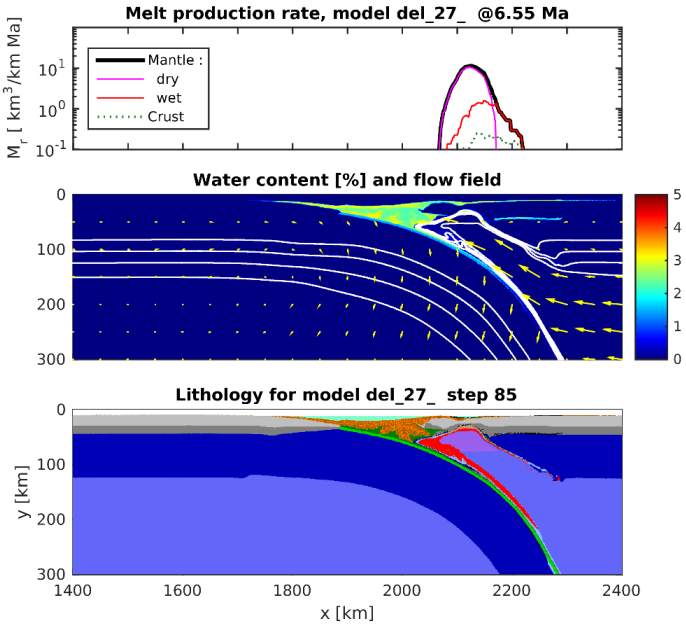

Figure 3.103: The results of the Experiment B7, show *melt production graph* (top), *water content with percentage* (middle), and *lithology graph* (bottom) at 6.55 Myr.

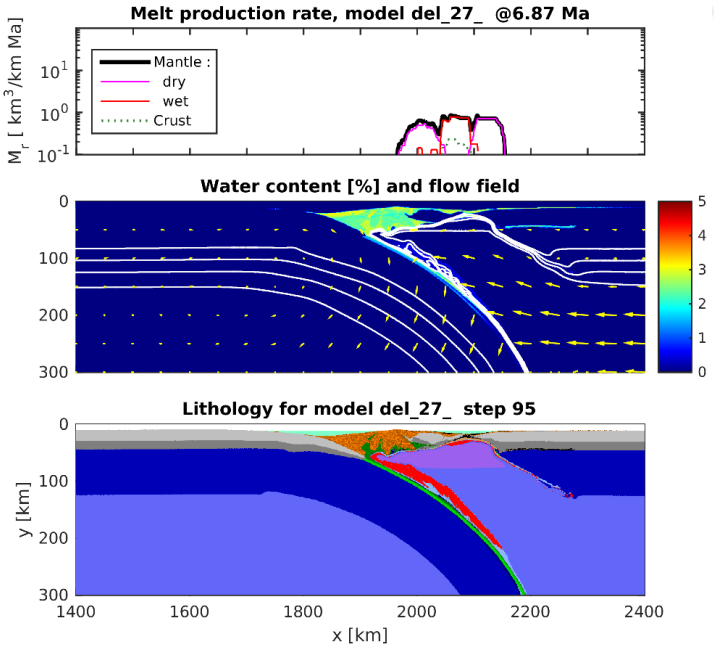

Figure 3.104: The results of the Experiment B7, show *melt production graph* (top), *water content with percentage* (middle), and *lithology graph* (bottom) at 6.87 Myr.

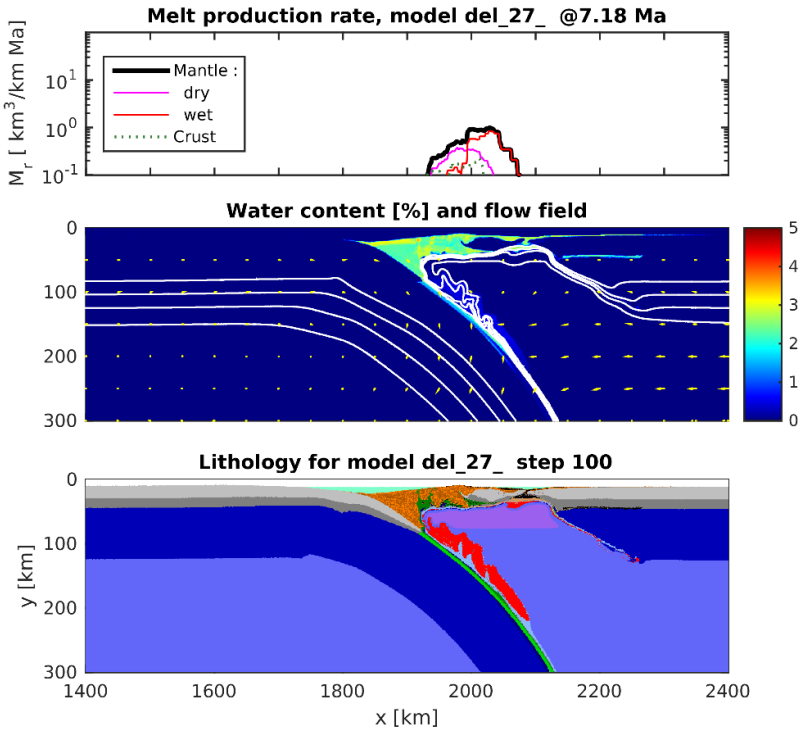

Figure 3.105: The results of the Experiment B7, show *melt production graph* (top), *water content with percentage* (middle), and *lithology graph* (bottom) at 7.18 Myr.

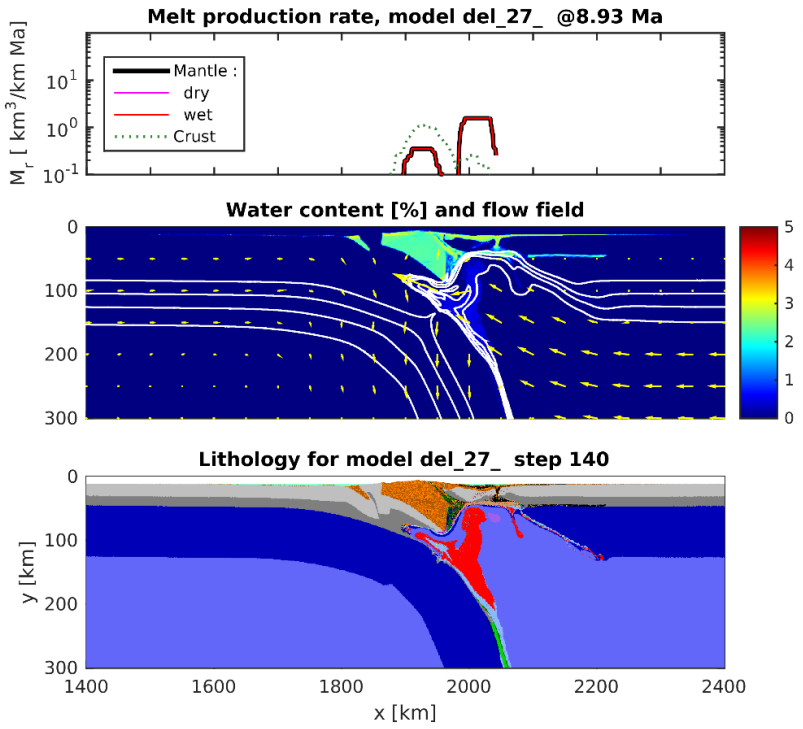

Figure 3.106: The results of the Experiment B7, show *melt production graph* (top), *water content with percentage* (middle), and *lithology graph* (bottom) at 8.93 Myr.

In the melt extraction graphs, the models show a two-peak attitude. This behavior has a direct relationship to the movement of subduction slab. The withdrawal of the slab 6.5 million years after the start of the model rapidly changes the dynamics in the mantle and causes a serious increase in melt production. This increase is supported by changes in mantle convection movements. Wet melt extraction is represented with red color and it takes ~200 km^3 maximum melt extraction value. Dry melt extraction is represented with purple color and it takes ~550 km^3 maximum melt extraction value. Crustal deformation extraction is represented with green color and it takes ~100 km^3 maximum melt extraction value. Total melt extraction is represented with black color and it takes ~700 km^3 maximum melt extraction value. The graph, in which each is represented on top of each other, shows the direct relationship between each other

In the total melt production graphs of this model, the first jump value is higher than the second jump value (Figure 3.107).

The sudden jumps in the graph showing the cumulative sum based on time represent the sudden dynamic changes made by the subduction slab. These changes correspond to ~ 6.5 and ~ 8.75 million years for the model (Figure 3.108).

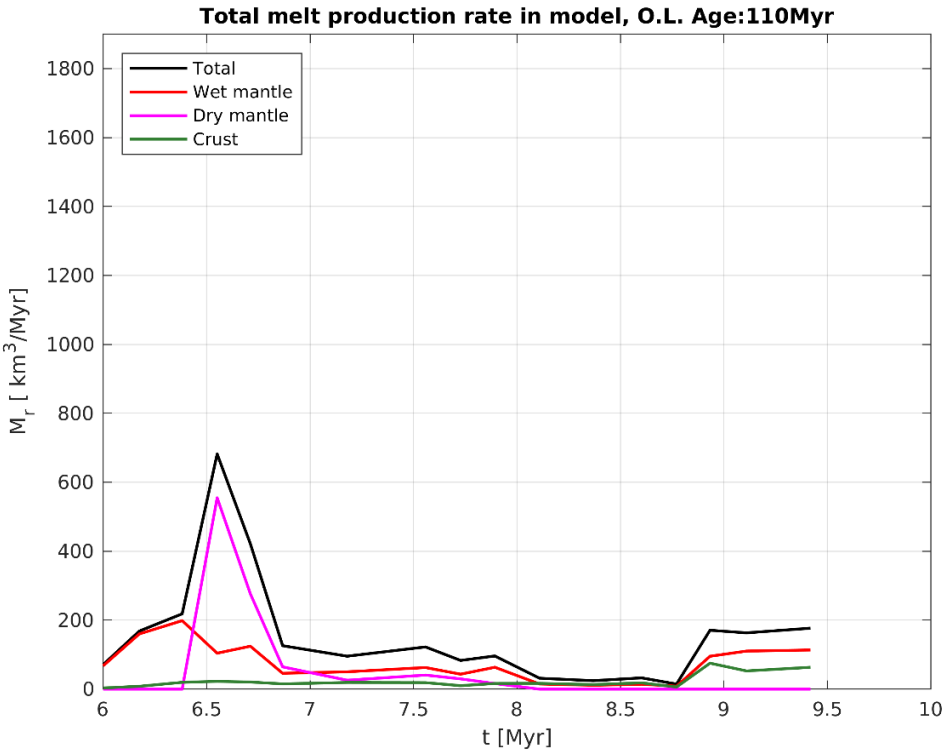

Figure 3.107: Result of the Experiment B7 with discrete volumetric melt production rate depending on time.

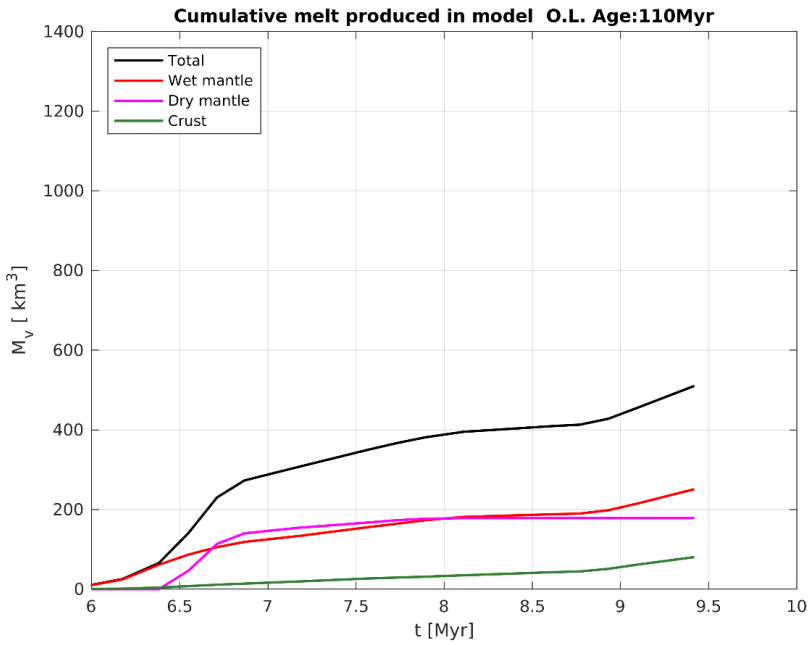

Figure 3.108: Result of the Experiment B7 with cumulative sum of discrete volumetric melt extraction rate depending on time.

3.2.15. Experimental set B8

In experimental set B8 , it is imposed that a convergence rate of 8 cm/yr from both side(right and left) of model Oceanic lithosphere age is determined as 120 Ma.Oceanic lithosphere thickness incresed due to modelling process. In models 35 km in thick continental crust , 8 km ocenaic cruscrust and 80 km in thick mantle lithosphere as determined. The rheologies determined as wet quartzite in contienetal crust (Ranalli, 1995), gabbro/basalt in oceanic crust (Ranalli, 1995) ,wetolivine in mantle lithosphere (Ranalli, 1995) and wetolivine in asthenosphere. Reference densities of continental crust, oceanic crust and mantle lithosphere and asthenosphere is 2700 kg/m3, 3000 kg/m3, 3300 kg/m3 and 3300 kg/m3, respectively.

3.2.16. Results of B8

After 12.10 m.y the intensity of the convection currents in the mantle is high and upward. Dry melt production migrated to the trench side and concentrated in a high area. Wet melt production is less than that of dry melt production and has spread (Figure 3.109). After 6.81 m.y. melt production is concentrated in two different regions. One of them is in the trench side and the other is in the back arc side (Figure 3.110). After 7.34 m.y. wet and prunes production is concentrated in the same region. The intensity of convection currents in the mantle is lowv(Figure 3.111).

In the final stage of the model is after 9.09 m.y. subduction slab is break off at ~200 km depth. The intensity of the convection currents in the mantle is high and downward. No melt production is observed (Figure 3.112).

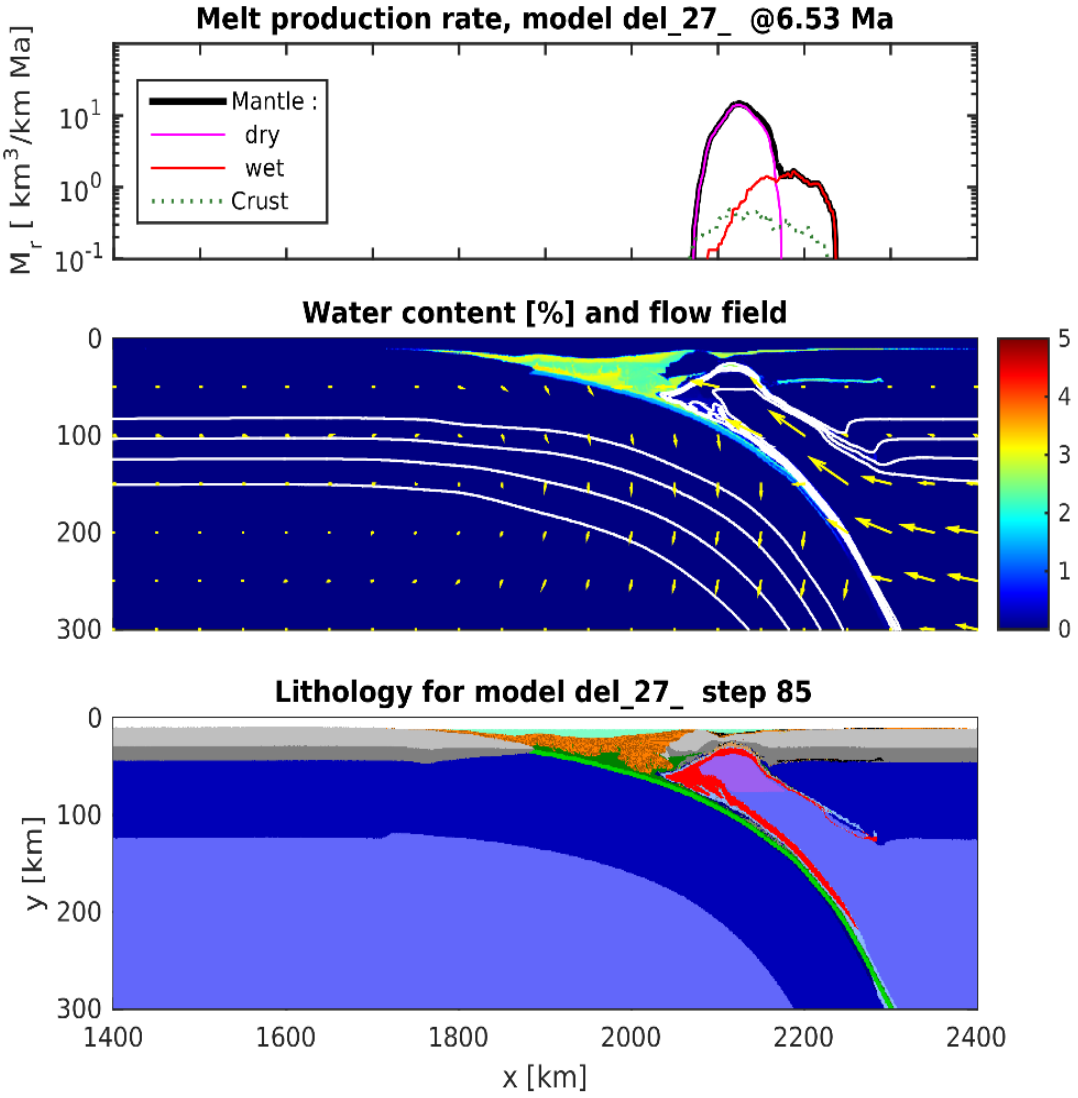

Figure 3.109 The results of the Experiment B8, show *melt production graph* (top), *water content with percentage* (middle), and *lithology graph* (bottom) at 6.53 Myr.

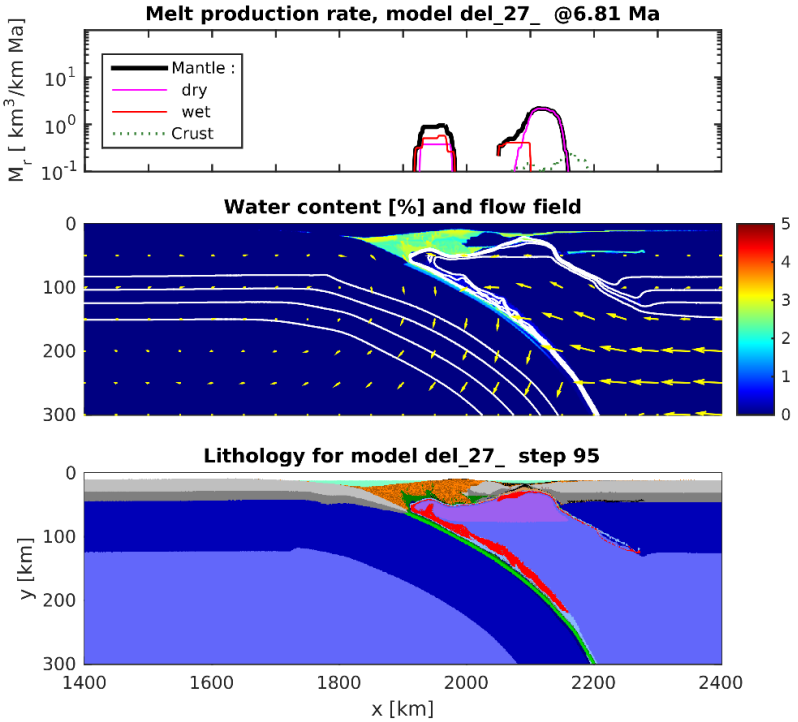

Figure 3.110: The results of the Experiment B8, show *melt production graph* (top), *water content with percentage* (middle), and *lithology graph* (bottom) at 6.81 Myr.

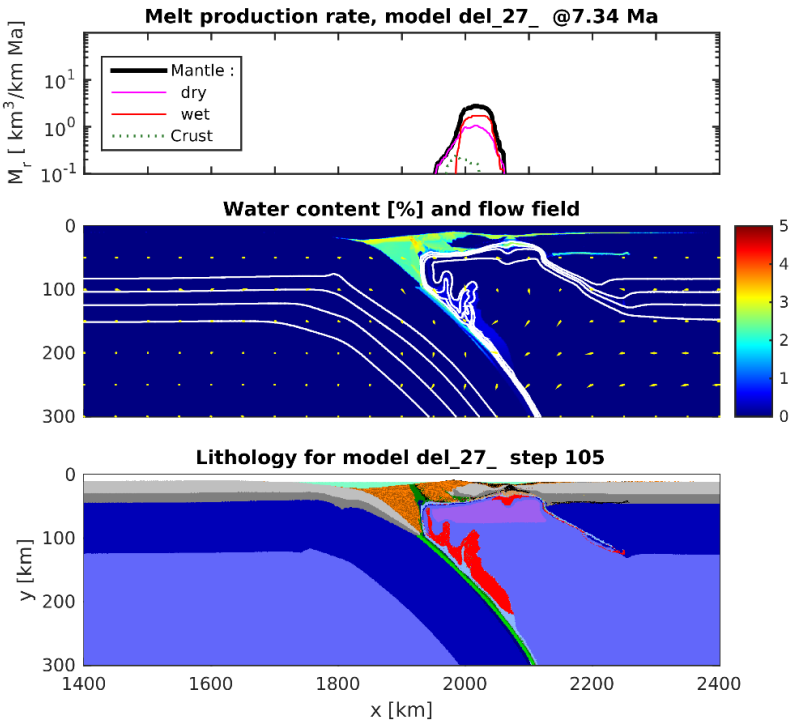

Figure 3.111: The results of the Experiment B8, show *melt production graph* (top), *water content with percentage* (middle), and *lithology graph* (bottom) at 7.34 Myr.

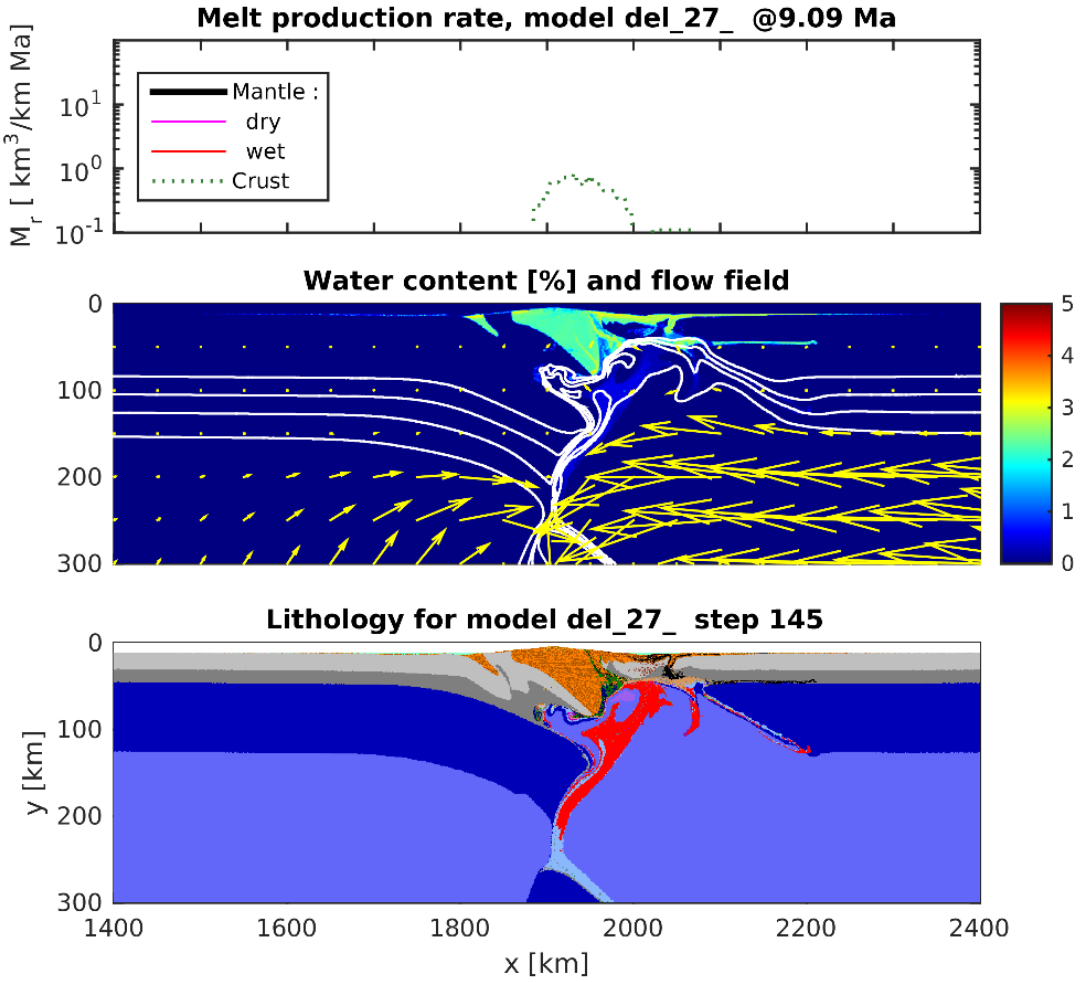

Figure 3.112: The results of the Experiment B8, show *melt production graph* (top), *water content with percentage* (middle), and *lithology graph* (bottom) at 9.09 Myr.

In the melt extraction graphs, the models show a three-peak attitude. This behavior has a direct relationship to the movement of subduction slab. The withdrawal of the slab 6.5 million years after the start of the model rapidly changes the dynamics in the mantle and causes a serious increase in melt production. This increase is supported by changes in mantle convection movements. Wet melt extraction is represented with red color and it takes ~250 km^3 maximum melt extraction value. Dry melt extraction is represented with purple color and it takes ~700 km^3 maximum melt extraction value. Crustal deformation extraction is represented with green color and it takes ~100 km^3 maximum melt extraction value. Total melt extraction is represented with black color and it takes ~900 km^3 maximum melt extraction value. The graph, in which each is represented on top of each other, shows the direct relationship between each other

In the total melt production graphs of this model, the first jump value is higher than the second and the third jump value (Figure 3.113).

The sudden jumps in the graph showing the cumulative sum based on time represent the sudden dynamic changes made by the subduction slab. These changes correspond to ~ 6.5 and ~ 7.25 million years for the model. Subduction slab is break off at 9.09 m.y (Figure 3.114).

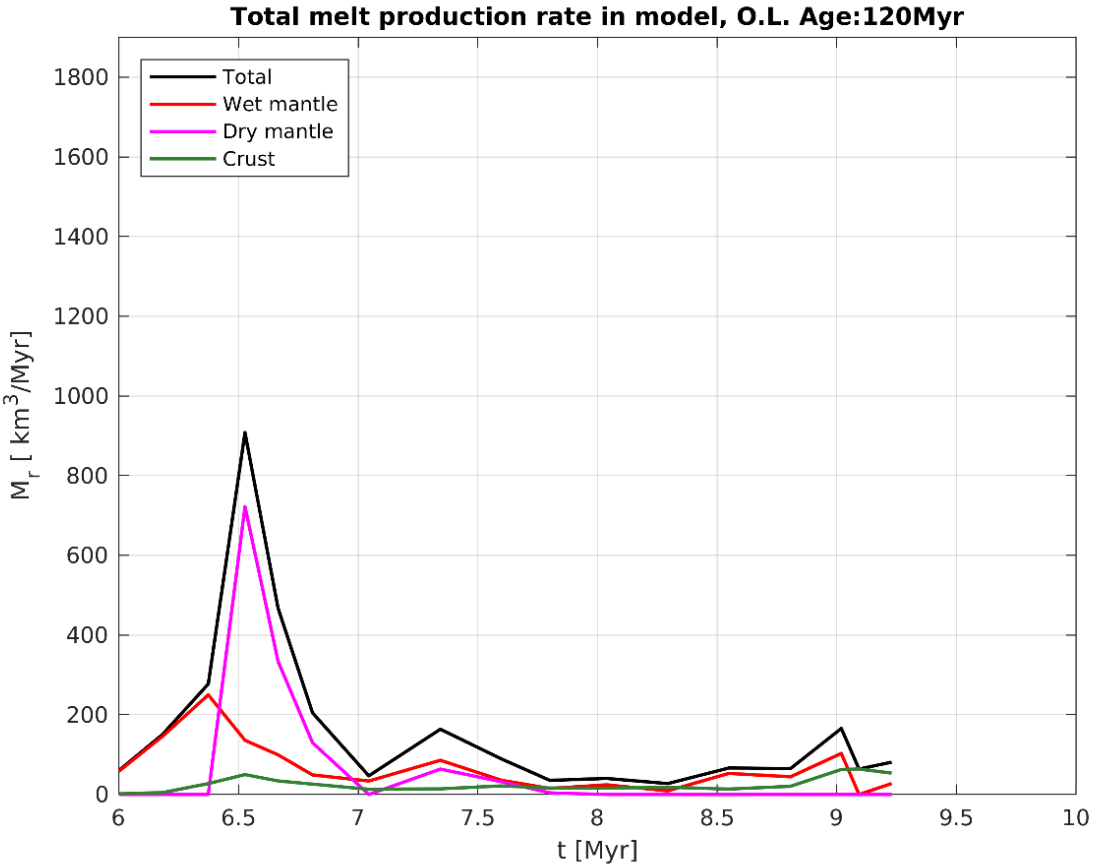

Figure 3.113: Result of the Experiment B8 with discrete volumetric melt production rate depending on time.

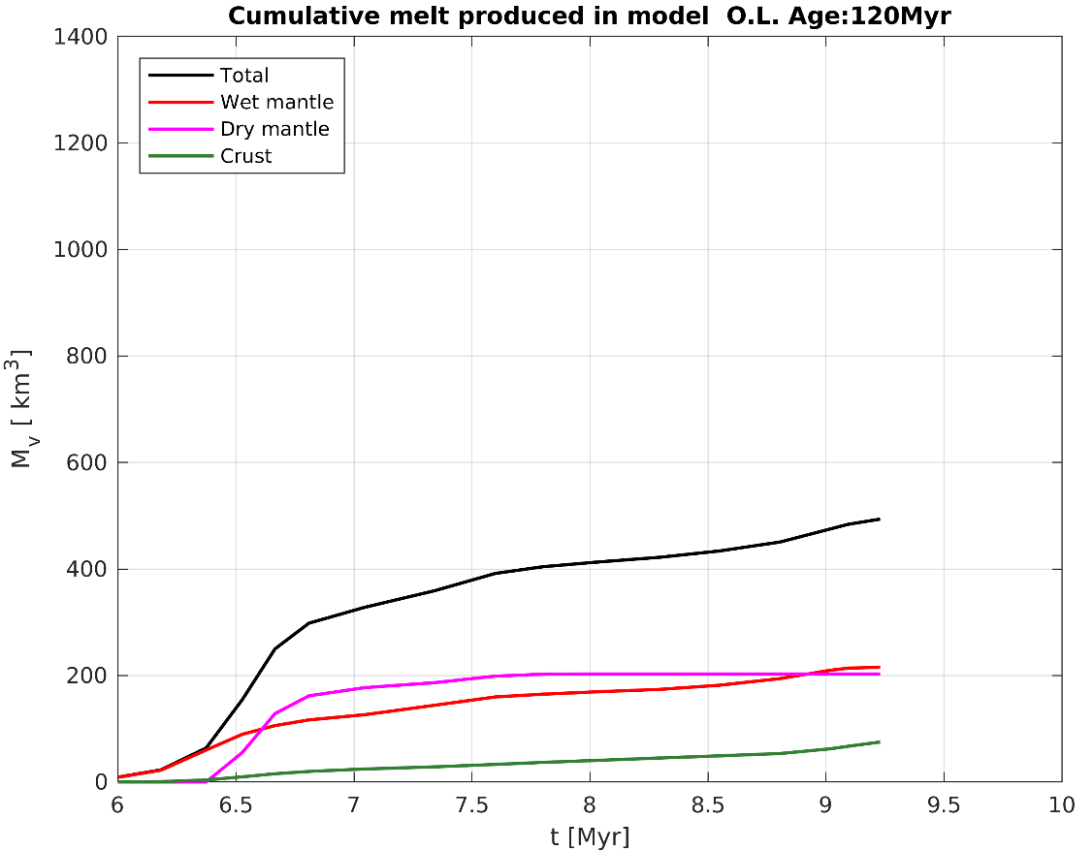

Figure 3.114: Result of the Experiment B8 with cumulative sum of discrete volumetric melt extraction rate depending on time.

3.3. Comparison of Experiments

In Experiment A3, Experiment A4, Experiment A5, Experiment A6, Experiment A7 and Experiment A8, subduction slab break off phenomena is observed. Melt extraction rates of these experiments have major peak before the break off and melting ends after the break off in ~1Ma time period. Results of Experiment A1 and Experiment A2 are correlating with subduction flat structure at ~660 km (see Table 3.2).

It is clear that there is a similarity between slab angles and melt generation graph. In all experiments, it is observed that when the slab angle increases at 11-12 Ma model time, it triggers melt generation. Before the Fourth phase, break off triggers melt generations and melt generation significantly decreases with break off. Melt generation of first time at Experiments are defined at Table 3.3.

Table 3.2: Slab Break off table.

Experiment Number	Oceanic Mantle Lithosphere Age (Ma)	Convergent Rate (cm/yr)	Slab Break off/ Slab Peel off	Slab Break off/Slab Peel off time (Ma)
A1	50	4	Slab Peel off	-
A2	60	4	Slab Peel off	-
A3	70	4	Slab Break off	14.31
A4	80	4	Slab Break off	13.95
A5	90	4	Slab Break off	14.09
A6	100	4	Slab Break off	13.94
A7	110	4	Slab Break off	14.21
A8	120	4	Slab Break off	14.09
B1	50	8	Slab Peel off	-
B2	60	8	Slab Peel off	-
B3	70	8	Slab Peel off	-
B4	80	8	Slab Peel off	-
B5	90	8	Slab Peel off	-
B6	100	8	Slab Peel off	-
B7	110	8	Slab Peel off	-
B8	120	8	Slab Break off	9.09

Table 3.3: First melt production time table

Experiment Number	Oceanic Mantle Lithosphere Age (Ma)	Fist Wet Melt Production Time; Volume [Ma]; [km^3]	Fist Wet melt Production Time;Volume [Ma]; [km^3]	Fist Crustal deformation Production Time; Volume [Ma]; [km^3]
A1	50	11,125; 2.786	11.779; 236.92	10.818; 0.487
A2	60	11.103; 0.528	11.697; 126.08	11.193; 0.699
A3	70	11.128; 4.789	11.644; 88.894	10.904; 0.472
A4	80	11.199; 20.802	11.612;122.680	10.792; 0.459
A5	90	11.010; 0.531	11.627; 211.320	10.852; 0.624
A6	100	11.466; 24.326	11.859; 85.716	11.068; 1.021
A7	110	11.122; 20.41	11.642; 316.77	10.65; 0.641
A8	120	11.343; 16.135	11.689; 80.823	10.928;1.303

4. OBSERVATIONS AGAINST THE MODEL RESULTS

Subduction mechanism is examined with various Earth science branches. In that case, models are comparable with global scale analysis, including geophysical and geological disciplines. Global distribution of oceanic lithosphere age is shown at (Figure 4.1).

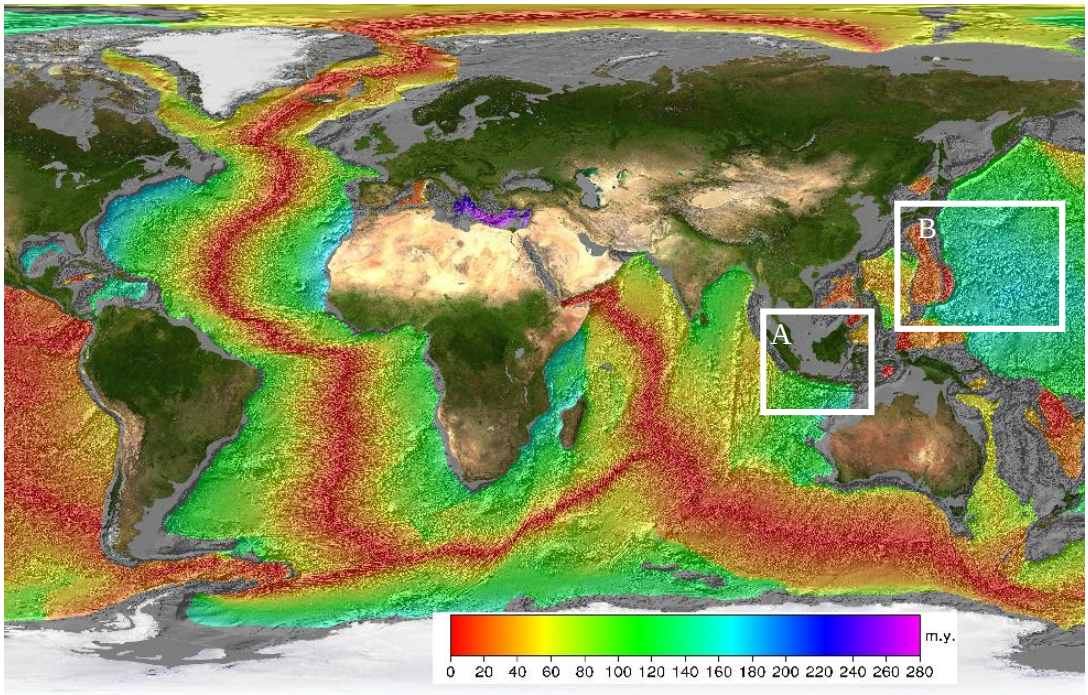

Figure 4.1: Oceanic lithosphere age distribution. Rectangular region representing rapid changing of oceanic lithosphere age at one subduction system. Region (A) is Sunda arc. Region (B) is Japan subduction (simply modified after Müller, Sdrolias, Gaina, & Roest, 2008) .

Subduction initiates by sinking of denser oceanic lithosphere along where two tectonic plates meet, which is called “tectonic boundary”. Due to plate motion curved trench axis and ridge (Kyushu basin ridge at Sunda arc and Wharton ridge at South of Japan arc) occurrence vertically placed at subduction axis. Spreading of the oceanic lithosphere differentiates the subducted lithosphere age.

4.1. Comparisons and Correlations for Sunda Arc

Sunda publication, one of the most active and complex subduction zones in the world, is compared with the models. In making these comparisons, the volcanic structure of the Sunda region and the solutions produced in the models were taken into consideration.

4.1.1. Tectonic setting of Sumatra and Java subduction system

The Sunda Arc is stretched by NW directed forces. This region includes Sumatra and Java, where Indo-Australian Plate has subducted beneath Eurasia plate (Pacey, Macpherson, & McCaffrey, 2013) . It has been suggested that the collision of Indian plate and Eurasia has been changed its direction around 55 Ma and then Sunda arc has become into a curvy shape as today (Aitchison, Ali, & Davis, 2008).

Convergent rate of Subduction zone is changed between -20cm/yr to 45 cm/yr, Oceanic lithosphere age is changed 10Ma -130 Ma until 80 Ma to recent time (Whittaker, Müller, Sdrolias, & Heine, 2007) .

Differences in oceanic lithosphere age and convergent rate are related with Wharton ridge. In terms of subducting, plate of Sumatra and Java part of Sunda system show difference at oceanic lithosphere age. Wharton Ridge has been subducting underneath Sumatra over the period 15 – 0 Ma (Whittaker et al., 2007) . During this period various aged oceanic lithosphere subducted under Sumatra and Java part of the Sunda system.

Eocene *(56 – 34 Ma)* initiation of the present day back arc basins took place along N-S trending rifts (Wharton ridge), strongly oblique to the NW-SE part of the margin.

These heterogenic tectonic setting effects on chemical distribution of magmatism and feature of subduction are represented at (Table 4.1).

Modern Sunda Arc volcanoes developed during the Quaternary *(2.58 – 0.012 Ma)*. Volcanos of Indonesia are part of the Sunda arc, a 3,000-km-long line of volcanoes extending from northern Sumatra to the Banda Sea. Quaternary volcanism in Java has mainly generated basaltic andesite to andesite effusive and explosive products. (Whitford, 1975) .

4.1.2. Comparison with Sunda Arc

At N-W part of the Java Island, two volcanos are located. They are namely Salak (Calc-alkaline) and Guntur (tholeiitic) volcanic province (Whitford, 1975). Location of the provinces are represented (see Figure 4.2). Relation between oceanic lithosphere and subduction break off is considerably linked.

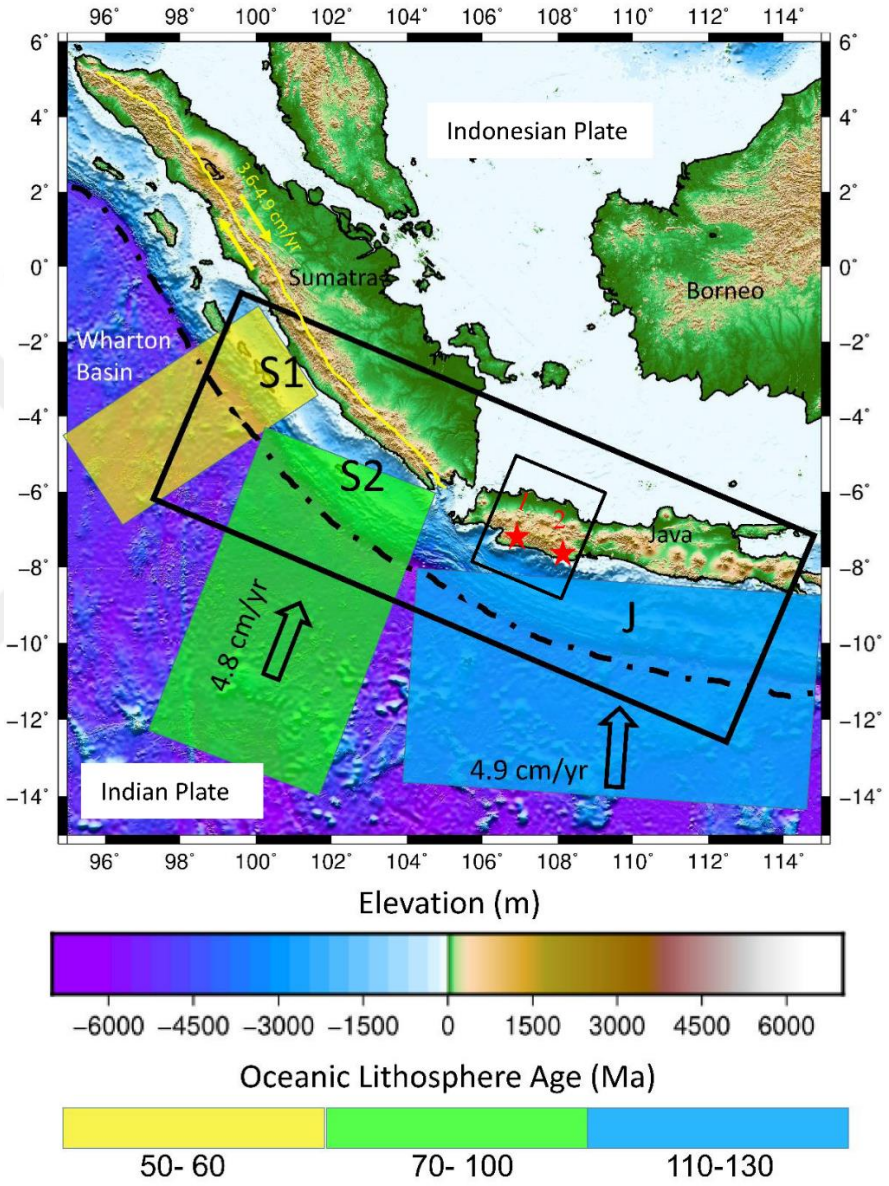

Figure 4.2: Map of Sumatra- Java subduction system. Dash line is trench profile. Arrows representing convergent rate of subducting trench (Artemieva, Thybo, & Shulgin, 2016). Yellow, green and blue area is representing oceanic lithosphere age distribution (modified after Müller et al., 2008) .Yellow line is representing right lateral strike slip fault with 3.6-4.9 cm/yr plate motion(Genrich & Stevens, 2000). Volcanic provinces are representing by stars; 1: Salak volcanic province (Calc-alkaline) ad 2: Guntur volcanic province (Tholeiitic).

Table 4.1: Table of geochemistry of Sunda arc modified after Whitford, 1975.

Volcano name	Islan arc Thoeliites	Calc-alkaline	Hig –K Alkaline	Rhyolitic Ignimbrite
Krakatau	+	+		
Tjikurai	+			
Da1unggung	+			
Guntur	+			
Papandajan		+		
Salak		+		
Danau complex		+		
Merapi		+		
Agung		+		
Seraja		+		
Rindjani		+		
Tangkuban Prahu		+		
Semeru		+		
Sangeang Api		+		
Kelud		+		
Kawah Idjen		+		
Tjerimai		+		
Slamet		+		
Merapi		+		
Lamongan		+		
Sumbing		+		
Merbabu		+		
Lawu		+		
Bramo		+		
Sundoro		+		
Dieng Complex		+		
Ungaran		+		
Muriah			+	
Lake Toba				+

Salak province is located at 6.8S, 107.0E and 2, 958m elevation. Salak province have Calc-alkaline chemical composition (Whitford, 1975). Salak Province is located around 250 km far from trench. Last time was erupted at 1948.

Guntur is located on the same line and far away from around 1280 km from Salak province and 260 km far away from trench. Last time was erupted at 1840.

Calc-alkaline and tholeiitic magmatism in the same province and the same distance from trench is correlating with our models

Seismic profile at (Figure 4.3) is observed at middle part of the Sumatra trench which has 50 Ma year old oceanic lithosphere subduction slab. Output of Experiment A1 (Figure 4.4) is correlating with seismic profile. They are correlating with accretionary prism width (200km) and melt production time (12.37 Ma). At the melt production graph, it is correlating with the order of melt production; wet melt (alkaline) near the trench, mix melt (alkaline, Calc-alkaline) at middle of volcanic arc and wet (alkaline) melt at back arc. It is also consistent with surface features S1 from Figure 4.2 by parallel with convergence axis such as; trench axis, volcanics islands, coast side and major volcanic front.

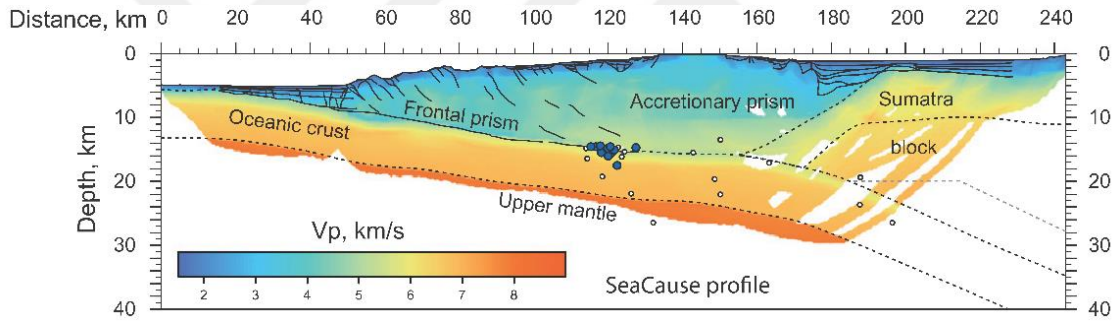

Figure 4.3: Marine seismic profile from middle part of Sumatra trench (Shulgin et al., 2013) .

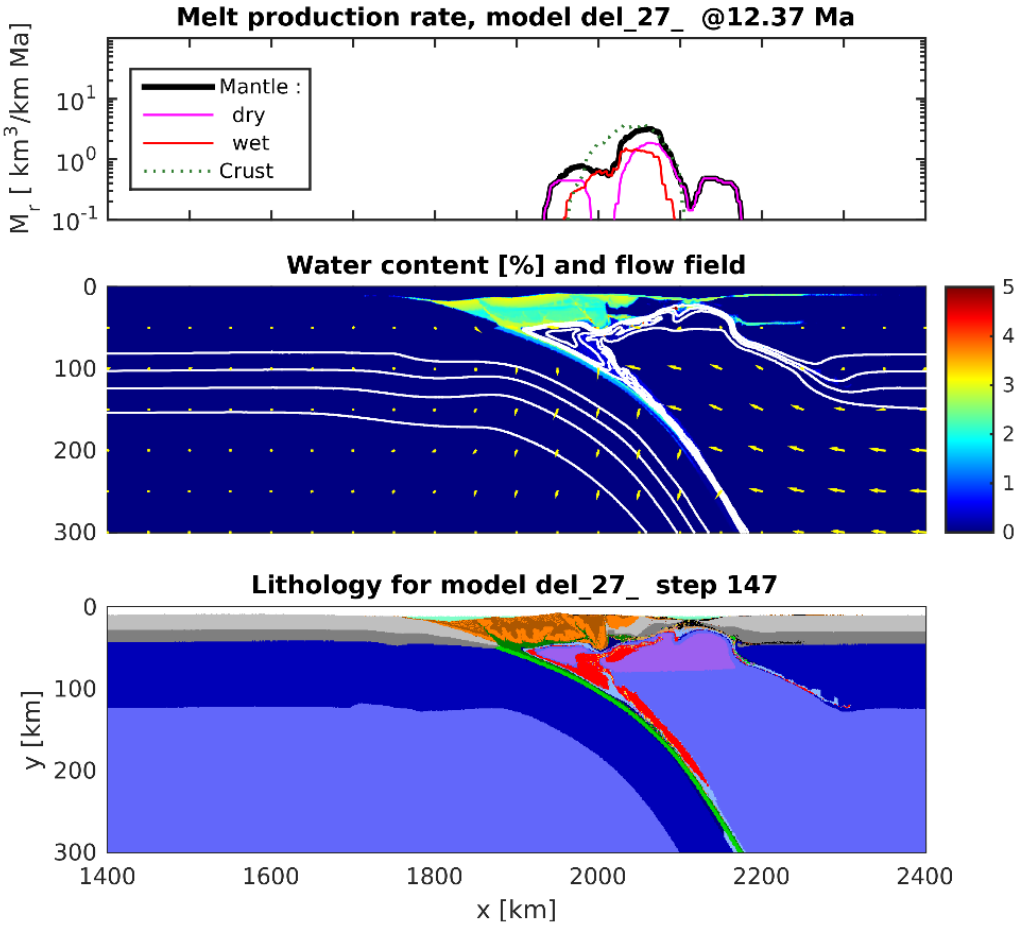

Figure 4.4: The results of the Experiment 1, show the geodynamic evolution of subduction and its *melt production graph* (top), *water content with percentage* (middle) scaled with colorbar, yellow arrows represents convection current flow and solid white lines illustrates thermal gradients from 700 to 1500 ºC with 200 ºC increment, and *lithology graph* (bottom) in 12.37 Myr.

4.2. Comparisons and Correlations for Japan Arc

Japan's Ryuku region and North West region, which have complex volcanic evolution, are compared with models. This comparison is based on tectonic evolution.

4.2.1. Tectonic setting of Japan subduction system

Tectonic evolution of Japan is dominated by subducting the Pacific Ocean beneath the Eurasian plate. Southern part of the Japan subduction has more complex structure with retreating slab. Retreating slab initiates a second order subduction system at back-arc basin region such as in Ruyuku subduction zone (Figure 4.5).

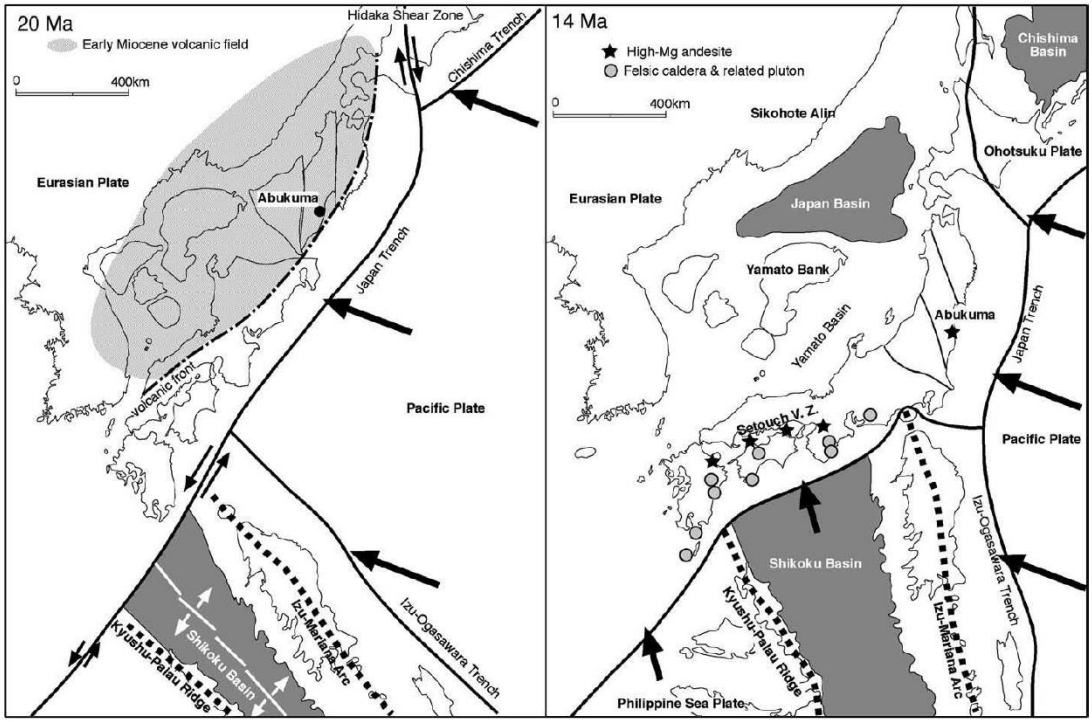

Figure 4.5: Tectonic evaluation around the Japan islands between Early to Middle Miocene *(~23 – ~5.3 Ma)* (Yamamoto & Hoang, 2009).

At NE part of the Japan, by analyzing the data about paleo-trench locations, it has been proposed that the location of the trench changes within the time. (Figure 4.6). According to Tatsumi, Otofuji, Matsuda, & Nohda (1989), alkaline volcanism has related with back arc opening and asthenospheric injection. High magnesium-alkaline magmas with a subduction related trace element signature are producing in low volatiles and low pressure condition at mantle wedge which is triggered unusual mantle flow from possible slab tear beneath the Japan trench (Kohut et al., 2006).

Western part of the pacific plate is subducting with 8 cm/yr convergent rate (Acocella, 2007). NE Japan has been occurred by arc magmatism, with a trench-parallel chemical chain volcanos, in the last 13 My (Yoshida et al., 2013) . Magmatic evolution is divided into 3 main phases; oceanic island chain with submarine basaltic to rhyolitic volcanism *(13–8 Ma)*, Late Miocene to Pliocene caldera-forming phase from *~8 to ~1.7 Ma* with a decrease in activity between *5 and 4 Ma*, and andesite stratovolcano arc *(1.7–0 Ma)* (Sato & Amano, 1991) . The onset of Calc-alkaline andesite volcanism in NE Japan occurred between *~1.7 Ma and 1 Ma* (Acocella, Yoshida, Yamada, & Funiciello, 2008). Major tectonic evolution and magmatism relations are defined in (Figure 4.7 and Figure 4.8).

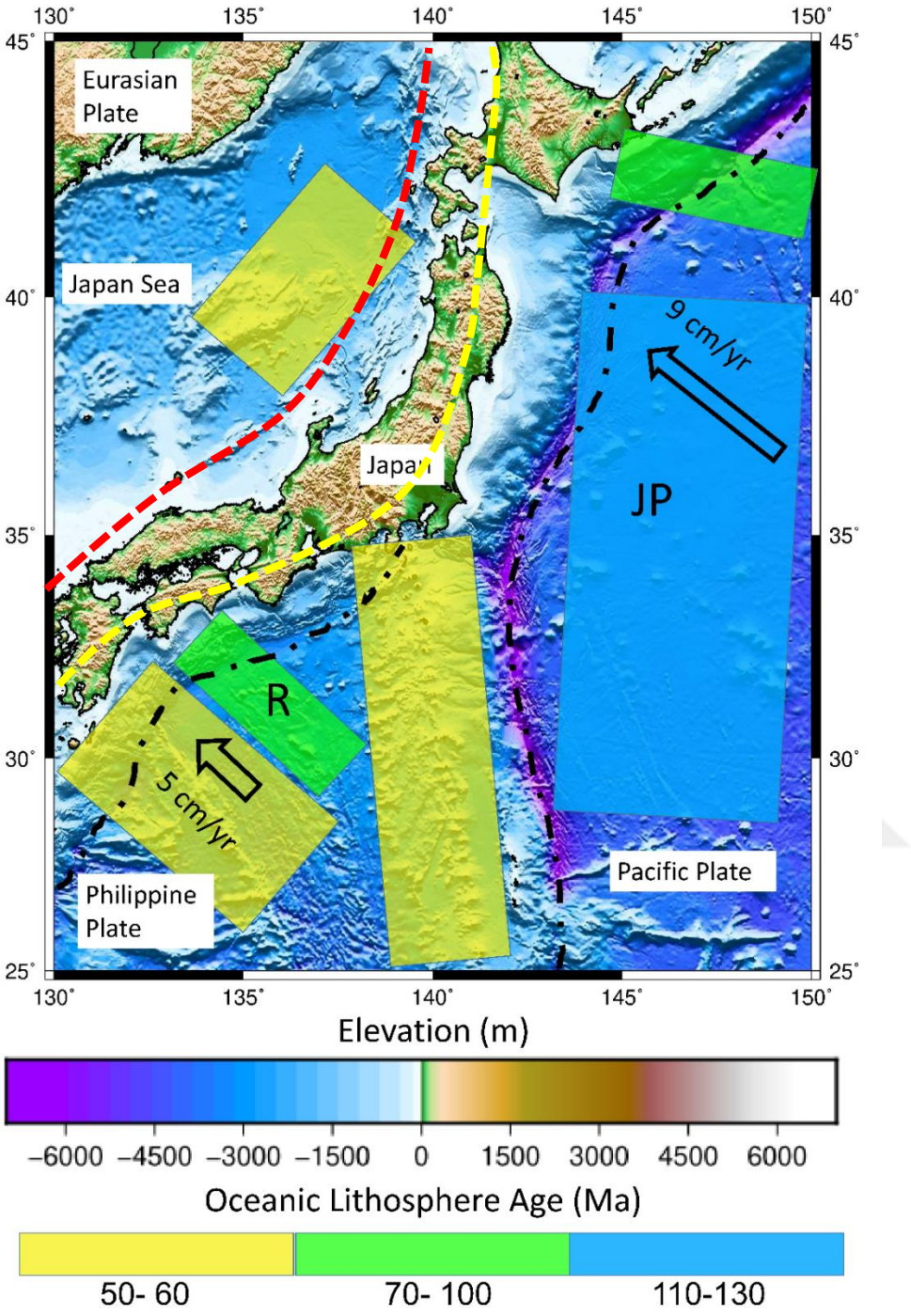

Figure 4.6: Trench velocity and oceanic lithosphere age distribution of the western Pacific, showing the subducting slab Map of Japan subduction system. Dash line is trench profile. Arrows representing convergent rate of subducting trench (Artemieva, Thybo, & Shulgin, 2016). Yellow, green and blue area is representing oceanic lithosphere age distribution (Müller et al., 2008) , (modified after Faccenna, Holt, Becker, Lallemand, & Royden, 2018).Red dashed line represents Neogene volcanic front and yellow dached line represents Quaternary volcanic front.

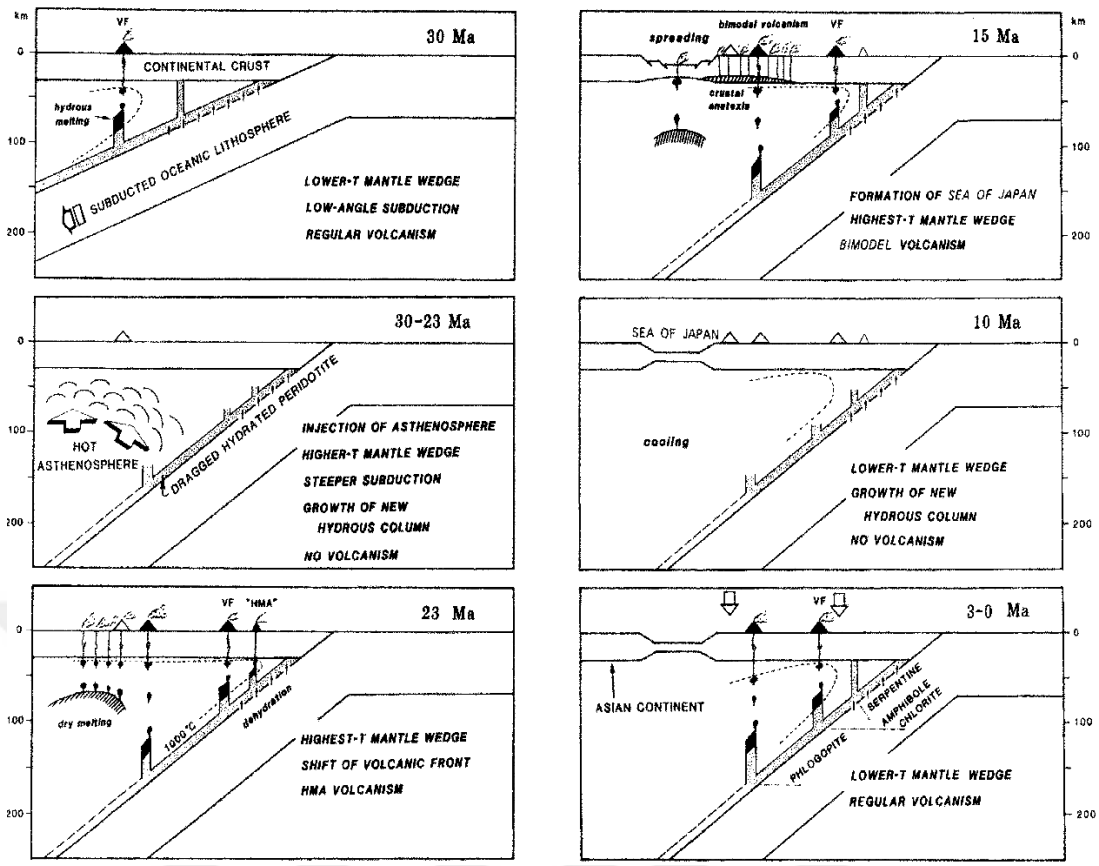

Figure 4.7: Tectonic evolution and magmatism differences at North East Japan. Broken lines are representing indicated 100C isotherm (solidus temperature of wet peridotite) HMA and VF represents normal volcanic front and uncommon near trench volcanic of high magnesian andesites, respectively. The back arc basin occurred during 20-14 Ma with hot asthenospheric injection into mantle wedge during the 30-23 Ma. (Tatsumi et al., 1989) .

The volcanism test set, B6-B7-B8, has developed gradually over the last 25 million years, as mentioned in the drawings, which briefly summarize the tectonic evolution of northwest Japan and describe the dry melts produced in the mantle wedge (see Figure 4.7). The development of dry melts triggered by the upward movement of the hot asthenosphere by convection currents in the mantle following the development of wet melt-induced volcanism at the beginning of the subduction is the development process based on tectonic evolution in Japan (Figure 4.8).

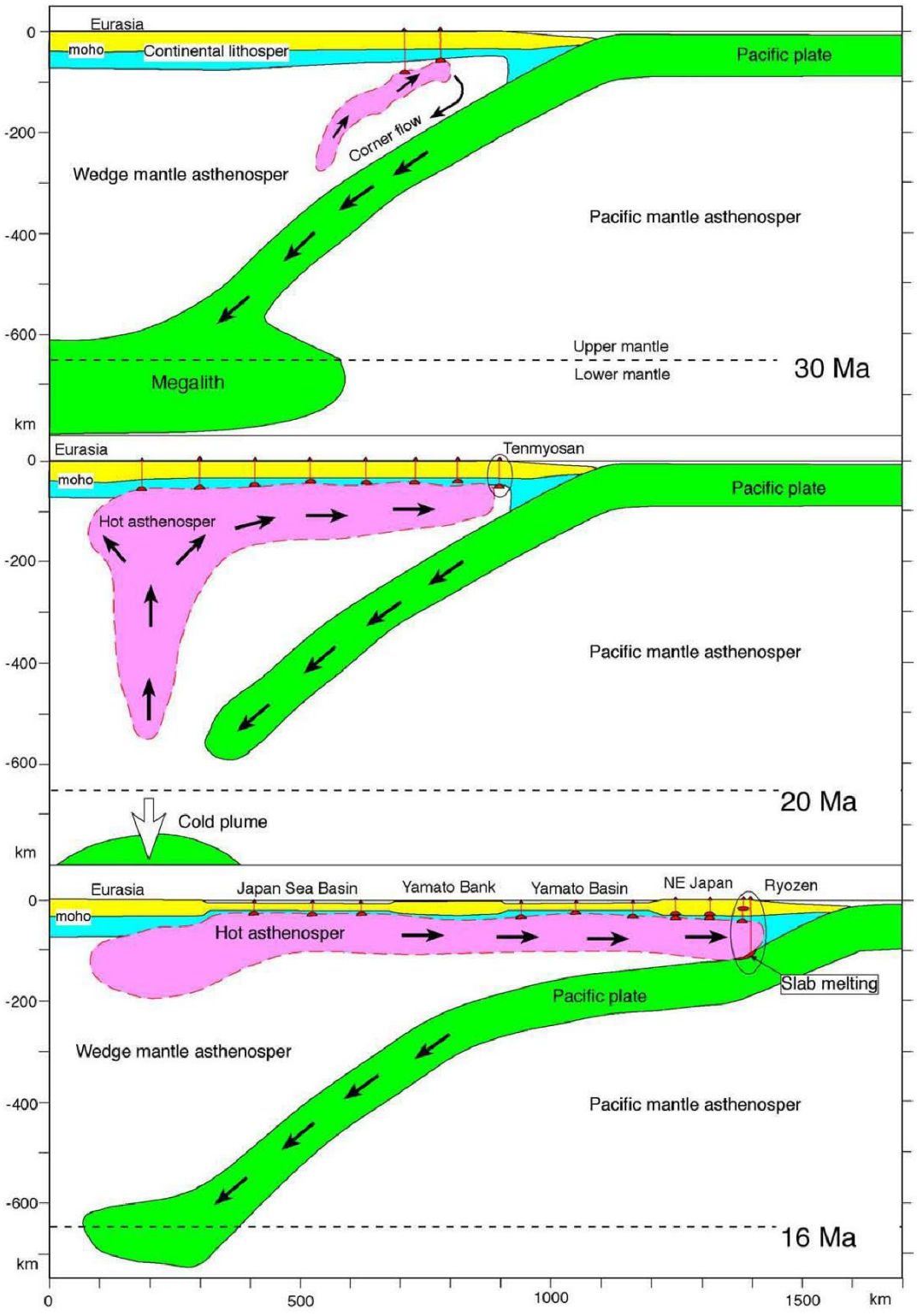

Figure 4.8: Illustration of the Japan subduction evolution (Yamato, Burov, Agard, Le Pourhiet, & Jolivet, 2008).

4.2.2. Comparison with northeast part of the Japan Arc

The models are similar in nature to the tectonic evolution of Japan. It is mentioned mechanisms (Figure 4.8), the models contribute to the interpretation of the source of melts in the mantle wedge.

Back arc spreading time and subducted slab age correlating with our model (Figure 4.9) which is represented below. Corner of the mantle wedge generated High Mg andesites and normal volcanic front and wet melt at back arc with thin lithosphere is correlating with 23 Ma phase of suggested models at (Figure 4.7) (Tatsumi et al., 1989)

.

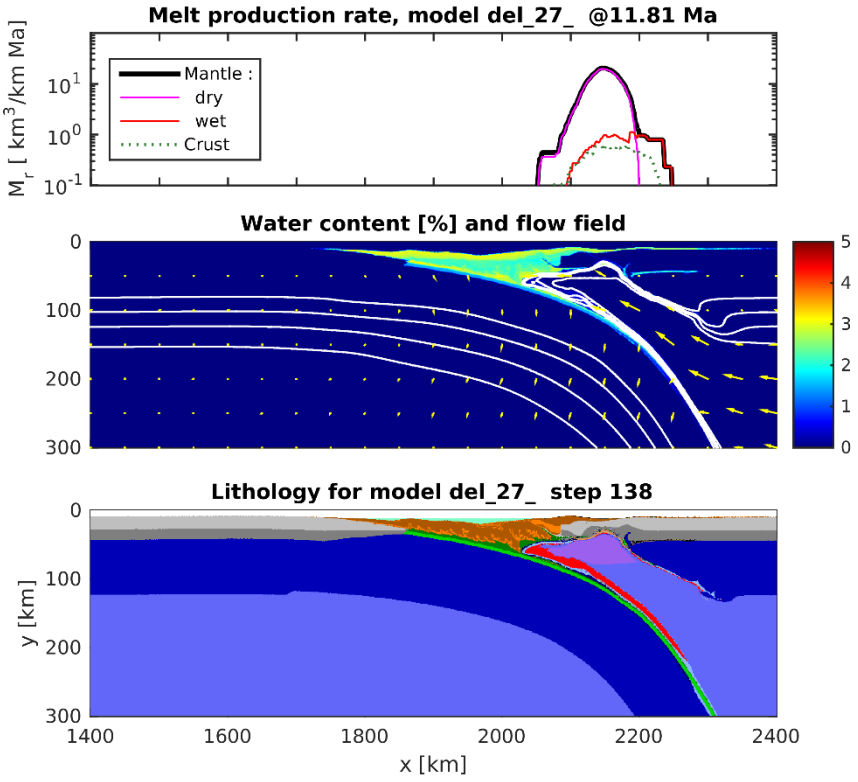

Figure 4.9: The results of the Experiment 8, show the geodynamic evolution of subduction and its *melt production graph* (top), *water content with percentage* (middle) scaled with colorbar, yellow arrows represents convection current flow and solid white lines illustrates thermal gradients from 700 to 1500 ºC with 200 ºC increment, and *lithology graph* (bottom) in 13.64 Myr.

5. CONCLUSION

To sum up, it is tried to clarify the complex structures (Japan and Sunda subduction regions) which are formed by the oceanic lithosphere ages and approach velocities that change at short distance on the same subduction zone as the experimental set A and B.

Young oceanic age lithosphere models such as shown in Experiment A3, Experiment A4, Experiment A5, Experiment A6, Experiment A7 and Experiment A8, subduction slab break off phenomena is observed. Melt extraction rates of these experiments, has major peak before the break off and melting is end after the break off in ~1Ma time period. Experiment A1 and Experiment A2 result are correlating with subduction flat structure at ~660 km.

If we take the results of experimental set B, which is compatible with the approach velocity of Japan, the experiment presents an approach to the tectonic evolution of northwestern Japan, which has a complex structure in terms of oceanic lithosphere ages of B7 and B8 and the time elapsed from the beginning of the model, and melt production behavior. An approach has been made with the developed models of dry-melts close to trench, whose production mechanism is still controversial.

It is clear that there is a similarity between slab angles and melt generation graph. In all Experiment, it is observed that when the Slab angle increase at 11-12 Ma model time, it triggers melt generation. Before the Fourth phase break off triggers melt generations and melt generation significantly decrease with subduction break off.

In the models, the continental lithosphere at the back of the oceanic lithosphere can be adapted to understand the possible mechanism of the Tamu massif (located at around 1300 km away from trench) in Japan. Possible collision time of massif is 10Myr, considering 9 cm/yr recent convergent rate.

REFERENCES

Acocella, V. (2007). Understanding caldera structure and development: An overview of analogue models compared to natural calderas. *Earth-Science Reviews*, *85*(3–4), 125–160. https://doi.org/10.1016/j.earscirev.2007.08.004

Acocella, V., Yoshida, T., Yamada, R., & Funiciello, F. (2008). Structural control on late Miocene to Quaternary volcanism in the NE Honshu arc, Japan. *Tectonics*, *27*(5), 1–24. https://doi.org/10.1029/2008TC002296

Aitchison, J. C., Ali, J. R., & Davis, A. M. (2008). When and where did India and Asia collide? *Geological Bulletin of China*, *27*(9), 1351–1370. https://doi.org/10.1029/2006JB004706

Artemieva, I. (2011). *The lithosphere An Interdisciplinary Approach*.

Elkins-Tanton, L. T. (2007). Continental magmatism, volatile recycling, and a heterogeneous mantle caused by lithospheric gravitational instabilities. *Journal of Geophysical Research: Solid Earth*, *112*(3), 1–13. https://doi.org/10.1029/2005JB004072

Gerya, T. V., & Meilick, F. I. (2011). Geodynamic regimes of subduction under an active margin: Effects of rheological weakening by fluids and melts. *Journal of Metamorphic Geology*, *29*(1), 7–31. https://doi.org/10.1111/j.1525-1314.2010.00904.x

Gerya, Taras V., & Yuen, D. A. (2003). Rayleigh - Taylor instabilities from hydration and melting propel "cold plumes" at subduction zones. *Earth and Planetary Science Letters*, *212*(1–2), 47–62. https://doi.org/10.1016/S0012-821X(03)00265-6

Johnson, H. P., & Pruis, M. J. (2003). Fluxes of fluid and heat from the oceanic crustal reservoir. *Earth and Planetary Science Letters*. https://doi.org/10.1016/S0012-821X(03)00545-4

Karato, S. ichiro. (2010). Rheology of the deep upper mantle and its implications for the preservation of the continental roots: A review. *Tectonophysics*, *481*(1–4), 82–98. https://doi.org/10.1016/j.tecto.2009.04.011

Kohut, E. J., Stern, R. J., Kent, A. J. R., Nielsen, R. L., Bloomer, S. H., & Leybourne, M. (2006). Evidence for adiabatic wet melting in the Southern Mariana Arc from high-Mg lavas and melt inclusions. *Contributions to Mineralogy and Petrology*, *152*(2), 201–221. https://doi.org/10.1007/s00410-006-0102-7

Kushiro, I., Syono, Y., & Akimoto, S. (2008). Melting of a peridotite nodule at high pressures and high water pressures. *Journal of Geophysical Research*. https://doi.org/10.1029/jb073i018p06023

Müller, R. D., Sdrolias, M., Gaina, C., & Roest, W. R. (2008). Age, spreading rates, and spreading asymmetry of the world's ocean crust. *Geochemistry, Geophysics, Geosystems*, *9*(4), 1–19. https://doi.org/10.1029/2007GC001743

Pacey, A., Macpherson, C. G., & McCaffrey, K. J. W. (2013). Linear volcanic segments in the central Sunda Arc, Indonesia, identified using Hough Transform analysis: Implications for arc lithosphere control upon volcano distribution. *Earth and Planetary Science Letters*, *369–370*(November 2017), 24–33. https://doi.org/10.1016/j.epsl.2013.02.040

Poli, S., & Schmidt, M. W. (2004). H 2 O transport and release in subduction zones: Experimental constraints on basaltic and andesitic systems . *Journal of Geophysical Research: Solid Earth*. https://doi.org/10.1029/95jb01570

Ranalli, G. (1995). *Rheology of the earth*. Chapman & Hall. Retrieved from https://www.springer.com/gp/book/9780412546709

Sato, H., & Amano, K. (1991). Relationship between tectonics, volcanism, sedimentation and basin development, Late Cenozoic, central part of Northern Honshu, Japan. *Sedimentary Geology*. https://doi.org/10.1016/0037-0738(91)90071-K

Schmidt, M. W., & Poli, S. (1998). Experimentally based water budgets for dehydrating slabs and consequences for arc magma generation. *Earth and Planetary Science Letters*. https://doi.org/10.1016/S0012-821X(98)00142-3

Shulgin, A., Kopp, H., Klaeschen, D., Papenberg, C., Tilmann, F., Flueh, E. R., … Djajadihardja, Y. (2013). Subduction system variability across the segment boundary of the 2004/2005 Sumatra megathrust earthquakes. *Earth and Planetary Science Letters*, *365*, 108–119. https://doi.org/10.1016/j.epsl.2012.12.032

Stern, R. J. (2002). Subduction zones. *Reviews of Geophysics*, *40*(4), 1012. https://doi.org/10.1029/2001RG000108

Stolper, E., & Newman, S. (1994). The role of water in the petrogenesis of Mariana trough magmas. *Earth and Planetary Science Letters*. https://doi.org/10.1016/0012-821X(94)90074-4

Tatsumi, Y., & Eggins, S. (1995). *Subduction zone magmatism*. Blackwell Science. Retrieved from https://www.amazon.com/Subduction-Magmatism-Frontiers-Earth-Sciences/dp/086542361X

Tatsumi, Y., Otofuji, Y. I., Matsuda, T., & Nohda, S. (1989). Opening of the Sea of Japan back-arc basin by asthenospheric injection. *Tectonophysics*, *166*(4), 317–329. https://doi.org/10.1016/0040-1951(89)90283-7

Turcotte, D. (2014). *Geodynamics | Structural Geology Tectonics and Geodynamics |Cambridge University Press*. Retrieved from http://www.cambridge.org/de/academic/subjects/earth-and-environmental-science/structural-geology-tectonics-and-geodynamics/geodynamics-3rd-edition?format=PB&isbn=9780521186230

Ueda, K., Gerya, T. V., & Burg, J. P. (2012). Delamination in collisional orogens: Thermomechanical modeling. *Journal of Geophysical Research: Solid Earth*, *117*(8), 1–25. https://doi.org/10.1029/2012JB009144

Whitford, D. . (1975). Strontium isotopic studies of the volcanic rocks of the Saunda arc, Indonesia, and their petrogenetic implications. *Geochimica at Cosmochimica Acta*, *39*, 321–344.

Whittaker, J. M., Müller, R. D., Sdrolias, M., & Heine, C. (2007). Sunda-Java trench kinematics, slab window formation and overriding plate deformation since the Cretaceous. *Earth and Planetary Science Letters*, *255*(3–4), 445–457. https://doi.org/10.1016/j.epsl.2006.12.031

Yamamoto, T., & Hoang, N. (2009). Synchronous Japan Sea opening Miocene fore-arc volcanism in the Abukuma Mountains, NE Japan: An advancing hot asthenosphere flow versus Pacific slab melting. *Lithos*, *112*(3–4), 575–590. https://doi.org/10.1016/j.lithos.2009.03.044

Yamato, P., Burov, E., Agard, P., Le Pourhiet, L., & Jolivet, L. (2008). HP-UHP exhumation during slow continental subduction: Self-consistent thermodynamically and thermomechanically coupled model with application to the Western Alps. *Earth and Planetary Science Letters*. https://doi.org/10.1016/j.epsl.2008.03.049

Yoshida, T., Kimura, J.-I., Yamada, R., Acocella, V., Sato, H., Zhao, D., … Imaizumi, T. (2013). Evolution of late Cenozoic magmatism and the crust–mantle structure in the NE Japan Arc. *Geological Society, London, Special Publications*. https://doi.org/10.1144/sp385.15

APPENDICES

Appendix A: Results of Experiment A1; second strain rate invariant, full domain material field, density field, temperature field and viscosity field, respectively.

Appendix B: Results of Experiment A2; second strain rate invariant, full domain material field, density field, temperature field and viscosity field, respectively.

Appendix C: Results of Experiment A3; second strain rate invariant, full domain material field, density field, temperature field and viscosity field, respectively.

Appendix D: Results of Experiment A4; second strain rate invariant, full domain material field, density field, temperature field and viscosity field, respectively.

Appendix E: Results of Experiment A5; second strain rate invariant, full domain material field, density field, temperature field and viscosity field, respectively.

Appendix F: Results of Experiment A6; second strain rate invariant, full domain material field, density field, temperature field and viscosity field, respectively.

Appendix G: Results of Experiment A7; second strain rate invariant, full domain material field, density field, temperature field and viscosity field, respectively.

Appendix H: Results of Experiment A8; second strain rate invariant, full domain material field, density field, temperature field and viscosity field, respectively.

Appendix I: Rheological and thermal properties of modeled rock materials.

Appendix A

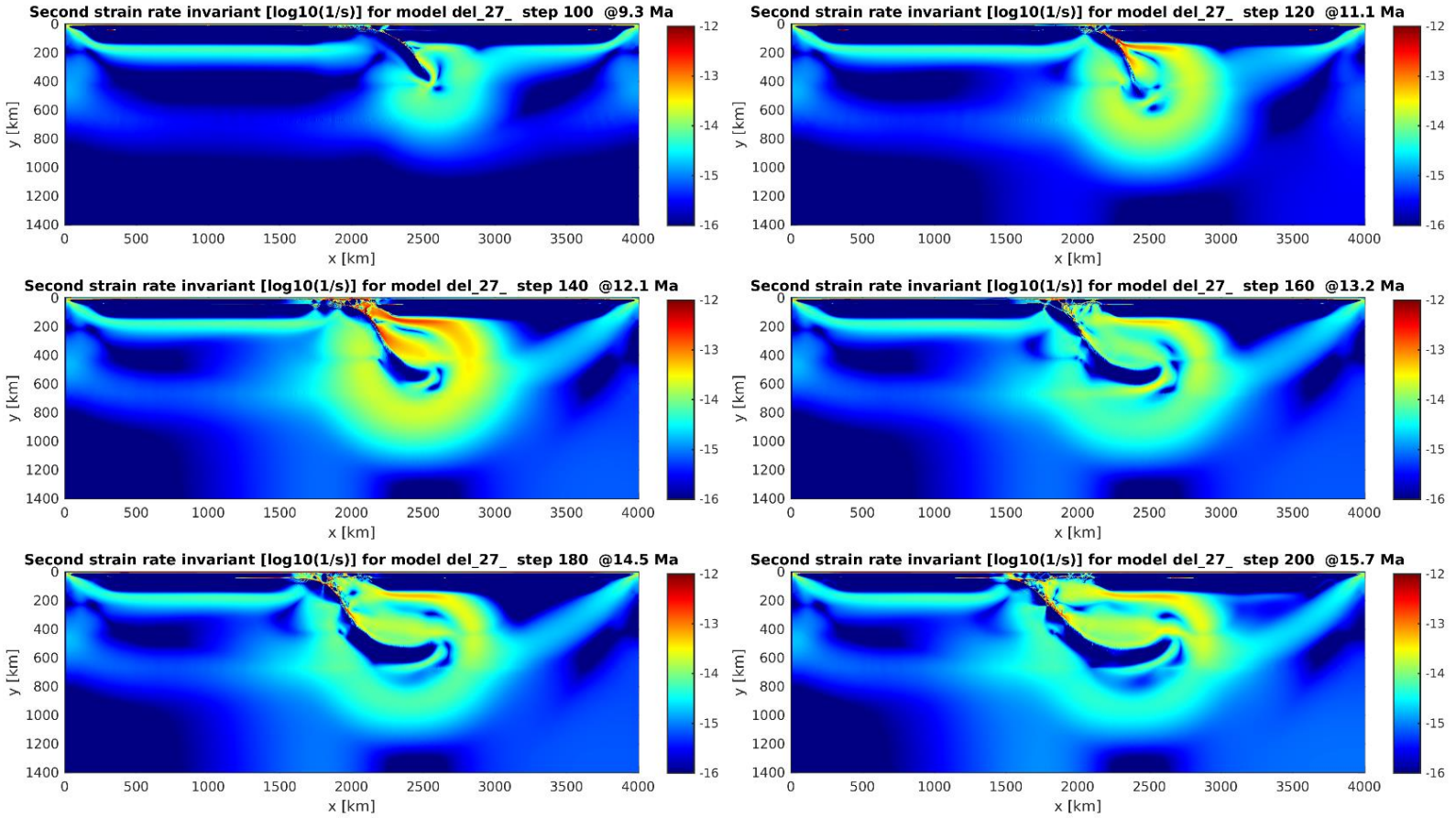

Figure A.1: Results of second strain rate invariants with x axis (km), y axis time (km) and second strain rate invariant (color bar.)

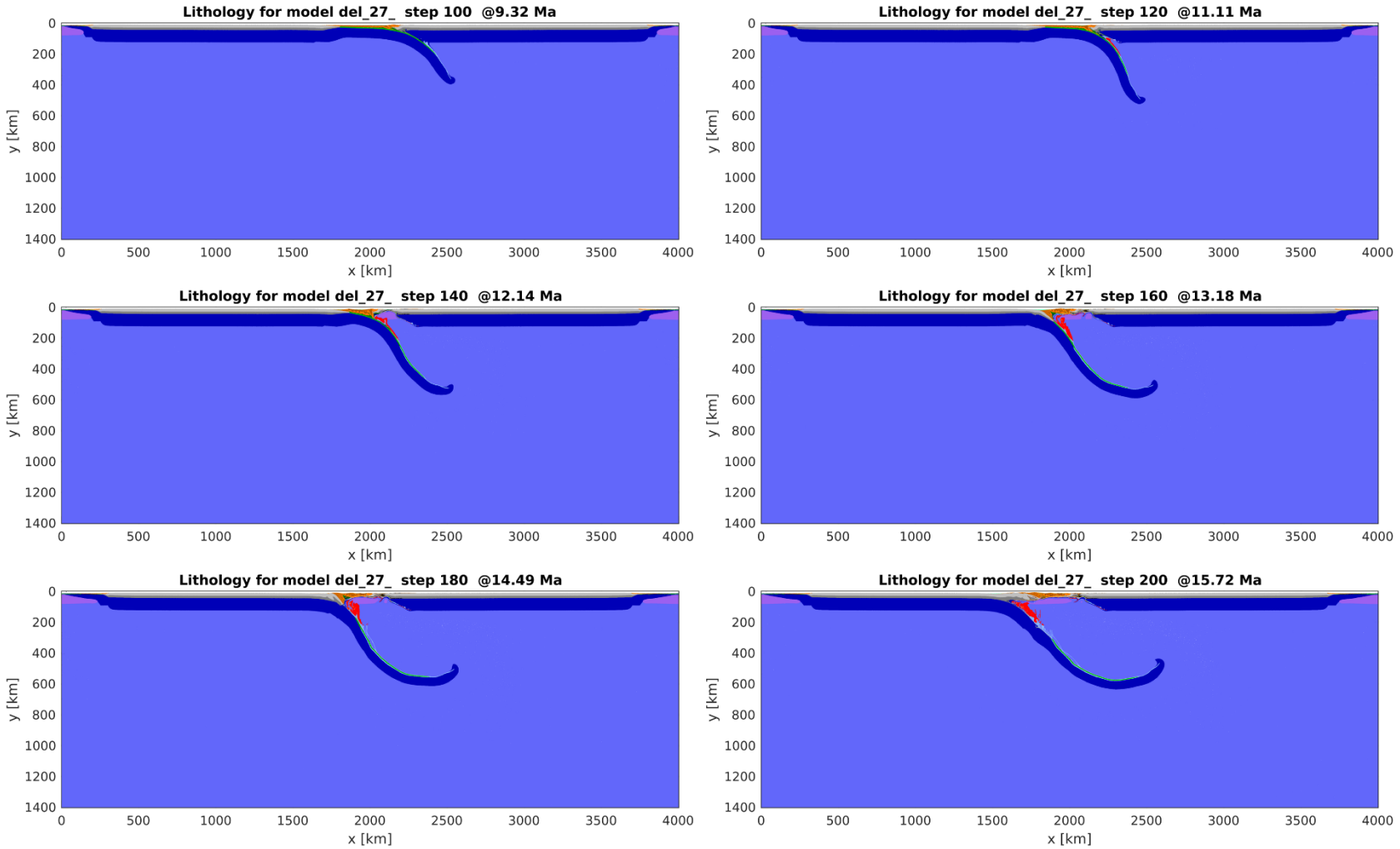

Figure A.2: Results of full domain material field with x axis (km), y axis time (km).

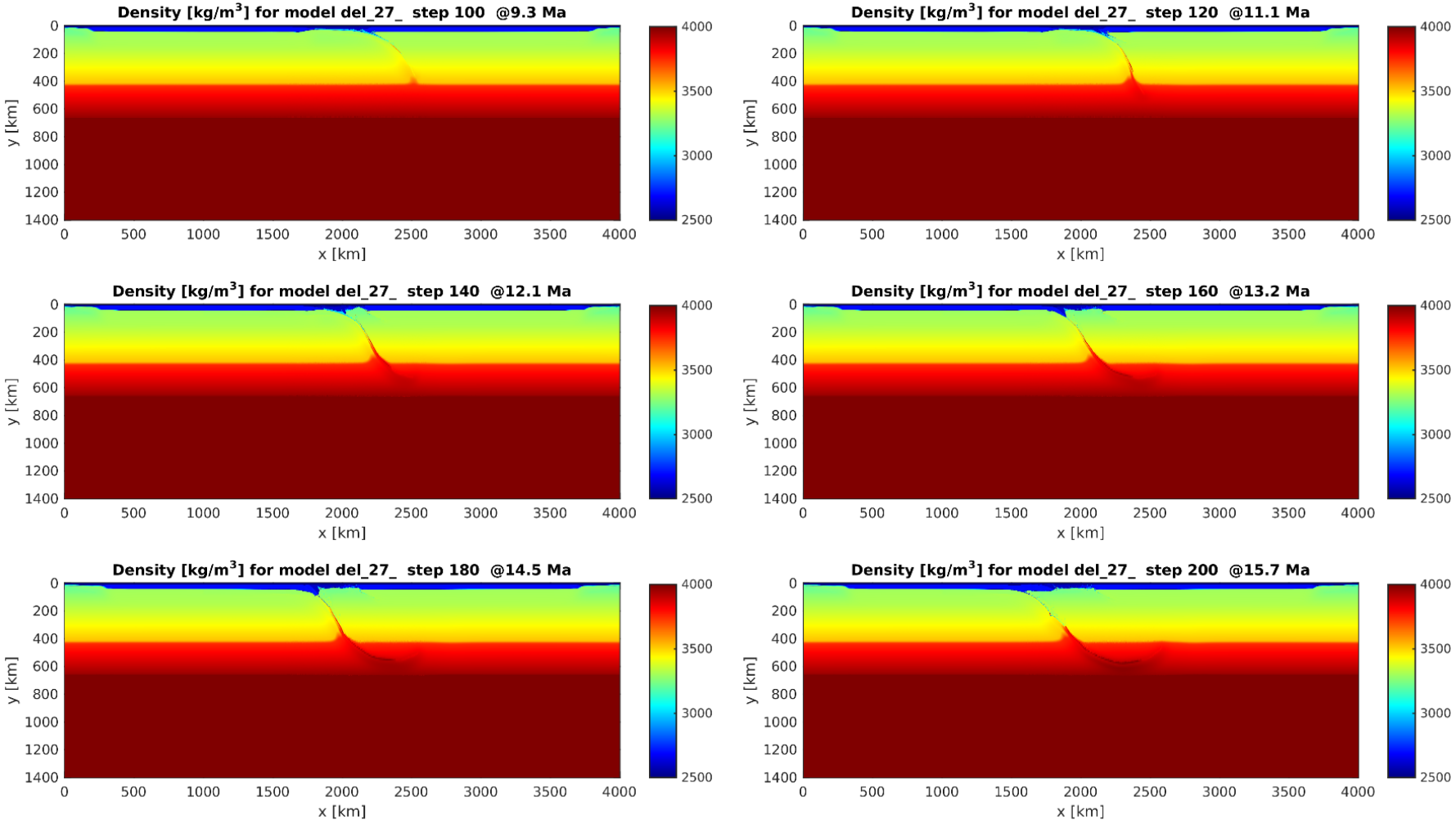

Figure A.3: Results of density field with x axis (km), y axis time (km) and density values are defined at color bar.

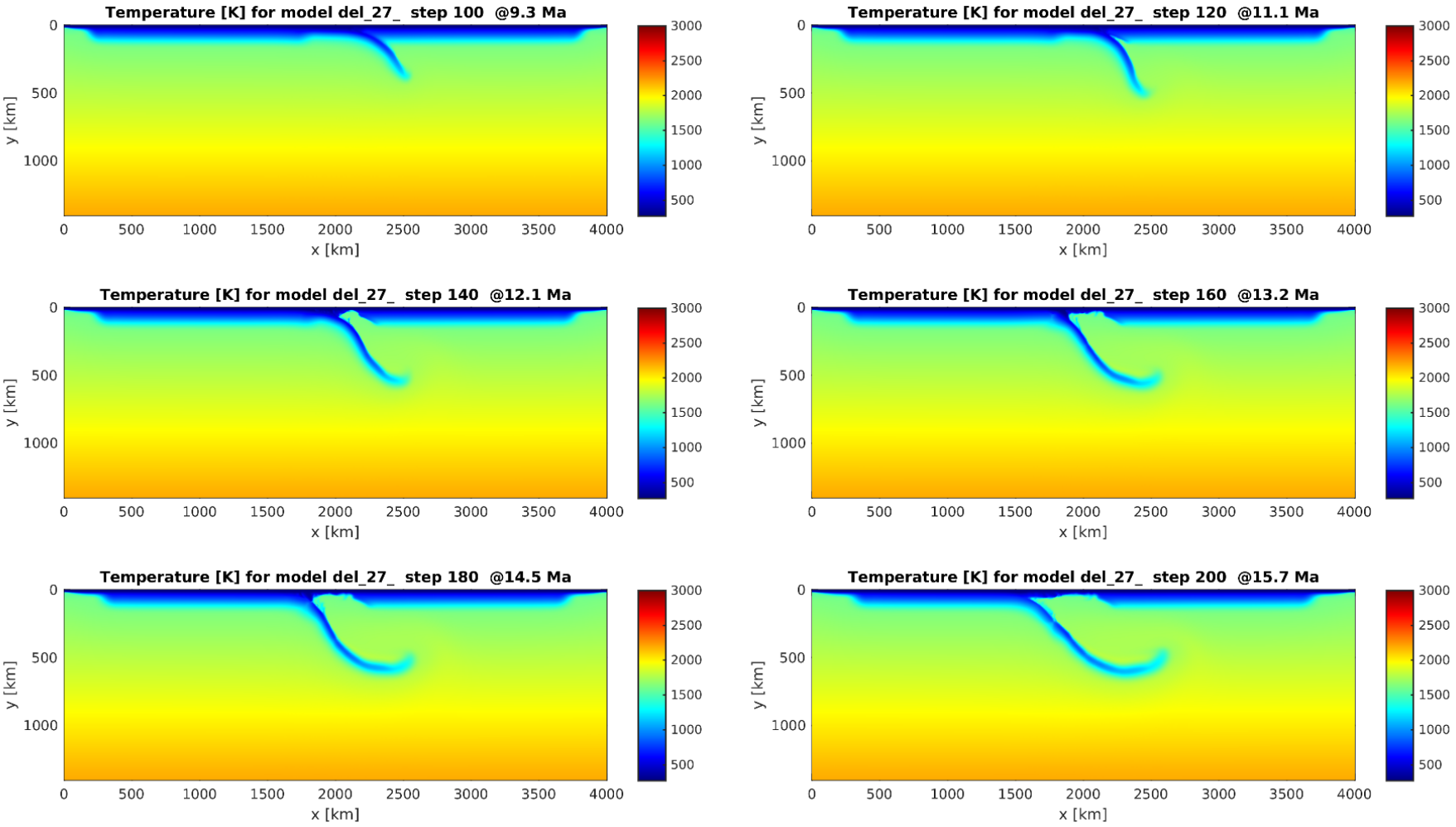

Figure A.4: Results of temperature field with x axis (km), y axis time (km) and temperature values are defined at color bar.

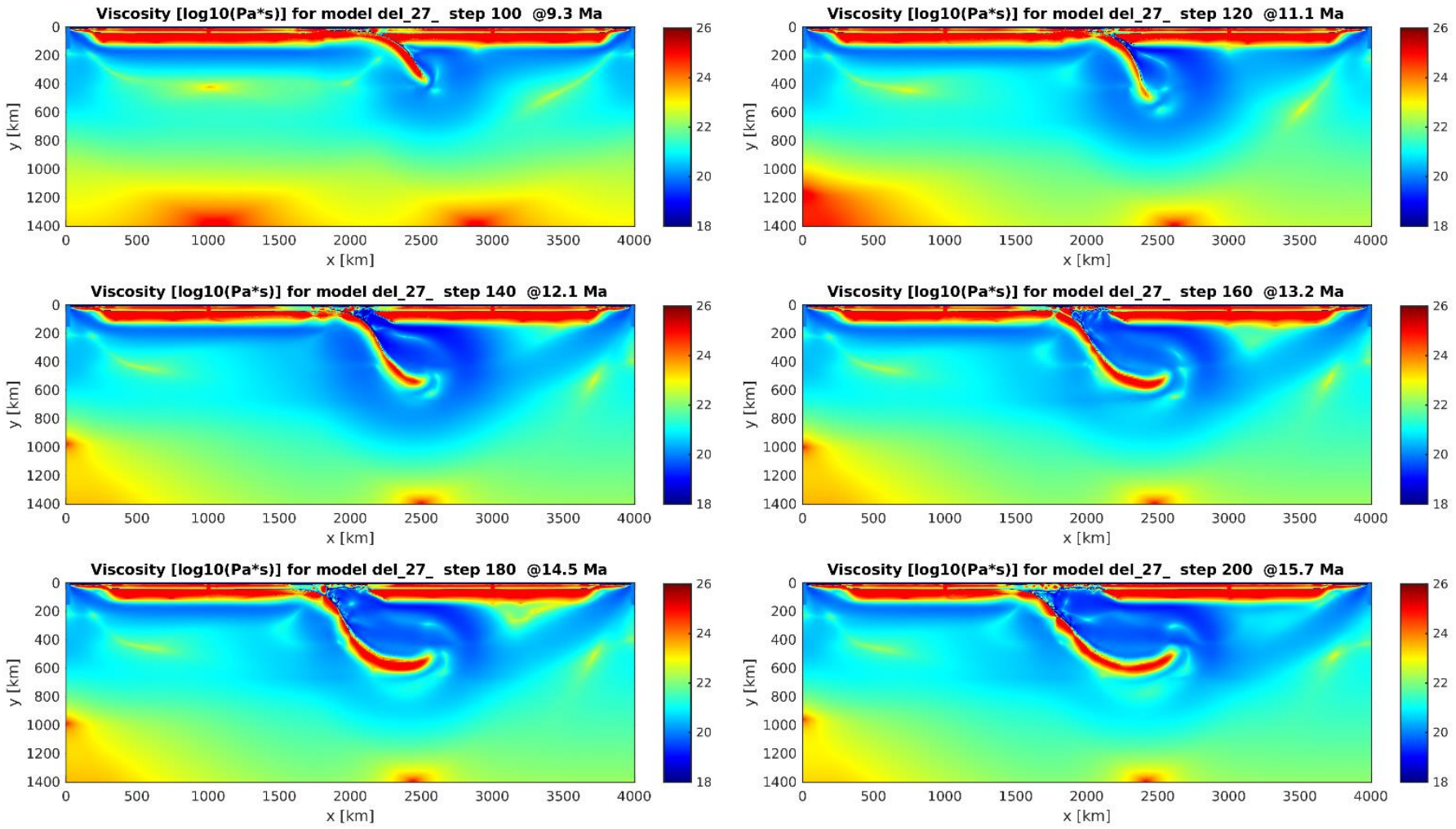

Figure A.5: Results of viscosity field with x axis (km), y axis time (km) and viscosity values are defined at color bar.

Appendix B

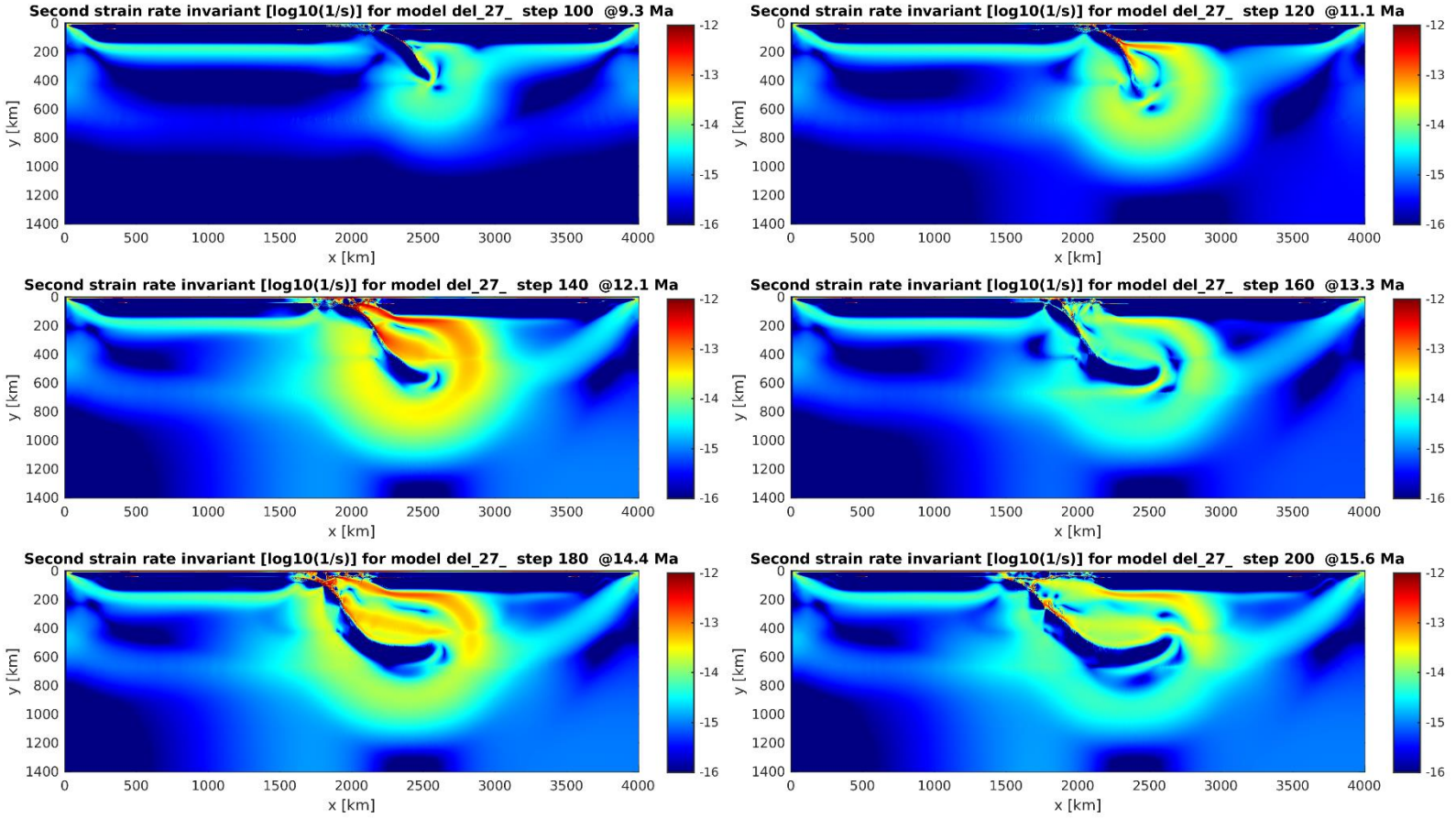

Figure B.1: Results of second strain rate invariants with x axis (km), y axis time (km) and second strain rate invariant (color bar.)

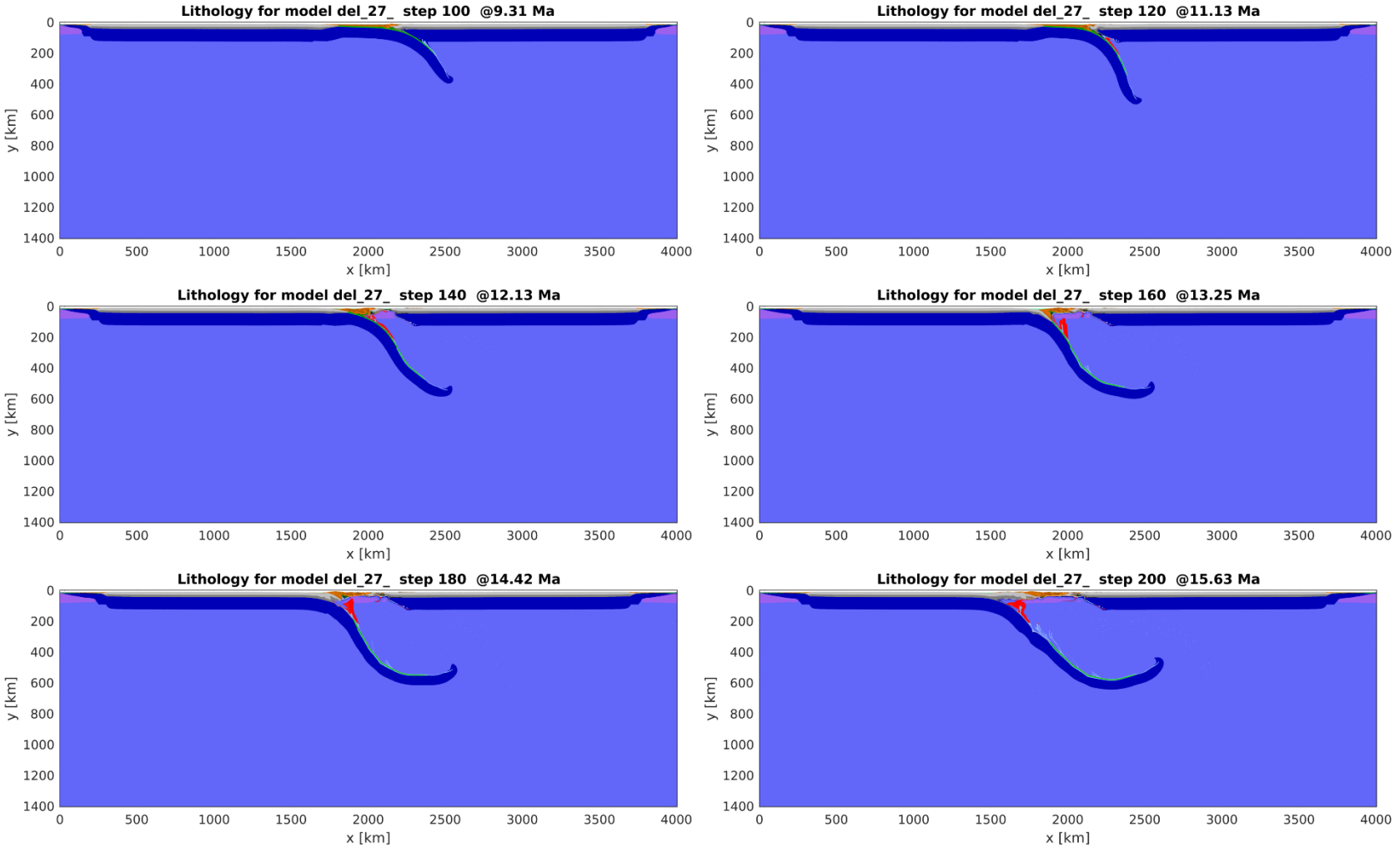

Figure B.2: Results of full domain material field with x axis (km), y axis time (km).

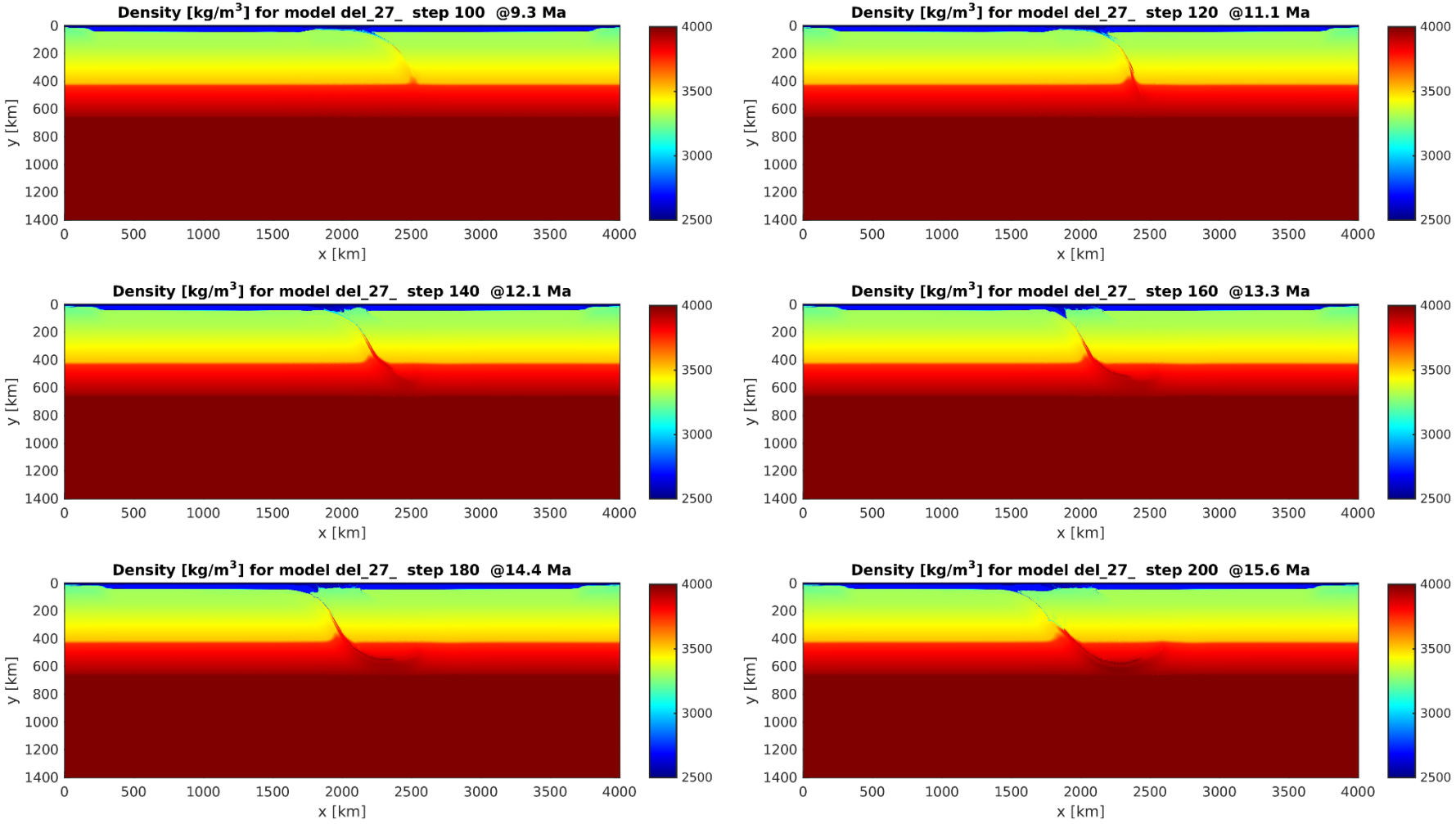

Figure B.3: Results of density field with x axis (km), y axis time (km) and density values are defined at color bar.

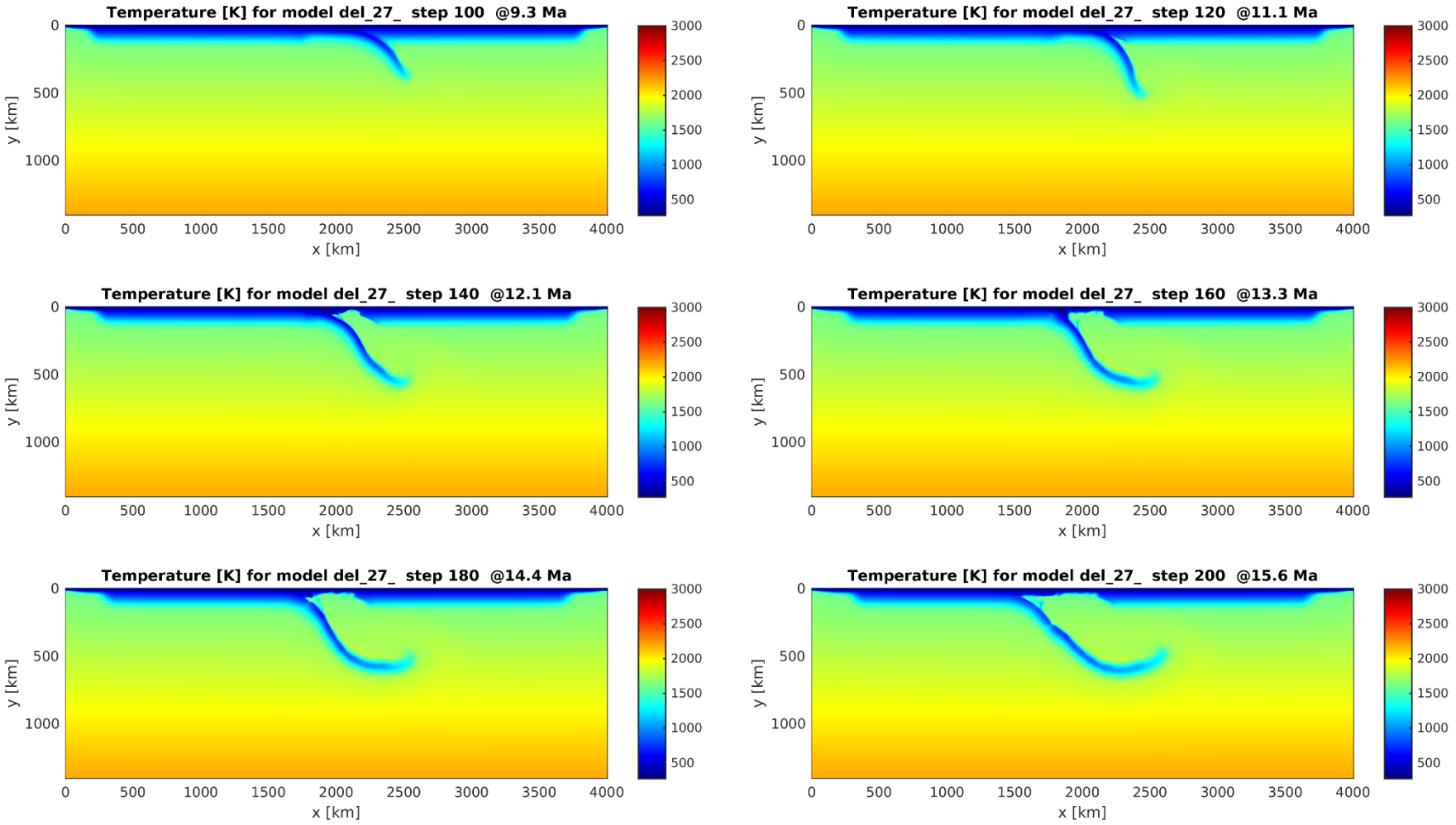

Figure B.4: Results of temperature field with x axis (km), y axis time (km) and temperature values are defined at color bar.

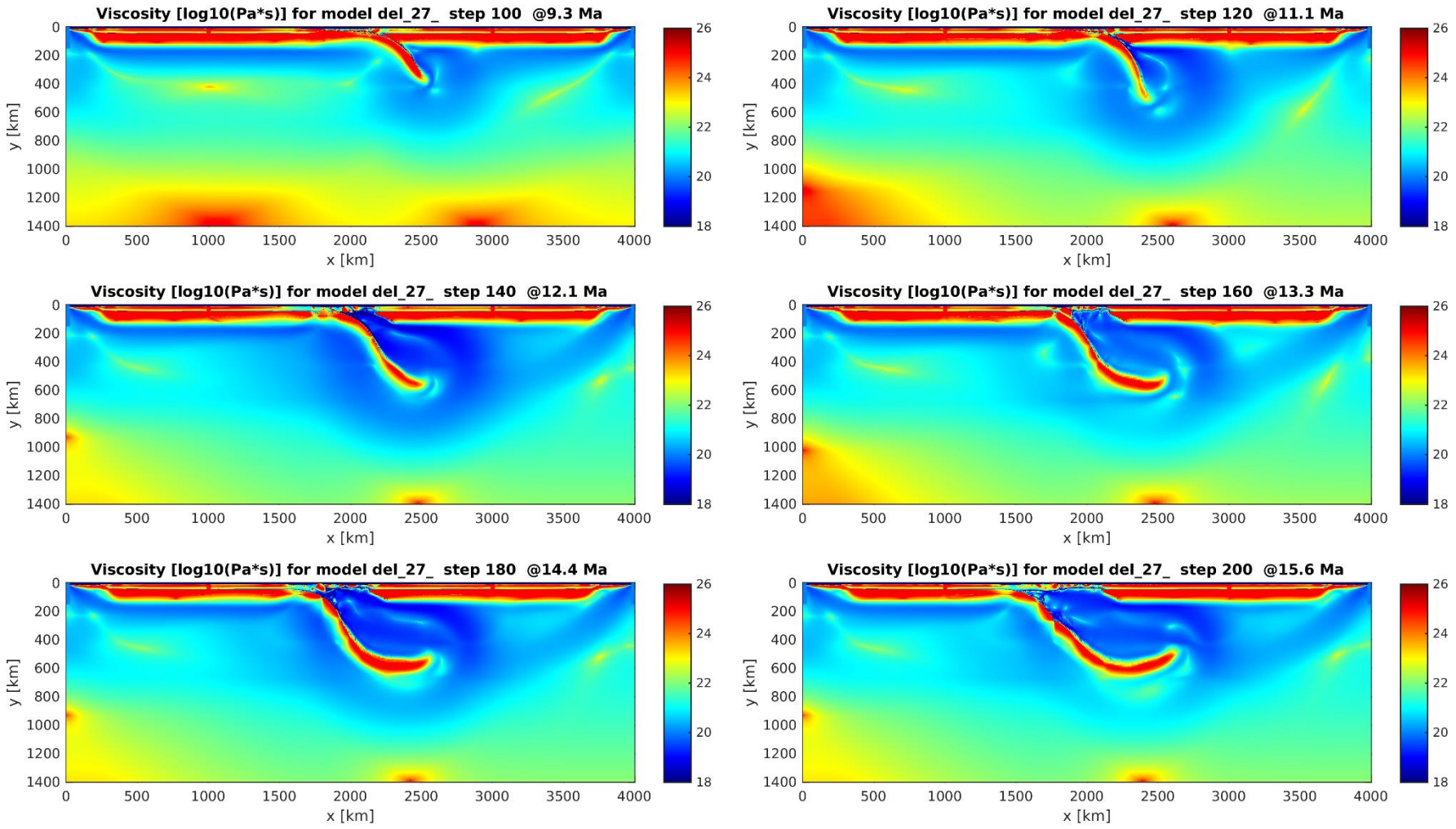

Figure B.5: Results of viscosity field with x axis (km), y axis time (km) and viscosity values are defined at color bar.

Appendix C

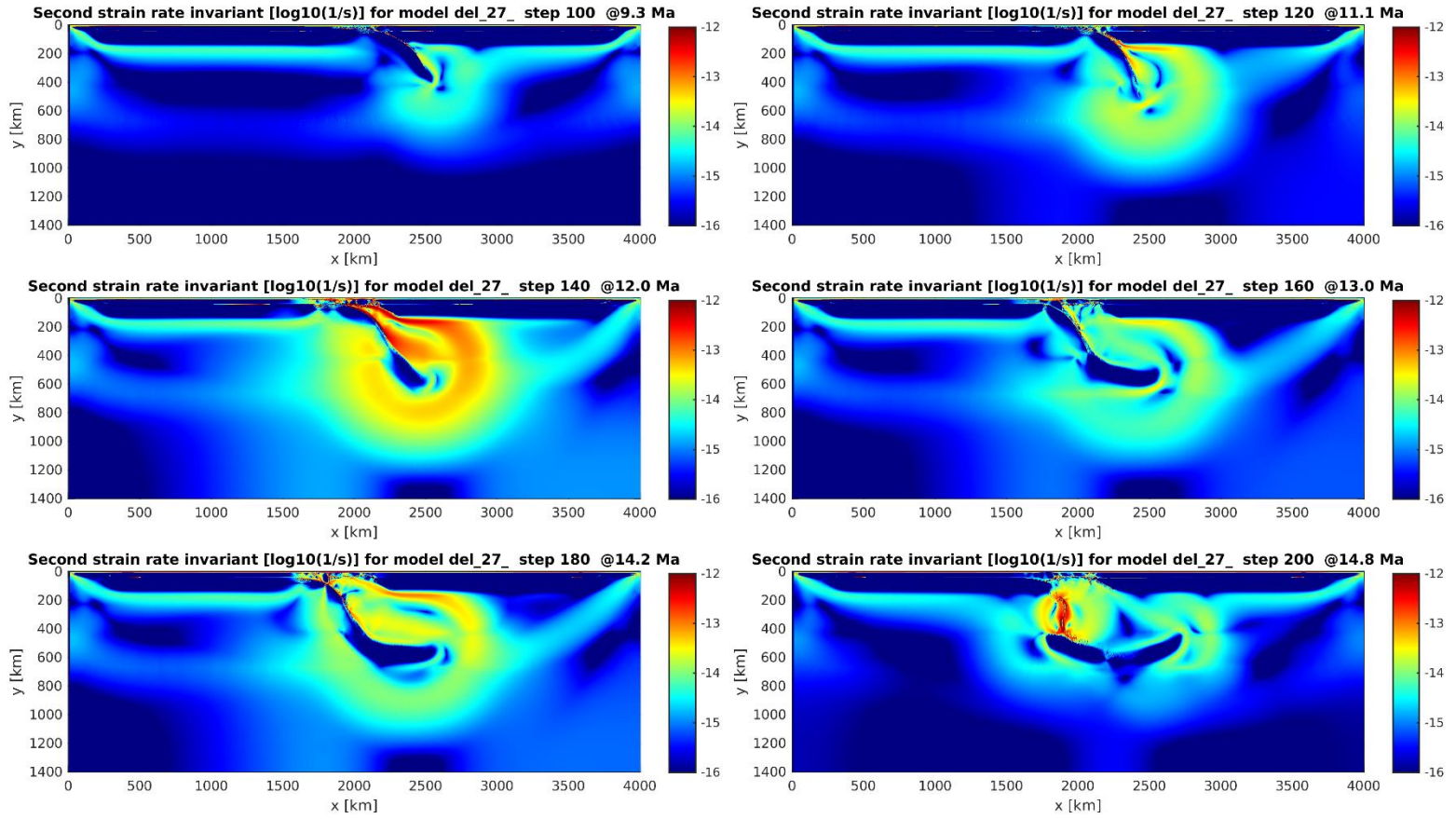

Figure C.1: Results of second strain rate invariants with x axis (km), y axis time (km) and second strain rate invariant (color bar.)

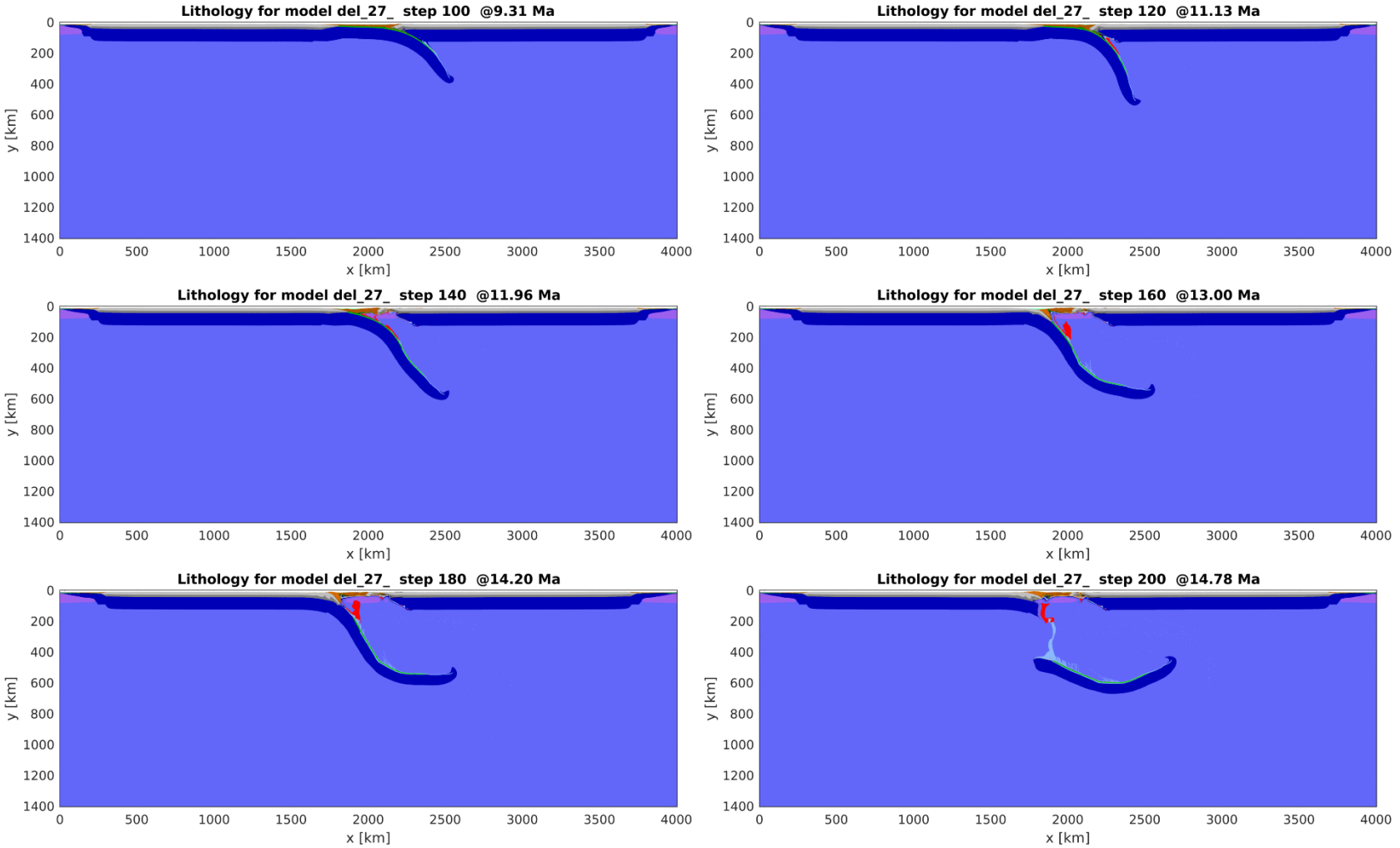

Figure C.2: Results of full domain material field with x axis (km), y axis time (km).

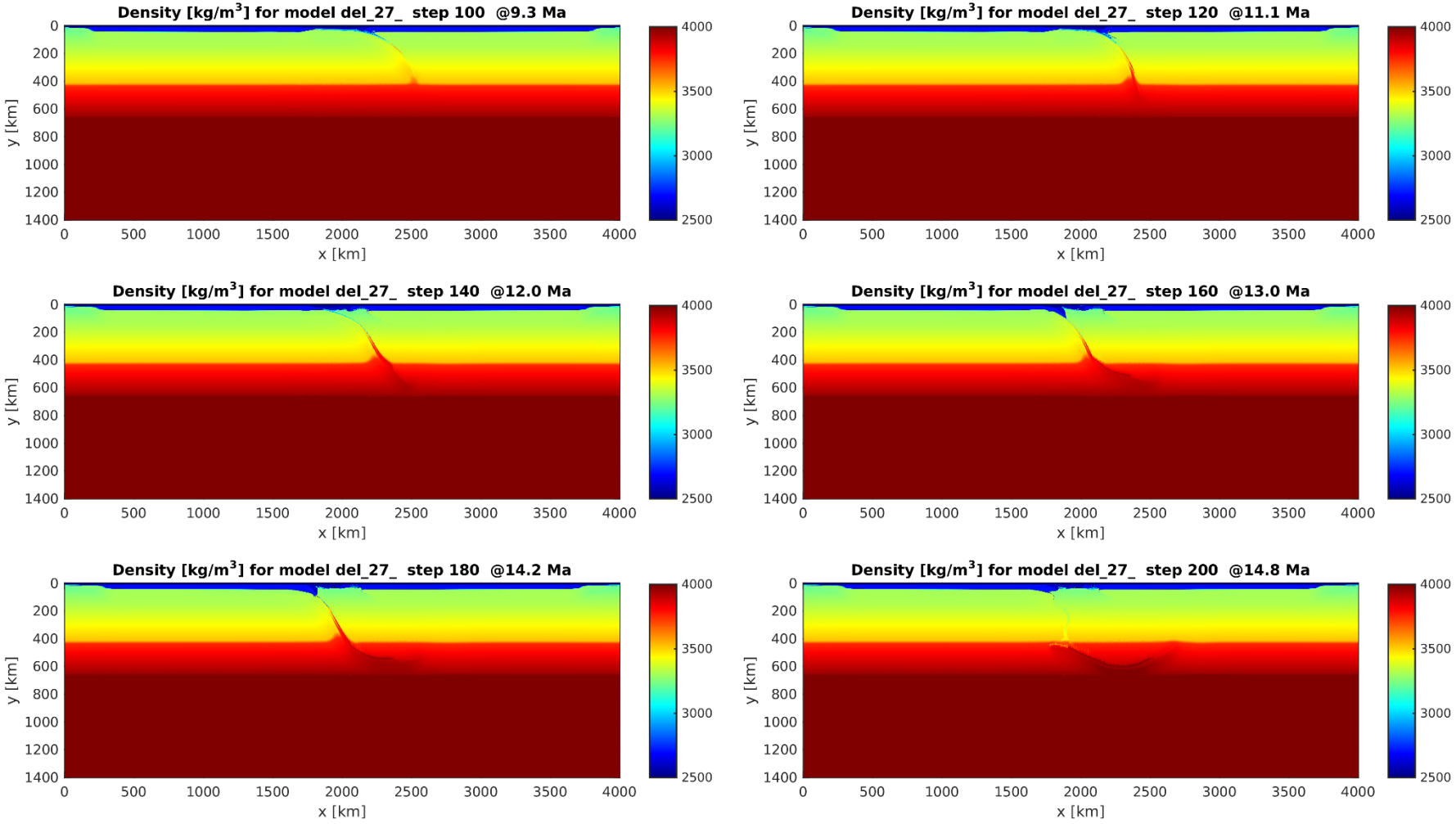

Figure C.3: Results of density field with x axis (km), y axis time (km) and density values are defined at color bar.

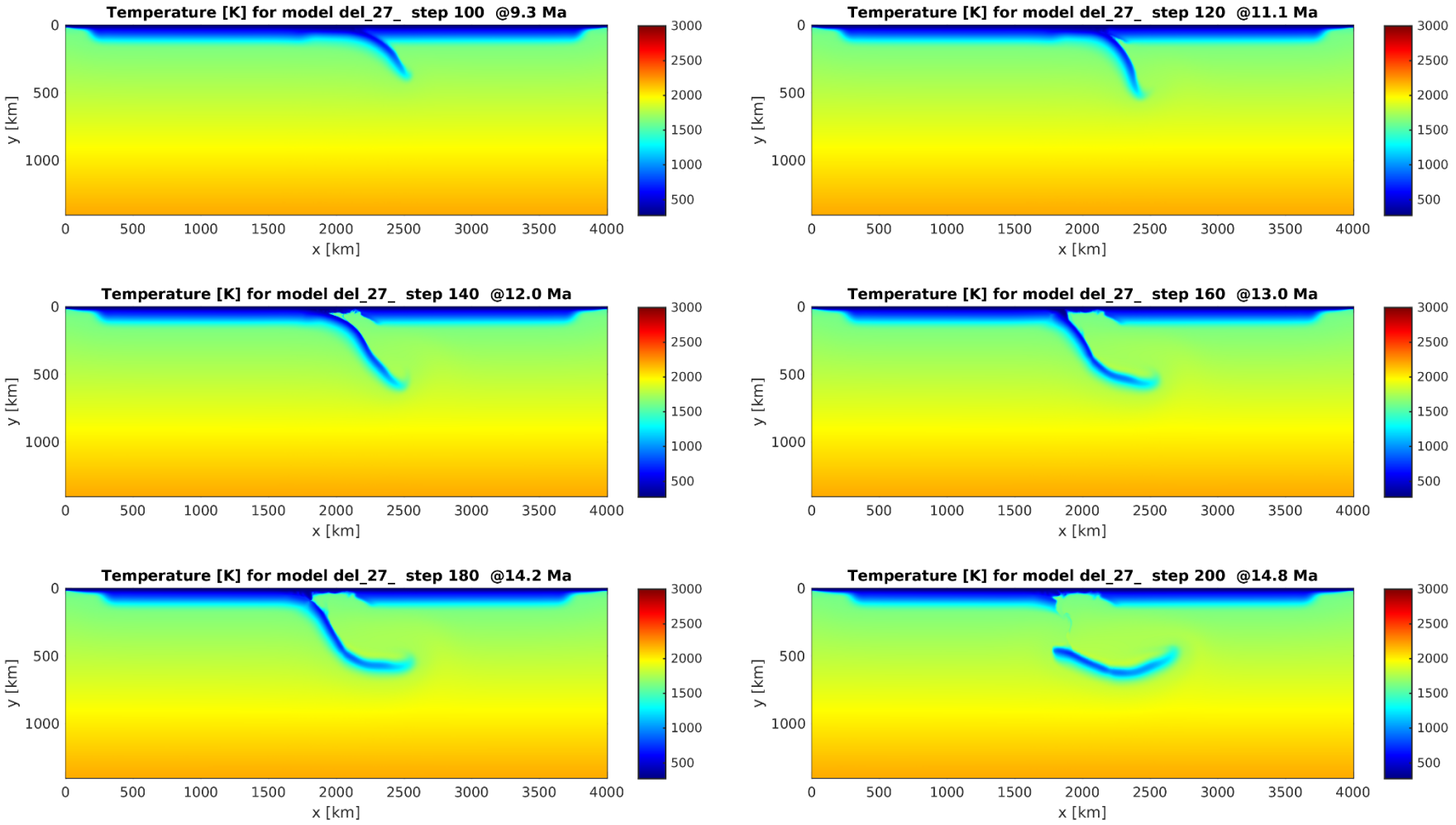

Figure C.4: Results of temperature field with x axis (km), y axis time (km) and temperature values are defined at color bar.

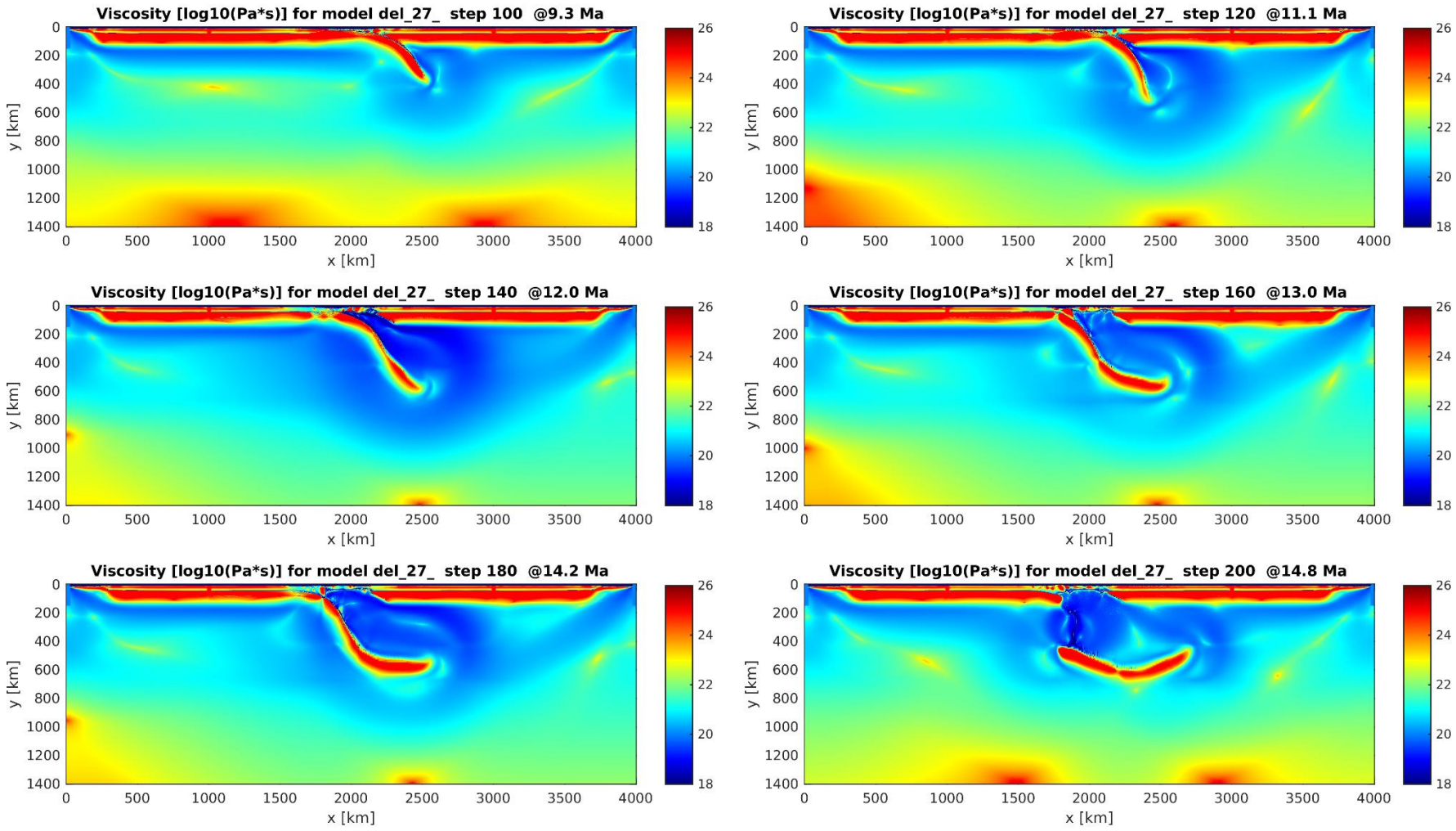

Figure C.5: Results of viscosity field with x axis (km), y axis time (km) and viscosity values are defined at color bar.

Appendix D

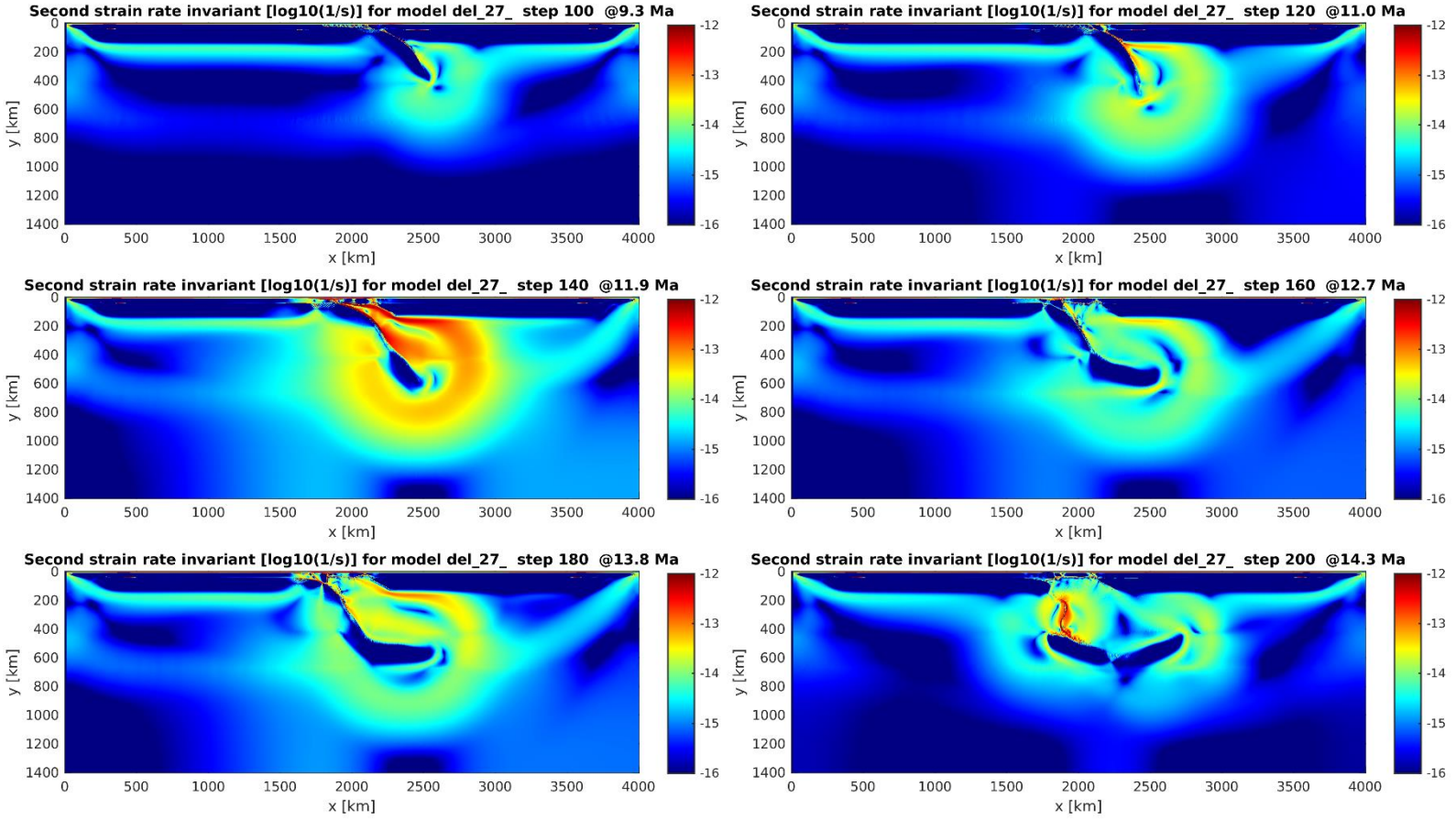

Figure D.1: Results of second strain rate invariants with x axis (km), y axis time (km) and second strain rate invariant (color bar.)

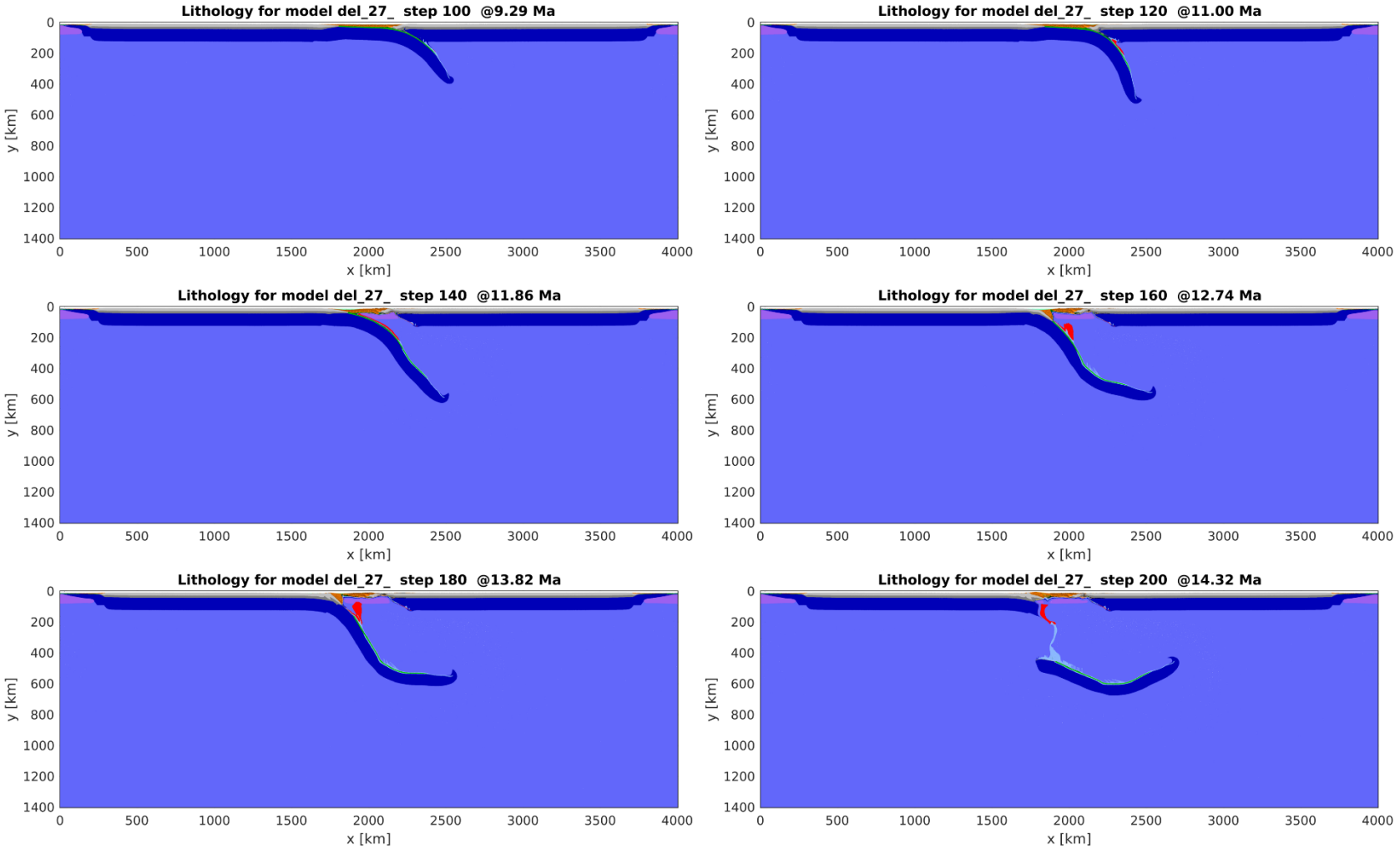

Figure D.2: Results of full domain material field with x axis (km), y axis time (km).

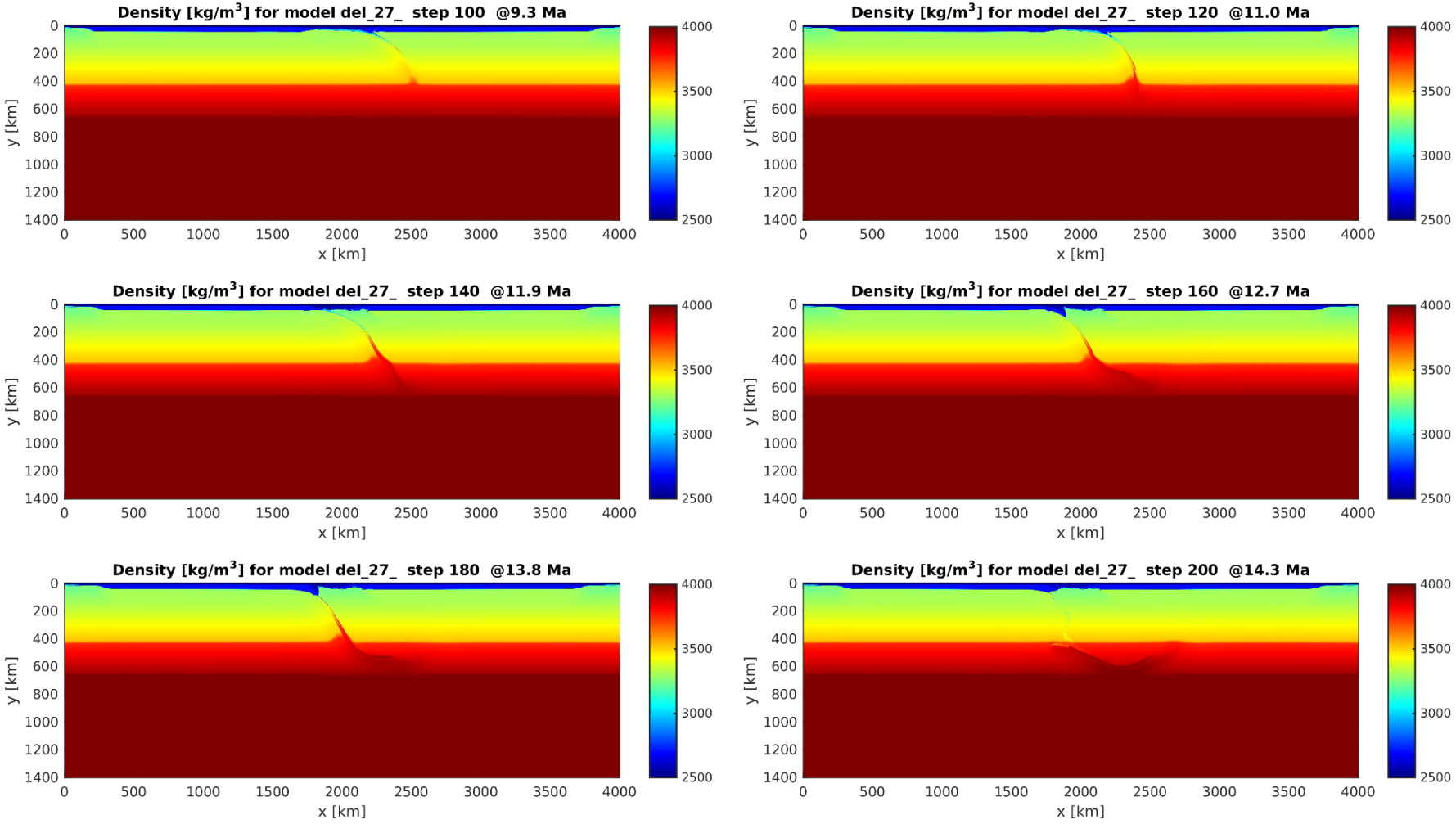

Figure D.3: Results of density field with x axis (km), y axis time (km) and density values are defined at color bar.

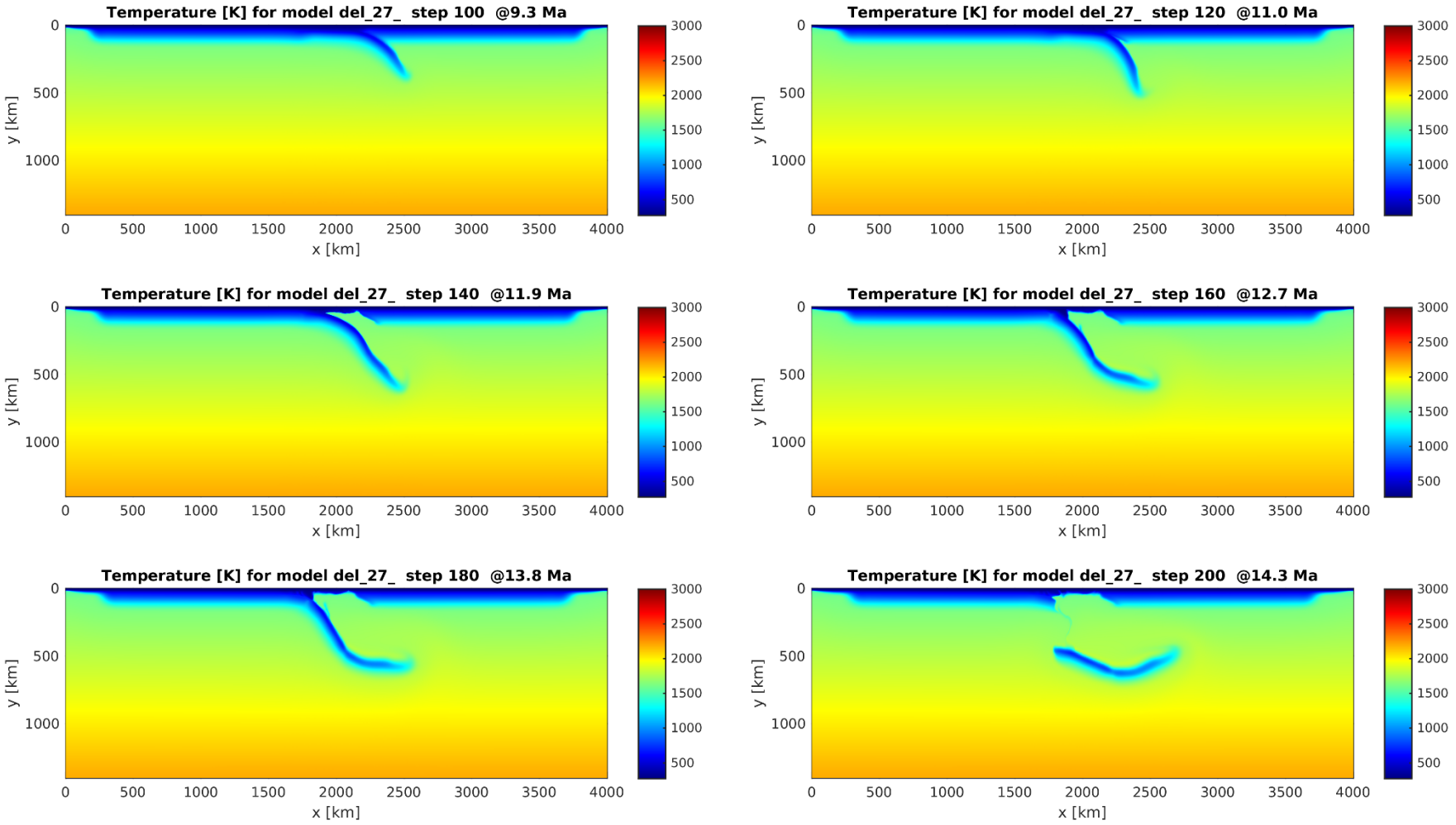

Figure D.4: Results of temperature field with x axis (km), y axis time (km) and temperature values are defined at color bar.

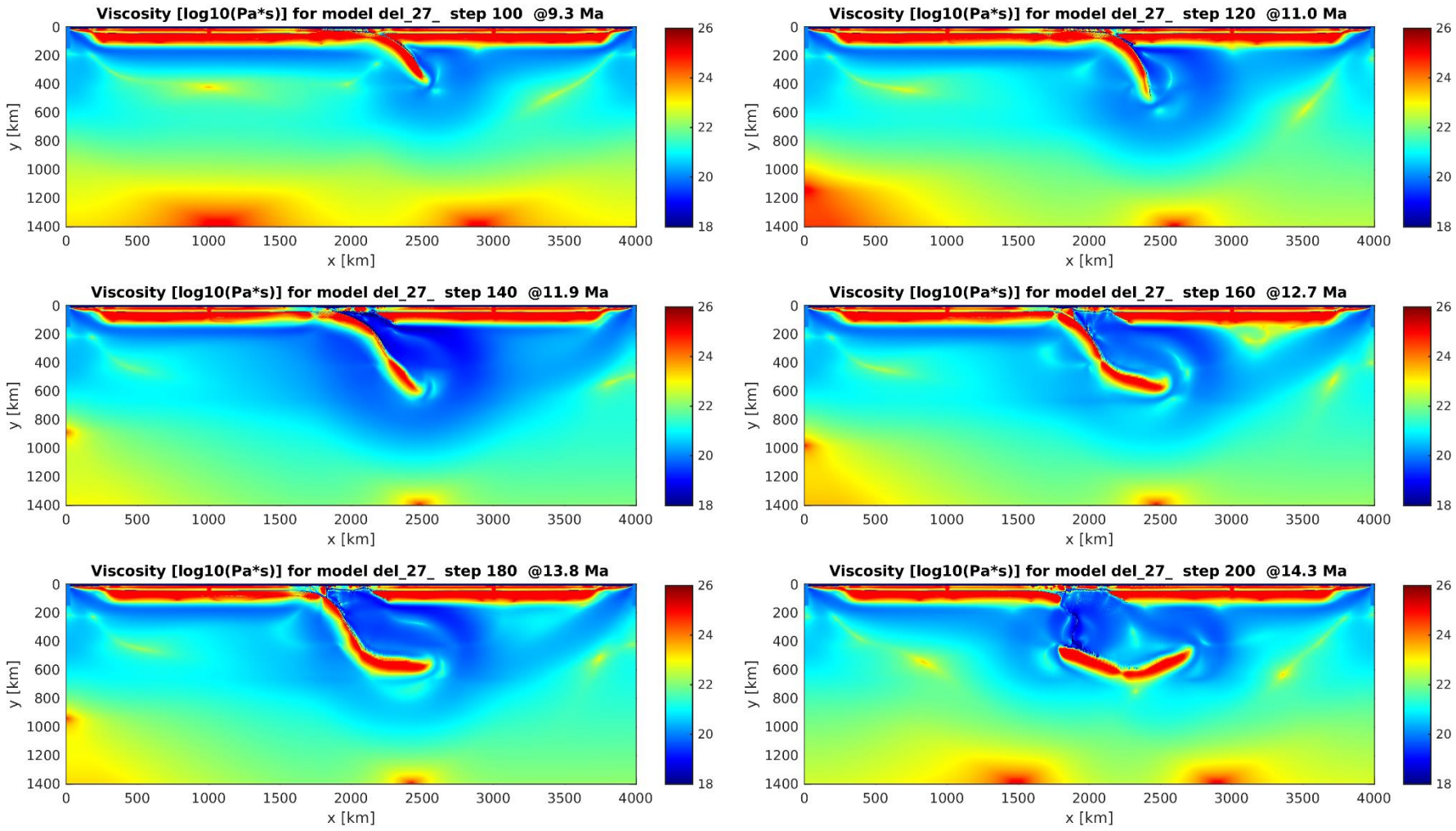

Figure D.5: Results of viscosity field with x axis (km), y axis time (km) and viscosity values are defined at color bar.

Appendix E

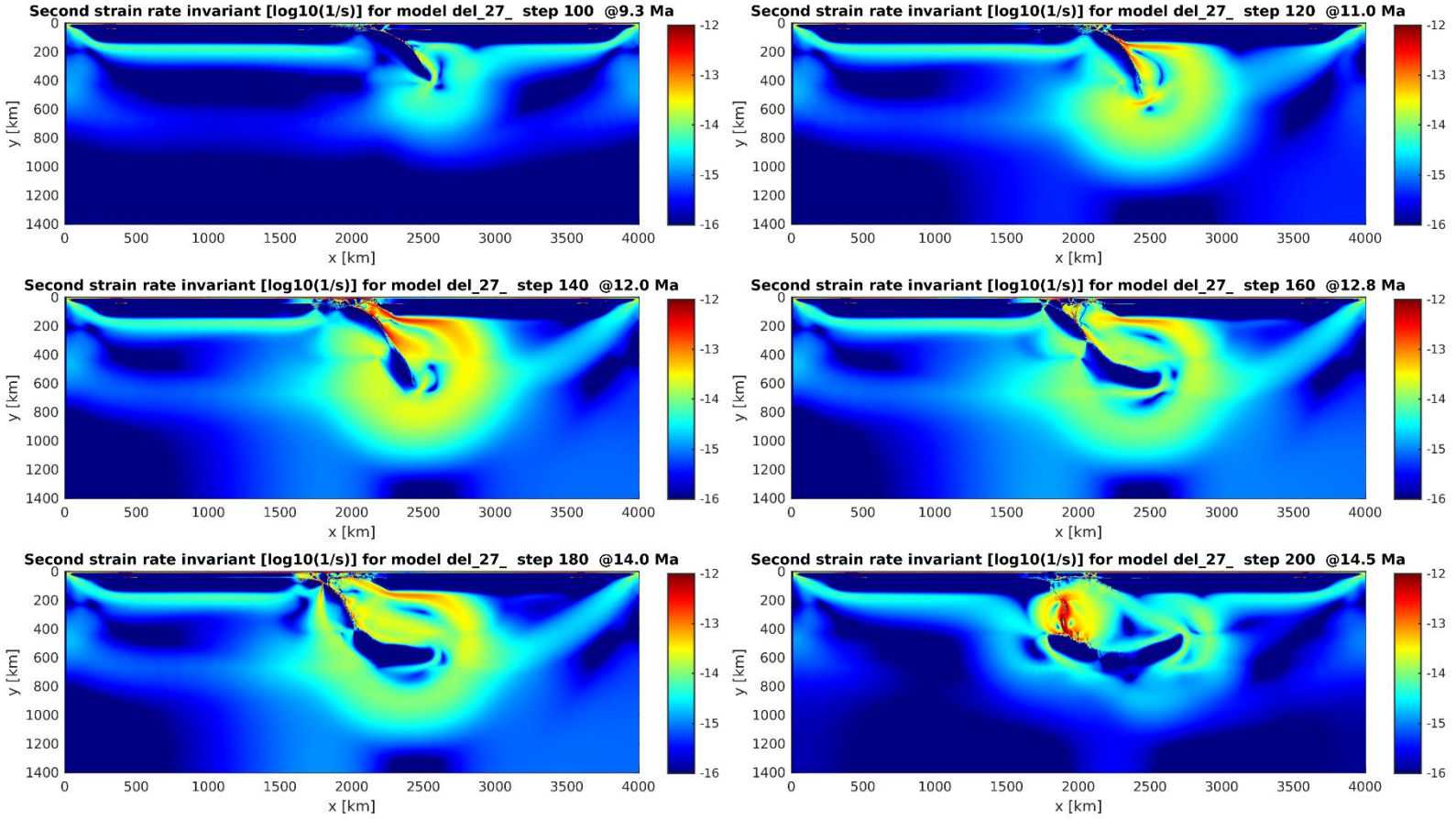

Figure E.1: Results of second strain rate invariants with x axis (km), y axis time (km) and second strain rate invariant (color bar.)

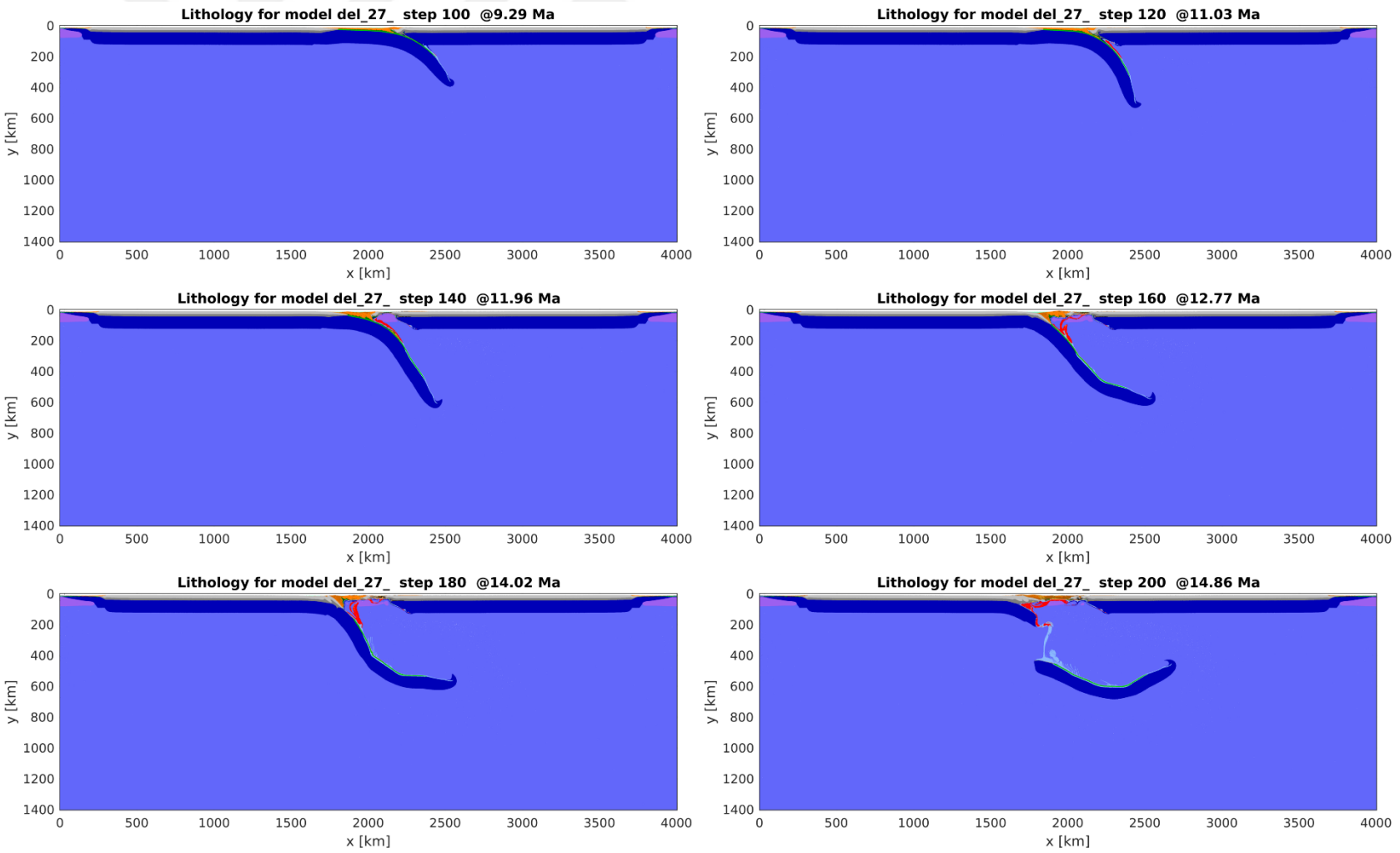

Figure E.2: Results of full domain material field with x axis (km), y axis time (km).

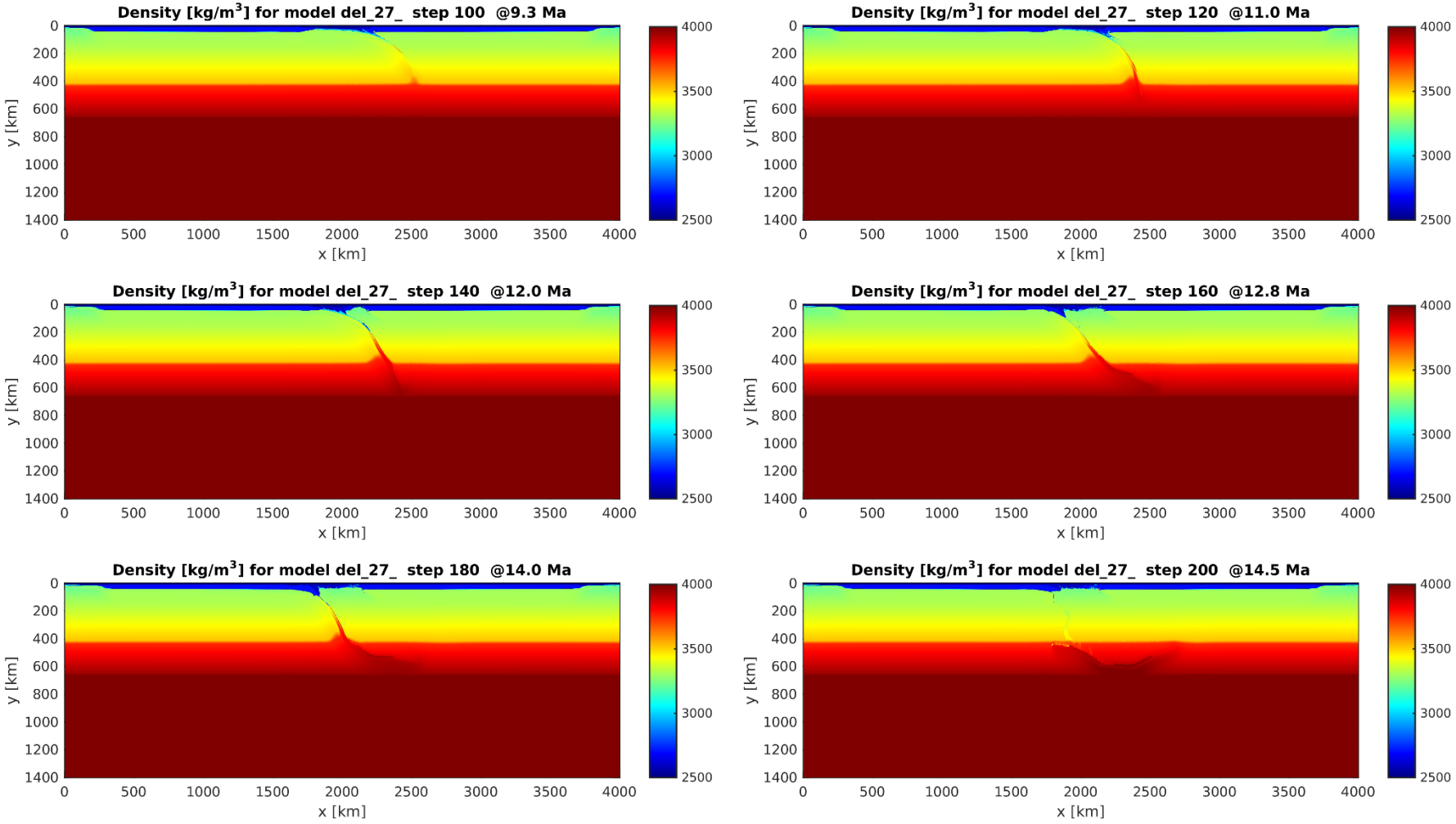

Figure E.3: Results of density field with x axis (km), y axis time (km) and density values are defined at color bar.

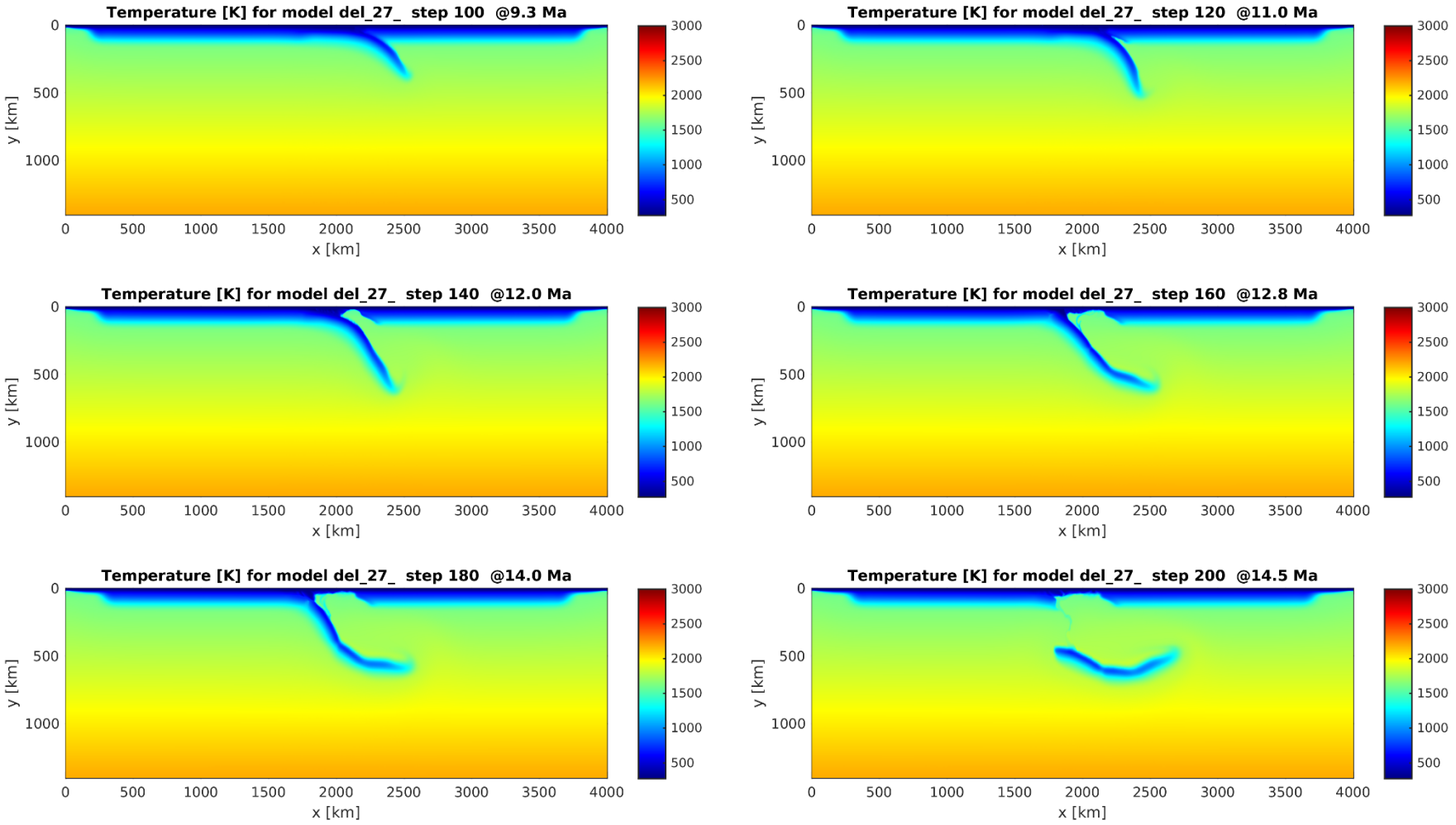

Figure E.4: Results of temperature field with x axis (km), y axis time (km) and temperature values are defined at color bar.

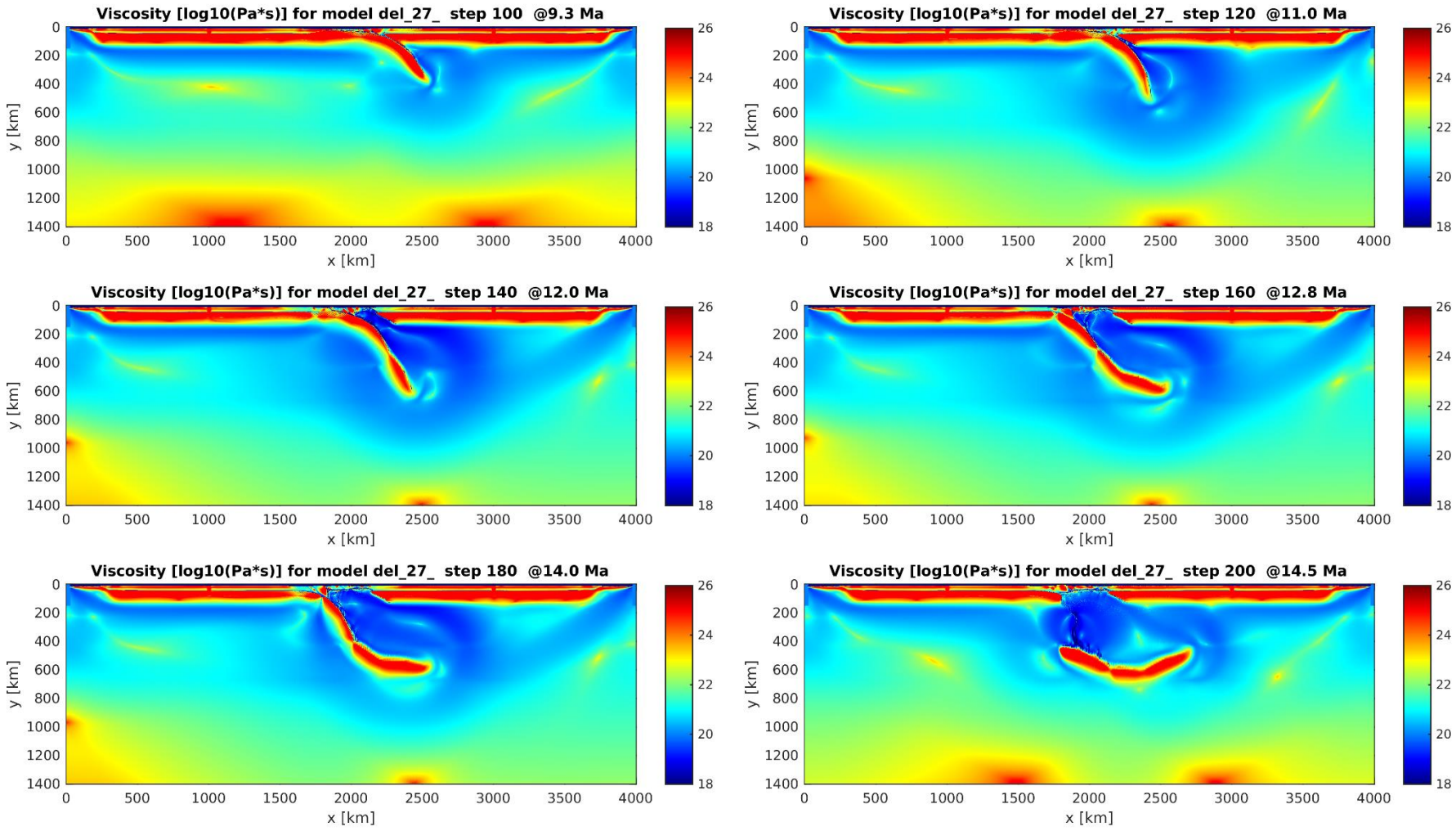

Figure E.5: Results of viscosity field with x axis (km), y axis time (km) and viscosity values are defined at color bar.

Appendix F

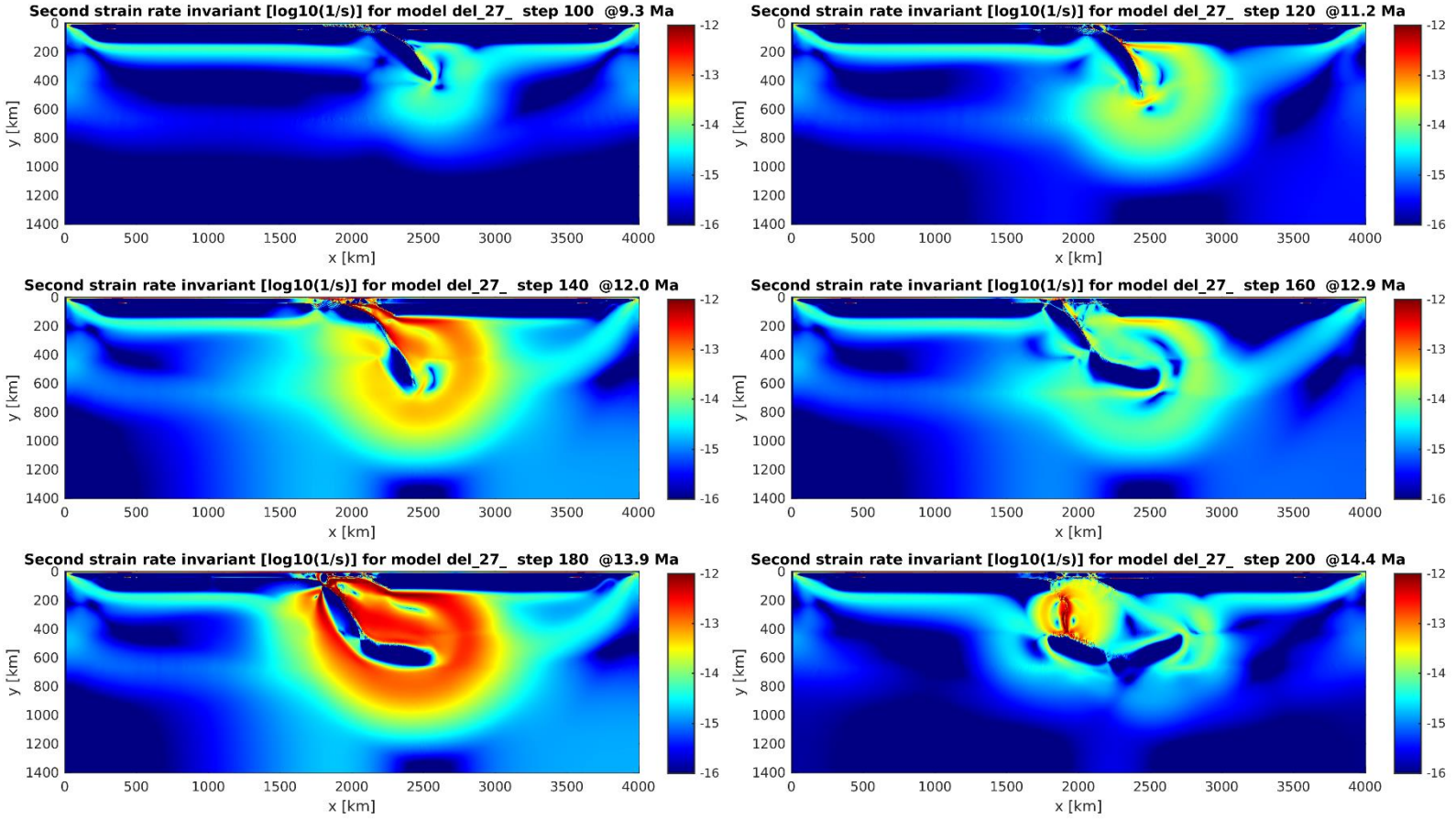

Figure F.1: Results of second strain rate invariants with x axis (km), y axis time (km) and second strain rate invariant (color bar.)

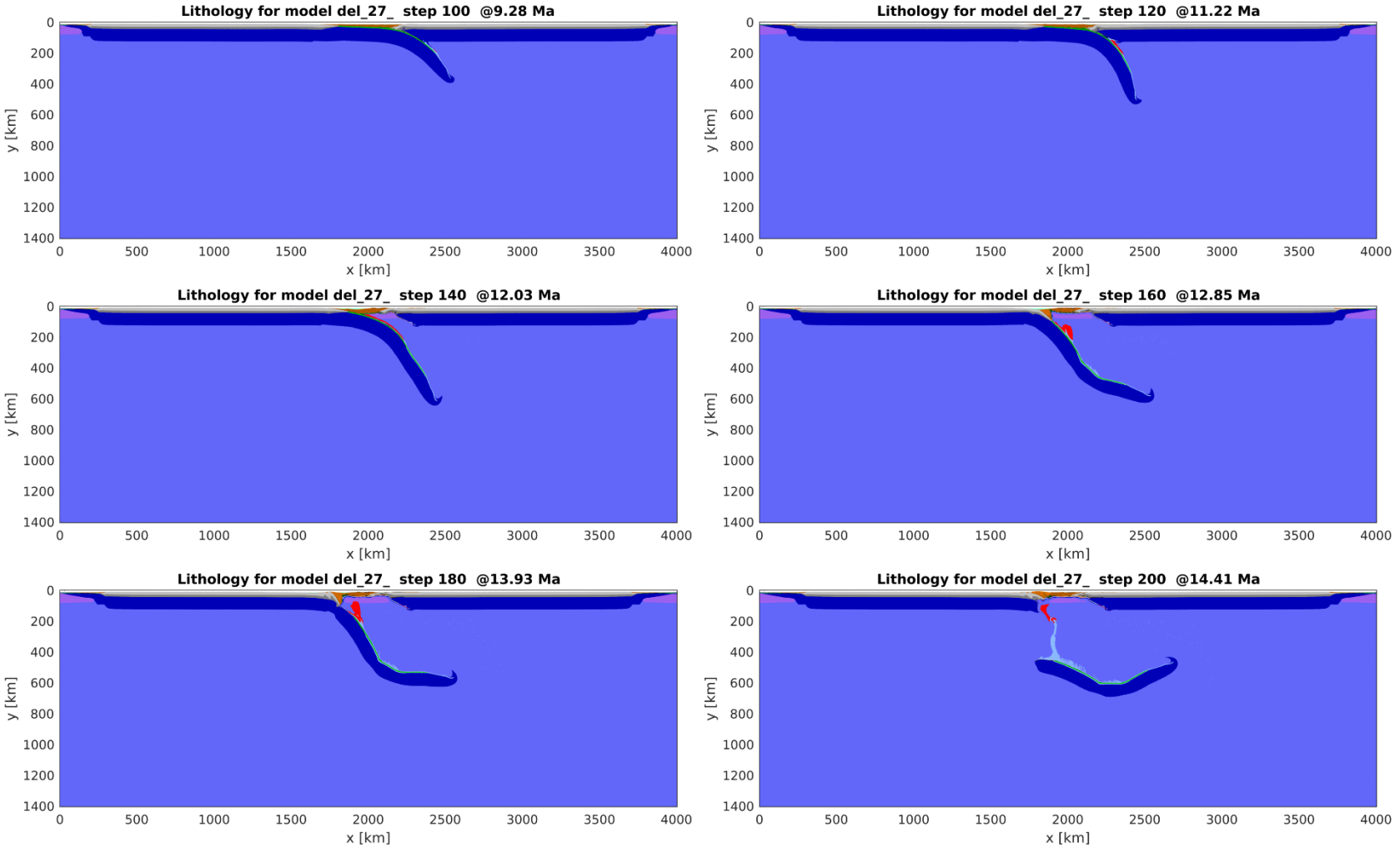

Figure F.2: Results of full domain material field with x axis (km), y axis time (km).

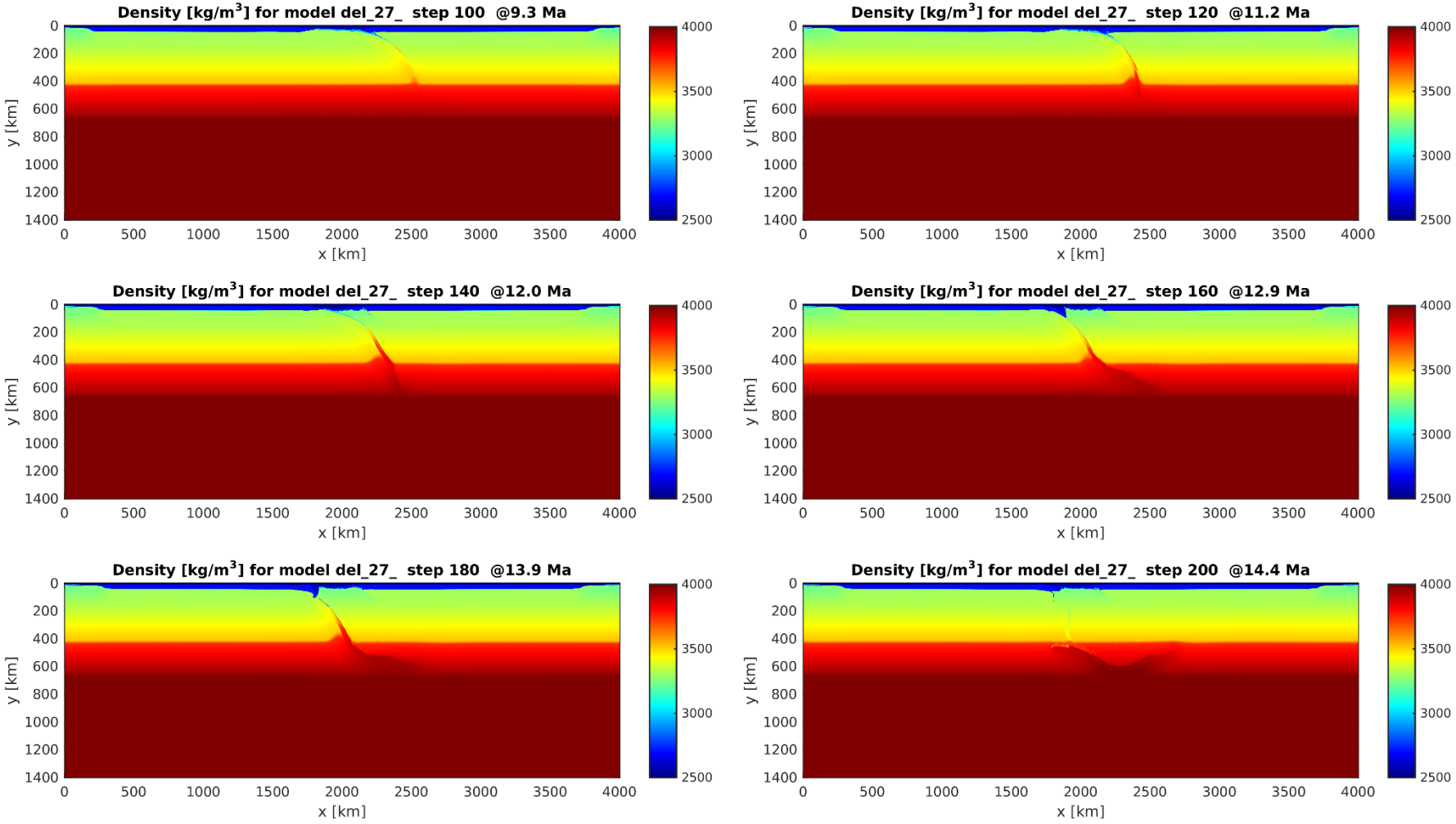

Figure F.3: Results of density field with x axis (km), y axis time (km) and density values are defined at color bar.

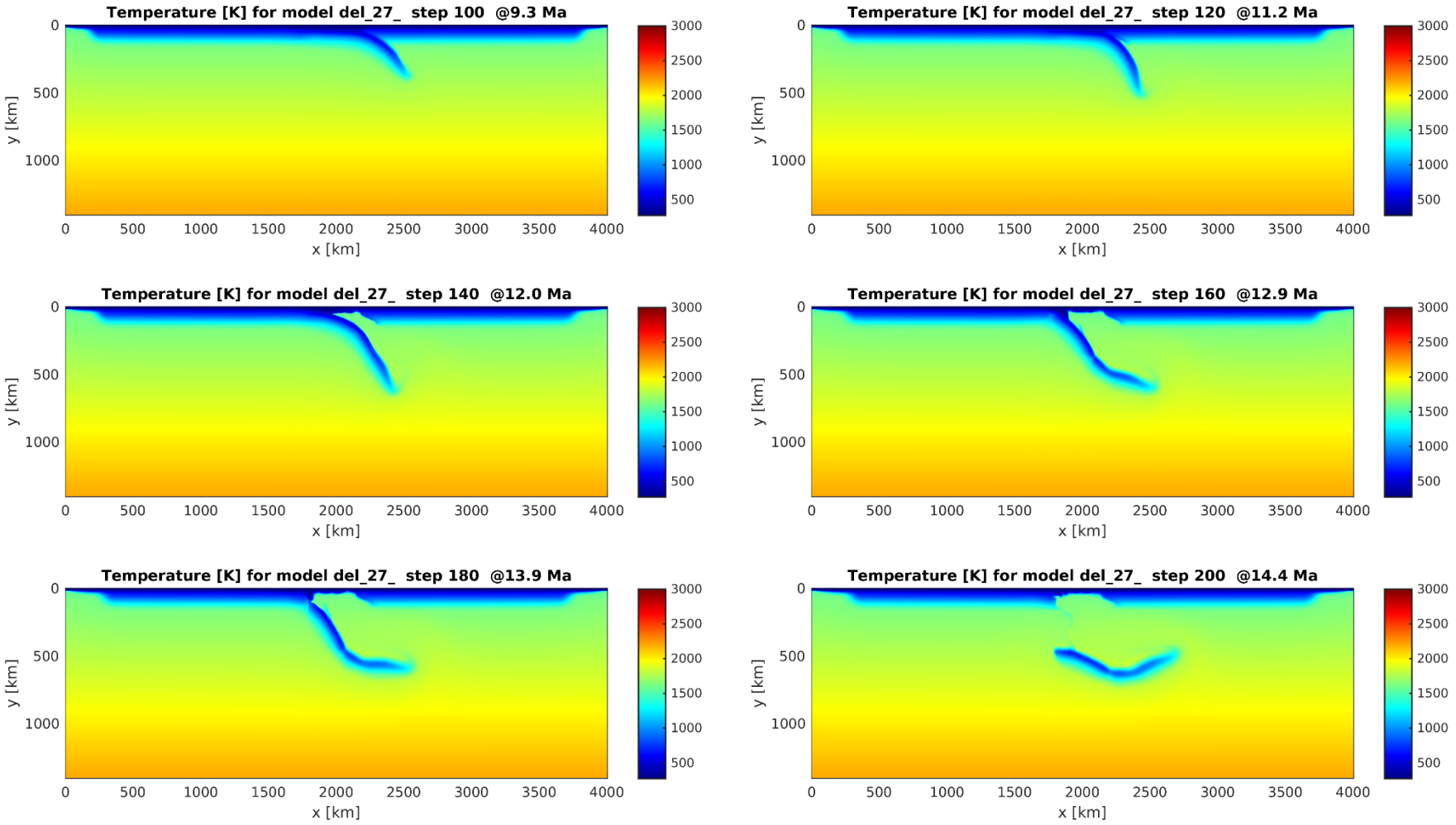

Figure F.4: Results of temperature field with x axis (km), y axis time (km) and temperature values are defined at color bar.

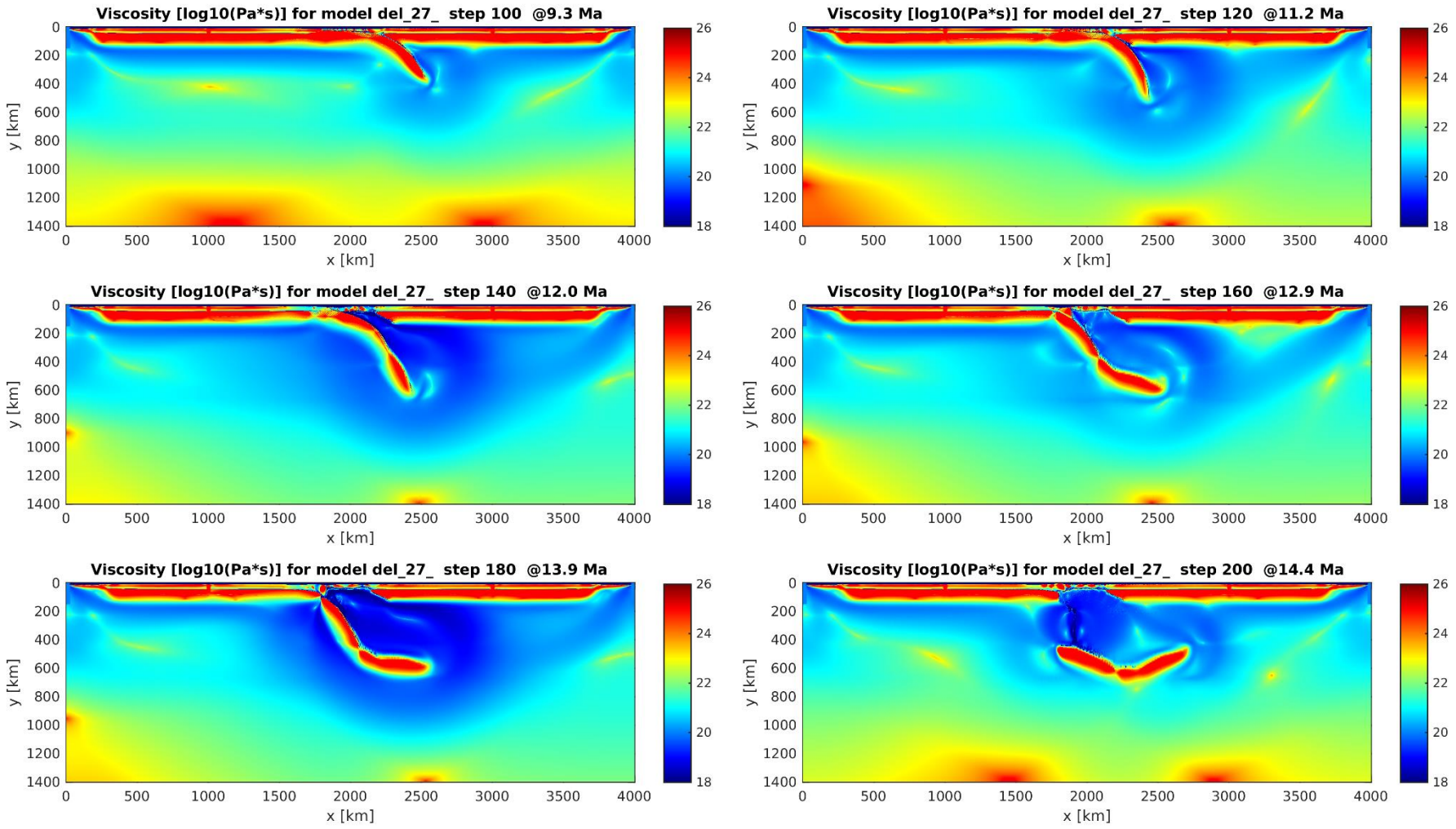

Figure F.5: Results of viscosity field with x axis (km), y axis time (km) and viscosity values are defined at color bar.

Appendix G

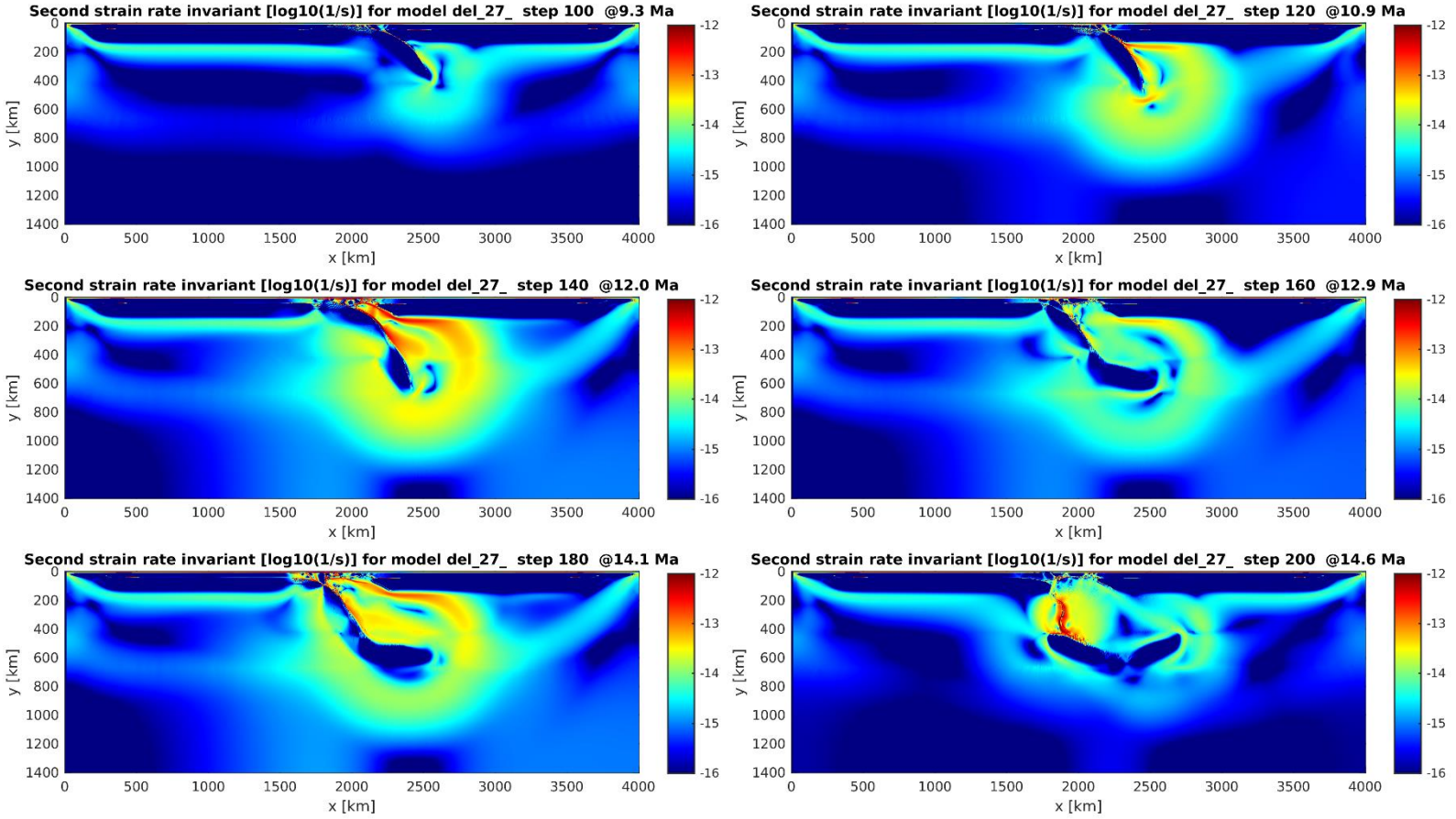

Figure G.1: Results of second strain rate invariants with x axis (km), y axis time (km) and second strain rate invariant (color bar.)

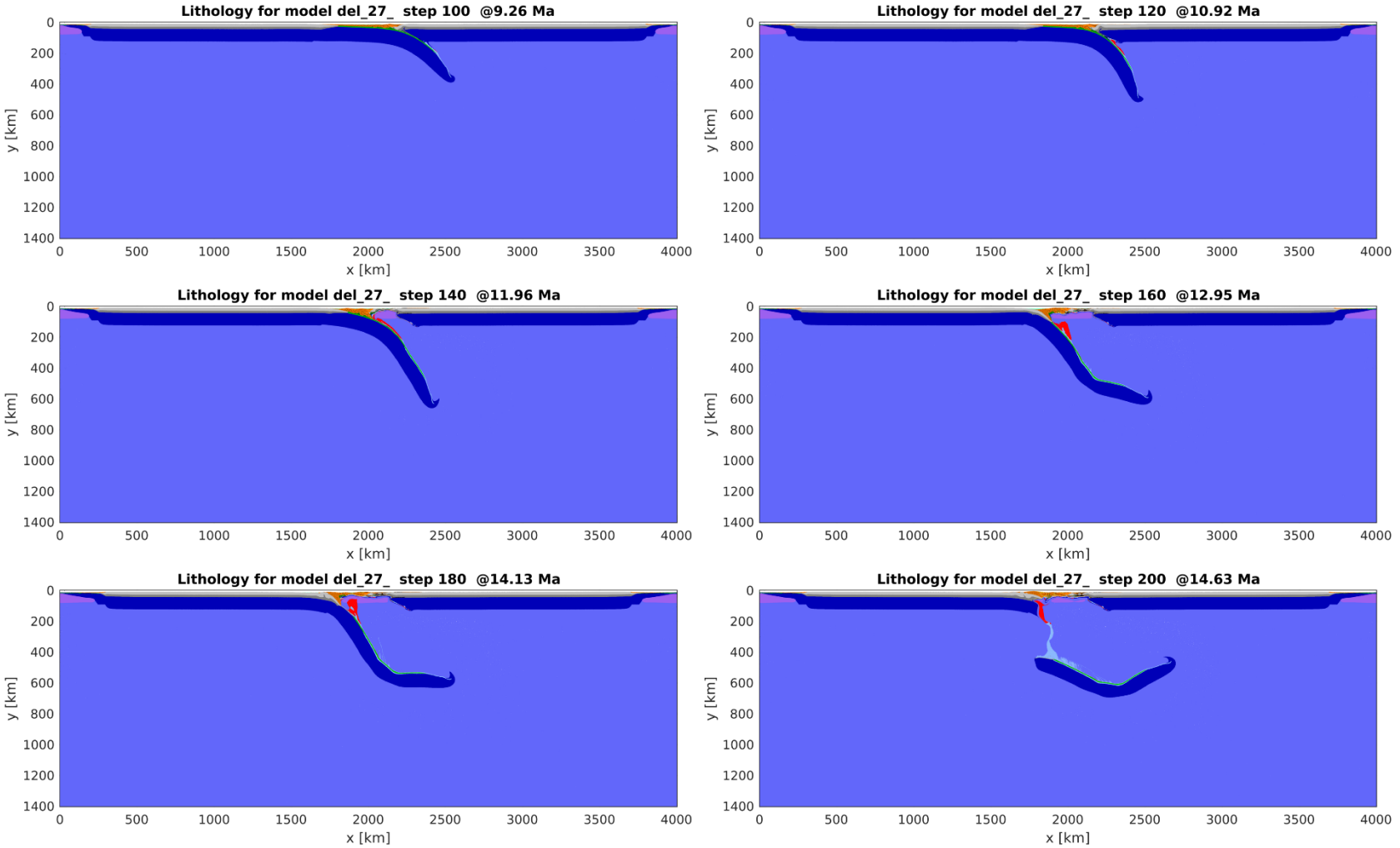

Figure G.2: Results of full domain material field with x axis (km), y axis time (km).

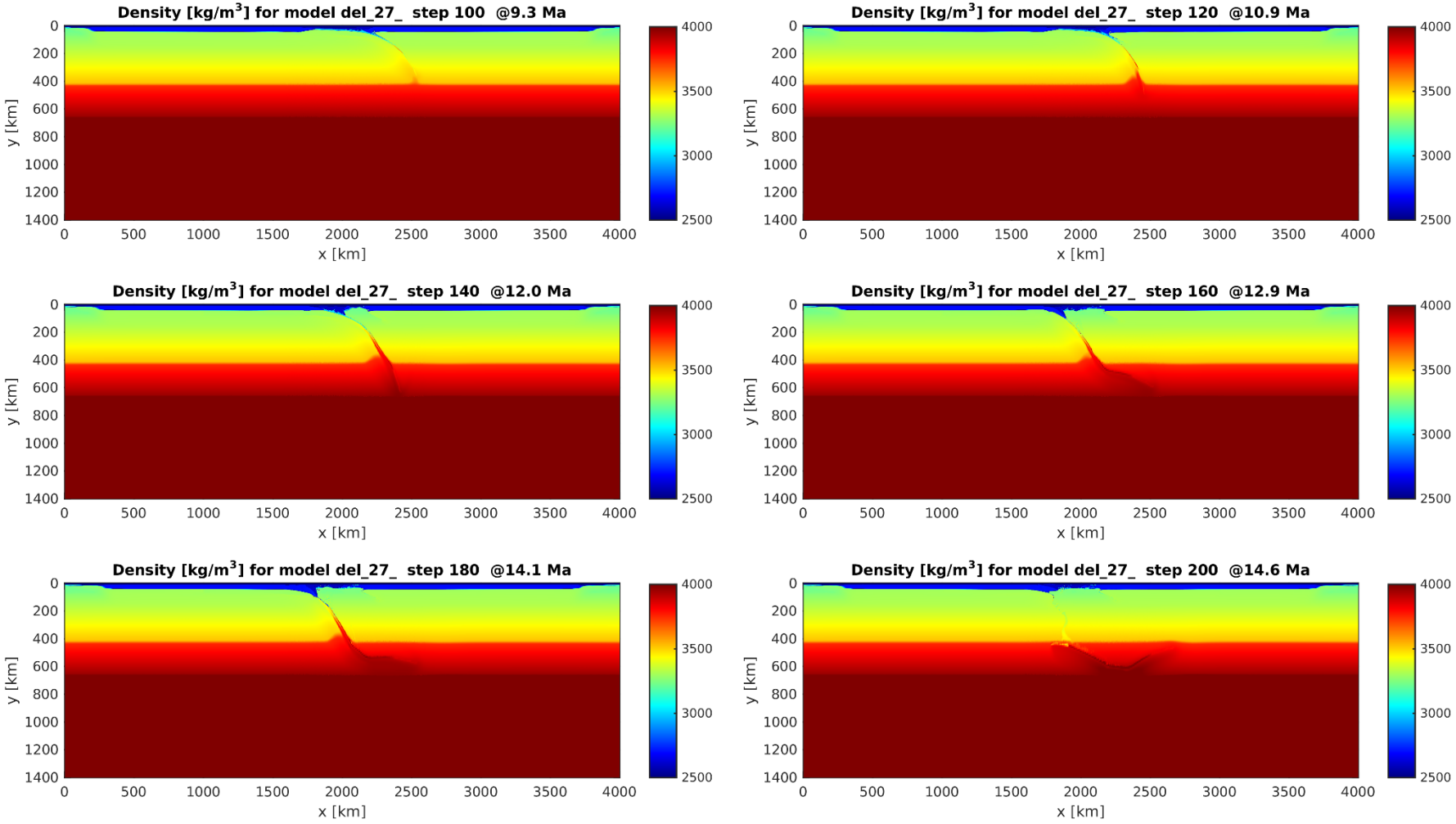

Figure G.3: Results of density field with x axis (km), y axis time (km) and density values are defined at color bar.

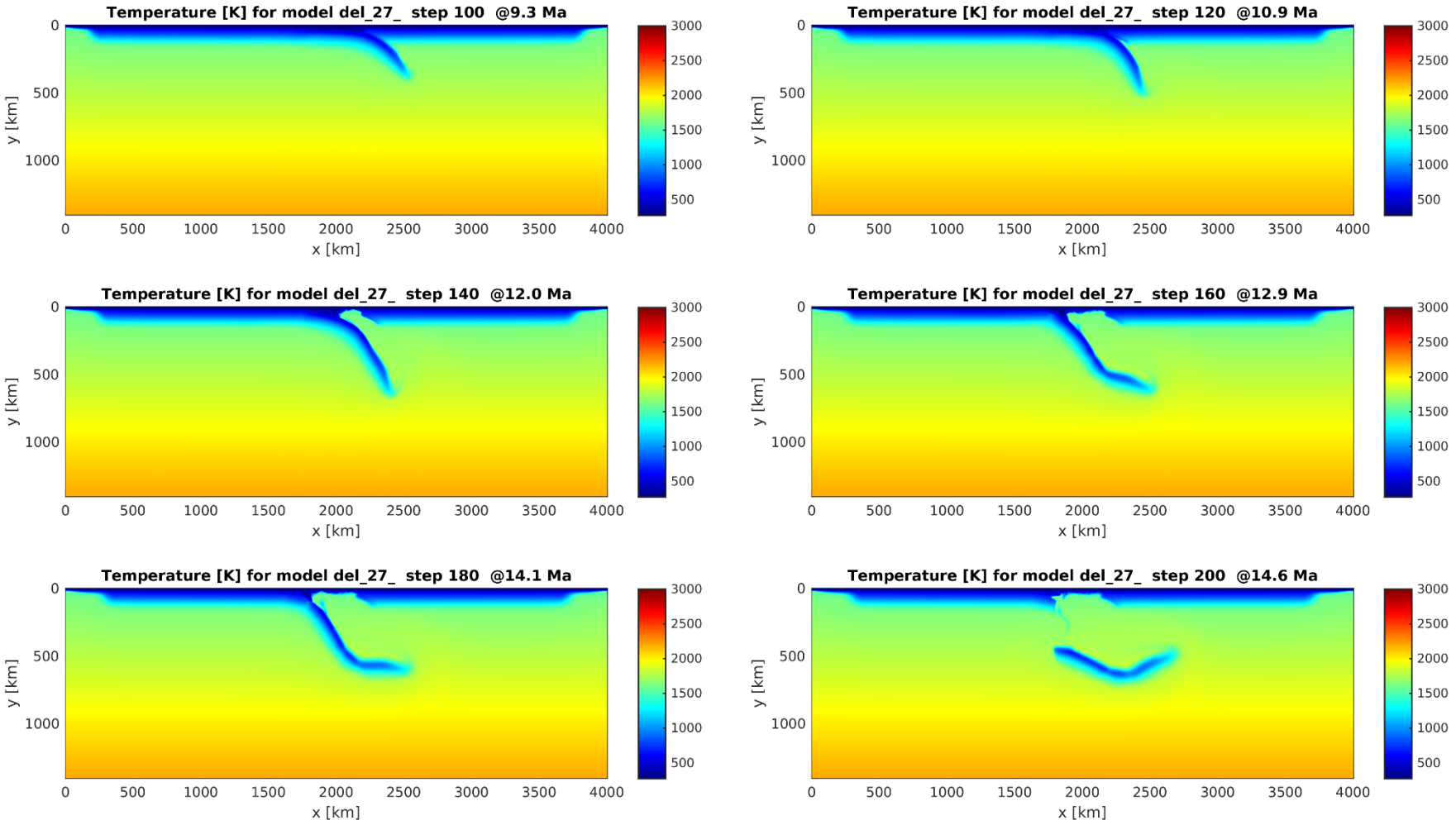

Figure G.4: Results of temperature field with x axis (km), y axis time (km) and temperature values are defined at color bar.

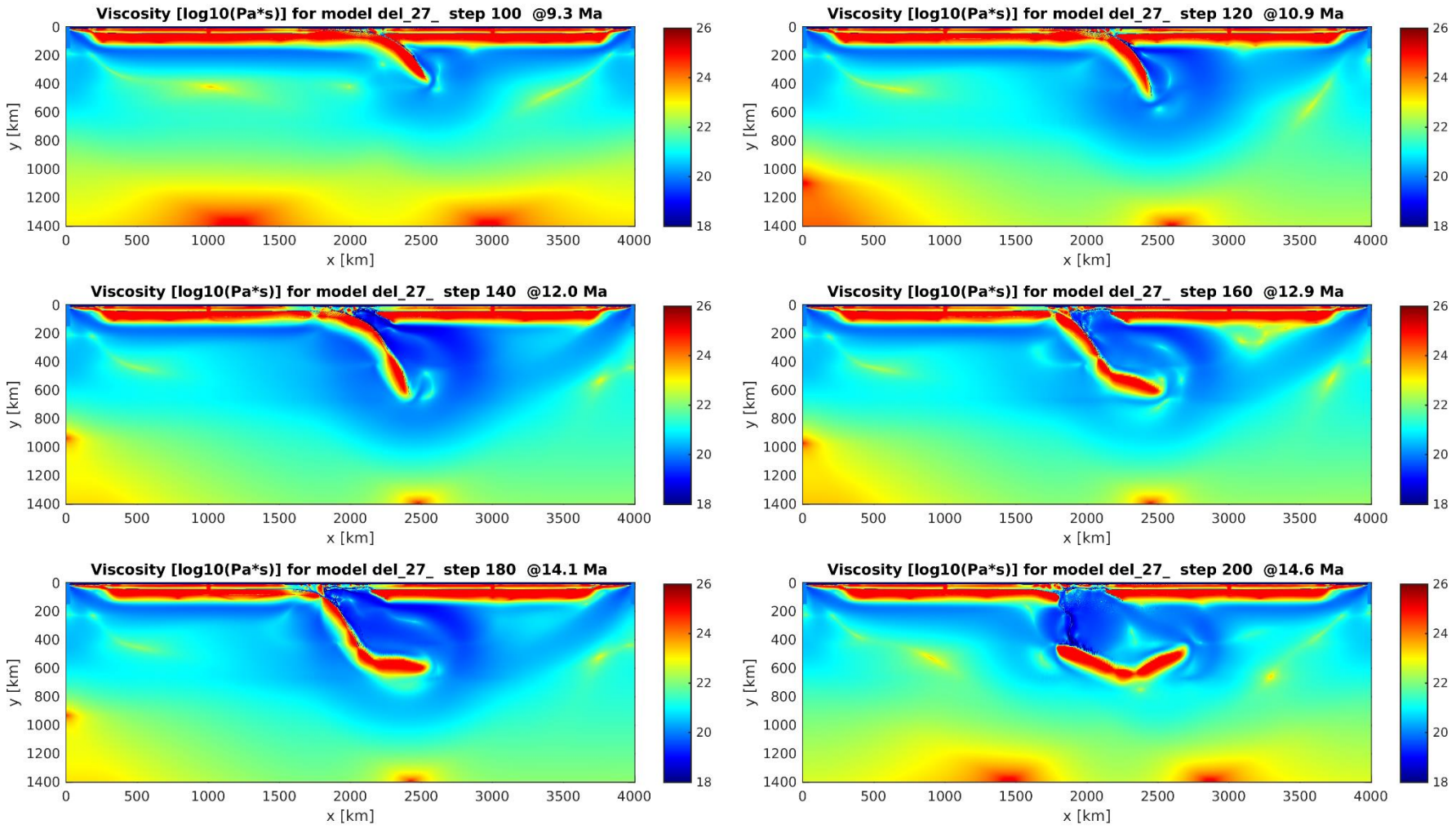

Figure G.5: Results of viscosity field with x axis (km), y axis time (km) and viscosity values are defined at color bar.

Appendix H

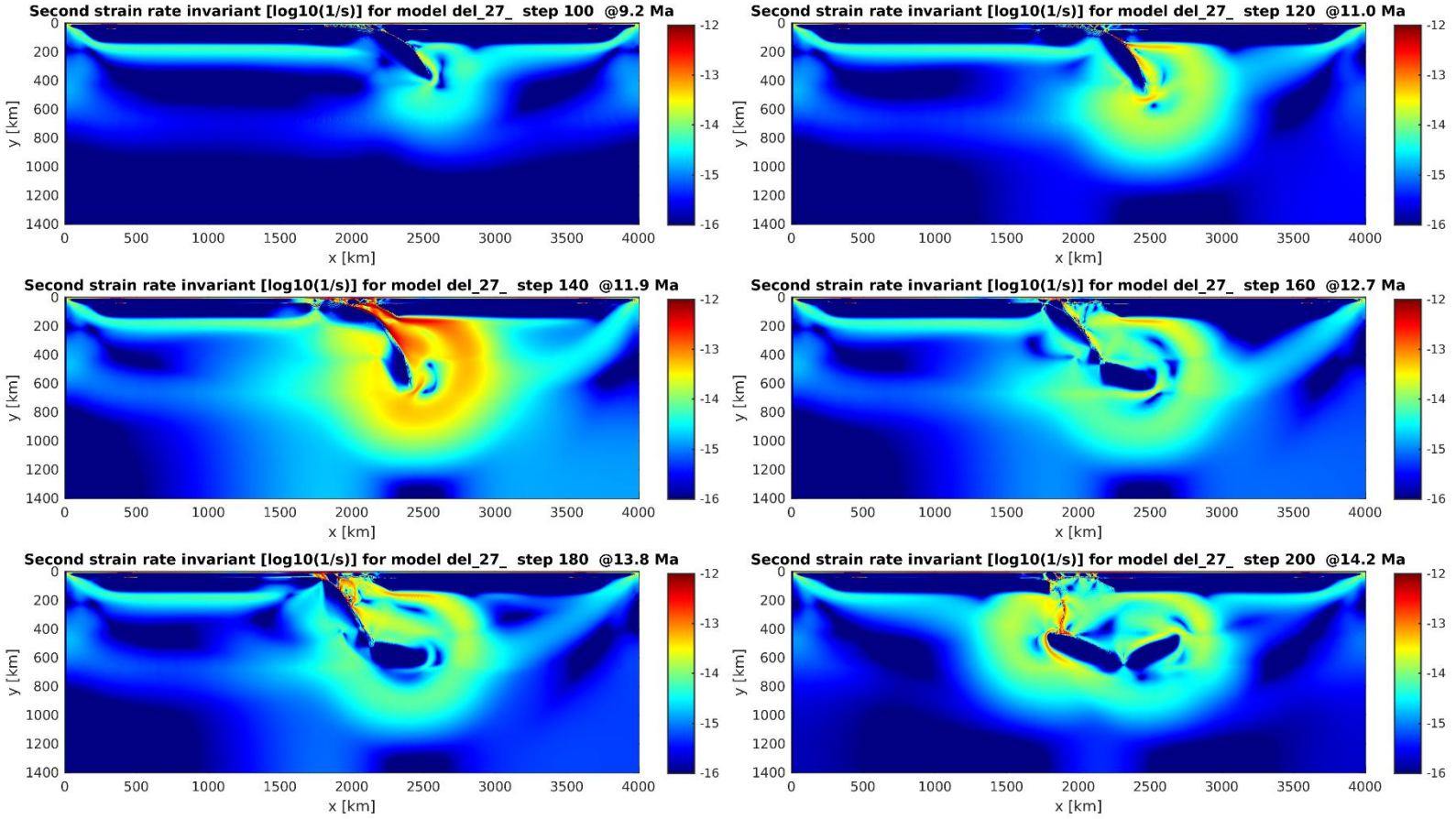

Figure H.1: Results of second strain rate invariants with x axis (km), y axis time (km) and second strain rate invariant (color bar.)

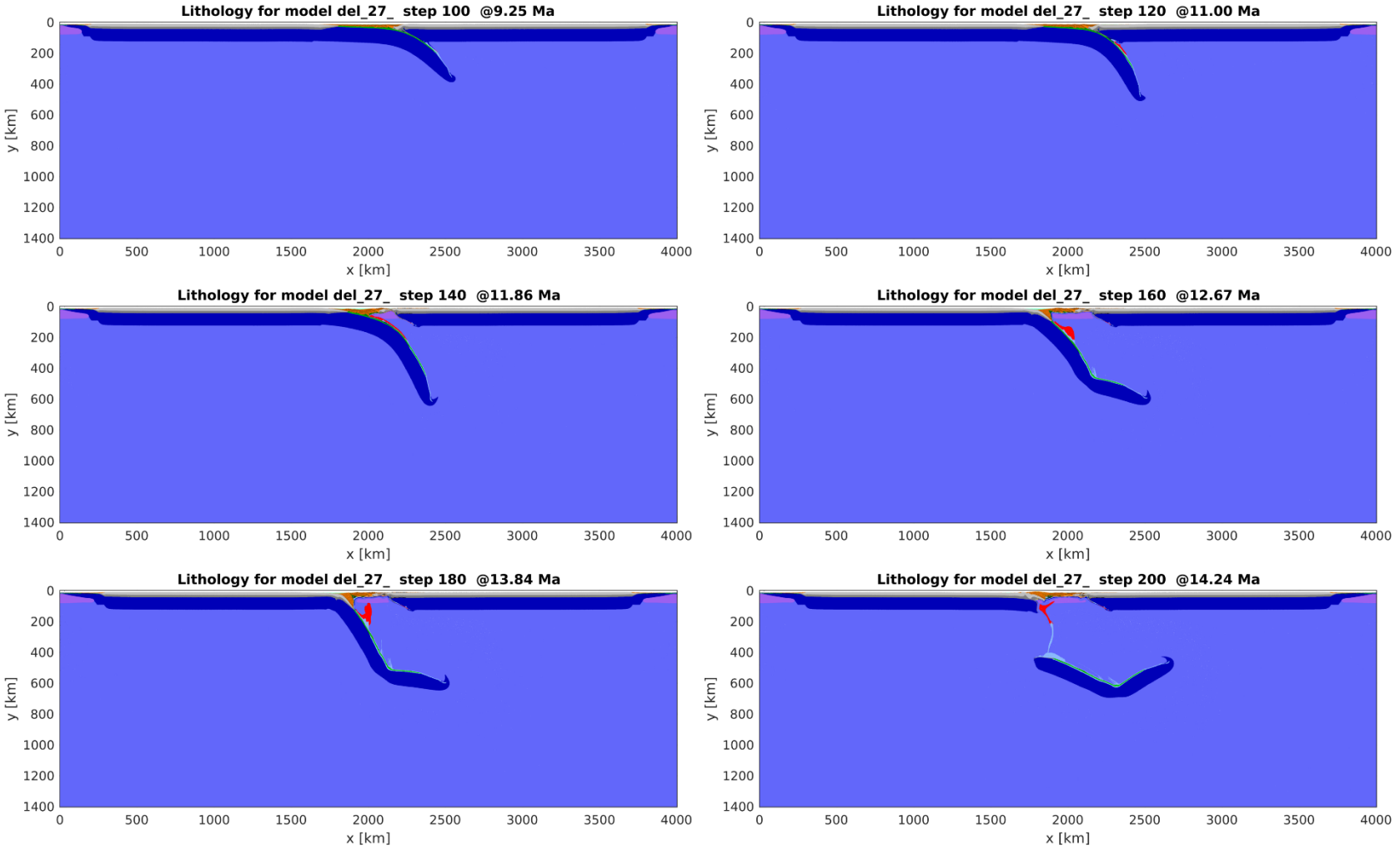

Figure H.2: Results of full domain material field with x axis (km), y axis time (km).

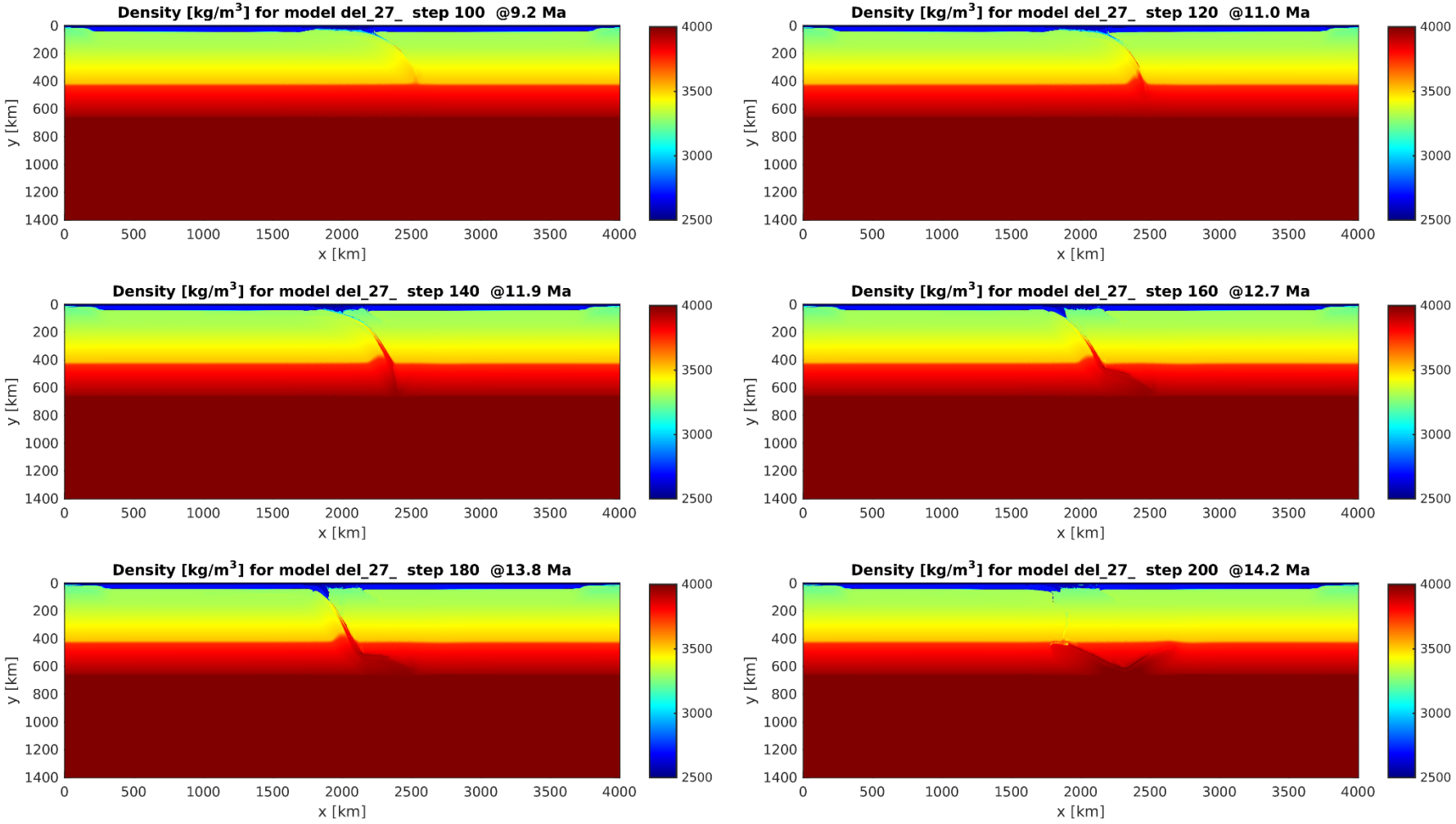

Figure H.3: Results of density field with x axis (km), y axis time (km) and density values are defined at color bar.

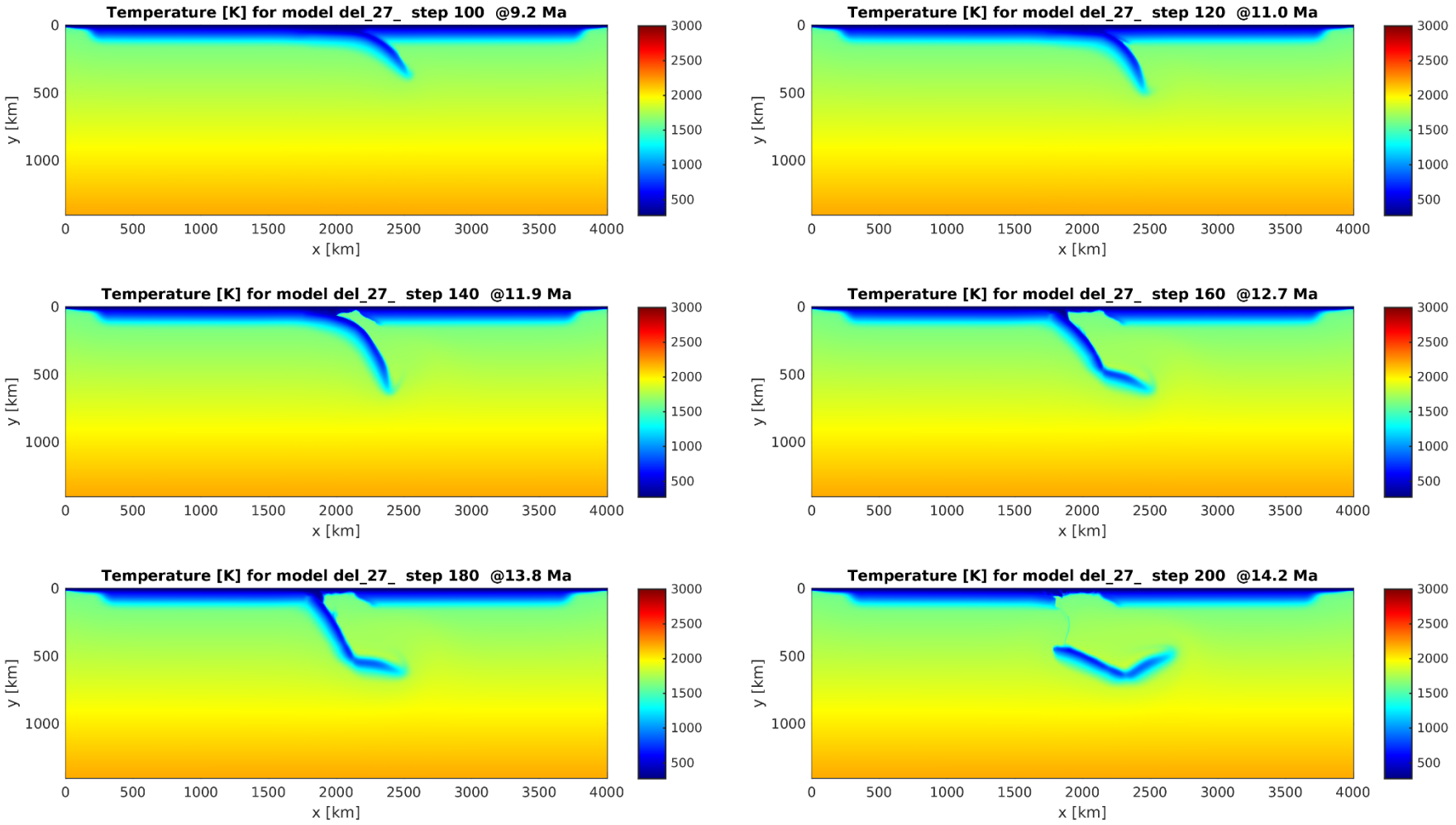

Figure H.4: Results of temperature field with x axis (km), y axis time (km) and temperature values are defined at color bar.

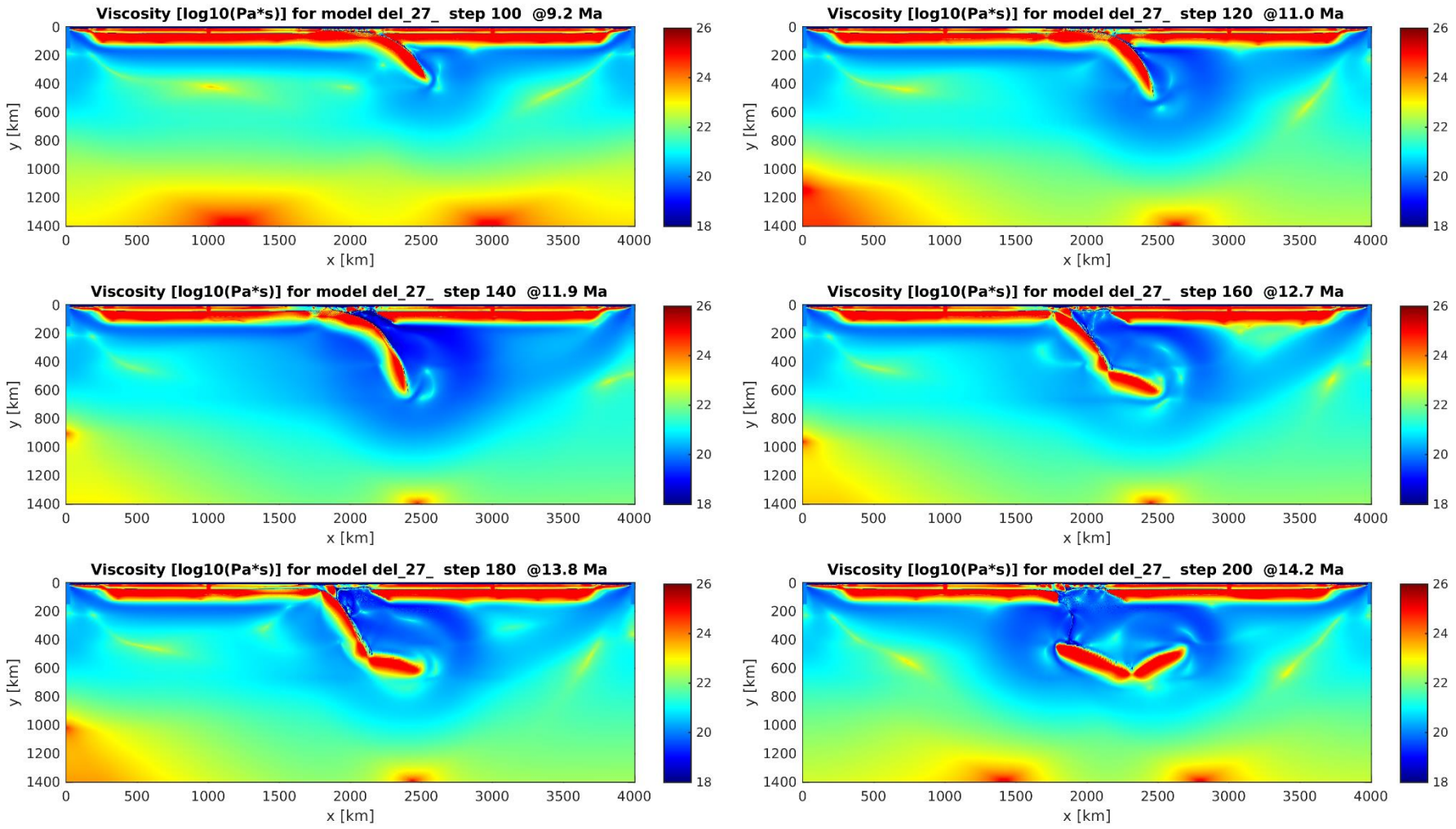

Figure H.5: Results of viscosity field with x axis (km), y axis time (km) and viscosity values are defined at color bar.

Appendix I

Table I.1: Rheological and thermal properties of modeled rock materials (after T. V. Gerya & Meilick, 2011).

Mechanical and Thermal Parameters	Density, (kg/m^3)	Flow law	Pre-exponential factor AD, [Pa^n s]	Activation energy E_A, [kJ/mol]	Activation volume V_A, [J/bar/mol]	Stress exponent (n)	Sine of coefficient of internal friction (sin(φ))	Heat production rate [J/kg]	$T_{solidus}$ [K]	$T_{liquidus}$ [K]	Radioactive Heating H_R, [μW/m^3]	Latent Heat H_L, [kJ/kg]	C_P [J/kg]	k [$W*m^{-1}*K^{-1}$]	Density ρ, [kg/m^3]
Sediments	2.60E+03	Wet Quartzite	1.97E+17	1.54E+05	3.00E-01	2.3	0.15	7.50E-04	**P < 1200 MPa:** 889 + 17900/(P+54) + 20200/((P+54)^2) **P > 1200 MPa:** 831 + 0.06*P	1262 + 0.009*P	1.5	300	1000	0.64 + 807/(T+77)*$e^{(0.00004*P)}$	2600
Upper Continental Crust	2.70E+03	Wet Quartzite	1.97E+17	1.54E+05	3.00E-01	2.3	0.15	7.50E-04	**P < 1200 MPa:** 889 + 17900/(P+54) + 20200/((P+54)^2) **P > 1200 MPa:** 831 + 0.06*P	1262 + 0.009*P	1	300	1000	0.64 + 807/(T+77)*$e^{(0.00004*P)}$	2700
Lower Continental Crust	2.70E+03	Wet Quartzite	1.97E+17	1.54E+05	3.00E-01	2.3	0.15	7.50E-04	-	1423 + 0.105*P	0.25	380	1000	1.18 + 474/(T+77)*$e^{(0.00004*P)}$	2800
Upper Oceanic Crust	3.00E+03	Gabbro	4.80E+22	2.38E+05	8.00E-01	3.22	0	7.50E-04	**P < 1600 MPa:** 973 - 70400/(P+354) + (7.78E+07)/((P+54)^2) **P > 1600 MPa:** 935 + 0.0035*P + 6.2E-06*P^2	1423 + 0.105*P	0.25	380	1000	0.64 + 807/(T+77)*$e^{(0.00004*P)}$	3000
Lower Oceanic Crust	3.00E+03	Basalt	4.80E+22	2.38E+05	8.00E-01	3.22	0.6	7.50E-04	-	1423 + 0.105*P	0.25	380	1000	1.18 + 474/(T+77)*$e^{(0.00004*P)}$	3000
Mantle Lithosphere	3.30E+03	WetOlivine	3.98E+16	5.32E+05	8.00E-01	3.5	0.6	7.50E-04	1394 + 0.133*P_{MPa} - 5.1E-06*P_{MPa}^2	2073 + 0.114*P	0.22	-	1000	0.73 + 1293/(T+77)*$e^{(0.00004*P)}$	3300
Asthenosphere	3.30E+03	WetOlivine	3.98E+16	5.32E+05	8.50E-01	3.5	0.6	7.50E-04	**P < 1600 MPa:** 973 - 70400/(P+354) + (7.78E+07)/((P+54)^2) **P > 1600 MPa:** 935 + 0.0035*P + 6.2E-06*P^2	2073 + 0.114*P	0.22	300	1000	0.73 + 1293/(T+77)*$e^{(0.00004*P)}$	3200
Reference	1, 2	10	10	10	1,10			1	4, 8	4	1	1, 2		3, 9	1, 2

1) Sine of coefficient of internal friction values when c=10MPa.

2) References; 1 = Turcotte & Schubert (2002); 2 = Bittner & Schmeling (1995); 3 = Clauser & Huenges (1995); 4 = Schmidt & Poli (1998); 5 = Hess (1989); 6 = Hirschmann (2000); 7 = Johannes (1985); 8 = Poli & Schmidt (2002); 9 = Hofmeister (1999), 10 = Ranalli (1995).

CURRICULUM VITAE

Name Surname **:** Mehmet Barış ŞEN

Place and Date of Birth **:** Istanbul-Turkey / 10.01.1994

E-Mail **:** senmeh@itu.edu.tr

EDUCATION **:**

- **B.Sc.** **:** 2018, Istanbul Technical University, Faculty of Mines, Geophysical Engineering Department
- **M.Sc.** **:** 2019, Istanbul Technical University, Eurasia Institute of Earth Sciences, Geodynamic Programme

PROFESSIONAL EXPERIENCE AND REWARDS:

- **2016 | Sumet Geology – Izmir/Turkey**
  30 days | Field work and data processing
- **2014 | Enerson Mühendislik – Istanbul/Turkey**
  30 days | Field work and data processing

PUBLICATIONS, PRESENTATIONS AND PATENTS ON THE THESIS:

- **Sen, M. B.,** Göğüş, O. H., 2019. Melt Production and Types in Mantle Drip Mechanism, Geophysical Research Abstracts, Vol. 21, EGU2019-1394-1, *European Geophysical Union General Assembly*, 7-12 April 2019, Vienna, Austria **(poster)**.
- **Sen, M. B.,** Göğüş, O. H., Ueda, K., 2019. Eriyik Üretimi Ve Manto Damlama Mekanizması Çeşitleri, MD-20178-24, *72st Geological Congress of Turkey*, 28 Jan- 01 Feb 2019, Ankara, Turkey **(oral)**.